Rock types and hydrocarbons distribution in an unconventional oil and gas field: Montney Formation, Septimus field, northeast British Columbia, Canada.

By

Stephany Hernandez Medina

A thesis submitted in partial fulfillment of the requirements for the degree of

Master of Science

Department of Earth and Atmospheric Science

University of Alberta

Abstract

The identification and characterization of flow units is as significant in unconventional reservoirs as it is in conventional reservoirs. In both reservoir types, this designation guides production designs by identifying high and low flow reservoir intervals. But in unconventional reservoirs – unlike conventional reservoirs – flow units may also predict the distribution of fluid type, related to the size and connectivity of the pore structures. In unconventional reservoirs, an improved understanding of how the pore system is affected by the depositional rock fabric or by diagenetic processes could lead to the comprehension of how these factors may have controlled the distribution of hydrocarbons.

This study focuses on the Montney play at and surrounding Septimus Field, in South Peace region, an example of a tight-oil/gas reservoir where hydrocarbon columns lack an obvious top seal and less dense fluids underlie more dense fluids. It applies a well-based data set, including wells with log suites and three wells with long cores, in investigate the roles of rock composition and fabric, mineralogy, diagenetic events, and petrophysical properties to develop. sedimentological and diagenetic models that aid our understanding of fluid distributions.

The dataset used in this study is a southwest-northeast transect of thirteen wells that penetrate the Montney Formation in the Septimus area. Our analysis applies a probabilistic cluster model (GAMLS) to well logs (gamma-ray, neutron porosity, and density) to identify and define rock types in the Montney Formation. Four end member-rock types (RT) were identified, and each rock type was initially defined by a unique log signature. Comparison to mineralogical, geochemical, and petrophysical (porosity-permeability relationship, pore throat and pore size) data developed from core samples indicates that each rock type is also characterized by unique rock properties.

Mineralogical analysis shows that the main mineralogical difference between the rock types is in the proportion of (%) K-feldspar + plagioclase, quartz and clays. Furthermore, these compositional differences are reflected in the fabric, mineral assemblage, and diagenetic events for each of the four rock types. Petrophysical analysis reflects that these compositional differences also had an impact on the porosity-permeability relationships, additionally to the presence of the bitumen saturation observed occluding the different pore types present for each rock type. We calculated capillary entry pressures under reservoir conditions and under different fluid properties to identify differences in the capillary entry pressure for the four rock types. Capillary entry pressures reflected the impact of the bitumen lining the pore throats of the rock types and in turn in the capillary entry pressures. We were able to confirm that rock types containing a medium to light oil have lower capillary entry pressures in comparison to the same rock types containing gas. In addition, this analysis confirms that oil with a lower surface tension penetrated more easily the pore throats of these rock types, occluding the remanent pore space and leading to production of gas, with a higher surface tension accumulate under oil (a denser fluid), leading to these unconventional fluid distributions at Septimus field.

In conclusion, we have demonstrated an effective workflow to define and map flow units in the Montney Formation. Our analysis shows that the Montney reservoir in Septimus field can be effectively classified from well logs as a combination of four rock types. We have also demonstrated that these rock types distinctly differ in their mineralogical composition, organic carbon content, rock fabric and, in turn, their petrophysical properties. Furthermore, we have demonstrated that rock types can be used to map petrophysical properties and compared to fluid distribution at a field scale.

Preface

This thesis was undertaken to identify the critical factors that discriminate between conventional and unconventional reservoirs and to develop predictive models for fluid distributions in unconventional reservoirs, in particular on the Septimus field of the Montney Formation in British Columbia. The objective of this research was to first identify through cluster analysis the different rock types present in the formation and understand the specific parameters associated with these rock types that force a reservoir system to be unconventional, and to have unusual fluid distributions.

Our cluster analysis subdivides the formation into four end member-rock types which are distributed along the southwest-northeast cross section through Septimus field. The mineralogical and petrophysical analysis of these four rock types identified important mineralogical and petrophysical differences between rock types, which are in turn reflected on the capillary entry analysis made at reservoir conditions under different fluid compositions.

The thesis is divided in four chapters; Chapter 1 describes the geological background of the Montney Formation and the depositional and diagenetic setting for the formation in Septimus field. Chapter 2 presents the methodology followed for each of the analyses, including the log interpretation applied to 13 wells in the study and the mineralogical, geochemical and petrophysical analyses applied to the three long cores studied for this research. Core sampling and description was done at the University of Alberta in Edmonton. Chapter 3 presents the results from the analysis described in Chapter 2. Chapter 4 presents the discussions related to each of the analyses and interpretations observed from the results in Chapter 3. In addition, this chapter describes the analysis made for capillary entry pressures for the different rock types at reservoir conditions and under different fluid compositions.

Stephany Hernandez was responsible for sample and data collection, log interpretation, and interpretation. Chenyang Feng provided the core descriptions and facies interpretations that are incorporated into this analysis. N. Vaisblat provided guidance and assistance with well log interpretation. R. Kofman provided training and assistance with sampling preparation, and porosity analysis to S Hernandez and conducted permeability measurement. Mathew Power provided QEMSCAN analyses through Vidence and SGS companies.

Stephany Hernandez composed the manuscript, with assistance from N. Vaisblat with respect to text on well log interpretation and from C. Feng with respect to facies descriptions and interpretations. Dr. Harris provided guidance and feedback on the interpretation of data and on the preparation of the thesis. Dr. Harris and Dr. Benoit Rivard provided funding for the conclusion of this project. This thesis will be modified in preparation for submission to a journal for publication.

Acknowledgements.

First, I would like to acknowledge CONACYT-SENER; without the funding provided by these two organizations, none of this would have been possible.

I would like to acknowledge and thank my supervisor Dr. Nicholas Harris for giving me the opportunity to expand my knowledge in an area that I am very passionate about. I want to thank him for his guidance throughout my research and for all the support he gave me since the beginning of this adventure. I would like to thank to my co-worker and now Dr. Noga Vaisblat for all the knowledge and support she gave me, her passion and love for science always inspired me and I am grateful for having the experience to work with someone like her.

I would also like to thank to the personnel from the University Mark Labbe, Randy Kofman and the personal from NanoFAB, thanks to them for their technical help this project was successful.

I would like to give a special acknowledgement to Dr. Benoit Rivard for the amazing support he gave me with funding. Without his help and Dr. Nicholas this project would not have been concluded. Thanks to Jilu Feng for his knowledge.

I want to thank to the undergraduate students Paige Fisher, and Brielle Anderson, and Youssef Zaharan (graduated IPG) – guys, without you those cores would have taken for ever.

I would like to give a special thank to my colleagues Evan, Chris, Haolin, Elaine, Martin, Victoria, Hui, and Chenyang – thank you for your friendship, in particular Dan – Dan, thanks for your friendship, support and for making me feel less homesick from time to time. I really appreciate it.

I would like to give an eternal thank to my closest friends, Pedro Navarro, Aurora Duran, Daniel Tapia, Gerardo Figueroa, Alessandra Di Castro, and Arturo Mora - guys, you deserve a standing ovation because without your support I would not have been able to go through all this, specially this last year, you really were my cheering squad. Finally, I want to thank and give all my appreciation to my family; mom, dad, Jair, and Kevin – thank you so much for everything, thank you for your support, for your love but most of all thank you for always being there for me.

A final acknowledgement to NSERC DISCOVERY GRANT No. NSERC RGPIN-2018-05695 for supporting the analytical part of the project.

Table of Contents

List of Tables.

List of Figures.

Chapter 1 - Introduction

The connection between rock properties and hydrocarbon distribution is a fundamental problem in unconventional reservoirs, in particular for tight -hydrocarbon systems. Tight -hydrocarbon systems are characterized by nano-scale pore networks, which affect capillary entry pressures in the rocks. This, in turn, influences fluid distribution present in the pore system. Our study focuses on the Montney Formation at Septimus field, an example of a tight-oil/gas reservoir where hydrocarbon columns lack an obvious top seal and less dense fluids underlie more dense fluids. More specifically, we test our dataset for links between petrophysical properties of the reservoir and fluid distributions.

The extrapolation of core data to field-scale fluid distributions in unconventional reservoirs presents an additional problem because of two factors: (1) the inherent heterogeneity of mudstone sequences, whether shales such as the Duvernay Formation (Knapp et al., 2017; Harris et al., 2019; Dong et al., 2020) or siltstones such as the Montney Formation (Vaisblat, 2020; Vaisblat et al., 2021); and (2) the relatively sparse sampling density with comprehensive petrophysical data sets. Because we want to compare petrophysical properties to fluid distributions at the field scale, we develop and apply a three-step methodology. First, we apply a well log interpretation approach to identifying rock types present in the reservoir. Second, we use the rock type analysis to select cores samples for mineralogical, geochemical and petrophysical analysis. As part of this step, we examine whether the samples grouped into clusters by log interpretation are defined by meaningful differences in rock properties. Third, we compare rock typing in combination with petrophysical properties to fluid distributions, in order to identify specific properties that may influence distinctions of oil-rich and gas-rich sections of the reservoir.

Our analysis applies a probabilistic cluster model analysis through well logs to identify and define rock types in the Montney Formation. Data on rock mineralogy and rock fabric from QEMSCAN and thin section analysis, total organic content from geochemical analysis, and pore system properties that include porosity, permeability, pore throat size and pore size, were drawn from samples from three wells with core in the Montney interval at Septimus field. These data were used then to corroborate distinctions between rock types identified through the cluster model and to identify differences between a well that produces oil and a well that produces gas. Then,

capillary entry pressure estimations were calculated for the rock types under reservoir conditions, accounting for differences in fluid properties between a medium to light oil and gas.

1.1 Geological background

1.1.1 Age and setting

The Lower Triassic Montney Formation is a major oil and gas reservoir in the Western Canada Sedimentary Basin (WCSB) (Figure 1.1). The WCSB comprises the eastern Canadian Cordillera and two major sedimentary basins: the Alberta Basin, which was on the continental margin in the Early Triassic, and the intracratonic Williston Basin (Crombez et al., 2017). A large sub-basin, termed the Peace River Embayment, was part of the Alberta Basin at the time of Montney deposition.

The Montney Formation was deposited as a west-dipping clastic wedge of Early Triassic age during a major transgressive – regressive cycle, deposited unconformably onto an eroded Carboniferous and Permian surface (Edwards et al., 1994). The Montney has been subdivided into three main members: the Lower Member, of Griesbachian to Dienerian age, which is an overall transgressive succession and is correlated with the Early Triassic transgressive-regressive cycle; the Coquina Dolomite Middle member, of Dienerian and Smithian ages, which is characterized by a major basin-ward, westward shift of the Montney shoreline, and the Upper Member, of Smithian to Spathian age, which is correlative with two, shorter-duration third-order transgressive sea level cycles (Figure 1.2) (Davies et al., 1997; Dixon, 2000; Moslow, 2000; Zonneveld and Moslow, 2018). The Montney Formation rests on a major unconformity upon the Permian Belloy Formation and is unconformably overlain by the phosphatic-rich member of the Doig Formation in the most eastern section of the basin and the Sunset Prairie Formation (further west in northeastern British Columbia. Farther east into Alberta, where the Doig Formation is absent, the Montney Formation is overlain by the Jurassic Gordondale Member of the Fernie Formation (Crombez et al., 2017; Vaisblat et al., 2021).

Depositional facies of the Montney Formation are interpreted to have varied from fine-grained shoreface, shelf siltstone, to shale, fine-grained sandstone turbidites, organic-rich phosphatic shale, and submarine fans deposits, deposited in water depths that generally increased from east to west (Davies et al., 1997, 2018; Zonneveld et al., 2011; Playter, 2013; Crombez et al., 2017; Euzen et

al., 2018; Zonneveld and Moslow et al., 2018). Grain size distributions in the Montney suggest that it was deposited in an arid climate, sourced from wind-blown, recycled quartz-rich shield material from the east (Vaisblat et al., 2021; Edwards et al., 1994; Davies et al., 1997). Sediments were deposited in a generally anoxic to dysoxic environment that experienced short-term fully oxygenated events recorded by several bioturbated intervals (Nassichuk, 2000; LaMothe, 2008; Zonneveld et al., 2010a, b, 2011; Moslow and Zonneveld, 2012; Playter, 2013; Crombez, 2016; Crombez et al., 2017).

Burial history models indicate that the Montney Formation experienced relatively shallow burial (no deeper than 1000 m) from the time of deposition through the end of the Jurassic (~100 million years period) (Ness, 2001; Ducros et al., 2017; Rohais et al., 2018). At the start of the Laramide Orogeny, which began in the Early Cretaceous, rapid subsidence and high sedimentation rates occurred in the WCSB, and at the peak of the Laramide Orogeny, the Montney reached its maximum burial depth and hence maximum temperatures (ca 57.8 Ma). The Montney Formation has been subjected to continuous uplift and erosion from the Paleocene to present days (Willett et al., 1997; Ness, 2001; Ducros et al., 2017; Rohais et al., 2018).

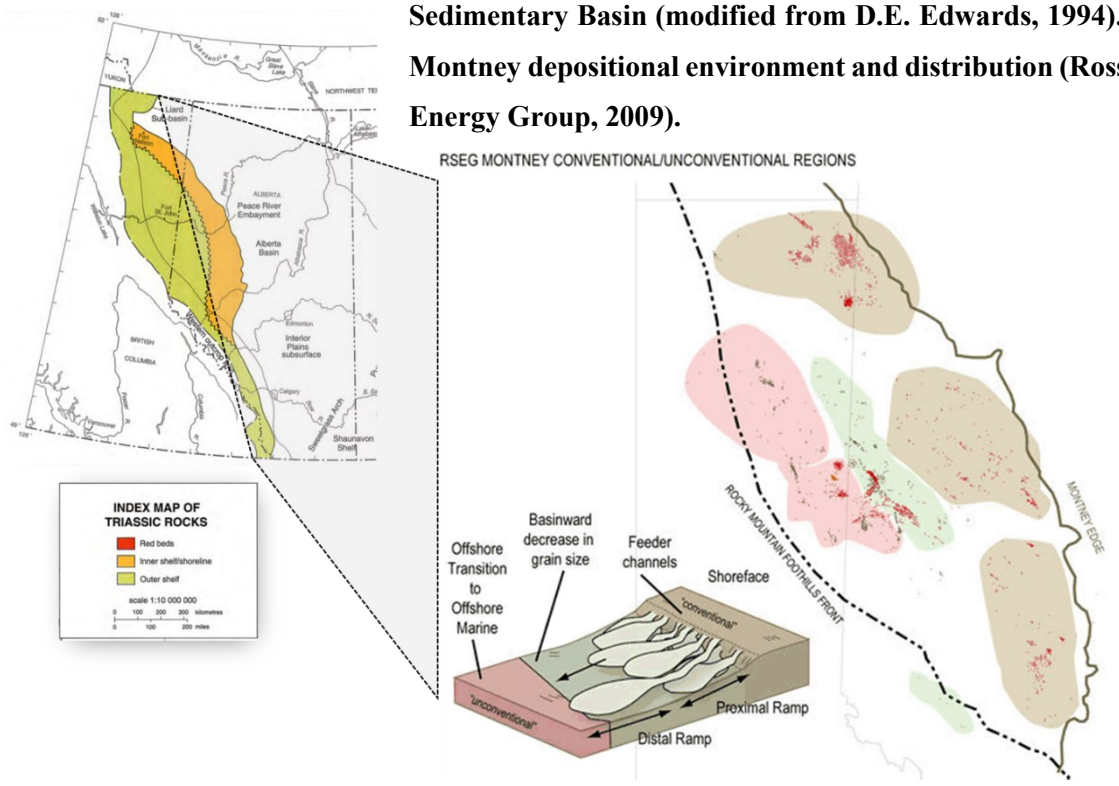

Figure 1.1 Left, Triassic rocks in the Western Canada Sedimentary Basin (modified from D.E. Edwards, 1994). Right, Montney depositional environment and distribution (Ross Smith Energy Group, 2009).

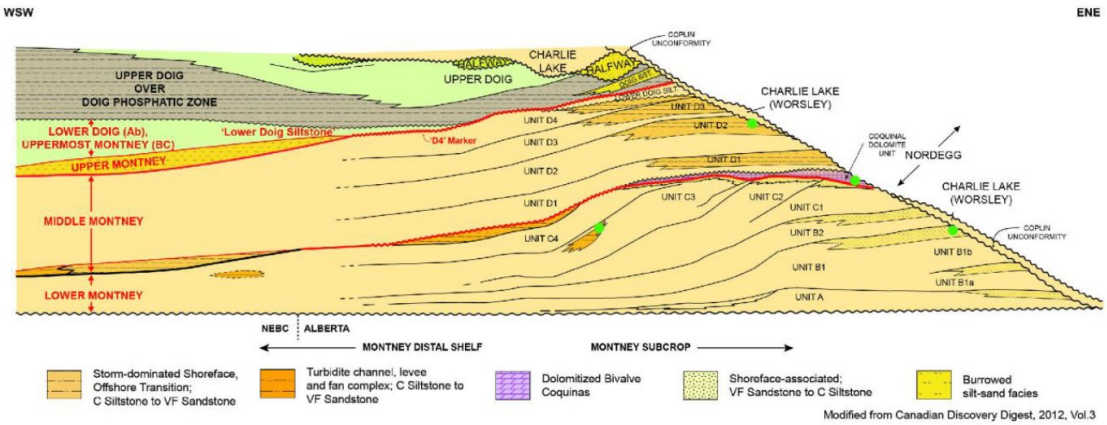

Figure 1.2 Montney's stratigraphy and depositional environments, representing from bottom to top the three main members. The Lower Member is characterized by a major transgressive succession that divides it from the Middle Member. The Upper Montney is characterized by sediments deposited on a storm-dominated shoreface and offshore transition (Seifert et al., 2015 modified from Davies).

Sedimentary Diagenesis - Diagenetic processes are significant to both rock composition and petrophysical properties. Sediments in the Montney consist primarily of detrital quartz, carbonates, and feldspars with lesser amounts of mica and clays. Minor amount of plagioclase, glauconite, zircon, and spinel are also present as detrital grains (Vaisblat, 2020). Calcite, dolomite, feldspar, and quartz cements are present. Pyrite also has been reported throughout the Montney as well as authigenic clays like illite, chlorite and illite-smectite (Vaisblat et al; 2017).

To understand the different diagenetic phases in the Montney Formation, it is important to consider the chemical conditions (pH, temperature) during diagenesis at the time. During the Early Triassic, oceanic waters were acidic, hot, and irregularly oxygen-depleted, and at the time of Montney Formation deposition, anoxic or dysoxic bottom water conditions have been interpreted based on the absence of trace fossils, sulfide pseudomorphs after pollen grains and spores, and enriched concentrations of trace elements (such as U, V and Mo) (Zonneveld et al., 2010; Crombez et al., 2017). A first stage of carbonate dissolution took place under these conditions, which have also been associated with dissolution of underlaying Permian carboniferous strata, possibly also related to hydrothermal fluid involvement (Vaisblat et al., 2021; Nassichuk, 2000; Liseroudi et al., 2017).

In the Montney Formation, the main diagenetic processes consist of porosity destruction through compaction and cementation and porosity enhancement through dissolution of grains and cements. Vaisblat (2021) distinguishes an early, shallow burial diagenetic stage from late, deep burial

diagenesis in the Montney Formation. It was during this early shallow burial stage that the Montney Formation lost some of its primary porosity through mechanical compaction and in lesser amount through cementation (mainly calcite cement). Petrographic evidence suggests that at that time, the rock had an open pore network that allowed space for massive fluid flow and mineral precipitation (Vaisblat et al., 2021).

Reduction of primary porosity in the Montney occurred under shallow burial conditions, when an influx of sea water led to the precipitation of overgrowths of quartz, dolomite, and clays. Authigenic clays were not affected by compaction, having formed after the quartz replacement and dolomite precipitation. Ferroan dolomite is common in the Montney, infilling primary porosity as a microcrystalline cement, euhedral dolomite rhombs, and partial and complete replacement of quartz. Precipitation of ferroan dolomite was a later diagenetic event, thus not affected by compaction (Vaisblat et al., 2021; Nassichuk, 2000). Deep burial diagenesis played a minor role and took place through pressure solution and precipitation of a late, secondary quartz cement phase (Vaisblat et al., 2021).

Most of the diagenetic processes affecting the Montney reservoir took place during shallow burial (<1000 m), and the precipitation of such large volumes of cements led to the homogenization of rock composition, greatly limiting variability between the lithofacies.

1.1.2 Study Area

This study focuses on the Montney play, in the South Peace region. The Montney play trend covers approximately 1.5 million hectares (3.8 million acres). The Montney Formation is up to 320 m thick and is an unconformity-bounded marine succession with mostly fine to locally coarse siltstone, that is bituminous, and dolomitic or calcareous (Zonneveld et al., 2011; Zonneveld and Moslow, 2014; Panek, 2000). Both the Upper and Lower Montney are horizontal drilling objectives (Adams, 2011; Oil and Gas Division Ministry of Energy and Mines).

Over the years, the Montney production has focused in two sub-regions, the Montney Regional Heritage Field, situated south of Fort St John, and the North Montney Field, northwest of Fort St John, east of the Rocky Mountain front range (Proverbs et al., 2018).

Production in the South Peace region comes primarily from the Dawson Creek/Fort St John area. In this region (Figure 1.3), recurrent compression during the Late Cretaceous associated with the

Late Carboniferous Dawson Creek Graben Complex influenced deposition of sediments, including the early Triassic Montney successions (Proverbs et al., 2018; Moslow, 2000).

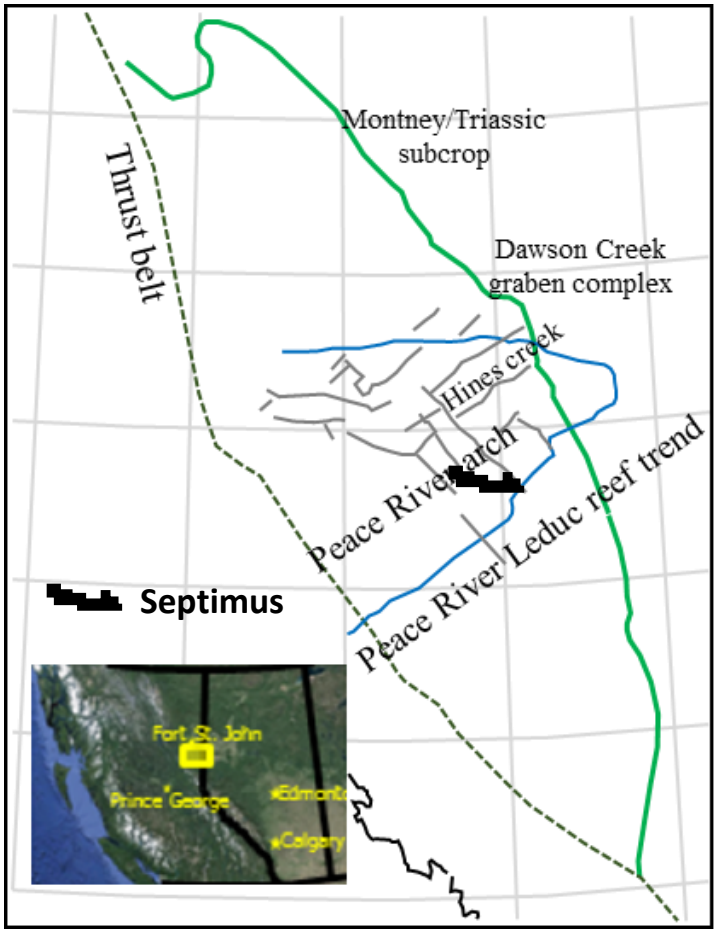

Figure 1.3 Major geological features associated to the area (after Davies, 1997a). It includes the eastern limit of the Rocky Mountain Fold and Thrust Bell, and the outline of the Peace River Arch. Depicted are some of the major faults that comprise the Late Carboniferous, Dawson Creek Graben Complex and figure in black is represented Septimus field. (modified from Proverbs et al., 2018; O'Connell et al., 1990; Barclay et al., 1990).

The focus of this study is Septimus field, with an area of approximately 2100 km^2 consisting of a single pool (Montney A pool – Upper and Lower Montney) that produces both dry and wet gas and has a small oil column in part of the field (Figure 1.4) (BC Ministry of Natural Gas Development, 2014). The field is located northwest of Heritage Field, approximately 19 km southwest of the city of Fort St John. Septimus field has been operated through the years by three companies, ARC Resources Ltd. (ARC), Canadian Natural Resources Ltd. (CNRL), and Crew Energy Inc. (BC Ministry of Natural Gas Development, 2014). ARC land holdings by 2015 were ~615 net sections (159 000 hectares), getting a daily production after three months during 2015 of 353 MMcf/day of natural gas, 3155 barrels/day of oil and 1947 barrels/day of natural has liquids (ARC Resources Ltd, 2015). Septimus field is a major project for CNRL, which has focused

drilling on the liquids-rich area. The Septimus area is one of the most active areas for Crew Energy Inc., representing 73% of its overall corporate reserves; Crew has drilled wells testing as high as 15 MMcf/day with an EUR per well of 5 Bcf (Crew Energy Inc., 2015).

We have focused on a southwest-northeast transect of thirteen wells that penetrate the Montney Formation in the area (Table 1.3, Figures 1.5 and 1.6). Of these wells, three had long cores available for sampling and analysis; two are gas producers, and one is an oil producer at the Montney interval. A comparison of these wells in terms of well log and petrophysical properties was a major objective of this research.

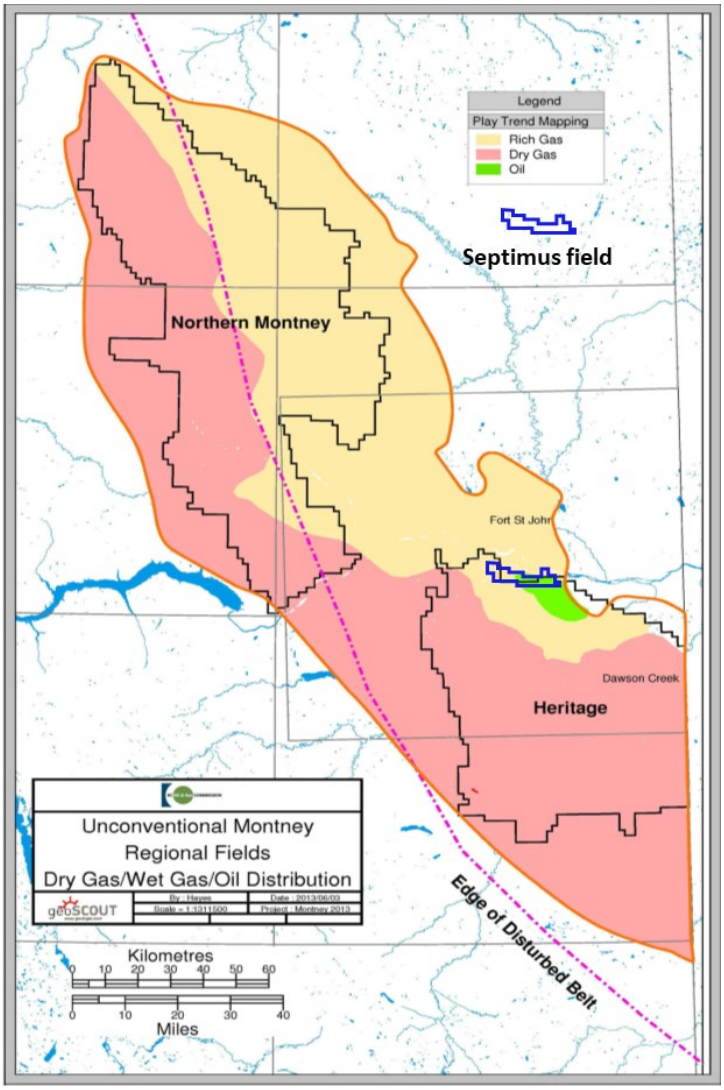

Figure 1.4 Montney Regional Fields and dry/wet/oil distribution (BC, Oil and Gas Commission Hydrocarbon, 2012).

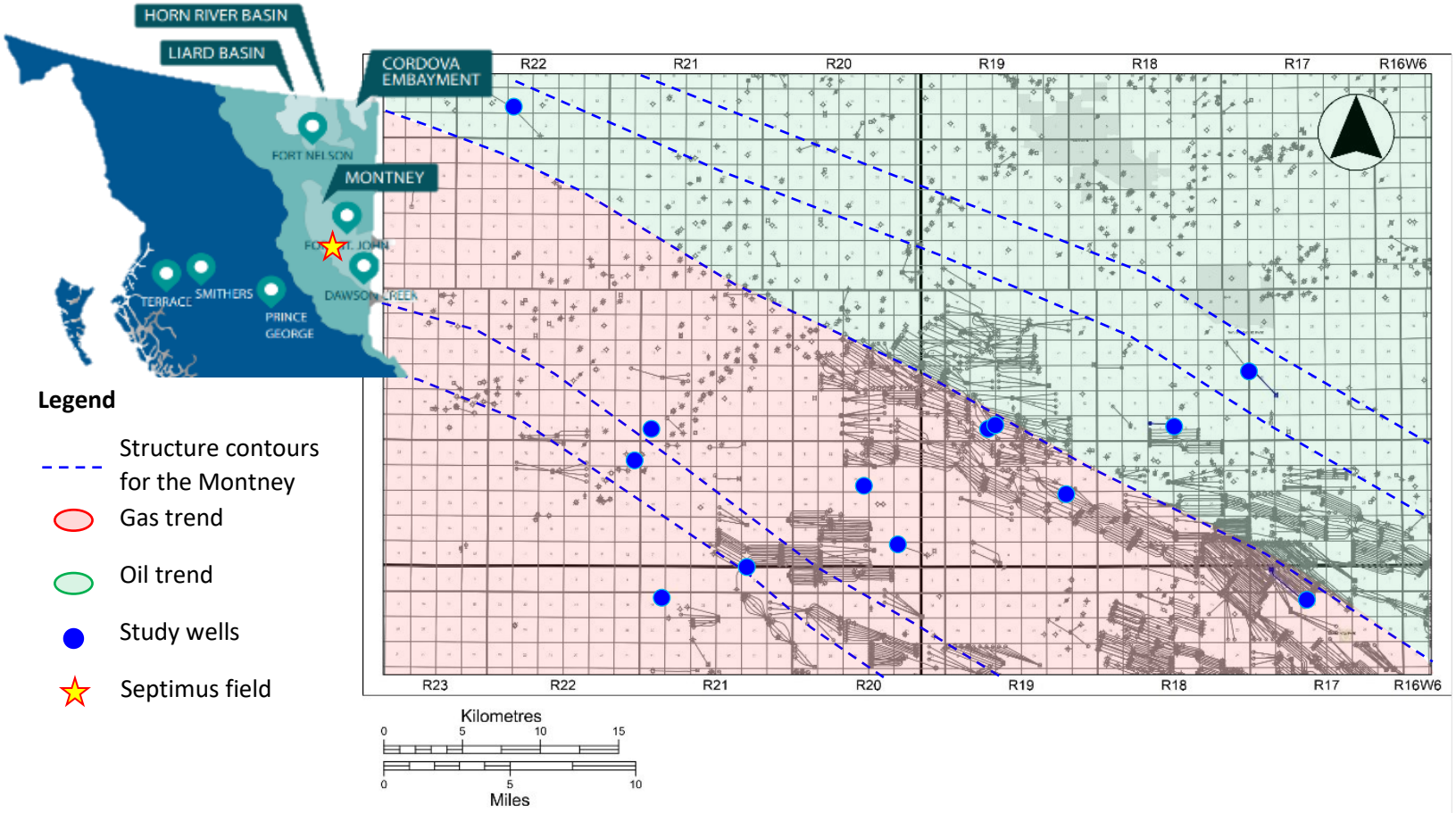

Figure 1.5 Location map of study area (yellow star in the inset map, upper left) covering Septimus pool and surroundings. Wells used for the petrophysical cluster analysis are in blue. Red and green areas are schematic representations of the gas and oil trends, respectively (based on well production reports and structural configuration for the Montney (modified from WCSB Gas Liquids & Light Oil Fairways Study, 2013, Canadian Discovery Ltd.)

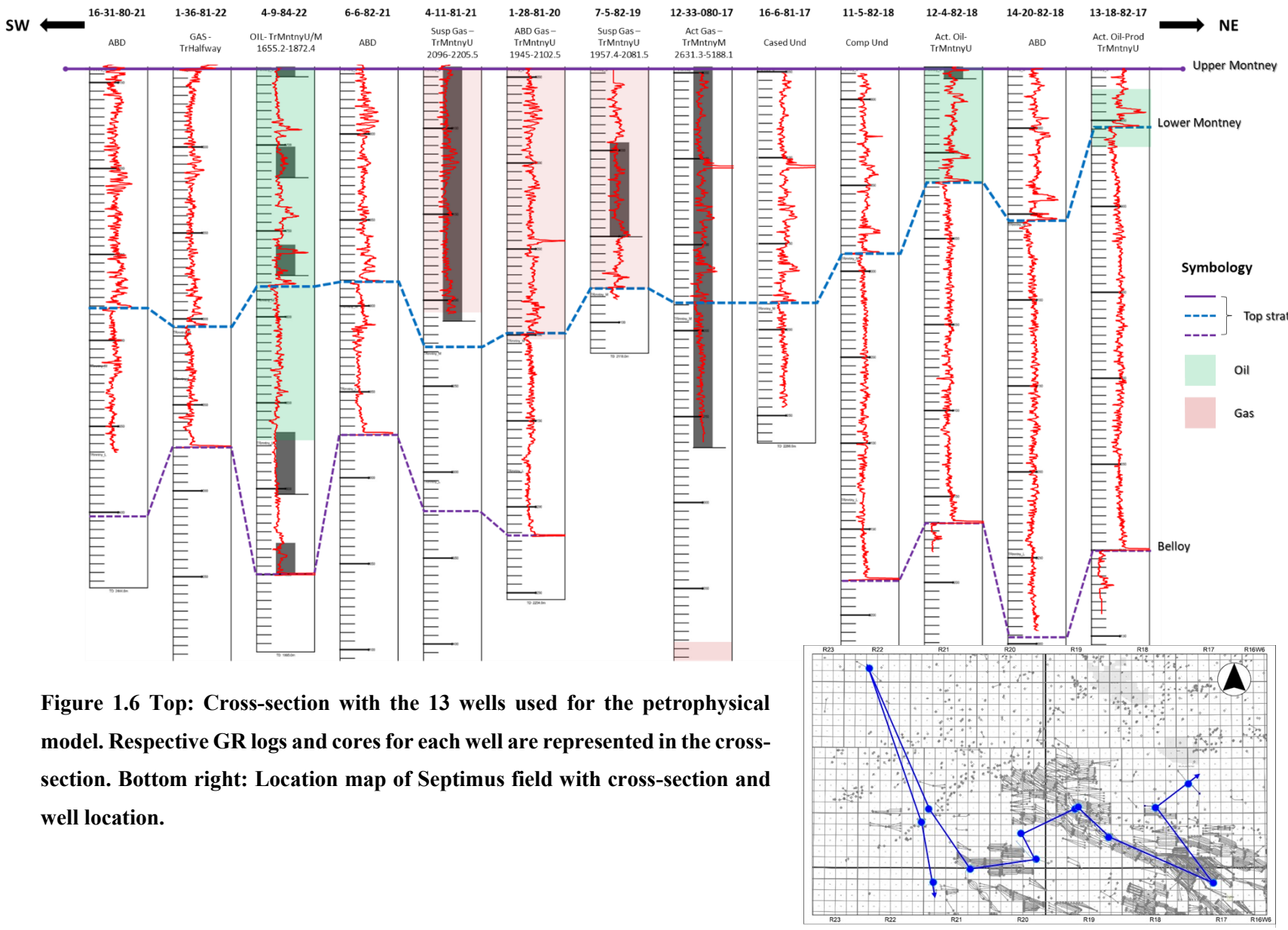

Figure 1.6 Top: Cross-section with the 13 wells used for the petrophysical model. Respective GR logs and cores for each well are represented in the cross-section. Bottom right: Location map of Septimus field with cross-section and well location.

Table 1.3 Dataset used from the 13 wells located at Septimus field. Arrows represent the 3 wells with cores at Montney interval, and which were selected for further analysis.

Well ID	Logs	Survey	Core Interval	No. Cores	Interval Recovery
16-31-80-21	GR, Nphi, and Rob	Vertical well			
1-36-81-22	GR, Nphi, and Rhob	Vertical well			
4-9-84-22	GR, Nphi, and Rhob	✓	1631-1660.3m 1701-1719m 1758-1776m 1867-1903.2m 1931.5-1949.5m	2 1 1 2 1	29.4m 18m 18m 36.2m 18m
6-6-82-21	GR, Nphi, and Rhob	✓			
4-11-81-21	GR, Nphi, and Rhob	✓	2030-2066.30m 2066.30-2103m 2103-2139.75m 2139.75-2175.90m 2175.90-2212.15m	1 1 1 1 1	36.30m 36.70m 36.75m 36.15m 36.25m
1-28-81-20	GR, Nphi, and Rhob	✓			
7-5-82-19	GR, Nphi, and Rhob				
12-33-080-17	GR, Nphi, and Rhob	✓	2046-2154.91m 2154.91-2186.34m 2186.34-2268.09m	1 1 1	108m 31m 81m
16-6-81-17	GR, Nphi, and Rhob	Vertical well			
11-5-82-18	GR, Nphi, and Rhob	Vertical well			
12-4-82-18	GR, Nphi, and Rhob	✓			
14-20-82-18	GR, Nphi, and Rhob	Vertical well			
13-18-82-17	GR, Nphi, and Rhob	Vertical well			

Well cores used for further analysis and identification of rock types (See table 2.3.1)

Chapter 2 - Methods

2.1 Log interpretation - GAMLS model

We used GAMLS to identify rock types end -members in the Montney formation. GAMLS (Geological Analysis via Maximum Likelihood System) performs a probabilistic cluster analysis of well logs. During clustering, every depth step is assigned to one or more modes (rock-types end members) with a probability between 0 and 1. (Eslinger et al., 1996; Figure 2.1.1). High mode probability assignment values indicate a higher likelihood of that depth belonging to that rock type. Depths that have two or more rock types assigned to them are interpreted to be mixtures of these rock types (Figure 2.1.1b). Input variables included the Gamma ray (GR), neutron porosity (NPHI) and the bulk density (RHOB) well logs.

For this study we required the software to identify four rock types with an unsupervised cluster analysis performed on all thirteen study wells. After assigning each end member a lithology, we identified the depth intervals in which a single rock type was allocated a probability of 70% or higher (Figure 2.1.1b). Following a meticulous depth shift, these intervals were identified in the three cores and samples from these depths were taken for further analysis. Selecting samples that are assigned to a specific rock type with a probability of 70% or higher assures that the properties investigated are mostly representative of a single rock type rather than a mixture of rock types. A comparison of samples selected from the different rocks types enables us to verify the mineralogical, geochemical and petrophysical differences and similarities between them.

2.2 Core logging and rock type association

Detailed sedimentological core log descriptions of the three cores analyzed for this research was provided by Chenyang Feng, who performed a detailed 1 (cm) description and interpretation of the lithofacies observed at the Montney Formation interval, identifying, and classifying facies on the basis of lithology, rock fabric, and sedimentary structures. The facies identified in core description where compared to rock types identified by the GAMLS analyses for well 100/04-11-081-21W6/00 to test whether there was any correspondence between rock types and lithofacies.

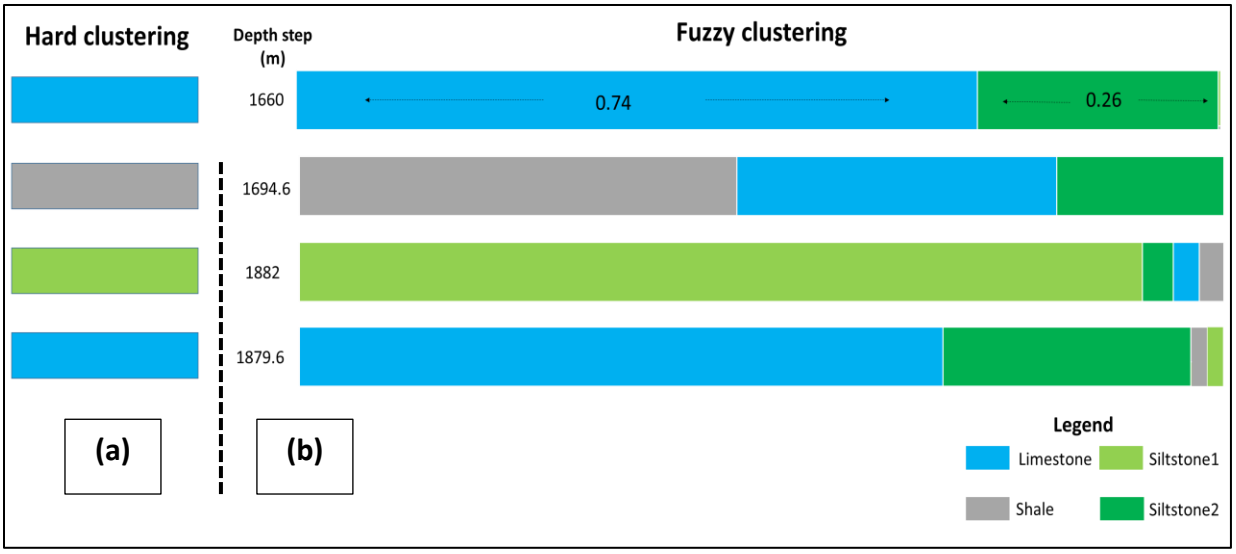

Figure 2.1.1 (Modified from Vaisblat, 2020) GAMLS cluster analysis is used for classifying and grouping samples based on similarities. (a) Representation of a hard clustering: data is exclusively assigned to one rock type. (b) Graphic representation of a fuzzy clustering used in this study. Each depth step is assigned one or more rock types and each rock type is assigned a lithology. The lithological description of each depth step depends on its probabilistic assignment of end members. Depth 1660 m is composed mostly of siltstone (74%) and lesser amount of limestone (26%) and can be classified as a calcareous siltstone. Intervals that were assigned a single rock type with a probability of 70% or higher were selected for further analysis (e.g. 1660 and 1882 m).

2.3 Quantitative analysis of minerals – QEMSCAN analysis

Mineralogical data on core samples were obtained from QEMSCAN analysis. This is an automated system that provides mineralogical and compositional data with the application of a scanning electron microscope coupled to up to 4 x-ray spectrometers that image and map the composition of a sample. Analysis was carried out at SGS Canada Inc. and at Vidence Inc. both in Burnaby, BC, Canada. A suite of samples representing the rock types identified by GAMLS analysis was selected from the three long cores. Prior to this step, a core to-log depth shift was performed to ensure that samples selected corresponded to specific rock types. A total of 51 core samples (Table 2.3.1) representing specific rock types were collected, in which samples identified as representing a specific rock type were chosen from intervals in which 70% of the contribution to the total rock composition was based on a single rock type. We sampled separately core 100/04-11-081-

21W6/00 every 1 (m) interval through the whole Montney. From each core, a continuous sliver was cut and divided into one-meter intervals. Then each one-meter sliver was sectioned in half, one half for further references and the rest of the sliver was then crushed to generate pseudo-cuttings. From each sample, a ~50 gr subsample was obtained for QEMSCAN analysis.

Samples were washed and then impregnated with resin; where the epoxy resin was present, backscatter electron brightness (BSE) value under SEM analysis is low, and no x-ray spectrum is acquired. Conversely, where minerals were present and BSE was high, an x-ray spectrum is acquired. The resultant x-ray spectrum was compared with a look-up table of known mineral compositions and chemical compositions and a mineralogical identification was made (Vidence Methods Summary, 2020).

2.4 Petrographic analysis (rock fabric):

Thin section analysis was performed to characterize rock fabric, including presence and nature of lamination, grain size, and to discriminate between diagenetic and depositional minerals. Thirty-two petrographic thin sections were selected from the set of 51 QEMSCAN samples and analyzed with an Axio Zeiss Scope.A1 optical microscope at the University of Alberta. Samples were impregnated with blue epoxy to reveal macroporosity. Thin sections were polished to 30 μm, each half section stained with a dilute-acid Alizarin-red-S and potassium ferricyanide solution to facilitate identification of carbonate minerals.

High resolution images of samples and compositional information were obtained through scanning electron microscopy (SEM), including energy dispersive spectroscopy (EDS) analysis, to identify the minerals present, describe the distribution of organic matter and examine the morphology, distribution, type, and sizes of pores at a micron and submicron-scale in the rock types. Twenty-four samples were analyzed by SEM. Samples were mechanically polished and then ion-milled with a Fischione Model 1060 SEM Mill at the University of Alberta and then coated with carbon before imaging. SEM analysis was supported with EDS, both performed on a Zeiss Sigma FESEM configured with in-lens secondary electron (SE) detector and a backscatter (BSD) detector, with an accelerating voltage of 20kV, at the nanoFAB facilities and in the Department of Earth & Atmospheric Sciences, both in the University of Alberta, Alberta.

Table 2.3.1 Database of samples selected from the three well cores and studies applied to each of them.

Well location	Hcb type	ID	Sample type	Depth [m]	QEMSCAN	LECO %TOC	ICP/ICP-MS	MICP	BET	PERM [md]	Porosity [%]	Thin section	SEM/EDS
4-11-81-21W6	wet gas	M1	cutting	2088.12	✓	✓	✓	✓	✓			✓	
4-11-81-21W6	wet gas	M3B	cutting	2195.8	✓	✓	✓	✓				✓	
4-11-81-21W6	wet gas	M3D	cutting	2100.4	✓								
4-11-81-21W6	wet gas	M1A	cutting	2093.22	✓	✓	✓	✓	✓			✓	✓
4-11-81-21W6	wet gas	M1C	cutting	2096.62	✓	✓	✓	✓				✓	
4-11-81-21W6	wet gas	M3E	cutting	2158.79	✓								
4-11-81-21W6	wet gas	M3	cutting	2133.09	✓	✓	✓	✓	✓			✓	✓
4-11-81-21W6	wet gas	M3A	cutting	2125.35	✓	✓	✓	✓				✓	✓
4-11-81-21W6	wet gas	M2	cutting	2136.37	✓								✓
4-11-81-21W6	wet gas	M1B	cutting	2174.01	✓	✓	✓	✓	✓			✓	✓
4-11-81-21W6	wet gas	M3C	cutting	2127.23	✓	✓	✓	✓					
4-11-81-21W6	wet gas	M1D	cutting	2074.57	✓							✓	
16-06-081-17 W6M	wet gas	M1	cutting	2068.03	✓	✓	✓	✓	✓	✓	✓	✓	✓
16-06-081-17 W6M	wet gas	M1B	cutting	2189.56	✓	✓	✓					✓	
16-06-081-17 W6M	wet gas	M1C	cutting	2249.42	✓		✓					✓	
16-06-081-17 W6M	wet gas	M2E	cutting	2124.46	✓								
16-06-081-17 W6M	wet gas	M1A	cutting	2106.47	✓						✓		
16-06-081-17 W6M	wet gas	M2	cutting	2096.37	✓	✓	✓	✓	✓	✓	✓	✓	✓
16-06-081-17 W6M	wet gas	M2A	cutting	2109.18	✓	✓	✓	✓				✓	✓
16-06-081-17 W6M	wet gas	M2B	cutting	2177.36	✓	✓	✓	✓		✓	✓	✓	
16-06-081-17 W6M	wet gas	M2C	cutting	2075.23	✓								
16-06-081-17 W6M	wet gas	M2D	cutting	2179.47	✓								
16-06-081-17 W6M	wet gas	M3	cutting	2136.24	✓	✓	✓	✓	✓	✓	✓	✓	✓
16-06-081-17 W6M	wet gas	M3A	cutting	2165.25	✓	✓	✓	✓	✓	✓	✓	✓	
16-06-081-17 W6M	wet gas	M3B	cutting	2186.01	✓	✓	✓			✓	✓	✓	✓
16-06-081-17 W6M	wet gas	M3C	cutting	2151.13	✓					✓	✓		
16-06-081-17 W6M	wet gas	M3D	cutting	2168.19	✓								
16-06-081-17 W6M	wet gas	M4A	cutting	2241.64	✓	✓	✓	✓		✓	✓	✓	✓
16-06-081-17 W6M	wet gas	M4	cutting	2206.28	✓	✓	✓	✓	✓	✓	✓	✓	✓
16-06-081-17 W6M	wet gas	M4B	cutting	2256.65	✓	✓	✓	✓		✓	✓	✓	✓
16-06-081-17 W6M	wet gas	M3E	cutting	2196.39	✓								
16-06-081-17 W6M	wet gas	M4C	cutting	2200.2	✓								
04-09-084-22W6	oil	M2D	cutting	1659.2	✓	✓		✓		✓	✓	✓	
04-09-084-22W7	oil	M4B	cutting	1867	✓	✓		✓				✓	✓
04-09-084-22W8	oil	M1C	cutting	1885	✓	✓				✓	✓	✓	
04-09-084-22W9	oil	M2F	cutting	1704.2	✓								
04-09-084-22W10	oil	M4C	cutting	1873.4	✓			✓					
04-09-084-22W11	oil	M4D	cutting	1878	✓					✓	✓		
04-09-084-22W12	oil	M2	cutting	1713.4	✓	✓		✓		✓	✓	✓	✓
04-09-084-22W13	oil	M2A	cutting	1768	✓	✓						✓	
04-09-084-22W14	oil	M2B	cutting	1941.6	✓	✓		✓				✓	
04-09-084-22W15	oil	M2C	cutting	1716	✓			✓					
04-09-084-22W16	oil	M1	cutting	1770	✓	✓				✓	✓		
04-09-084-22W17	oil	M1A	cutting	1703.4	✓	✓						✓	
04-09-084-22W18	oil	M3	cutting	1770.8	✓	✓		✓		✓		✓	✓
04-09-084-22W19	oil	M3B	cutting	1776	✓			✓				✓	
04-09-084-22W20	oil	M3A	cutting	1765.2	✓								
04-09-084-22W21	oil	M3C	cutting	1763.2	✓			✓		✓	✓		
04-09-084-22W22	oil	M2E	cutting	1656.2	✓	✓		✓				✓	
04-09-084-22W23	oil	M4	cutting	1870.4	✓	✓		✓				✓	
04-09-084-22W24	oil	M1B	cutting	1881.8	✓	✓				✓	✓	✓	
04-09-084-22W25	oil	M4A	cutting	1900.9	✓			✓					

2.5 Geochemistry

LECO %TOC: Thirty-two samples (8 samples for well 100/04-11-081-21W6/00, and 12 samples each for cores 100/12-33-080-17W6/02 and 100/04-09-084-22W6/00) were analyzed for %TOC (Total Organic Content) by a LECO Carbon Analyzer at Geomark Laboratories, Humble, Texas. The samples selected were identical splits of QEMSCAN samples.

Whole-rock major, minor, and trace element compositions: Twenty samples (10 samples each from wells 100/04-11-081-21W6/00 and 100/12-33-080-17W6/02), were analyzed at Bureau Veritas Labs in Vancouver, BC. These samples were also identical splits of the QEMSCAN samples. Samples were cleaned and crushed into powder (pulverized until material passes through a 200 mesh) and then analyzed using Inductively Coupled Plasma (ICP) and ICP-Mass Spectrometry (ICP-MS). Major oxides such as SiO^2, Al^2O^3, and CaO were analyzed by ICP, following lithium borate fusion and dilute acid digestion, and 45 trace elements were analyzed by ICP-MS. An internal Bureau Veritas Laboratories standard SO-18 was analyzed with the rock samples (see Appendix 1).

2.6 Petrophysics

Petrophysical measurements included: helium (He) porosimetry, pulse decay permeability, mercury injection capillary pressure (MICP) analysis for measurement of pore throat diameters, and nitrogen adsorption-desorption experiments to measure internal surface area and calculate pore diameters.

A.- Porosity and permeability measurements were measured in 24 plugs, 12 plugs from well 100/12-33-080-17W6/02, which is a gas well, and 12 plugs from well 100/04-09-084-22W6/00, an oil producer. Plugs from the oil-producing well were washed prior to testing in a Dean-Stark device using a solution made of 30% acetone, 23% methanol, and 47% chloroform for 12 hours or until the solution showed no evidence of hydrocarbons present (images of the solution are provided in Appendix 2). The 24 samples were then dried in an oven for 24 hours at 100 °C to remove any remaining fluid. A helium pycnometer, a Pentapyc 5200e, was used to measure grain density; then by applying equation (1) and the calculated bulk density from our plugs, porosity was calculated.

$$\phi = 1 - \left(\frac{Bulk\rho}{Grain\rho}\right) \ldots (1)$$

Permeability was measured on core plugs with a Coretest NDP-605 NanoDarcy Permeameter, which is designed to measure low and ultra-low permeabilities. Samples rested at the target confining and pore pressure between 23 – 24.5 hrs, in order to stabilize, before taking measurements; the instrument then propagate a differential pressure pulse through the plug and recorded upstream pressure, downstream pressure, and differential pressure. For our samples, we applied a confining pressure of ~2 kpsi, a pore pressure of ~1 kpsi, and temperature ~29 °C. The differential pressure pulse was ~10 psi and the target pressure stability 0.08 %/min.

Porosity and permeability measurements were conducted in the Department of Earth & Atmospheric Sciences at the University of Alberta.

B.- Thirty-two samples were analyzed by mercury injection with a Micrometrics Autopore IV 9520 mercury porosimeter at AGAT Laboratories in Calgary, Alberta. Samples were first dried in a vacuum oven at 60 °C under a vacuum gauge pressure of -15 mmHg for 24 hrs. They were then loaded into an appropriately-sized penetrometer (which consisted of a sample cup connected to a metal-clad, precision-bore, glass capillary stem) and loaded into the mercury porosimeter. The test is composed of two stages; first is a low-pressure stage in which intrusion of mercury is measured in several steps, from vacuum to 30 psi. At this stage, the bulk density is calculated. In the second stage intrusion of mercury is measured, in several steps, from 30 to 60 000 psi (Nikolas Minions, personal communication).

C.- Nitrogen adsorption-desorption (BET) analysis was applied to 8 samples (4 samples each for wells 100/04-11-081-21W6/00 and 100/12-33-080-17W6/02, representing each of the 4 rock types) to obtain information on pore volume versus pore size distribution. The device measures the amount of nitrogen gas adsorbed onto external and internal sample surfaces as pressure is increased and, similarly, the amount desorbed while pressure is decreased; these data then was used to calculate surface area and pore size distribution. Adsorption and desorption isotherms were measured using a Quantachrome Autosorb-1 at the University of Alberta. Samples first were crushed and sieved to 0.5-1 mm. Samples between 0.5-1 g were then degassed under high vacuum for 24 hours at 120 °C and analyzed at 77.35 K. Surface areas were calculated for the 8 samples using the BET model in P/P0 range of 0 to 0.3 (Brunauer et al., 1938; Schettler et al., 1989).

Chapter 3 - Results

3.1 Elevation and GOR distribution

An elevation map (reference to MSL) and GOR m3 map (gas-oil ratio) in Septimus field were configured. From Septimus field and surroundings, we selected a total of 2210 wells with top-Montney elevations (public dataset) and 726 wells, with oil and gas production; using this dataset, the GOR from the first 12 months of production was calculated on a well-by-well basis. (Figure 3.1.1).

We observed that at Septimus field, the top-Montney Formation elevation dips from north to south with depths ranging from -2250 to ≥ -3000 msl. GOR ratios describe a liquid-rich pool in the northeastern part of the field, with rapid transitions to much drier (gas-rich) compositions to the south and west following the same trend as the regional Tmax map for the Montney Formation.

3.2 Log Interpretation

We create a model of rock type distribution in the Montney reservoir at Septimus field through GAMLS analysis that classifies the formation as a mixture of four different rock types (RT), based on log responses in through the 13 study wells (Figure 3.2.1a). In this analysis, RT 1 and RT 4 correspond to parts of the section with the lowest GR values (~48-110 API). RT 1 represented with the lowest GR and NPHI (~7%) responds and relative lower RHOB values (~2.6 cc). RT 4 is represented with the highest NPHI (~10 to 15%), and highest RHOB of the rock types (~2.7 cc). RT 2 represented intervals of the Montney section with the highest GR response (~130 to ~180 API), relatively high NPHI (~10%), and relatively low RHOB (~2.5) response. RT 3 represented the intervals with the smallest RHOB response (≤ 2.5 cc), relatively high GR (~128 API) and relatively low NPHI (~8%) responds (Figure 3.2.1b).

The entire Montney interval, represented in cross-section by Figure 3.2.2, is arrayed as mixtures of these four end member rock types, based on this analysis. In general, RT 1 is the most abundant, (present in most of the section where it typically makes up 50-80% of the rock), followed by RT 3, which typically makes up (~40%), RT 4 (5-15%), and in less proportion, RT 2 (~5%). We observe that from the middle of the cross-section to the northeast (from W6 to HZ), the Upper Montney interval is represented mainly by RT 3 followed by RT 1, whereas the rock types in the

Lower Montney consist of subequal proportions of RT 1 and RT 3. While RT 2 and RT 4 form thin intervals intercalated throughout the formation.

In the southwest part of the study area, RT1 is less abundant and thin intervals of RT 2 are more abundant in the Upper Montney. Greater vertical and lateral variations in the distribution of the rock types are evident, and a thick interval mostly consisting of RT 4 is present at the bottom of the section, especially prominent in W2.

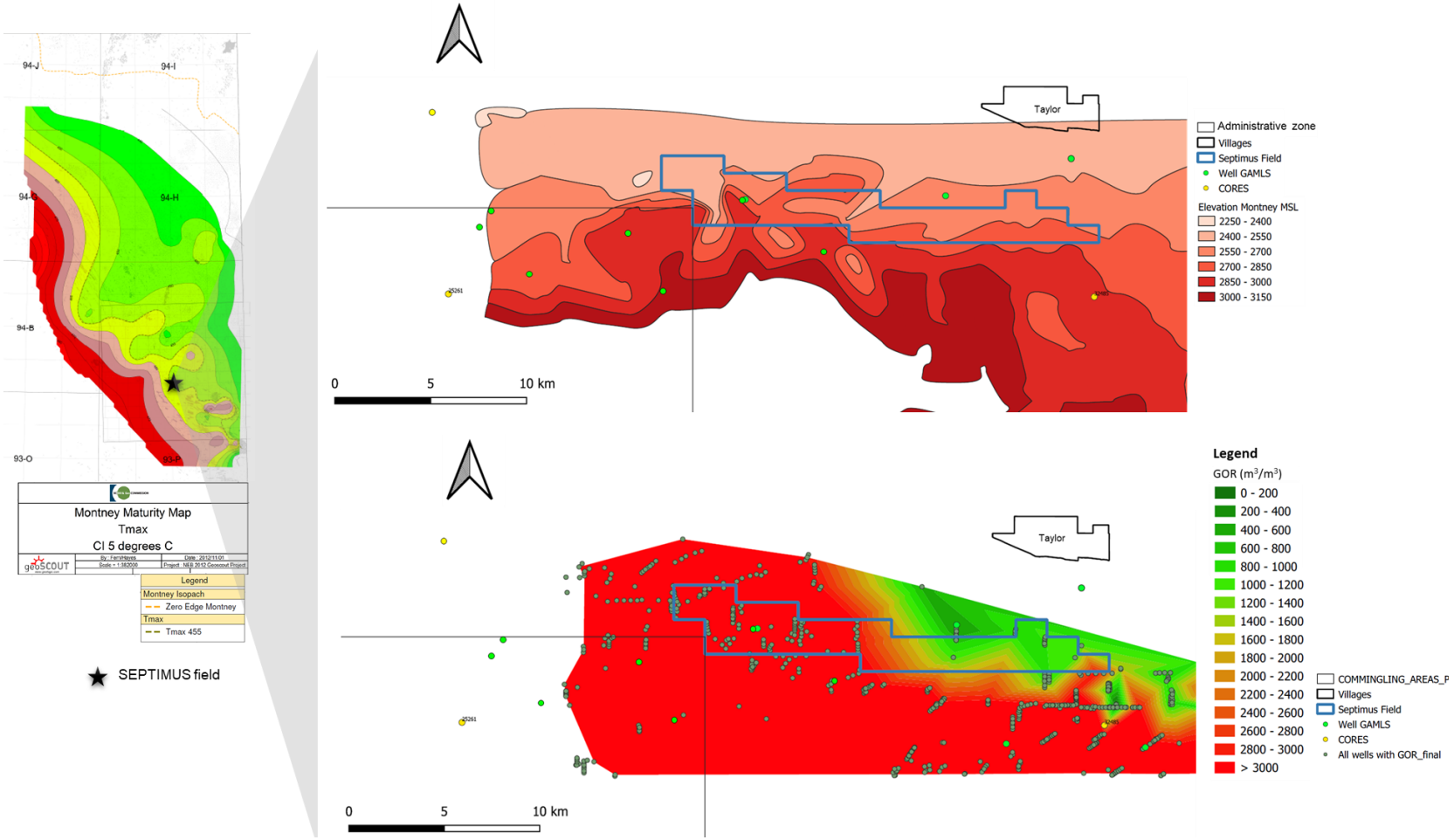

Figure 3.1.1 Left, Montney Maturity Map (BC Oil and Gas Commission, 2012), Septimus location is marked (black star). Top map: Elevation Montney calculated from formation tops in wells around the study area and Septimus field, data is referred to the mean sea level (MSL). Bottom map: Gas-oil ratio (GOR) estimated from the first 12 months (m3/m3). Both maps show correlation with the regional maturity map (Tmax) for the Montney Formation.

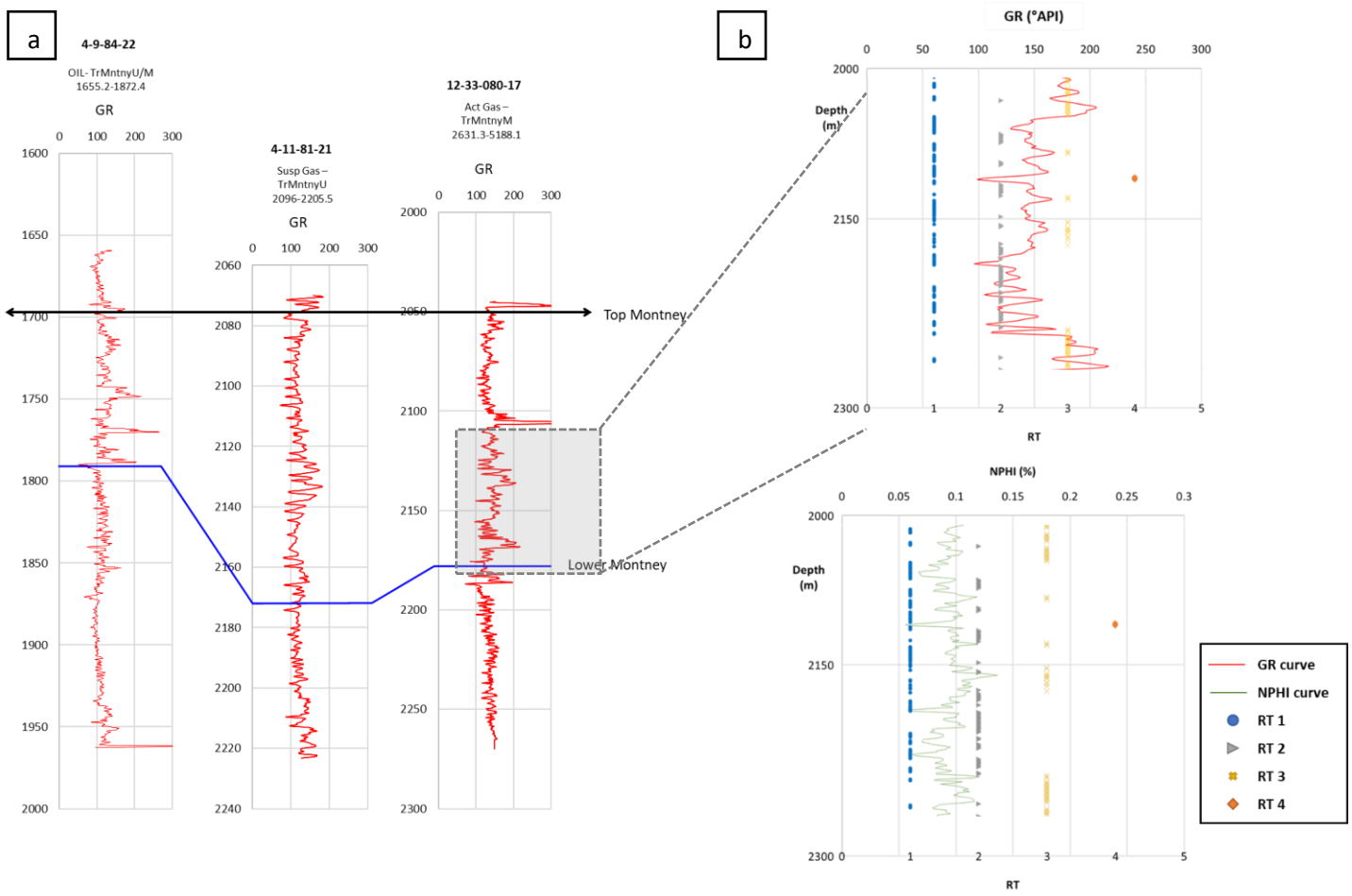

Figure 3.2.1 a and b (a) Typical GR response for the Montney Formation. (b) GR and NPHI logs with example on how GAMLS do the assignation of each rock type according to the log response. For our model, four distinctive log responses were identified and classified as different rock type. During clustering every depth-step is assigned to one or more rock types, with a percentage from 0 to 1, high percentage-rock type indicate a higher likelihood of that depth belonging to that rock type. Depths that have two or more rock types assigned to them are interpreted to be mixtures of these rock types.

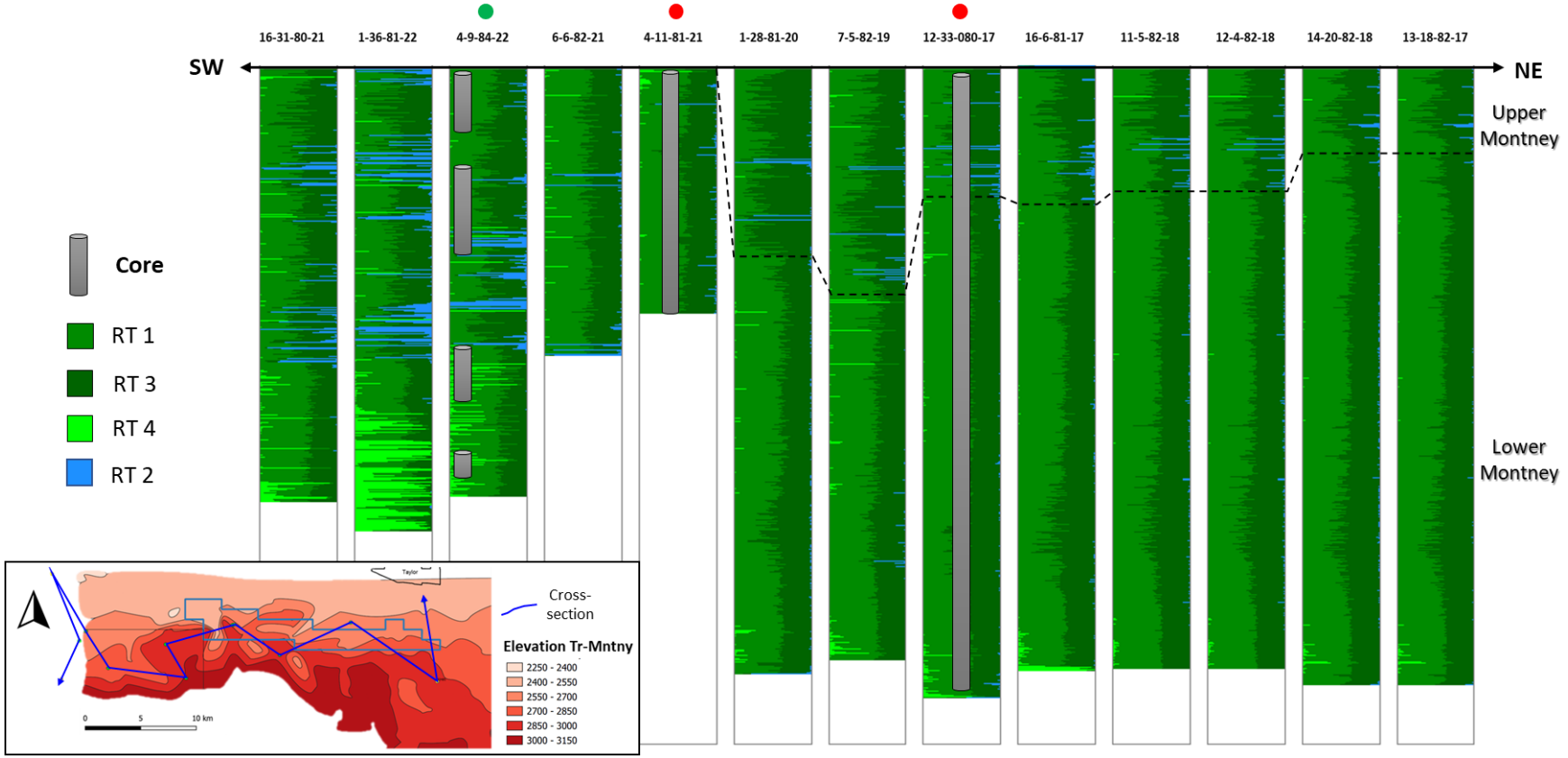

Figure 3.2.2 GAMLS model cross section result representing the vertical distribution of the 4 different rock types identified in the Montney Formation through our 13 wells. Also, there is the representation of the location of the three cores analyzed. The general stratigraphical configuration on the reservoir did not show dramatical variations on the vertical and lateral distribution of the four rock types, in comparison to well located more west of the field, where possibly the depositional setting of the Montney had more variations. This characteristic is important, though it is also matching with the variations between types of hydrocarbon reported on the wells.

3.3 Core log description and rock type comparison.

Four lithofacies were described by C. Feng in cores from wells 4-11-081-21W6, 16-6-81-17W6 and 4-9-84-22W6, summarized in this section from his work. Lithofacies 1 is a fine to coarse siltstone, with an array of sedimentary structures that include wavy parallel laminations, lenticular bedding, flow and current ripples, truncations, scour, and fill structures, and evidence of soft sediment deformation; Lithofacies 1 is interpreted to have been deposited in a lower shoreface depositional environment. Lithofacies 2 is a medium to coarse siltstone interbedded with fine to medium grained siltstones. This facies presents wavy parallel and lenticular bedding with soft sediment deformation and sporadic trace fossils; it is interpreted as deposition in an offshore transitional setting. Lithofacies 3 is a medium- to coarse- grained siltstone interbedded with wavy parallel laminated fine- to medium- grained siltstone, with lenticular bedding, wavy parallel laminations, scour and fill structures, current ripples, and load casts; it is interpreted as having been deposited in a distal position related to mass wasting processes (also knowns as slope movement or mass movement). Finally, Lithofacies 4, is a medium to coarse grain siltstone with concretions, and a distinctive set of sedimentary structures, that include wavy parallel bedding, rippled laminations, current ripples, climbing ripples, normal grading, with scour and fill structures, and concretions. This facies was deposited in a setting proximal to depositional environment in which mass wasting processes predominated (process by which material moves downslope as a solid mass under the influence of gravity, and with characteristics of a flow as in debris flows or mudflows) (Britannica et al., 2015).

C. Feng observed that in the well cores, lithofacies 3 is the most abundant followed by lithofacies 4. Lithofacies 2 is less abundant in the three wells, in particular at well 4-11-081-21W6 (Figure 3.3.2 and Appendix 3), and lithofacies 1, was observed only in the shallowest interval of cores 16-6-81-17W6 and 4-9-84-22W6 and was completely absent in 4-11-081-21W6.

GAMLS output for these wells was compared to facies descriptions from the cores. No clear correspondence between facies and rock types identified by GAMLS could be established, although as noted below in section 3.6, the rock types distinguished by the GAMLS analysis do vary in terms of terms of fabric (lamination and grain sizes). The absence of a strong relationship between facies and rock types may be related to the strong diagenetic overprint on the Montney Formation that tends to have the more significant impact on rock properties (Vaisblat, 2020). In

addition, facies and log data are recorded at different scale: cm-scale or finer in terms of facies records but tens of cm up to a meter in terms of log records.

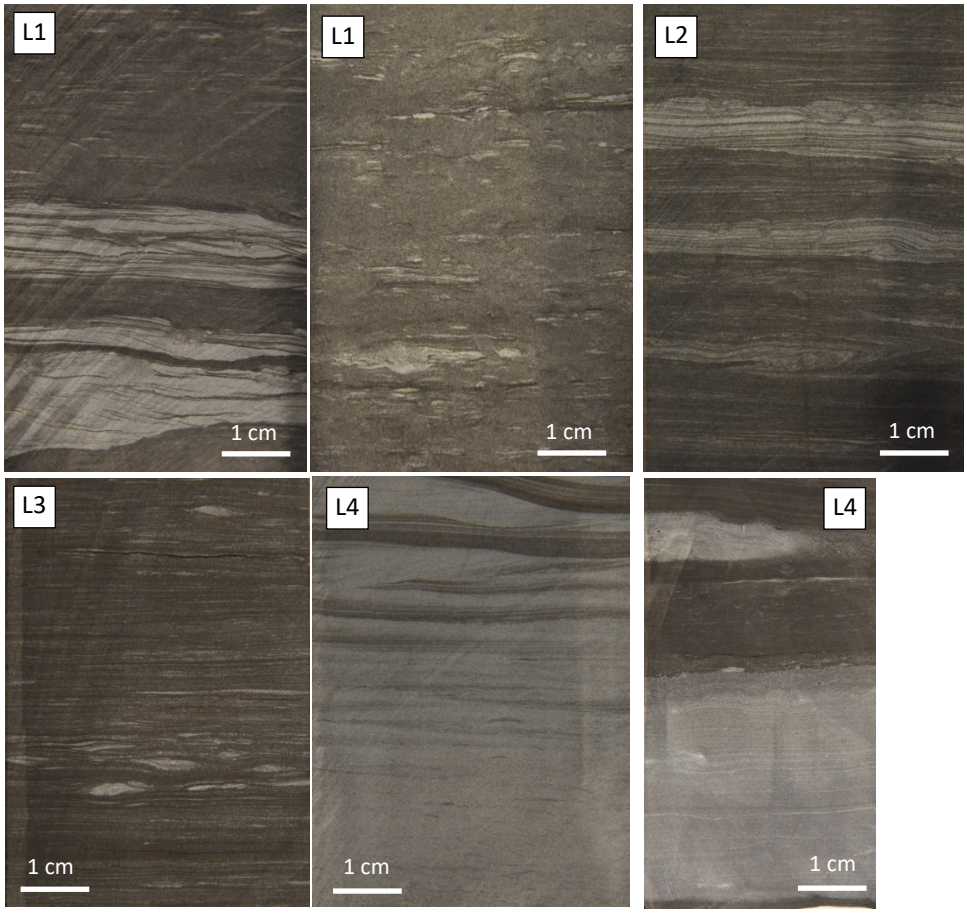

Figure 3.3.2 Representative photographs of the 4 lithofacies described at well 4-11-081-21W6, 16-6-81-17W6 and 4-9-84-22W6 (C. Feng, 2020) (L1) Lithofacies 1, fine-coarse siltstone with wavy parallel lamination, lenticular bedding. (L2) Lithofacies 2, medium-coarse to fine-medium siltstone with wavy parallel bedding. (L3) Lithofacies 3, medium-coarse- grained siltstone interlaminated with wavy parallel laminated fine- to medium-grained siltstone. (L4) Lithofacies 4, medium to coarse-grain siltstone and concretions.

3.4 Rock composition

- QEMSCAN (Mineralogy analysis):

The major mineral composition of the Montney samples based on QEMSCAN analysis is depicted in spider plots, which represent the rock as mixtures of carbonate minerals (calcite + dolomite), quartz, clays (illite and illite-smectite + Fe illite and illite-smectite), K-feldspar + plagioclase, and

micas (Figure 3.4.1 a to d). Each spider plot represents a set of samples from one rock type, in which the several samples in the diagram were selected based on a >70% representation of a single rock type from the GAMLS analysis.

RT 1 (Figure 3.4.1a) is characterized by the highest carbonate content, with dolomite concentrations (average 18 %) in excess of calcite (10%). RT 1 also has the lowest concentrations of major silicate minerals (quartz 26%; K-Feldspar + plagioclase 14%; clays 11%). RT 2 and 4 have somewhat similar mineralogical compositions, but RT 2 differs from RT 4 with higher quartz content (37% versus 26%), higher feldspar content (21% versus 15%), and slightly lower carbonates and clays concentrations. RT 3 contains the highest clay content (16%) with quartz (32%), feldspars (20%), and carbonates (20%). Proportions of the major minerals in RT 3 are subequal, in contrast to other rock types where one mineral tends to predominate (Figure 3.3.1c). Micas are present in low abundance (5-6% total) in all four rock types, consisting of muscovite, biotite, and chlorite.

A Student T-test was applied to our mineralogical results from each rock type to assess the significance of mineralogical differences between groups. A dependent and paired t-test were applied to the most abundant minerals present in each group of samples (see Table 3.4 in Appendix 4), using an alpha value of 0.05 (the significance level α is the probability of making the wrong decision when the null hypothesis is true: if values are $\geq \alpha$ there is a significant difference between groups). For each T-test a t-value and a p-value are obtained. The t-value refers to the ratio between the difference between two groups and the difference within the groups. A p-value is the probability that the result from the sample data occurred by chance, therefore low t and p values support an interpretation that mineralogical differences between the groups are significant. For our statistical analysis, where the "p-value" $\leq \alpha$ (0.05), there is no significant difference in the mean value between groups but if "p-value" $\geq \alpha$, then the null hypothesis is true, consequently there is a significant difference between groups.

For RT 1 and RT 2, the mineralogical compositions are primarily defined by carbonates (calcite + dolomite), K-feldspar, plagioclase, and quartz. For this group of samples, for carbonates we calculate a t= 1.9 with a p-value= 0.07, for feldspars a t= 0.78 with a p-value=0.43, and for quartz a t=1.49 with a p-value=0.15; this means that for RT 1 and RT 2 the null hypothesis is true, namely that there is a significant compositional difference between the rock types in terms of feldspar and

quartz contents. A comparison of carbonate content between RT 1 and RT 2 yields a small p-value; thus, these two rock types have similar carbonate contents.

For RT 1 and RT 3 we applied the same mineralogical composition, plus clays (illite & illite-smectite and Fe-illite & illite-smectite) as the basis for comparison. For carbonates, we calculate a t=2.45 with a p-value= 0.02, for feldspars a t=1.04 with a p-value=0.31, quartz with a t=1.45 and a p-value=0.16, illite & illite-smectite a t=0.74 and p-value=0.47, and for Fe-illite & illite-smectite a t=1.30 and a p-value=0.20. RT 1 and RT 3 demonstrate a significant difference between the contents of for feldspars, quartz, and clays but no significant difference between these two rock types in terms of carbonate content.

A comparison of RT 1 and RT 4 yielded significant differences in terms of feldspar, quartz, and clay (feldspars a t=1.04 with a p-value=0.39, quartz a t=1.39 with a p-value=0.18, illite & illite-smectite a t=0.36 and a p-value=0.72, and Fe-illite & illite-smectite a t=1.33 with a p-value=0.20) and for carbonates a t=0.05 with a p-value=0.95. RT 1 and RT 4 p-values confirm the null hypothesis.

Comparisons between RT 2 versus RT 3, yield significant differences in feldspar, quartz, and clay contents but no significant difference with respect to carbonate (carbonates a t=4.45 with a p-value=0.0001, feldspars a t=1.44 with p-value=0.16, quartz a t=1.49 with p-value=0.15, illite & illite-smectite a t=1.29 and a p-value=0.20, and Fe-illite & illite-smectite a t=0.84 with a p-value=0.40). Comparisons between RT 2 versus RT 4 yield significant differences for carbonates, feldspars, and clay but not for quartz (carbonate: t=0.52 with p-value=0.55, feldspars: t=1.04 with p-value=0.55, quartz: t=2.14 with p-value=0.04, illite & illite-smectite t=0.34 and a p-value=0.73, and Fe-illite & illite-smectite a t=1.86 with a p-value=0.07). Comparisons of RT 3 versus RT 4 yields significant differences for quartz and clay minerals but not for carbonate and feldspar (carbonates: t=4.18 with p-value=0.0005, feldspars: t=1.04 with p-value=0.001, quartz: t=1.01 with p-value=0.32, illite & illite-smectite: t=1.07 and a p-value=0.29, and Fe-illite & illite-smectite: t=1.66 with a p-value=0.11).

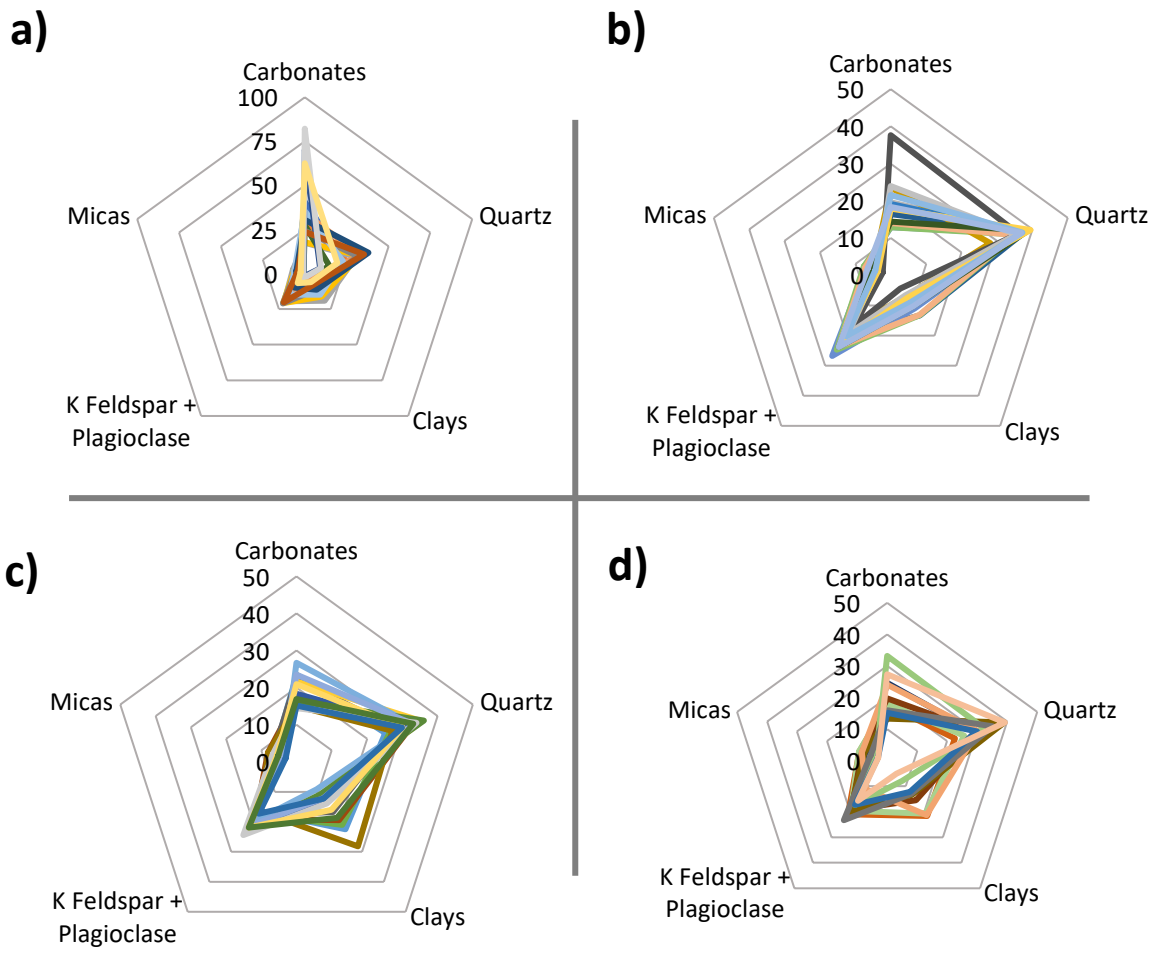

Figure 3.4.1 a to d. Spider plots representing main mineralogical composition (QEMSCAN analysis) for the 4 rock types identified. In addition to the QEMSCAN analysis, t-test analysis confirmed that there was no significant difference between set of samples from the same rock type but, there were significant differences between rock types, assuming that 4 different mineralogical composition are present in the Montney Formation. (a) group of samples representing main mineralogical composition for RT 1, (b) RT 2, (c) RT 3 and (d) RT 4.

3.5 Geochemistry

-LECO TOC:

Total organic carbon (TOC) values from LECO analysis in 32 sample ranged ~0.4 to 3.8 wt%, with an average of 1.67 wt% (Figure 3.5.1). Rock types identified by GAMLS analysis display some differences in TOC: RT 3 has the highest %TOC, with values ranging between 1.3 and 3.88 wt (average of 2.77 wt%). TOC in RT 1 and 2 are similar, averaging ~ 1 % TOC, except for one sample for RT 2 with a value of 3.74 wt%. RT 4 samples represented the lowest TOC and a relatively narrow distribution of values.

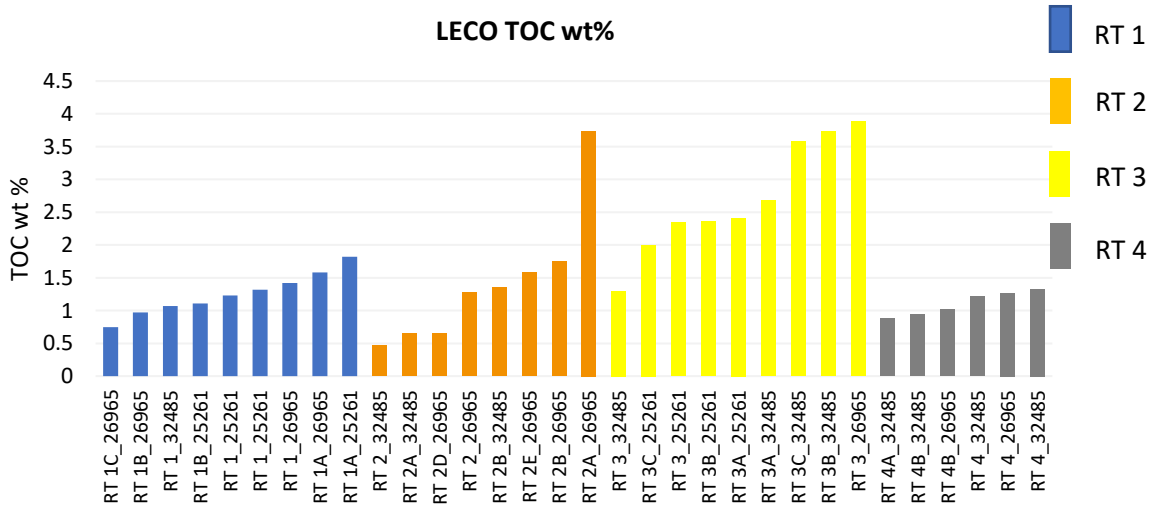

Figure 3.5.1 Plot with representative set of samples of each rock type from the three well cores analyzed, showing %TOC values obtained through LECO TOC. RT 3 represents the rock type with the highest %TOC content of all.

-Whole rock characterization:

Uranium, thorium, and potassium concentrations from ICP-MS analysis were examined because of their influence on GR logs (Fig. 3.5.2a). Potassium is concentrated in K-feldspar and some clay minerals, while thorium concentrations may be related to clay minerals and heavy minerals (S. Ashoori et al., 2016; Nur Asyraf, 2015; Nafta-Gaz, 2016). Uranium is commonly associated with organic matter in shales (S. Lüning and S. Kolonic, 2003; Hemmesch et al. 2014).

RT 3 has elevated uranium concentrations (~11 ppm in average) in comparison to other rock types, consistent with the relatively high TOC. RT 4, RT 1 and 2 had the lower concentrations, with RT 2 having the lowest concentration of U (~4 ppm in average) (Figure 3.5.2b). Th and K values did not vary

significantly between rock types, with Th ranges from ~5 to 9 ppm and K from ~2.2 to 4.2 %. Th/K ratio are consistent with illite clay.

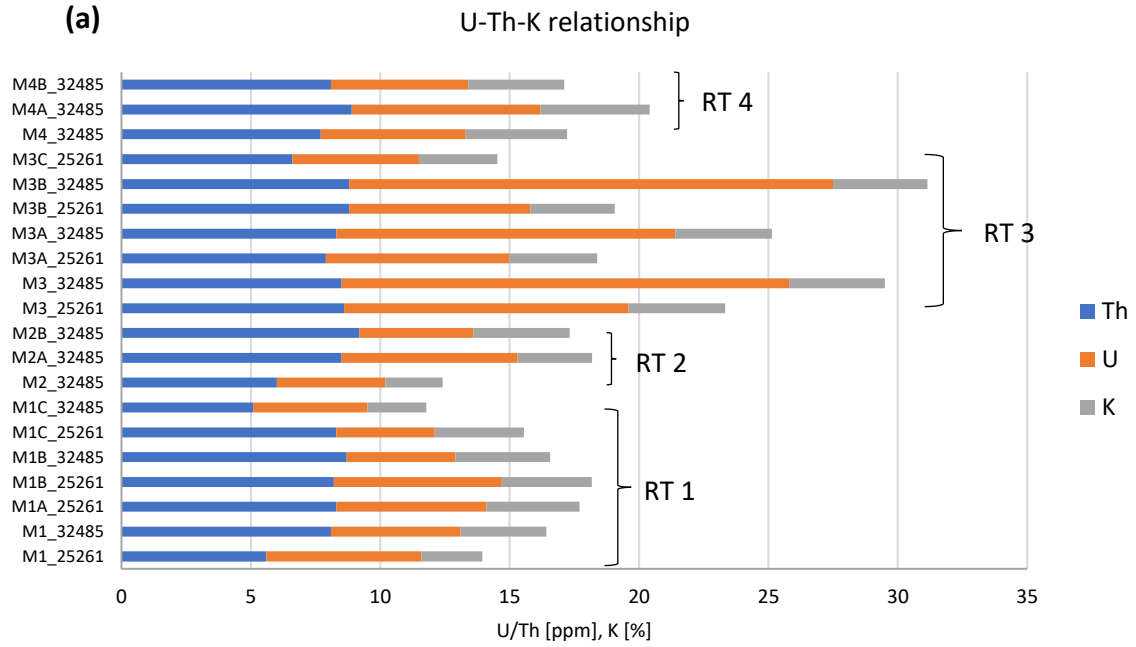

Figure 3.5.2a U, Th, and K relationship for the different rock types. There were no notable variations in Th and K either between set of samples. RT 3 samples show distinctly elevated U (ppm) content in comparison to other rock types.

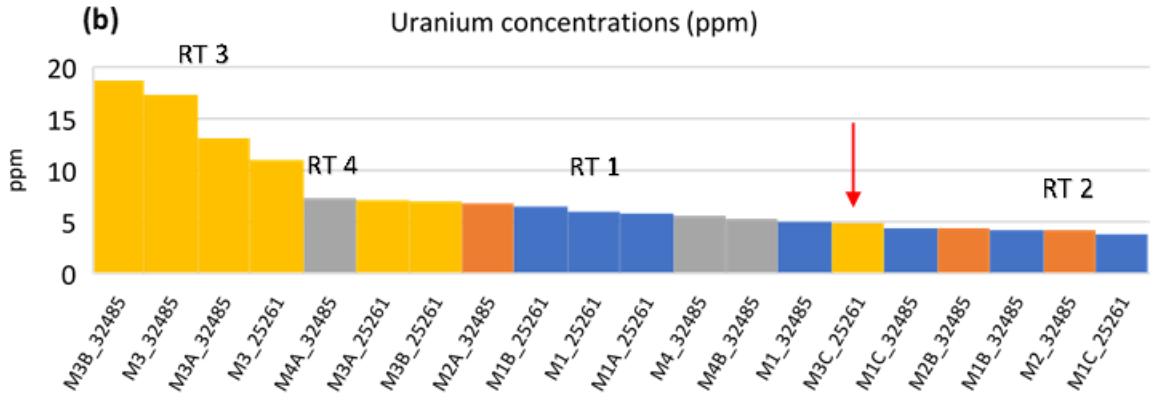

Figure 3.5.2b Uranium concentrations for the different set of samples from the 4 rock types. RT 3 in general has the highest uranium concentrations, except for one sample (M3C_25261, red arrow). RT 1, 2 and 4 overall showed no significant differences in the U concentrations.

3.6 Rock fabric:

RT 1: RT 1, with the highest carbonate content, is a laminated to well laminated, slightly argillaceous dolomitic, calcareous siltstone in which the main framework grains include quartz, calcite, dolomite, and detrital micas in a matrix of detrital clays and organics. Framework grains range in size from very fine silt to very fine sand and are sub-angular to sub-rounded. Laminae are defined by variation in calcite and dolomite/Fe-dolomite cement and clay content (Figure 3.6.1 A). Thicker laminae are slightly coarser grained and well-cemented (Figure 3.6.1 B). Most of the intergranular volume observed in RT 1 consists of cements, micas, pyrite, and phosphate grains (Figure 3.6.1 B to D). RT 1 shows modest carbonate dissolution, mainly of dolomite (Figure 3.6.1 C and D), creating some of the intraparticle porosity, distinctive in RT 1.

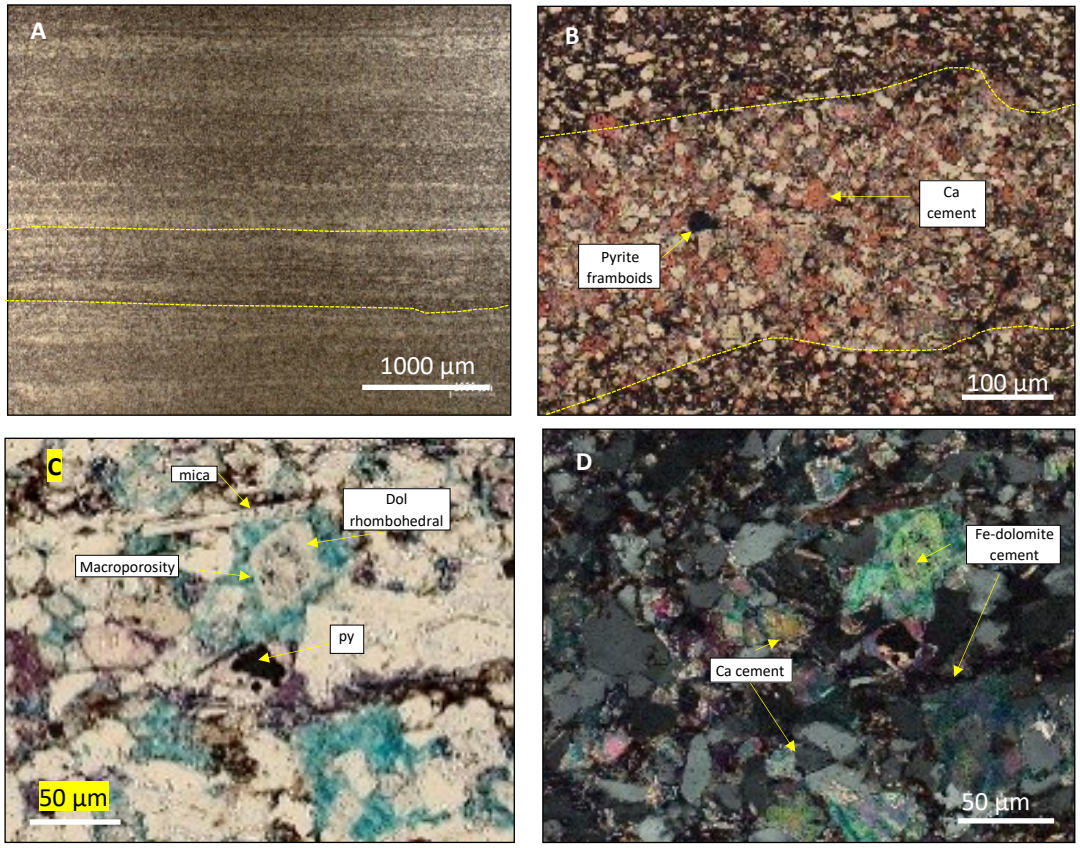

Figure 3.6.1 A to D. (a) Well defined laminae, which are distinguishable with the increase of clay layers; (b) "cleaner" intervals are coarser- grained and well cemented (yellow outlines delimit thicker laminae which are coarser and well cemented by calcite and/or Fe-dol/dol). (c and d) carbonates are dominant RT 1 and as a result the amount of calcite, Do/Fe-dol cements are abundant.

RT 2: RT 2, with the highest quartz content of the rock types, is a laminated to faintly laminated, slightly argillaceous dolomitic siltstone. The detrital framework consists largely of abundant very fine silt to very fine sand sized grains, which include quartz, plagioclase, and dolomite, and in lesser amounts K-feldspar, calcite, detrital micas and dolomite. It is well- to moderately- sorted, with angular, sub-angular, and sub-rounded grains. The fabric is mostly grain -supported and in some intervals detrital clays and organics are evident. In some RT 2 samples, the contacts between laminae are well defined and sharp. Grains and laminae are well cemented by quartz and, to a lesser extent, by calcite and dolomite/Fe-dolomite (Figure 3.6.2 A and D). Quartz overgrowths, pyrite replacement cements, and framboidal pyrite, are also consistently present in this rock type.

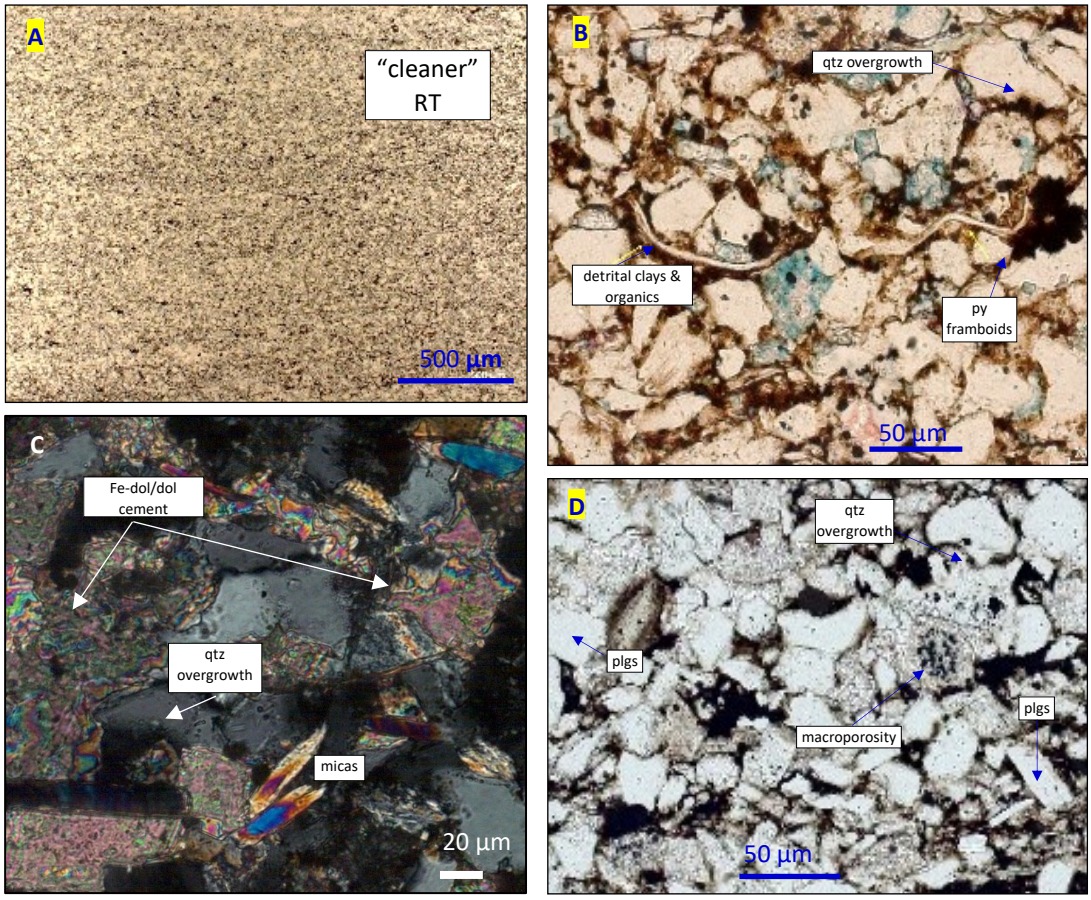

Figure 3.6.2 A to D. (a to c): faintly to more massive appearance; RT 2 is the "cleaner" rock type from all, which refers to the low clay content. (b) Matrix is mainly grain supported but at some intervals detrital clays and organics occlude some of the pore space available. (c) Fe-dolomite/dolomite cement are common for RT 2 and in lesser amounts calcite cement. Quartz overgrowths and micas are present. (d) Petrographic thin section showing some intraparticle

porosity, consistent in dolomite grains. Most of the organic matter for RT 2 is present as solid bitumen.

RT 3: RT 3, with the highest clay content of the rock types, is a faintly laminated to massive, slightly argillaceous siltstone. Framework grains include quartz, and in lesser proportion, plagioclase, K-feldspar, and micas and are very fine silt to very fine sand sized (finer- grained than the other 3 rock types) and moderately sorted. Detrital matrix clays and organics are observed infilling most of the interstitial volume, leaving almost no primary pore space; most of the porosity was observed in organic matter. Where present, laminae are usually graded from silt to sand size grains, cemented by Fe-dolomite and in lesser amounts calcite, and increasing upwards in clay content (Figure 3.6.3 A and B). Calcite and dolomite/Fe-dolomite cements were observed (Figure 3.6.3 D). Framboidal pyrite and pyrite replacement are also noted, along with quartz "patches" and quartz overgrowths (Figure 3.6.3 C and D).

RT 4: RT 4 is a well-laminated to laminated, slightly argillaceous, dolomitic, calcareous siltstone. Framework grains consist mainly of angular, sub-angular, and sub-rounded fine silt to very fine sand (Figure 3.6.4 B), primarily K-feldspar and quartz, and in less proportion plagioclase and dolomite. It is compositionally similar to RT 2 but contains a higher amount of detrital clays and organics than RT 2, which fill much of the available pore space. In most samples, the laminae are graded, defined primarily by grain size, cement, and clays (Figure 3.6.4 A). Basal surfaces are sharp and individual laminae are typically coarse, well- cemented, and show some macroporosity between grains. The dominant cement type is dolomite/Fe-dolomite (Figure 3.6.4 B, C). Framboidal pyrite, pyrite replacement and micas are consistently present in this rock type; micas such as chlorite, are deformed by grains of pyrite or phosphate enhancing interparticle porosity (Figure 3.6.6 D, E, F).

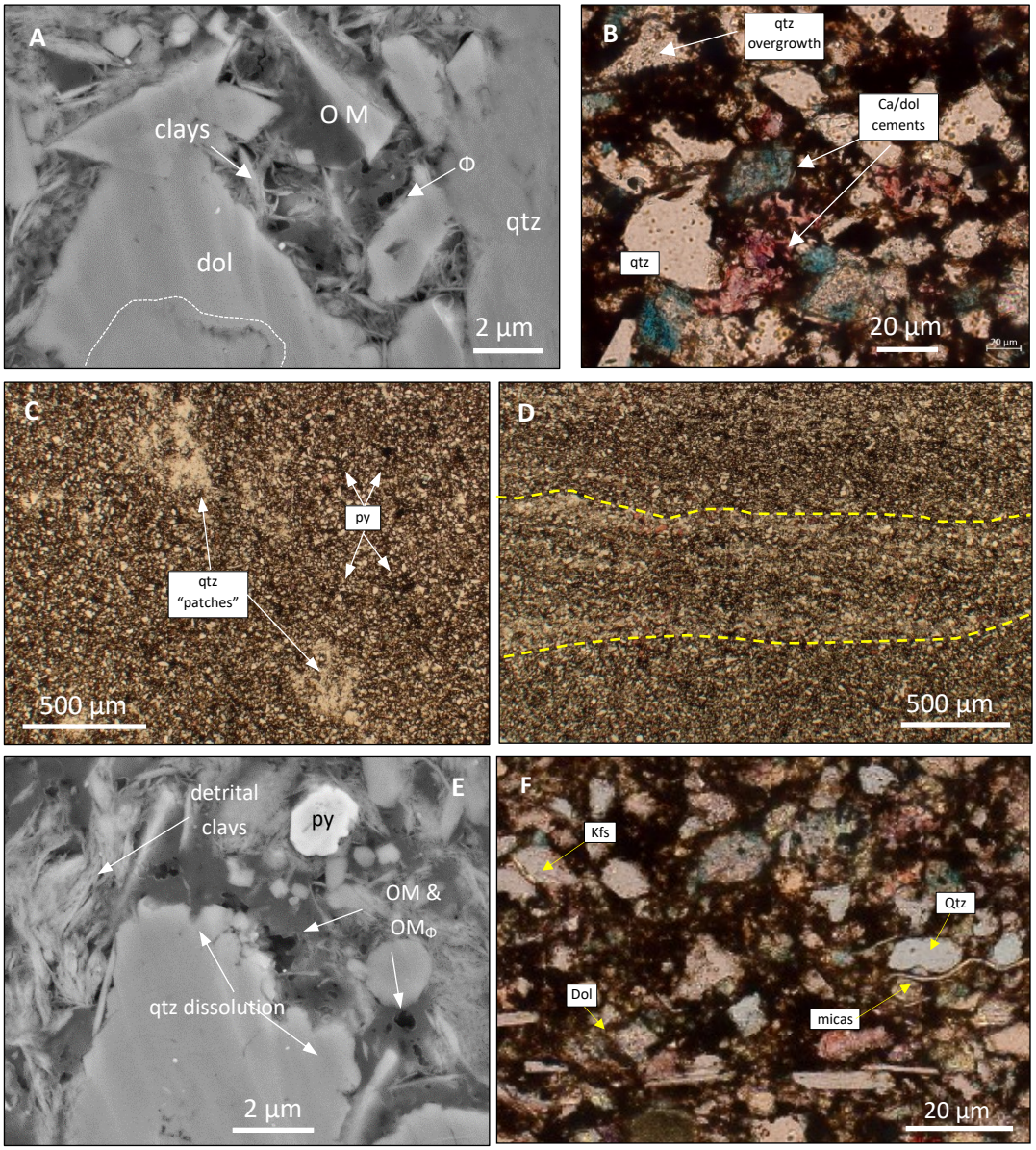

Figure 3.6.3 A to F. (a/e) SEM images of a representative sample of RT 3. Detrital silt/clay matrix is interstitial to framework grains, which include quartz and in less amount dolomite. (b/f)) Through petrographic thin sections the same behavior was observed, high detrital clay concentrations, organics, and Ca and dolomite/Fe-dolomite cement infilled pore space. (c/d) Quartz "patches" as horizontal bioturbated laminae cemented by quartz were distinctive features in RT 3.

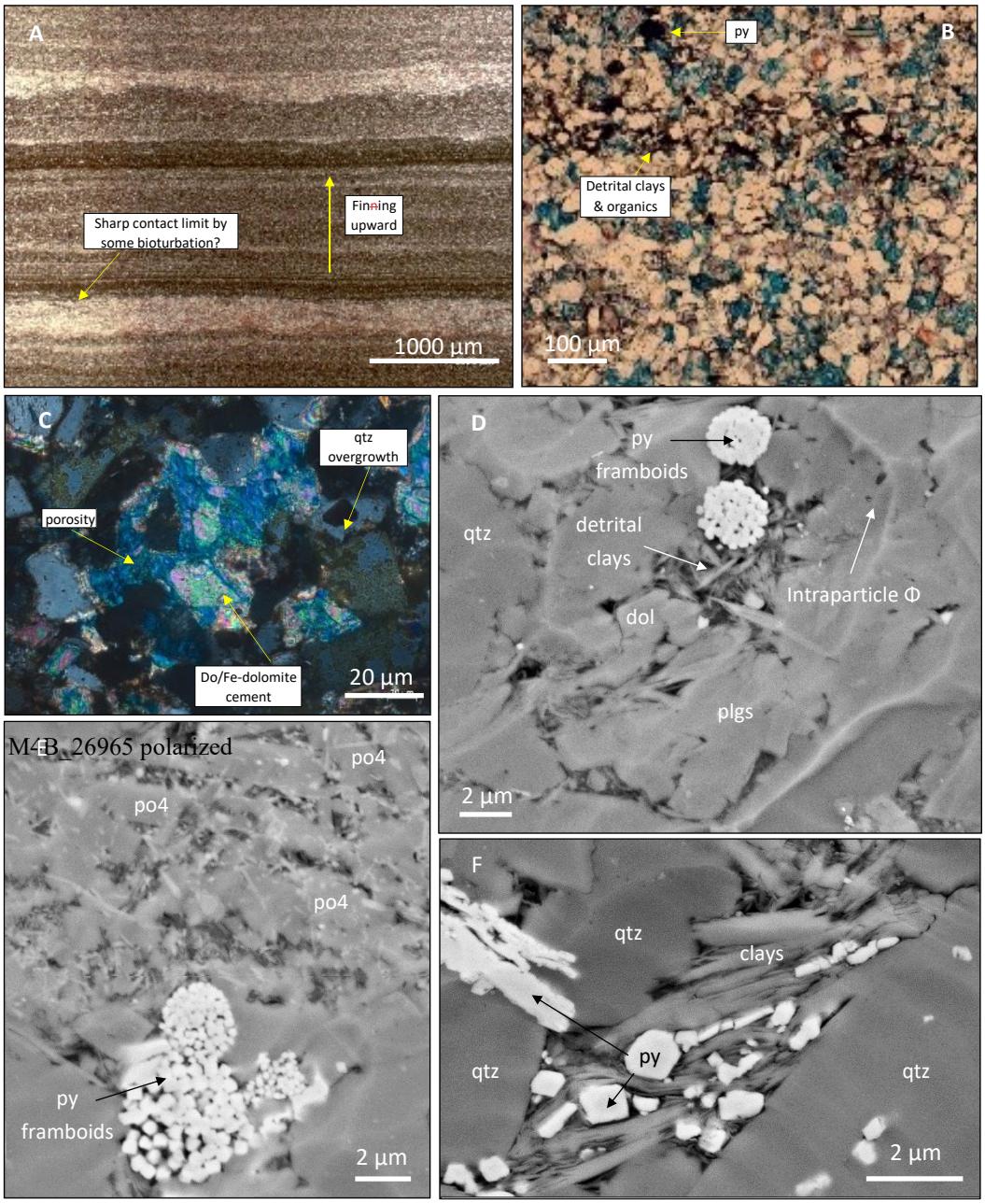

Figure 3.6.4 A to F. (A) Thin section for RT 4, laminae are well defined by grain sizes and amount of clays. At some intervals, the contact between laminae is sharp and limited by some bioturbation? (B) and (C) Samples with less clay and organics content showed interparticle space cemented by Do/Fe-dol cement. (D/E/F) Through SEM RT 4 showed a major presence of pyrite substitution, either in grains, framboids or laminae, as for phosphates, both enhancing RT 4 pore space. Detrital clays also infill most of the pore space available.

3.7 Pore distribution and morphology

Through SEM images we were able to identify the different types of pores based on their size, and shape. Samples of the different rock types in the Montney Formation show that most of the pores present are classified as mesopores (d~3.5-48.8 nm) and in lesser amounts macropores (d>50 to ~570 nm). We also follow Loucks et al (2012) classification scheme for pores, and, based on SEM images, recognize: organic-matter pores, interparticle pores (interparticle pore between mineral particles), and intraparticle pores (intraparticle pores within mineral particles) (Figure 3.8A to C).

In RT 1, 2 and 4, interparticle pores are the most abundant pore types followed by intraparticle pores and in lesser amounts organic-matter pores. Interparticle pores between grains and clay plates and intraparticle pores are micron to submicron scale macropores. These macropores and mesopores observed in our samples are present in the organic matter aggregates filling micron scale macropores (Figure 3.8D).

Most of the intraparticle pores observed in our samples were associated with dolomite, calcite, and quartz grain, locally with organic matter, and within pyrite framboids (Figure 3.8B and G). This type was consistently present in RT 1 but is also represented in RT 2 and RT 4. In RT 2, the dominant pore type is interparticle, observed to occur between quartz grains and/or K-feldspar grains. RT 2, in contrast to the other three rock types, organic matter was observed as solid bitumen, which either "coats" grains or as bridges-pores material, leading to some connectivity between pores.

Pores in RT 3, in contrast to RT 1, 2 and 4, are mainly organic-matter pores (micropore size) (Figure 3.8 C and G). Almost no interparticle and intraparticle pores are present as SEM observations showed that this RT is highly occluded with detrital grains (quartz, dolomite, and K-feldspar), detrital clays, and organic matter.

RT 4 samples display interparticle, intraparticle, and organic matter-pores. Interparticle pores were observed between detrital grains (mainly quartz, and K-feldspar), in lesser amounts between detrital clay particles, and between detrital grains and organic matter (Figure 3.8F), and in some intervals, interparticle space occurred between these grains, micas, and phosphate grains. Intraparticle pores in RT 4 were observed in K-feldspar, quartz, and phosphate grains, and in lesser amounts dolomite and calcite grains.

The three different pore types observed in our samples vary substantially in terms of size and shape. Organic-matter pores are the smallest pores observed through SEM and are represented by a simple shape spherical form. Interparticle and intraparticle pores are between ~4 to 7 times larger than organic-matter pores (Figure 3.8F and E). These pores have a much more complex pore shape that depends on the detrital grains and the matrix composition.

SEM images show that some of the pores occur mostly with wide bodies and narrow necks, as open-wedge pores, and slit-shape or parallel-plate pore types, consistent with BET analysis (Fig. 3.7 a to e; Fig. 3.9.6; Fig. 3.8F).

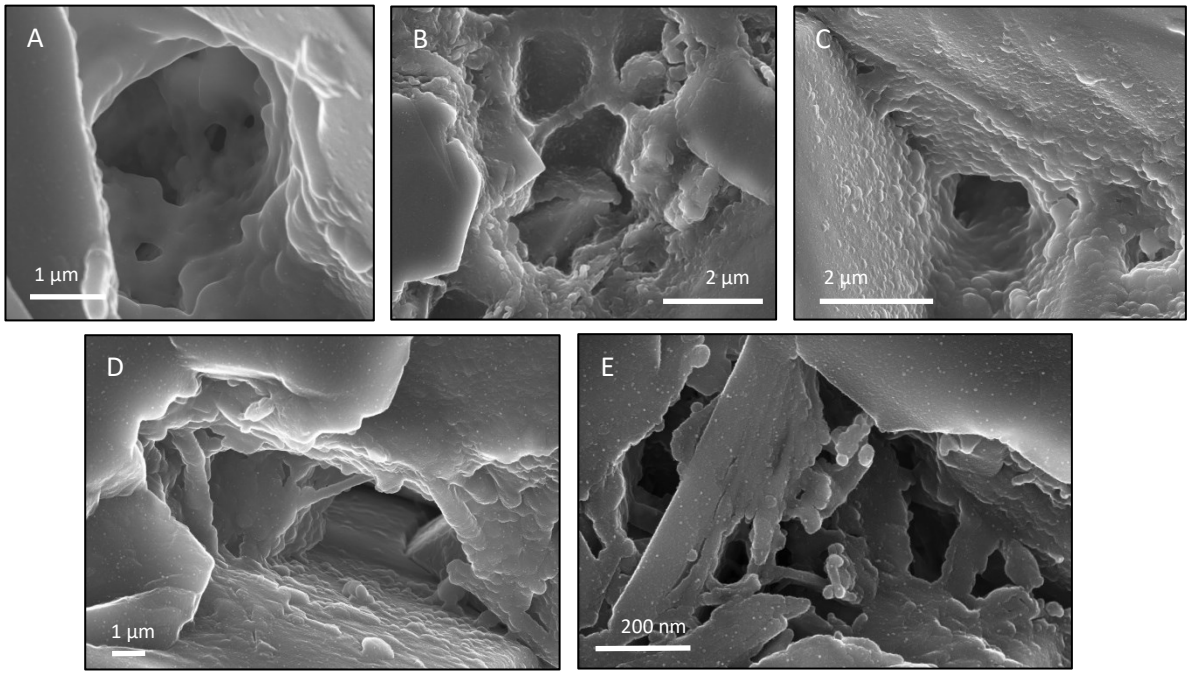

Figure 3.7 a to e SEM images of representative pore shapes observed in RT 1, RT 2, and RT 4. As our BET analysis, pores with narrow necks, wide bodies, and open-wedge pores were observable. No slit-shape or parallel-plate cracks were identified through SEM analysis.

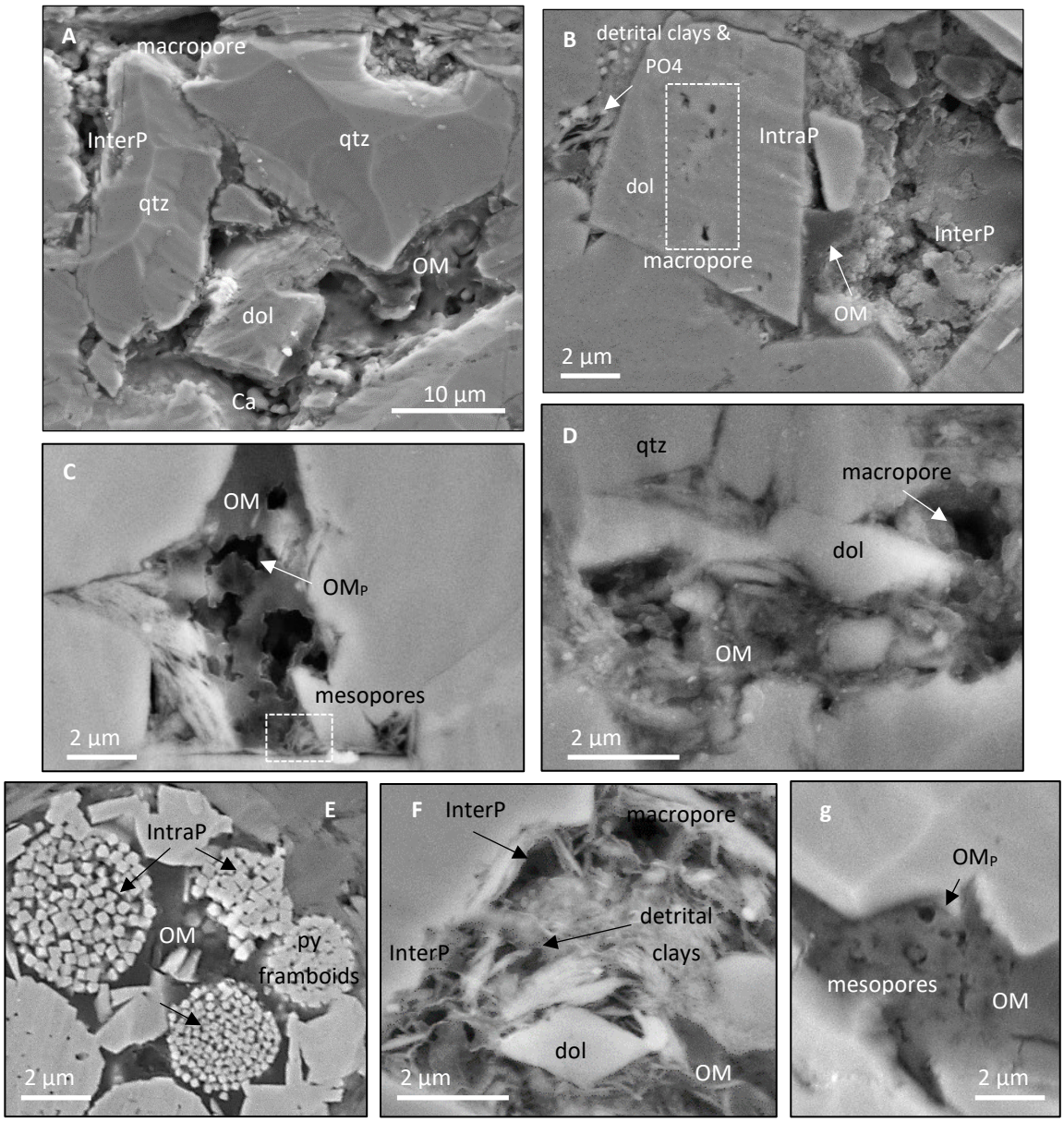

Figure 3.8 A to E. Representative SEM images of the different pore types and sizes present in the four rock types. (a and b) Interparticle pores were observed between detrital grains characteristic of each rock type, between OM and/or detrital clays. Most of the pores were macropore sizes and this type of pores are more common for RT 1, 2 and 4 and in less amount in RT 3. (b) Representative image of intrapore, this type of pores are present in detrital calcite, dolomite, and quartz grains. RT 1 with a major carbonate composition is characterize with these type of pores. (c) Representative SEM image for organic matter pore, these type of pores were observed in our four rock types, but RT 3 is defined with a major presence of this type of pores. (d) Interparticle pore space (macropore) infilled by detrital grains and organic matter, with also some organic matter pores. (e) Intrapore space was also observed in pyrite framboids, infilled with organic matter and/or detrital clays. (f and

g) Comparison between interparticle pores (left) and organic matter pores (right). Organic matter pores are the smallest and are represented by a simple shape form, in comparison to the more complex interparticle pores.

3.8 Petrophysical properties:

-Porosity: helium porosity and macroporosity analysis.

Helium porosity measurements were made on from 12 oil well core plugs (Figure 3.8.1a) and 12 gas well core plugs (Figure 3.9.1b). Helium porosity and macroporosity estimated from QEMSCAN analysis was subsequently compared. Porosity values from helium pycnometry range from 0.1 to 6.7%. RT 2 reported the highest porosities, with ranges from (1 to ~7 %), followed by RT 1 with porosities from (~1 to ~6%). RT 3 and RT 4 on the contrary, are rock types with lower porosities being RT 3 ranges from (0.1 to ~2%) and RT 4 ranges from (~1 to ~3%).

Porosity reported from QEMSCAN analysis identifies pores with a minimum diameter of 2 to <10 μm, which here is termed macroporosity. Macroporosity values vary between 0.05 to ~9%, RT 3 is the rock type with the highest macroporosity from ~4 to 9%, followed by RT 2 from ~2 to 8.5%. RT 1 reported macroporosity values of 0.05 to ~4% and RT 4 being the rock type with lowest microporosities, reported values of ~0.4 to 2.6%.

RT 2 has a strong positive correlation (R2= 0.9) between helium porosity versus macroporosity, followed by RT 1 with a strong positive R2= 0.8 between He-porosity and macroporosity. For RT 3 and RT 4 a strong positive correlation between porosities (R2= 0.7 and 0.6, respectively) was observed. RT 3 helium porosities reported the lowest values, while for macroporosity reported the highest values. This could refer that for RT 3 a large fraction of the pores in the samples consist of macropores (pores >2), rather than micropores, while for RT 4 this characteristic was inverted, major evidence of micropores rather than macropores.

There is also systematic variation in porosity between the oil well and the gas well samples (Figure 3.9.2). Each rock type in the oil well is represented by significant lower porosities (between 1 to ~3 units of difference) in relationship with the data obtain for the gas well.

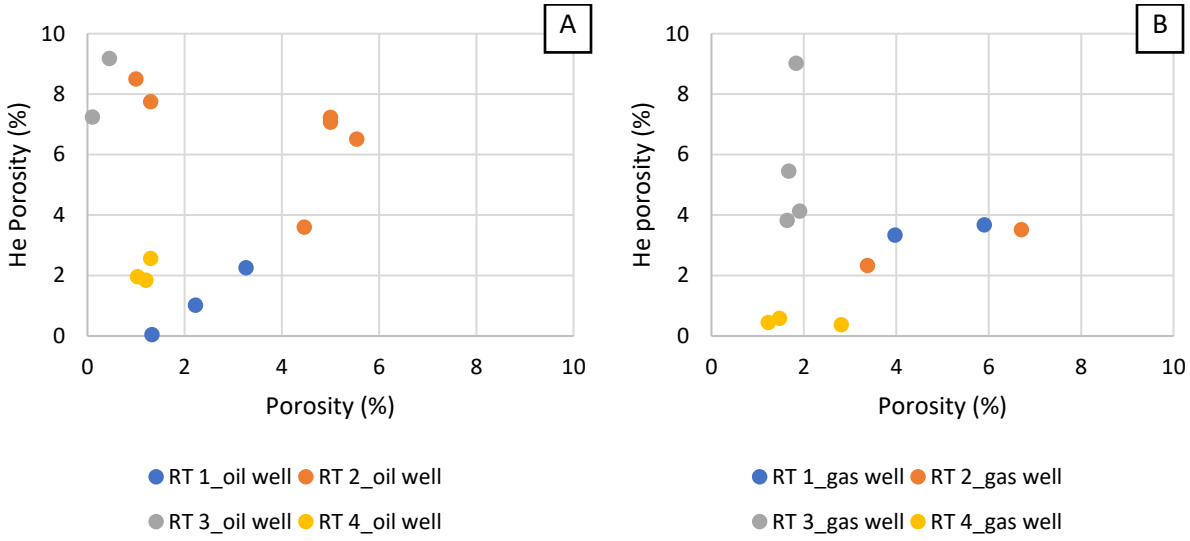

Figure 3.9.1 Matrix He-porosity (%) versus macroporosity (%) values (QEMSCAN) for the four rock types. RT 3 helium porosity is consistently higher than porosity measured through QEMSCAN analysis, which indicates that a large fraction of the pores in RT 3 consist of micropores, smaller than 2 µm.

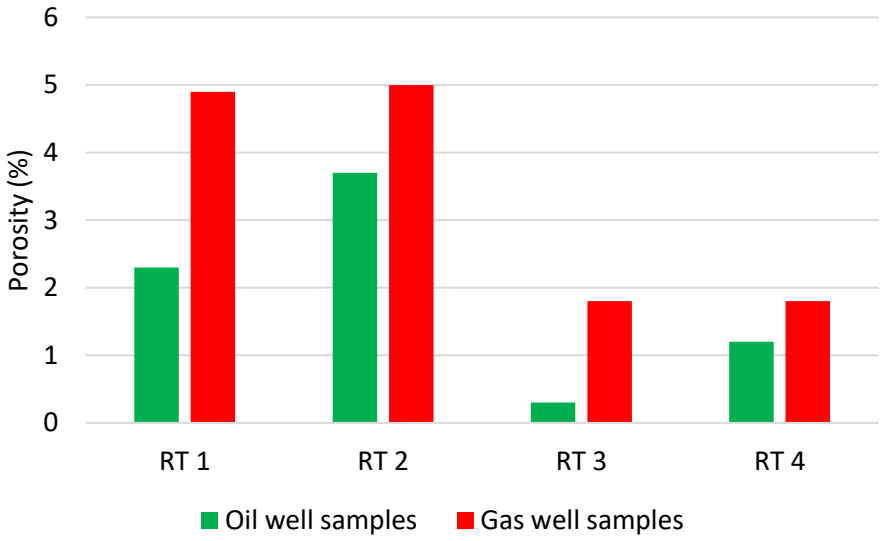

Figure 3.9.2 Relationship between porosities estimated for the four rock types in the oil well (green) vs porosities estimated for the 4 RTs in the gas well (red). RTs in the oil well show significantly lower values in comparison to the same rock type in the gas well.

- ***Permeability***

RT 1 samples on average, have the highest range of permeability, from ~100 nd to ~190 nd. RT 3 samples have somewhat lower permeability, with values of ~80 nd to ~230 nd, except for one sample with 9 nd from the gas well producer. RT 2 and RT 4 are less permeable, with ranges of ~30 nd to ~190 nd for RT 2, while RT 4 has the lowest permeabilities, from 20 nd to 70 nd.

Permeability ranges from samples in the oil well represent significantly higher values in comparison to samples from the gas well, which are represented by lower permeabilities overall (Figure 3.9.3). Permeability measurements within a single rock type group show significant variations in samples from the oil well, but more consistency in samples from the gas well (Figure 3.9.4).

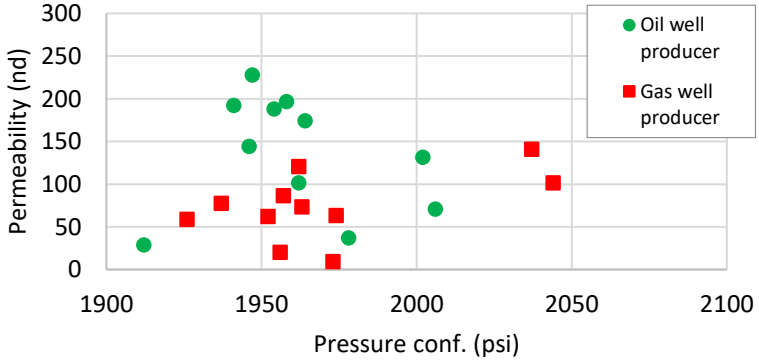

Figure 3.9.3 Cross-plot with representative rock type samples from the oil well (green) and the gas well (red). In general, the differences between permeabilities observed through pulse decay were mainly observed in the type of fluid present in the formation (oil/gas) rather than between rock types.

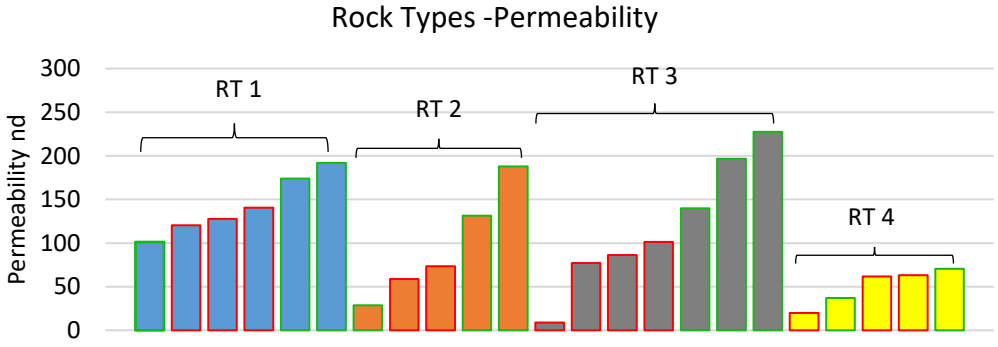

Figure 3.9.4 Histogram with plug permeability values from the four rock types. Samples from the oil well are marked in green and samples from the gas well are marked in red. RT 1 and RT 3 in both

wells are represented by the higher permeability values, while RT 2 and RT 4 are represented by lower permeability values overall.

- ***Mercury Injection and BET analysis.***

RT 1 and RT 2 are characterized by relatively large pore throat diameters, as measured by MICP experiments (Figure 3.9.5). RT 1 pore throat diameters range from 0.02 nm to 17.9 nm with a median pore throat diameter of 10.7 nm. RT 2 pore throat diameters range from 9.5 nm to 23.3 nm with a median of 7.8 nm, with a wider range of pore throat diameters in comparison to the other rock types. RT 3 and RT 4 are characterized by smaller pore throat diameters. RT 3 pore throat diameters range from 0.01nm to 12 nm (Figure 3.9.5 C) with a median pore throat diameter of 5.9 nm. RT 4, values ranged from 6.2 nm to 10.4 nm with a median value of 5.8 nm.

BET analysis shows that RT 2 has the largest average pore diameter 18 nm. RT 1 and RT 4 show similar values for pore diameter, with an average pore radius of ~16 nm. RT 3 samples have the smallest average pore diameter 9.2 nm. Thus, RT 3 samples have both small pore diameters and small pore throat diameters. RT4 samples, however, have small pore throats but pore diameters that are comparable to RT 1 and RT 2.

Three representative hysteresis loops are characteristic of the four rock types based on BET analysis (Figure 3.9.6 A to D). The forms of each hysteresis loop can be classified into Types A, B, and C, following the terminology of Zhang et al. (2016). Type A was typical of RT 1 and RT 4; this type is characterized by straight loops, corresponding to pores with narrow necks and wide bodies. RT 2 displayed Type C loops that are associated with open-wedge pores. RT 3 displays Type B loops, indicating a variety of pore types and pore throat diameters, typically related to slit-shape pores type and/or parallel -plate cracks (Cao and Li et al., 2016; Zhang et al., 2016).

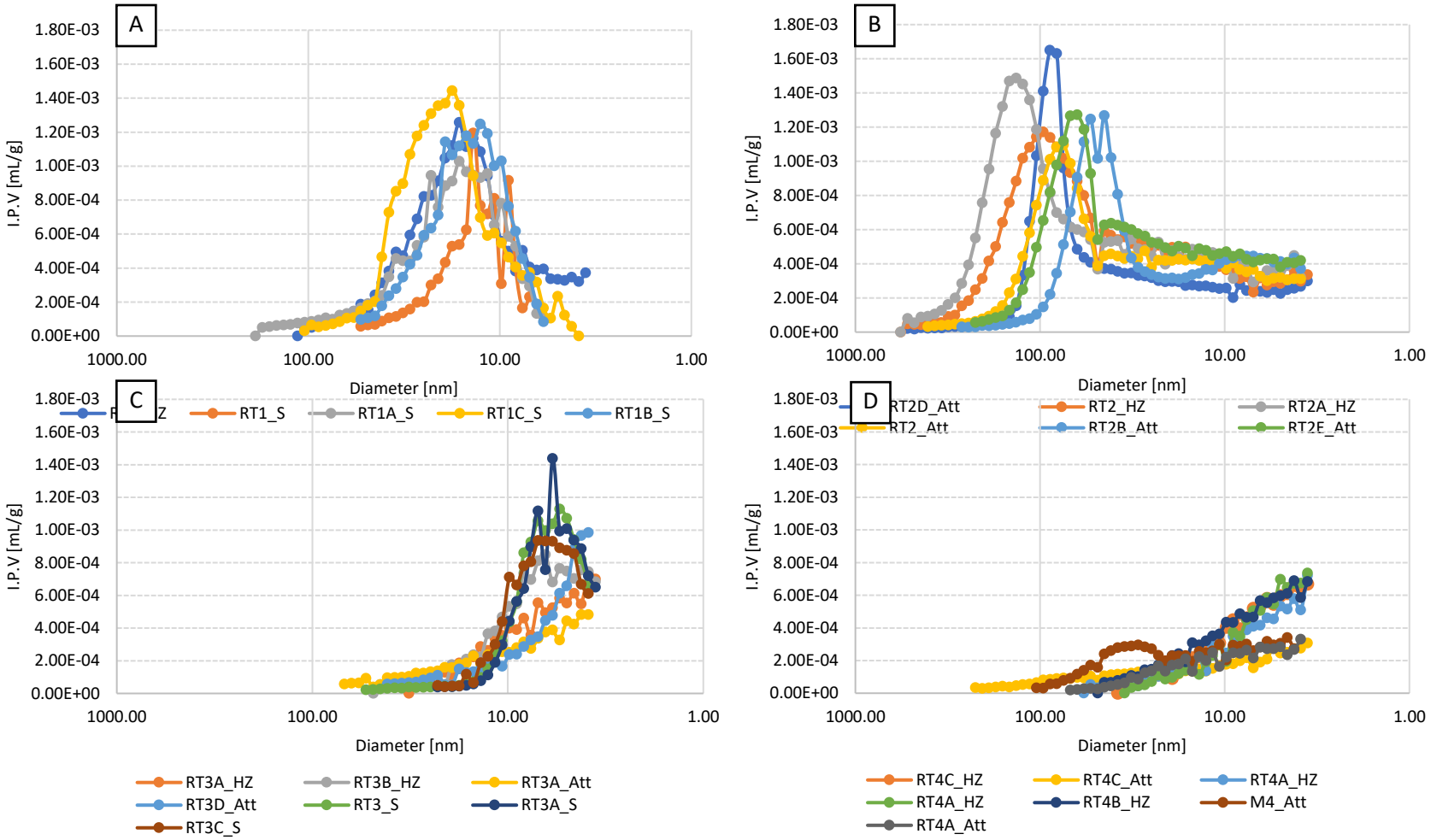

Figure 3.9.5 MICP curves representing the 4 different pore throat diameter distribution vs the intrusion pore volume related to each rock types identified. RT 2, with less carbonates and clay content than other rock types, has the bigger pore throats. This contrasts with RT 3 and 4 that contain higher amounts of clays and organics, whose pore throats sizes are smaller.

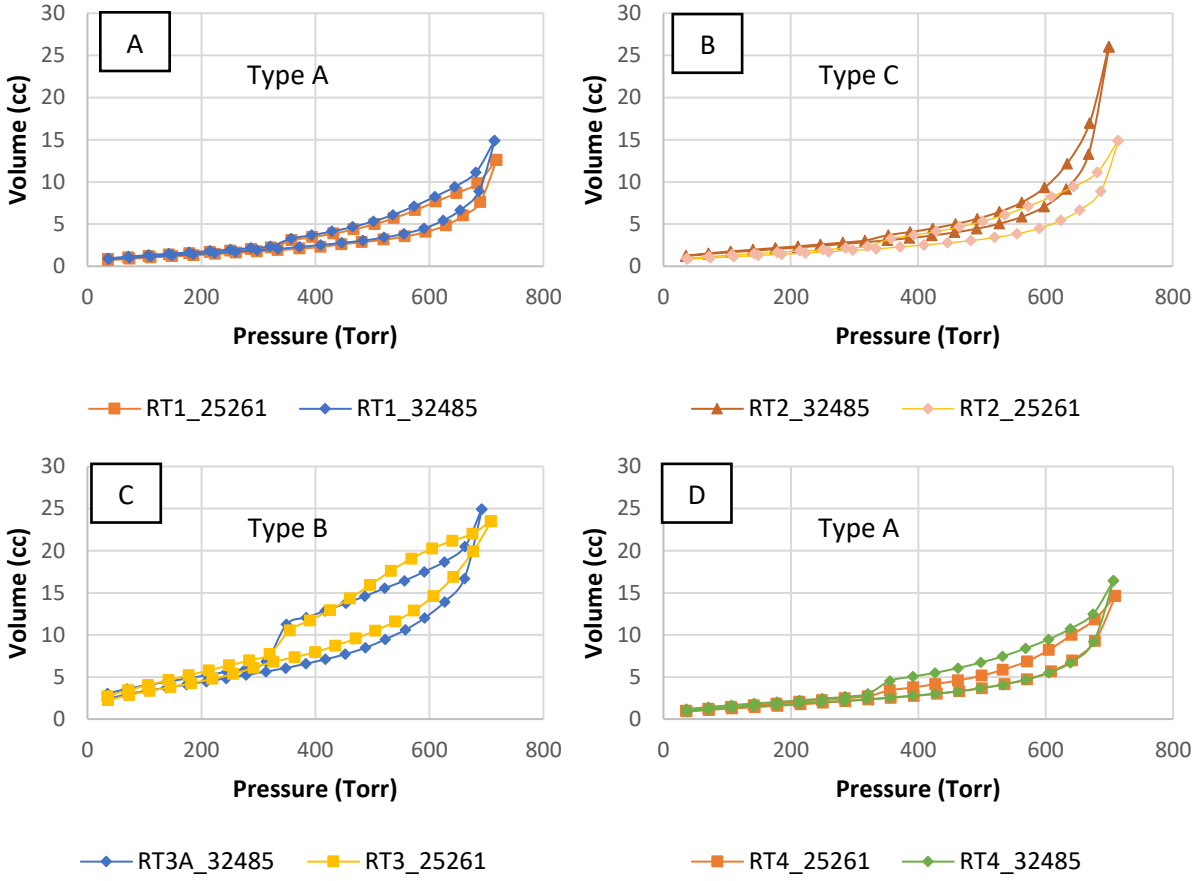

Figure 3.9.6 Representative adsorption-desorption isotherms for each of the four rock types identified. From hysteresis loops, we suggested that 3 main form types where consistent; Type A, Type B and Type C (Y Zhang et al., 2016).

Chapter 4 - Discussions

4.1 Mineralogical composition

-Variations between the rock types

Rock fabric and mineralogy are important controls on pore systems in unconventional reservoirs and thus influence fluid flow (Vishkai et al., 2018; Clarkson et al., 2012; Gan et al., 1972; Loucks et al., 2009, 2012; Nelson, 2009). More specifically, the abundance, shape and size of pores depends on grain size and sorting, the degree and type of cementation, and the nature of organic matter emplacement (Nelson et al., 2015). An understanding of mineralogical composition and its variation between rock types is a fundamental element of this research.

The dominant lithology in the Montney Formation in the Septimus reservoir is a shaly siltstone with large quartz concentrations and subordinate amounts of carbonate minerals (calcite and dolomite), K-feldspar + plagioclase, and clays (illite, mixed layer illite - smectite and interstratified Fe-illite - illite - smectite). These minerals are present through the entire Montney interval, although their proportions vary between rock types (Figure 4.1.1).

The differences between these four rock types mainly refers to the mineralogical proportion (%) of K-feldspar + plagioclase, quartz, and clays. For carbonates these proportion were not significant except between RT 4 versus RT 1 and RT 2. In summary, RT 1 is classified as the rock type with the highest carbonate content, RT 2 the rock type with lowest clay content and with a major feldspar composition, and RT 3 as the rock type with a major clay composition. RT 4 showed no distinctly elevated contents of any particular mineral but was statistically distinctive from the other three rock types.

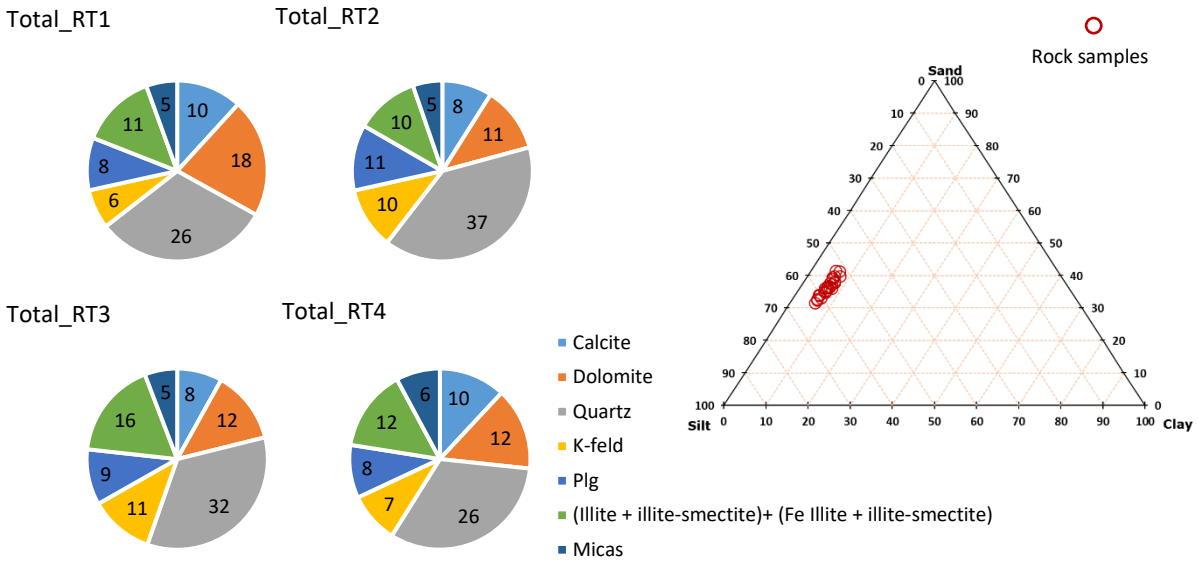

Figure 4.1.1 Average mineral composition (%) for each rock type; quartz being the most abundant, followed by carbonates and feldspars. On the top right, representative grain sizes (from QEMSCAN analysis) distribution from well 100/04-09-084-22W6/00.

- ***Detrital composition versus diagenetic alteration.***

Diagenesis refers to the physical and chemical processes that affect sedimentary rocks after and in between their deposition and weathering. Present-day mineralogy of the Montney Formation reflects a depositional composition that was subjected to diagenetic alteration (Krause et al., 2012, Wust et al., 2016, Vaisblat et al., 2021).

The Montney Formation was deposited under acidic and reducing conditions, and under these conditions, oceanic water tends to have high alkaline elements concentrations such as sodium, potassium, and calcium, and in less amount magnesium and iron (Tribovillard et al., 2006; Caracciolo et al., 2014; Vaisblat, 2020). Previous studies of the Montney Formation concluded that this supersaturated water flowed through a pre-existing open network of pores, possibly driven by reflux from shallow water lagoons (Vaisblat et al., 2021), leading to precipitation of abundant cement at relatively shallow burial depths.

Compositional differences between the four rock types can be attributed to two main factors, one related to the depositional setting, and the other related to diagenetic alteration. RT 1 and 4 are similar in fabric and texture, characterized by a relatively large amount of silt-size grains, well to

moderately sorted, sub-rounded to rounded, with a relative lower amount of clays; in RT 3 and RT 2, on the contrary, the amount of sand-size grains is greater, both rock types are moderately sorted, with angular, sub-angular, and sub-rounded grains, and RT 3 has higher amount of clays than RT 2 (Figure 4.1.2).

RT 2 is primarily present in the Upper Montney interval (Figure 3.2.2) and can therefore be associated with the last stage of deposition, where the Montney Formation comprised sediments deposited in a storm-dominated shoreface and offshore transition (Seifer et al., 2015; Feng, 2021). RT 1, 3 and 4 can be found stratigraphically and laterally through the entire Montney interval and are more associated with the complex turbidite channels associated with the Lower Montney Formation in the Peace River Arch region of northwest of Alberta and Northeast British Colombia (Sereda et al., 2017; Zonneveld et al., 2011).

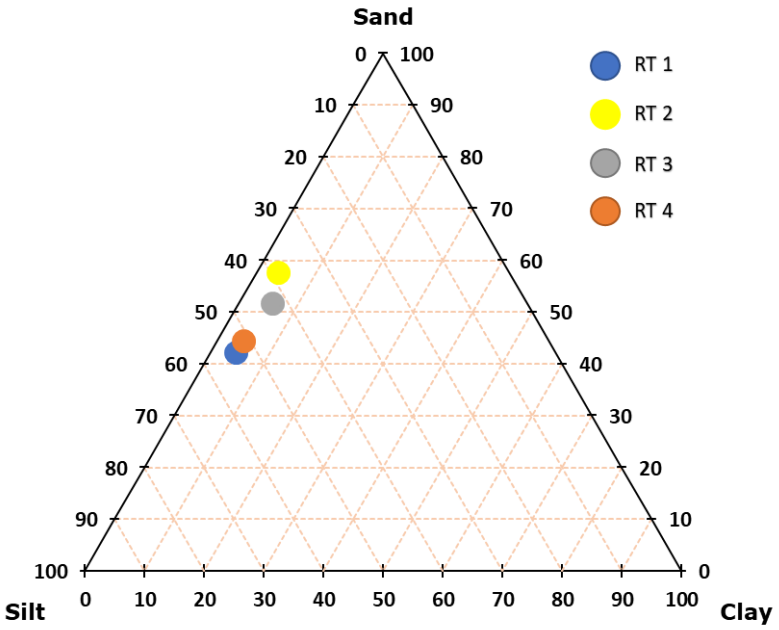

Figure 4.1.2 Ternary diagram representing the main grain size distribution for each of the four rock types. The data represented is the average of each RT from the 3 well cores analyzed.

Diagenetic modification of the original sediment is the second factor responsible for compositional variability. Diagenesis also modified original porosity through mechanical compaction, cementation, dissolution, and replacement (Vaisblat et al., 2021). Paragenetic sequences differ between rock types, particularly between RT 2 and the other rock types. In Septimus samples, diagenetic features include minor to moderate compaction, early phosphate formations, and early

pyrite precipitation, carbonate and quartz cements, late pyrite precipitation, dissolution of grains (carbonate, feldspars, and quartz), and cements, and emplaced hydrocarbon.

- ***Paragenetic sequence***

Following a classification by Vaisblat (2021), we grouped diagenetic processes into (1) early diagenesis, taking place while pore waters communicated with the ocean, (2) shallow burial diagenesis, taking place within a few hundred meters of the surface, (3) late diagenesis, during deeper burial or subsequent uplift. The summary of the diagenesis processes is presented in Table 4.1.

- *Early diagenesis and shallow burial diagenesis*

The phosphatization of bioclasts, growth of phosphatic nodules and formation of grain coats are the main diagenetic processes included in the early diagenesis stage (Figure a to b 4.1.3 and 4.1.5 c and d). Following burial, mechanical compaction and cementation, which are controlled by the sediment composition, these are the principle features that influence primary porosity. It was during this shallow stage when the framework became slightly compacted as the interstitial water in the formation was expelled due to compaction. Clays and cementation by carbonate minerals during this stage, play a significant role as both prevented excessive compaction, but at the same time infilled primary porosity, reducing both porosity and permeability of sediments (Revil et al., 2002; J. Lai et al., 2016; Vaisblat et al., 2021).

Clays in the Montney Formation are dispersed within a matrix of hard grains and are primarily present in RT 3 and RT 4. QEMSCAN analysis showed that the major clay present is a detrital MLIS, consisting primarily of illite (90-95%) and with a minor smectite component (~5%), confirming Vaisblat et al.'s (2021) analysis from measurement of clay expandability. Most of the detrital clays were altered from smectite to illite-rich compositions at an early diagenetic stage during shallow burial. Previous studies (Vaisblat, 2020; Edwards et al., 1994; Zonneveld and Moslow, 2014, 2018; Vaisblat, 2021) reported a significant amount of swelling clays only at the northeastern margin of the formation, related to the Ring-Border and Dixonville deltas as a source of sediment. The distribution of these swelling clays near and at the same burial depth as non-swelling MLIS clays suggests that a low temperature reaction (60-80 °C) for an extended period

of time and under relatively shallow burial conditions (high porosity and high permeability) was responsible for illitization of the MLIS (Moore, 2000; Vaisblat et al., 2021).

Reducing conditions and precipitation of iron-rich diagenetic minerals such as pyrite, ferroan carbonates and chlorite are typical during early burial diagenesis. Numerous studies of modern marine and nonmarine sediments demonstrate that framboidal pyrite typically forms within the water column of a euxinic water column or in the first few centimeters of sediment below the sediment-water interface, due to the bacterial interaction between H2S produced by the organic matter present and these iron-rich ferroan minerals in the sediment; shortly after burial (Wilken et al., 1996; Love et al., 1983). Therefore, the well-formed framboid pyrite observed throughout the Montney Formation in our samples (Figure 4.1.4a to c and 4.1.7a to c) indicate that pyrite precipitated in early stages.

Carbonate cements are common in the Montney Formation, and the petrographic evidence presented here (Figure 4.1.5a to c) indicates that it occurs both as non-ferroan and ferroan phases. The early carbonate cement is primarily a non-ferroan calcite (syn-depositional), which plugs primary porosity and replaces feldspar grains. Small amounts of ferroan calcite cement also precipitated during this early stage. This ferroan calcite fills remnant porosity and replaces detrital clay (Figure 4.1.5a and b). Also early in the shallow diagenetic history, the introduction of magnesium-rich formation water into the sediments caused selective dolomitization of the siltstone (Machel, 2004; Vaisblat et al., 2021). Subhedral to euhedral dolomite rhombs are present, occluding intergranular porosity and replacing or displacing detrital matrix, framework grains and early-stage calcite cement (Figure 4.1.5c).

Two generations of quartz cement are present in lesser amount than the carbonate cements and have been attributed to several possible internal sources of silica (Vaisblat et al., 2021). Our SEM and petrographic observations support Vaisblat's interpretation that some of the silica was provided from the silt-size quartz grains (in less amount) and from biogenic silica, including silica nanospheres that resulted from bacterial activity (Al Rajaibi et al., 2015; Milliken and Olson, 2017; Dong and Harris, 2020) (Figure 4.1.6b). Studies of the Montney Formation, particularly in Alberta, have suggested that biogenic silica is an important source in at least two intervals within the Montney (Wust et al., 2018).

Another source of quartz cement is pressure solution. Pressure solution is considered to be a major source of quartz cement in sandstones and generally is associated with high temperatures during deep burial (Bloch et al., 2002). Makowitz and Milliken (2003) suggested that, in fine grained sediments, fractures in quartz grains, enhance dissolution through pressure solution, and because microfractures in grains can develop in any effective stress, pressure solution under shallow burial conditions, is a viable source of quartz cement in the Montney (Figure 4.1.6c) (Makowitz and Milliken, 2003; Vaisblat, 2020).

- *Late diagenesis*

In the Montney Formation, black organic matter observed in SEM and petrographic thin sections, is mostly solid bitumen largely incorporated into the detrital clay matrix (Figure 4.1.5 A to D). Previous studies suggested that organic matter present in these siltstones formed from oil that migrated into the formation, presumably sourced from the Doig Formation or the Gordondale Member of the Fernie Formation (farther east the basin) (Riediger et al., 1990). The oil was altered extensively, possibly by thermal cracking (Sanei et al., 2015), leaving what presently observed as a solid bitumen. Further burial, under the presence of undersaturated pore fluid, and possibly due to the leaching reactions induced by the CO2 and hydrocarbon degradation, less stable framework grains such as feldspar, and dolomite, were subjected to partial dissolution (Figure 4.1.5c to e and 4.1.6a) (Surdam and Crossey, 1989; Yuan et al., 2015).

We lack quantitative data to assess the degree of cement development at this stage, furthermore, the occurrence of fibrous illite in all intervals of the Montney Formation makes difficult to determine if this late dissolution took place prior/after or contemporaneously to the precipitation of these clays; therefore the late fibrous illite is represented as the last diagenetic event at this location.

Table 4.1 Paragenetic sequence for the Montney Formation in Septimus.

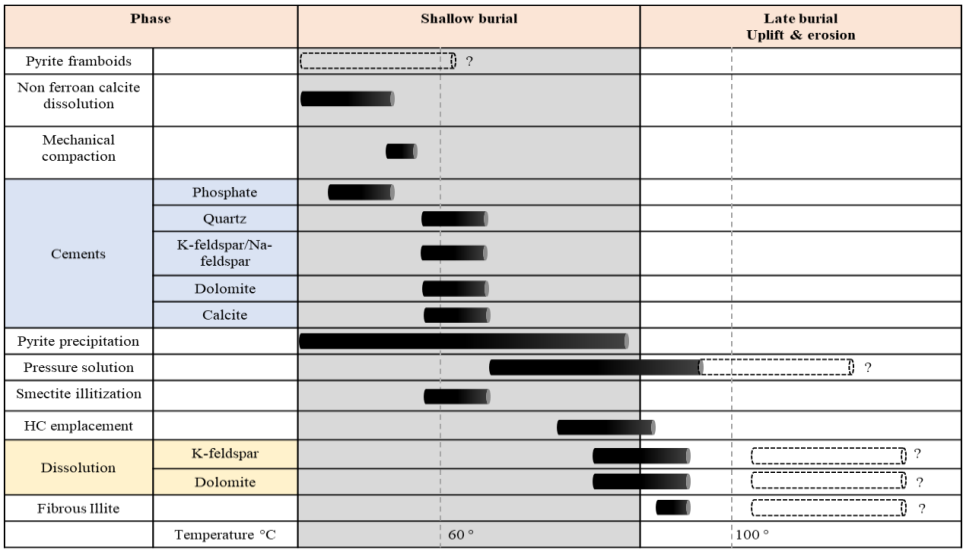

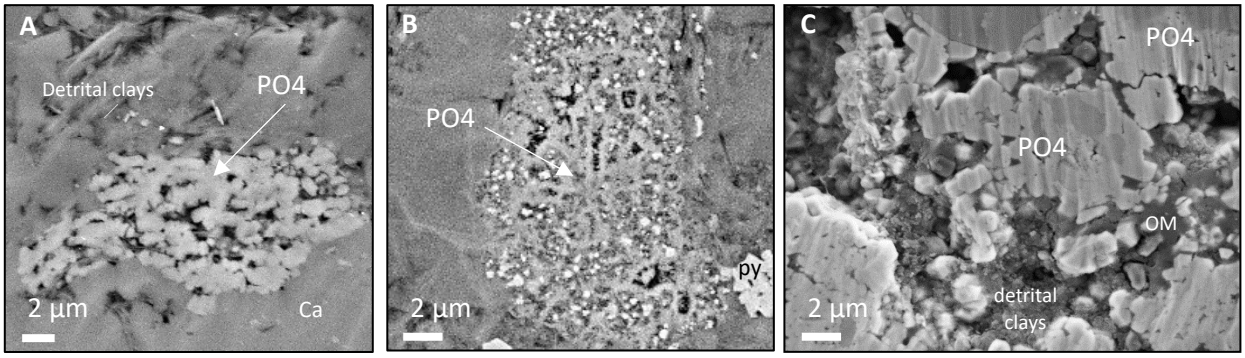

Figure 4.1.3 Representative SEM images of phosphate present in rock types. Phosphate occurs as (c) grain coatings, and/or (a and b) pore filling cement. Dissolution on phosphates was also present.

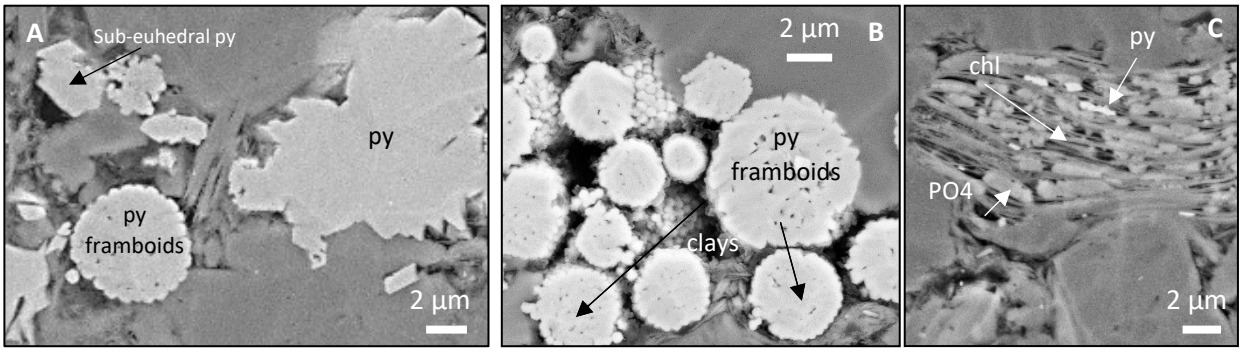

Figure 4.1.4 Pyrite. Samples from the four rock types showed through SEM images evidence of pyrite all along the Montney Formation. Pyrite occurs in a range of forms, (a) euhedral crystals, pyrite framboids, and as cement. (b) Pyrite framboids occludes interparticle pore space between detrital grains, clays, and/or OM. (c) Pyrite and phosphate grains are present between sheets of micas as well.

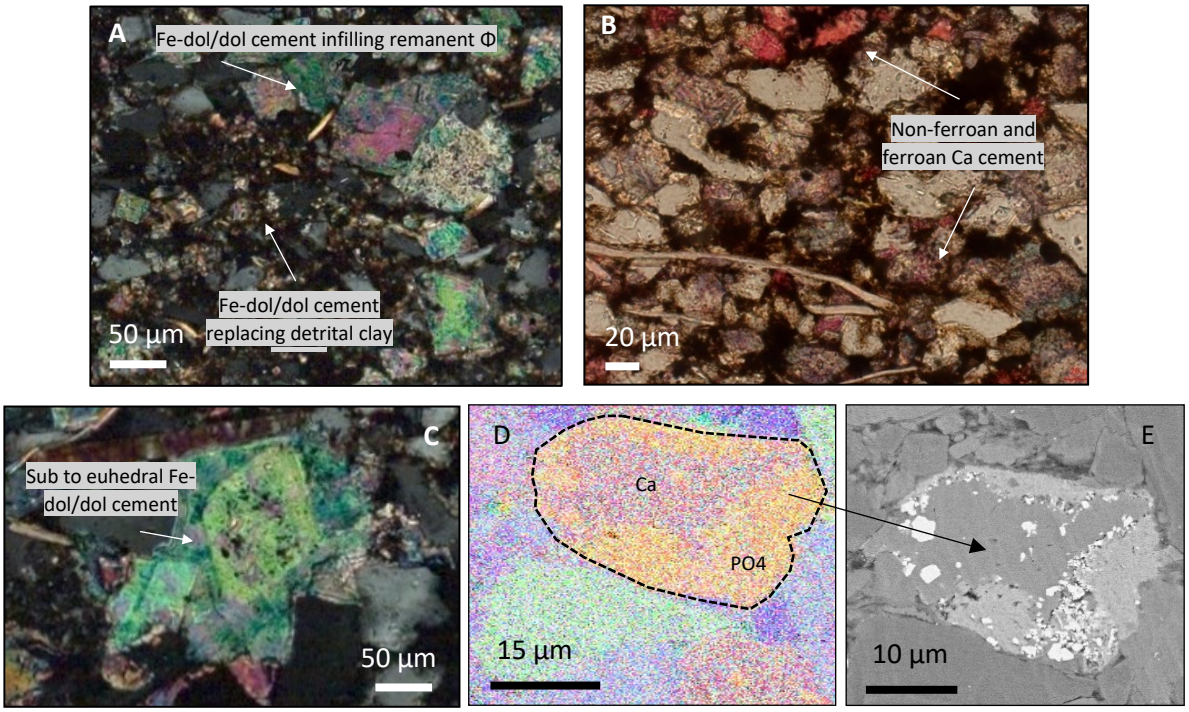

Figure 4.1.5 Petrographic thin sections of carbonate minerals. (a) Fe-dolomite/dolomite cements infilling remanent porosity and replacing detrital clay matrix. (b) carbonates occur as ferroan and non-ferroan phase (c) Subhedral to euhedral Fe-dolomite/dolomite rhombs replacing early calcite cement as some framework grains. (d and e) EDS and SEM image of an early stage of phosphates and pyrite replacement on a carbonate grain.

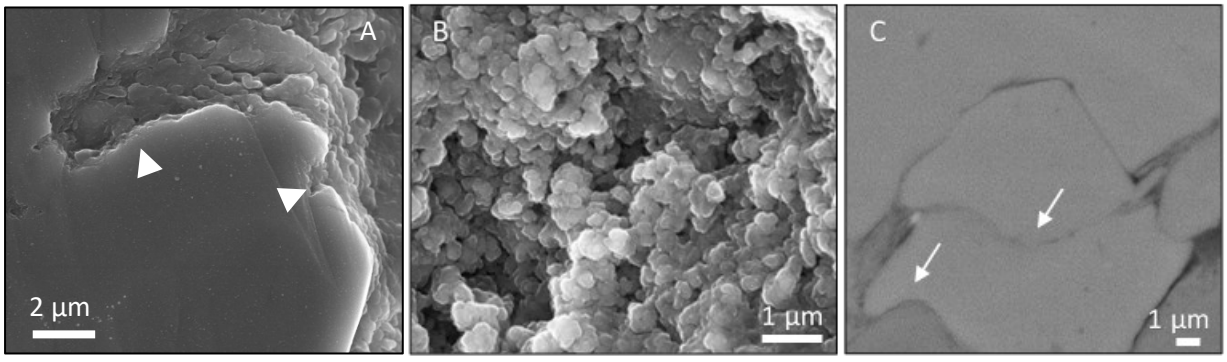

Figure 4.1.6 a to c Evidences of the different sources for the mixture of quartz in the Montney Formation. (a) SEM image of detrital quartz grain (possible dissolution). (b) SEM image of silica nanospheres. (c) SEM image showing pressure solution between detrital quartz grains.

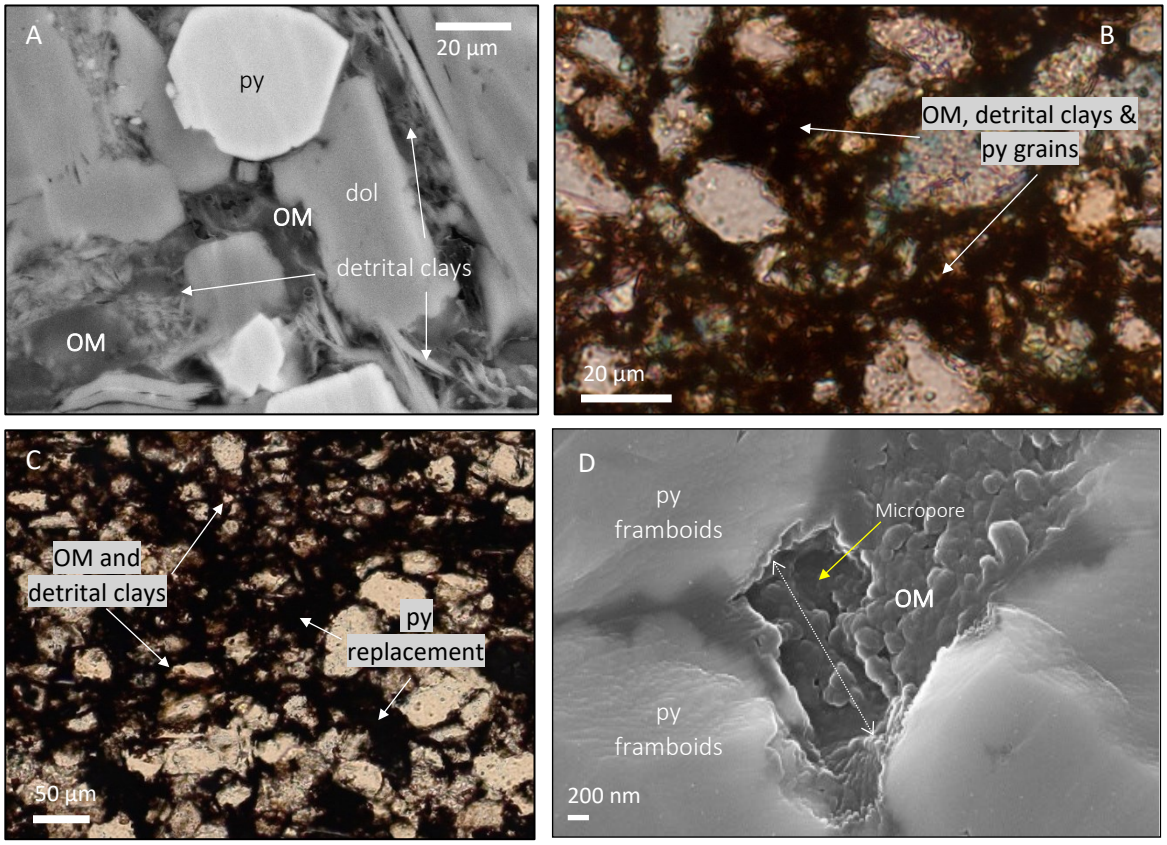

Figure 4.1.7 A to D. Evidence of organic matter present as a solid bitumen and mostly mixed with the detrital clay matrix, detrital grains, and pyrite replacement in the four rock types.

4.2 Rock typing (log expression) and rock types

- Log characteristics and mineralogical relationship

The distinctive log responses that characterize our model and lead to the definition of four rock types can be related to mineralogical and TOC contents of the Montney Formation. RT 1 is distinguished by the lowest GR and NPHI, and relatively high RHOB values. These observations can be related to the higher presence of carbonates in comparison to K-feldspar + plagioclase, and low clay content (discussed in 3.1 and 3.4). RT 4 log's signature, highest NPHI and RHOB, and low GR can be explained by the higher presence of quartz content, lower %TOC, and higher clay content than RT 1.

RT 3 is distinguished in terms of log characteristics by the lowest RHOB, relatively high GR, and relatively low NPHI, related to the high clay content, and high %TOC. Finally, RT 2 is recognized on logs by the highest GR, high NPHI and relatively low RHOB peaks, related to the high amounts

of K-feldspar compared to the other rock types, relative low concentrations of TOC, and very low clay concentrations (cleanest rock type of all).

This analysis shows that rock types (with distinctive mineralogical compositions) can be mapped with confidence across Septimus field. To the extent that pore systems and petrophysical properties can be associated with rock types, discussed in the following sections, rock typing from logs can also be used to map petrophysical properties at a field scale.

4.3 Pore systems

- Morphology and distribution of pores.

Pore systems can be classified by petrographic evidence; in this case, we follow the classification by Loucks et al. (2012), who considers interparticle pores, intraparticle pores, pores in organic matter, and fracture pores. Because fracture pores rarely comprise a significant fraction of the pore space, pore systems are commonly represented on ternary diagrams in which the apices are the first three pore types. Petrographic and SEM examination of the Montney samples from Septimus field indicates that interparticle and intraparticle pores are the most abundant with subordinate organic-matter pores.

The distribution, and morphology of pores can provide information about their genesis and development (Jiao et al., 2014). Thermal maturity and OM composition are some of the factors involved with the development of pores (Curtis et al., 2012; Milliken et al., 2013). Interparticle and intraparticle pores are typical in shales and mudrocks at shallow to intermediate burial stages, and at low thermal maturities (Dong et al., 2019). At thermal maturity stages equivalent to hydrocarbon-generation window, under deep burial stages, organic matter pores are highly developed (Jiao et al., 2014; Loucks et al., 2012; Dong et al., 2019). As hydrocarbon is generated from organic matter, these pores can expand and merge (Loucks et al., 2009, 2012).

A comparison of cores in this study shows that samples from the oil producer display fewer organic matter pores than samples from the gas producers. Therefore we conclude that the morphology and distribution of this complex pore network system has been influenced by the rock composition (mineralogy) and organic carbon content.

- ***Porosity and permeability relationship.***

Analyzed He-porosity values from plugs ranged from 0.5 % to 6.7 % with a median average of 2.8 %. Porosities differ not only between rock types, but also significant differences in the porosities were observed from the oil well versus the gas well. We observed that plugs from the oil producer generally have lower porosities in comparison to the gas core plugs (between 1 to 2 units of difference) (Figure 4.3.1).

Plug permeabilities for the four rock types generally vary over a small range from ~50 nd up to ~150 nd in average, but significant differences in permeability in samples from a specific rock type are evident depending on whether gas or oil is produced. Permeabilities for the plugs from the oil producer were slightly higher than permeabilities estimated in the gas producer (Figure 4.3.2).

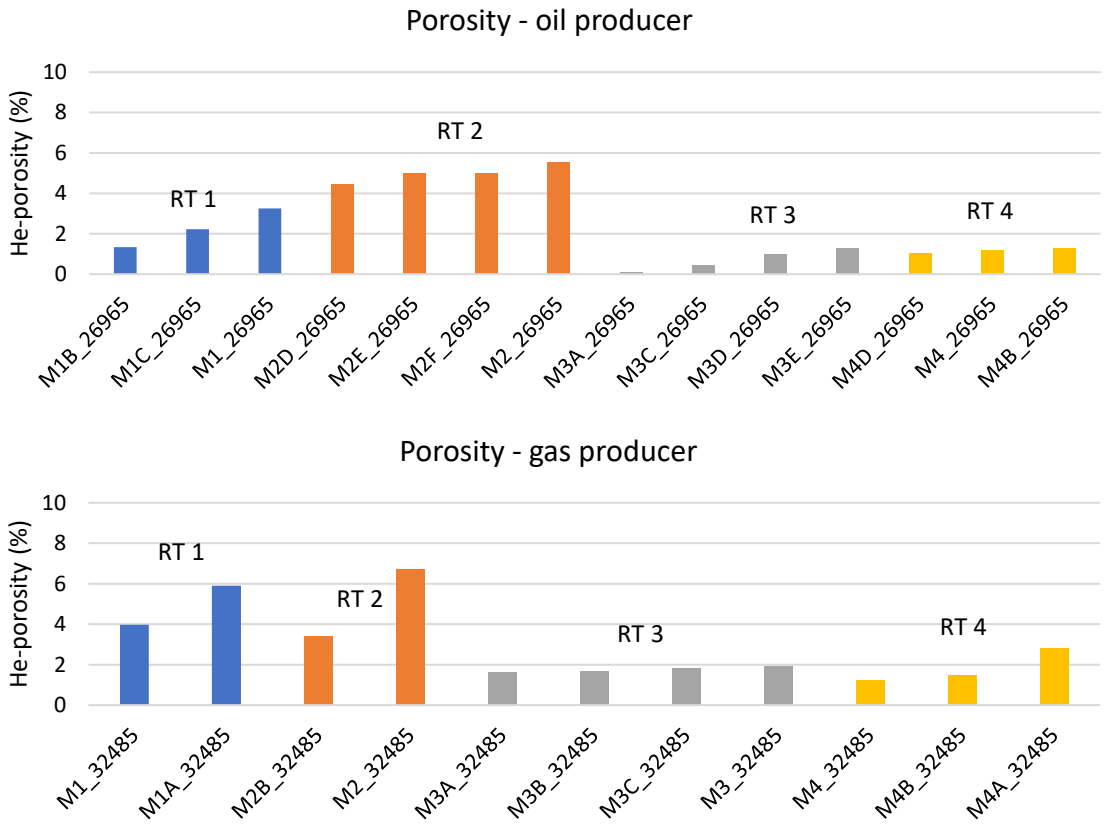

Figure 4.3.1 Porosity values obtain from plugs from the oil producer (upper) and gas producer (lower) representing each set of samples for the four rock types described. Overall, RT 3 and RT 4 are rock types with the lowest porosity values.

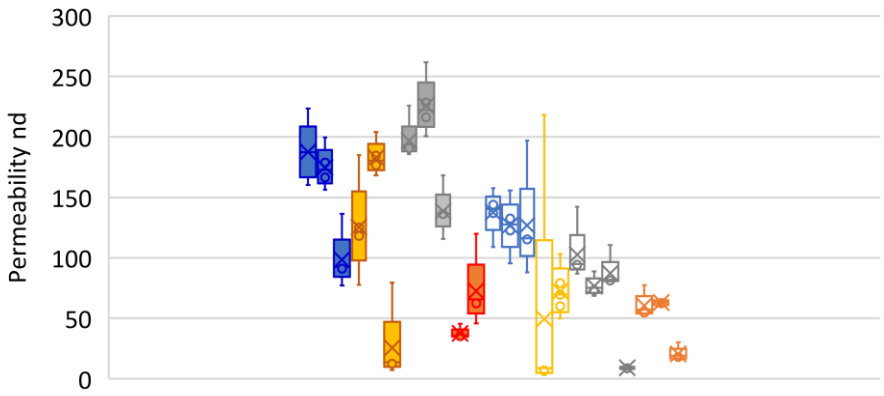

Figure 4.3.2 Permeability values obtain from the oil and gas wells in core plugs representing each set of samples for the four rock types described. Figures with unfilled symbols represent samples analyzed at the gas producer. Overall permeability in same rock type showed slight variation between gas and oil producers, with samples from the oil producer exhibiting higher permeabilities.

Compositional variables (mineralogy, TOC) generally show little relationship to porosity and permeability, at least when considered individually. He-porosity was unrelated to mineralogical composition (Figures 4.3.4a except Fig. 4.3.4b and Appendix 5), except to note that samples with less than 10% clay had porosities above ~4.5%. In a study of mudstones, Yang and Aplin (2010) observed a systematic control of both porosity and permeability by clay content, in contrast to our observations here in which clays has no clear influence on porosity- or permeability relationship. The lack of a relationship in our dataset may result from the relatively limited range of clay content present in the Montney in comparison to the Yang and Aplin (2010) dataset.

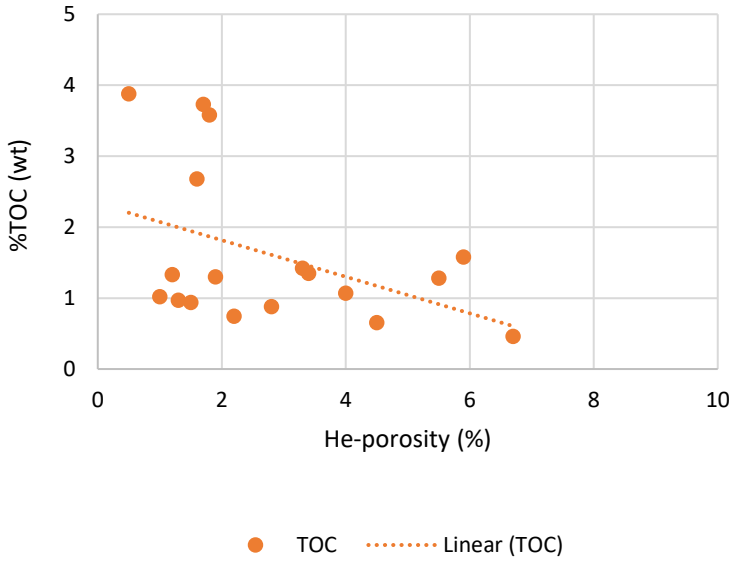

Figure 4.3.3 He-porosity (%) vs %TOC (wt) plot with representative samples (orange dots) for the four rock types. A small negative relationship was observed between these two properties, which implies that TOC somehow is influencing the porosity loss in the rock types.

Rock type analysis successfully differentiates petrophysical properties of samples. Since rock types are differentiated by composition and fabric, this analysis suggests that a mineral assemblage – rather than individual minerals – influences porosity reduction. RT 2 mineral assemblage consists of very fine sand-size grains with a component of fine silt grains. RT 2 samples are grain supported, cemented by Fe-dolomite/dolomite and in less amount Ca cement, with less clays and organic matter occluding the pore space compared to the rest of rock types. RT 1 and RT 4 differ from RT 1 and RT 3 in terms of mineral assemblage, fabric, and TOC. These two rock types contain predominantly fine silt grains with a component of very fine sand-size grains. RT 1 samples are either grain-supported, cemented by Fe-dolomite/dolomite and Ca cements, or cemented by clays and organic matter, whereas for RT 4, grains are supported by a matrix that is pervasively occluded with detrital grains, clays and organics and in less amount Fe-dolomite/dolomite cement.

RT 3 assemblage differs from the rest as this rock type the proportion of fine silt grains and very fine sand-size grains is almost 50/50 and which are supported by a matrix pervasively occluded with detrital grains, clays and organic matter leaving almost non-visible pore space. Therefore, mineral assemblage, fabric, and TOC (somehow) for our rock types does influence in the porosity loss, RT 1 and RT 2 representing rock types with relatively higher porosities (with a ~1:1 ratio between macroporosity vs He-porosity) whereas RT 3 and RT 4 represent rock types with lower porosity values (Fig. 4.3.1).

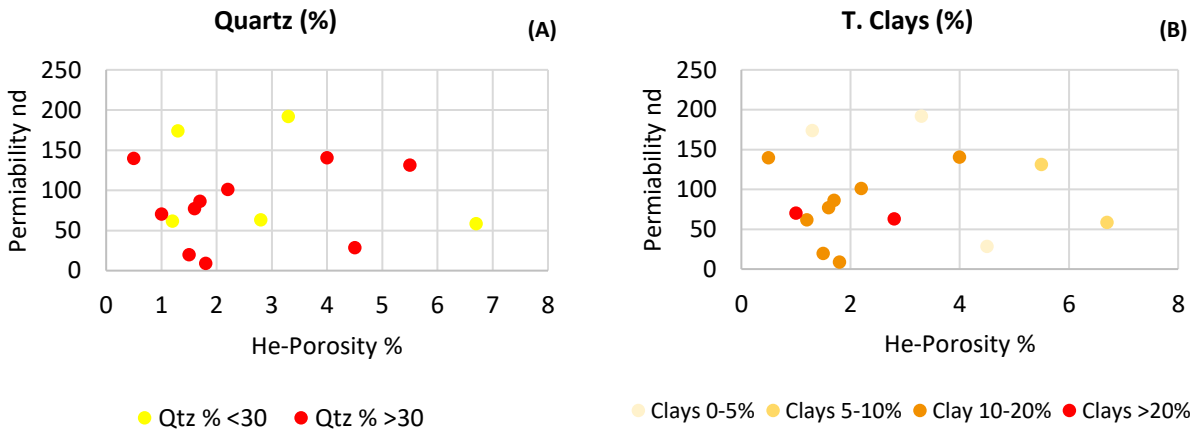

Figure 4.3.4 He-porosity vs permeability relationship. (A) Samples are classified according to their quartz % content, though quartz concentrations for most of our samples was >30% (72% of samples), no clear relationship between porosity vs permeability was observed. (B) shows the

association between clay content and porosity (44% of the samples with total clays 5-10%), dots in red represents RT 3 and RT 4 samples with total clays > 10 % and having values in the ranges of ~0.4-3 % porosity.

- ***TOC/bitumen saturation (Sb) control on porosity***

We convert TOC to bitumen saturation, following Wood and Sanei et al. (2015), who calculated the bitumen saturation in the Montney as a function of %TOC (wt) and porosity (%) (equation 2). Applying this to our data, we observe that samples with an S_b>0.3 typically have lower porosities in comparison to rock types with a lower S_b value (Figure 4.3.5a).

$$S_b = \frac{\%TOC}{\%TOC + \%\,\Phi} \ldots (2)$$

Where:

- S_b= Bitumen saturation
- %TOC = LECO TOC
- % Φ = porosity calculated through grain size and bulk density

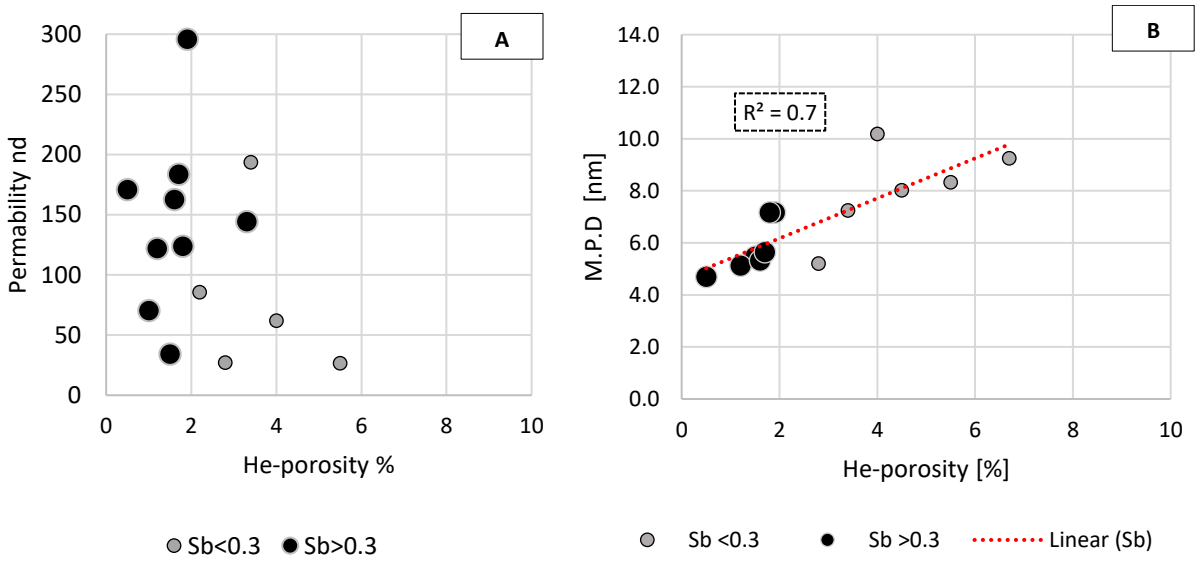

Figure 4.3.5 (a) He-porosity (%) vs permeability (nd) plot associated to bitumen saturation, we identify that though there is no clear positive or negative relationship between these two properties, bitumen saturation influence porosity for the different rock types. (b) Porosity (%) vs M.P.D. (nm) associated to bitumen saturation.

Moreover we observed a strong positive relationship (R^2=0.7) between porosity versus the median pore diameter, (Figure 4.3.5b), in which samples with high He-porosity and M.P.D. are associated with elevated bitumen saturations. This is also shown in Figure 4.3.6. as a negative relationship (R^2=0.5) between the bitumen saturation and the median pore diameter (Figure 4.3.6). These relationships suggest that matrix permeability is being controlled predominantly by the pore throat size, rather than porosity (Wood et al., 2015, Akai et al 2018, Vaisblat et al., 2020) and, in turn, by bitumen saturation.

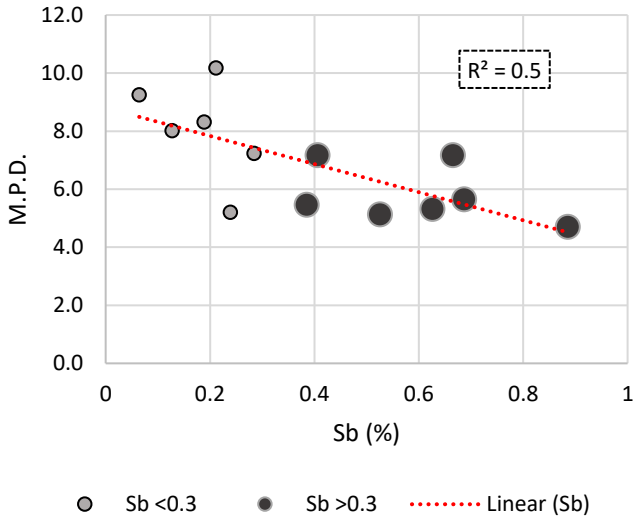

Figure 4.3.6 Cross-plot of bitumen saturation vs median pore diameter. Rock types in general show a strong negative relationship R^2=0.5. This confirms that most of the organic matter present occludes the pore network in the formation.

Consequently, examination of Figures 4.3.3, 4.3.4 (a and b), and 4.3.5 (a and b) suggest then that porosity for the four rock types in the Montney is influenced somehow by the mineralogy (mineral assemblage and fabric), clay content, and TOC; being the bitumen saturation the parameter with a major impact in the porosity of the rock types.

- ***Rock types control on permeability***

Rock type analysis successfully differentiated permeability. RT 1 and RT 3 overall were the rock types with the higher permeability values, while RT 2 and RT 4 had lower permeabilities (Figure 4.3.2). Unlike conventional reservoirs in which permeability is in part a function of porosity (following the Kozeny-Carmen relationship), no clear relationship between porosity and permeability is evident in our data set (Figure. 4.3.4).

Permeability is weakly related to major mineral constituents (carbonates, quartz, feldspars, and clays). We identify a relatively small positive relationship between permeability and carbonate

content, and a small negative relationship between permeability and the clay content (MLIS content) (Figure 4.3.7 a and b). No relationship was evident between permeability and feldspars and quartz content. These associations are important because hard mineral content (quartz and carbonates) tends to retard compaction, and clay content tends to promote compaction, which is effective at reducing porosity and permeability in shales and siltstones.

Permeability overall reflects the interconnection between pores and depends on the abundance and distribution of cements and detrital matrix. Based on the pore network system at the study location, we observed that permeabilities in the rock types are reduced by diagenetic chemical reactions rather than by compaction, therefore the permeability reduction can be related mainly to the precipitation of theses cements (described in this study - carbonates predominantly and in less proportion quartz cement), microporous illite, as the presence of the solid bitumen within the pore network.

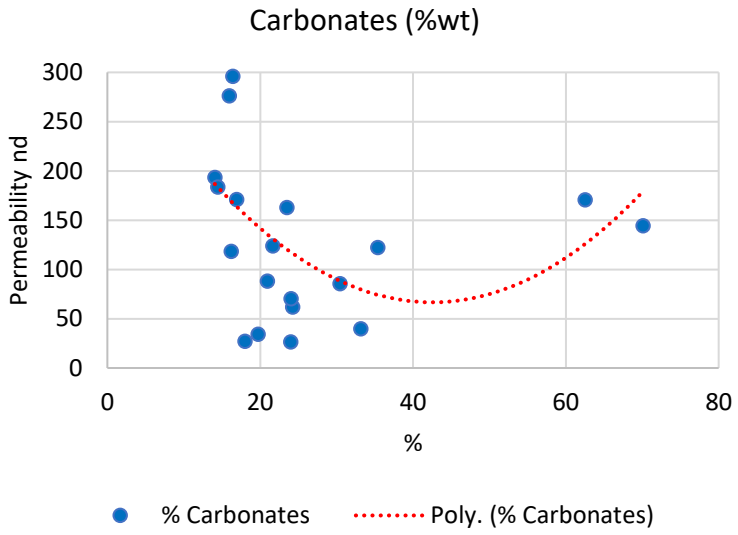

Figure 4.3.7a Plot with representative plug samples from oil and gas well showing the relationship between carbonate (%) vs permeability (nd).

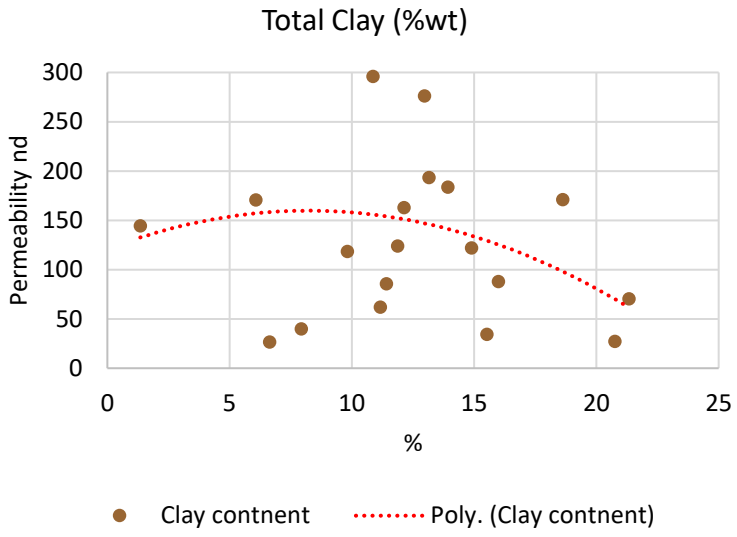

Figure 4.3.7b Clay content (%) vs permeability (nd). Both showed a small positive and negative relationship confirming that rather than compaction, diagenetic chemical reactions (cements) are one of the main controllers in the permeability of the different rock types.

- ***Hydrocarbon production and their relationship with to porosity-permeability***

For mudstone/shale reservoirs, the nanometer-scale pore network system controls the occurrence, migration, and production of shale gas (Curtis, 2002). Figure 4.3.2 showed that the type of hydrocarbon produced from the well is related to significant differences in permeabilities for the same rock type. The relationship between the S_b and the effect on permeability indicates the complex impact of organic matter in the pore development (Wang et al., 2020), and likewise in the hydrocarbon production. Bitumen, when present as a solid, has an impact on reservoir quality as other cements (carbonates and silica), or authigenic clays, therefore the bitumen present in the rock types, Figures 4.3.7a and b, and the presence of clays, are part of the diagenetic evolution of this complex pore system (Lomando et al., 1992).

From our porosity analysis we confirm that S_b can significantly reduce total effective porosity, furthermore, permeability is also significantly reduced by restricted or closed pore throats (Lomando et al., 1992). Consequently, the distribution and occurrence of bitumen on well field, in addition to the type of hydrocarbon explain the difference on the porosity-permeability relationship in each of the wells analyzed.

4.4 Capillary entry pressure calculations.

4.4.1 Capillary entry pressure and governing equation

Capillary pressure refers to the pressure difference between the oil phase and the water phase across a curved oil-water interface (Schowalter et al., 1979; Fanchi, 2002; Leverett, 1941) or as the pressure that is required to force a fluid (hydrocarbons) through a pore throat and displace the pore wetting fluid (Jennings et al., 1987) (Figure 4.4.1). Capillary entry pressure is related to 3 factors: the radius of the pore throats, the hydrocarbon-water interfacial tension, and wettability (Schowalter, 1979). These properties in turn, control the fluid behavior in the pore system (Jennings et al., 1989).

The capillary pressure (P_C) is given then by the following equation (3) (Purcell, 1949):

$$P_C = \frac{2\sigma \cos \vartheta}{r} \dots (3)$$

Where:

- σ = interfacial tension
- θ = the contact angle
- r = the pore-throat radius

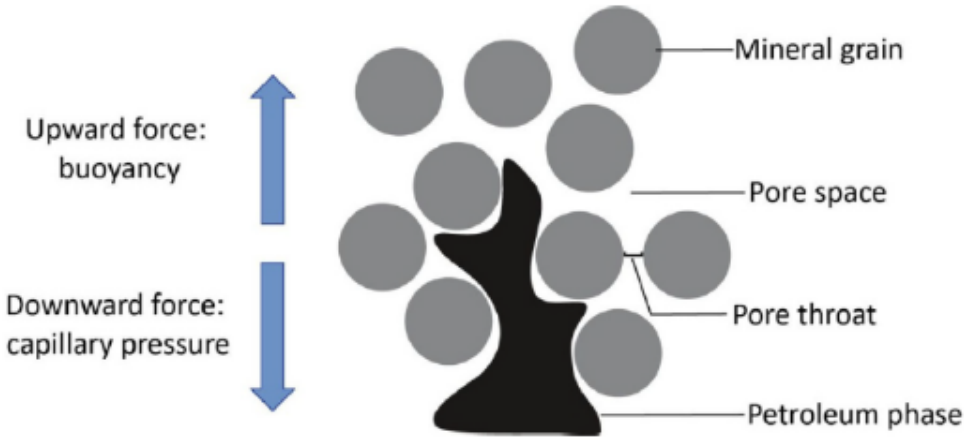

Figure 4.4.1 Schematic representation of the main forces involved during the fluid (hydrocarbons) distribution; for hydrocarbon migration to occur, the buoyancy forces need to exceed the capillary forces (Carruthers, 2003).

We explore whether petrophysical differences between the four rock types identified in this analysis could have influenced the distribution of oil versus gas at Septimus field. In our analysis, capillary entry pressures were calculated from data obtained by MICP analysis, applying estimates of reservoir temperature and reservoir pressure and assuming different reservoir fluid compositions. Displacement pressures were obtained by MICP analysis from samples representing the 4 rock types, applying pressures at 10% Hg saturation. Capillary entry pressures were calculated following the methodology summarized in Schowalter (1979), which requires knowledge or estimates of reservoir temperature, pressure, and fluid composition (summarized in Table 4.4.1 for Septimus field). Fluid properties from the Septimus reservoir and from plots (11) and (12) from (Schowalter et al., 1979), we estimated an interfacial tension of 2.2 dynes/cm (Schowalter, 1979) for an oil of 46 °API (from the oil well producer) and 22 dynes/cm for the gas on the gas well producer (a relative wet gas with a composition of C_1 77%, C_2 13%, C_3 6%, nC_4 1.6%, nC_5 %0.3, C_6 %0.2, and C_7 0.1%).

Table 4.4.1 Main reservoir conditions used to estimate capillary entry pressure for the oil well (100/04-09-084-22W6/00).

Frm. Depth (ft)	Prospect Pres. (psi)	Hg air to Hcb/Water cfe	Temp (F)	Oil °API	Relative density (gas)	Interfacial Tension - GAS (lb/foot)	Interfacial Tension - OIL (lb/foot)	Hydraulic Pres Grad (psi/foot)	Frm water density (lb/in^3)
6690.94	4349.11	0.056 (gas) 0.002 (oil)	212	46	0.733	1.623E-6	1.6226E-7	0.65	0.036
Data from geological report	HP= (Hydraulic Pres Grad x Depth)	From graph (Schowalter, 1979)	(Seifert et al., 2013)	Production report WA26966		Calculated from graph (Schowalter et al; 1979)		cte	Calculated under reservoir conditions using sea water as a base case

MICP data require conversion from a mercury-air system to a hydrocarbon-water system. Following Schowalter (1979), the conversion factor can be calculated from the interfacial tension calculations for the two types of hydrocarbons present in the reservoir from plot (3) (Figure 4.4.2).

$$(P_C)hw = \frac{\gamma hw * cos\theta hw}{\gamma ma * cos\theta ma} x(P_C)ma \ldots (4)$$

Where:

- P_{Chw} = capillary pressure for hydrocarbon-water system
- γ_{hw} = interfacial tension for hydrocarbon-water system (dynes/cm)
- θ_{hw} = contact angle (wettability)
- γ_{ma} = interfacial tension of mercury + surface tension
- θ_{ma} = surface tension between mercury-air and rock

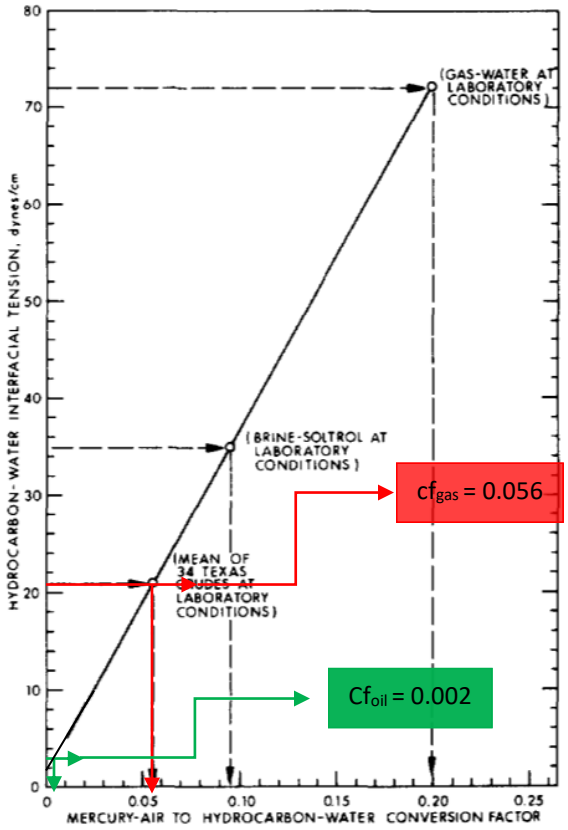

Figure 4.4.2 Nomograph to determine mercury-air to hydrocarbon-water conversion factor (Schowalter, 1979). Conversion factors calculated at reservoir conditions for well 100/04-09-084-22W6/00 (oil producer) and well 100/12-33-080-17W6/02 (gas producer).

From figure 4.4.2 we obtain the conversion factors for oil and gas in water. The capillary entry pressure under subsurface conditions is then calculated by multiplying the Hg-injection measurement (from MICP) by the conversion factor for each hydrocarbon type. Then equation (3) can be calculated as:

$$P_C = Hg_{cfe} * D.P_{RT} \dots (5)$$

Where:

- P_C = Capillary entry pressure
- Hg_{cfe}= Mercury-air to hydrocarbon-water conversion factor
- $D.P_{RT}$ = Displacement pressure for each rock type

- ***Results***

Nineteen samples (10 samples from the gas well and 9 samples from the oil well in our data set) were analyzed through this methodology. Figures 4.4.3 (a to h) represent capillary entry pressure

(psi) versus total pore volume (%) (curves represent Hg-intrusion from ~150 psi to 60 000 psi), assuming two different hydrocarbon fluids, one a 46˚ API oil and one a gas with 77% methane (composition described above). In each case, total pore volume reflects that percentage of pore space occupied by mercury in an MICP experiment, thus pore throat diameters decrease, and capillary entry pressures increase with increasing pore volume. Differences between samples reflects varying pore throat size distributions. In addition, the type of hydrocarbon also controls capillary entry pressure as a result of differences in interfacial surface tension between the hydrocarbon phase and water.

Each of the rock types presents a distinctive capillary entry pressure relationship. We consider capillary entry curves for both oil and gas intrusion into representative samples for each rock type, and we distinguish samples based on whether they were taken from the oil- or gas-producing wells in order to test for systematic differences. Comparisons can be made for gas intrusion, for example, between RT 1 in the oil-producing well and the gas-producing well. The capillary entry pressure curves for RT 1 and RT 2 follow a smooth "s" pattern (Figure 4.4.3 a to d). For RT 2, oil intrusion at 10 % (of total pore volume) occurs at ~5 psi average in the oil well and ~3 psi average in the gas well. Gas intrusion occurs at ~615 psi and ~99 psi in samples from the two wells, respectively. Oil intrusion for samples from RT 1 occurs at higher pressure ~7 psi and ~12 psi (oil and gas well respectively), and gas intrusion occurs at ~2065 psi and ~343 psi. In both cases, once 10% intrusion occurs the capillary entry pressure slightly flattens and then keeps increasing with a smooth slope until the maximum pressure is reached (Figure 4.4.3 a and b). Capillary entry pressures for RT 3 and RT 4 are much higher than for RT 1 and RT 2. Oil intrusion occurs for RT 3 at ~20 psi (at oil well) and ~25 psi (at gas well) and gas intrusion at ~5875 psi and ~700 psi respectively, while RT 4 oil intrusion occurs at ~10 psi and 25 psi (oil and gas well respectively), and gas intrusion at ~288 psi and 710.5 psi. The capillary pressure curves for these two rock types follow different configurations; once the 10% intrusion occurs the capillary entry pressure flattens and stabilizes until reaches the maximum pressure (Figure 4.4.3 e to h).

- Discussion

- *Capillary entry pressure relationship with fluid segregation.*

The distribution and flow of fluids in a reservoir depends on the interaction between the fluids (oil, gas, and water), and the rock structure (Fanchi et al., 2002). Rock samples with different

permeability, porosity, and pore-size distribution will yield different capillary entry pressure curves. From our MICP results, the pore-size distribution curves (Figure 4.4.4 a to h) demonstrate two main configurations, RT 1 and RT 2 show a two parts curve, a bell-shaped part, and a tail part (longer for RT 2), whereas RT 3 and 4 did not show neither the bell-shape nor the tail.

These pore-size distribution curves lead to the different capillary entry pressure estimations for each of the rock types. Because RT 1, and RT 2 have a wider range of pore-size distribution, the capillary entry pressures estimated are lower than for RT 3 and RT 4, in addition, the tail part for RT 1 and RT 2 (from MICP), which represent the smallest pores present (and these within solid bitumen), in the capillary entry estimations results in an increase of it, which explains the "s" pattern observed in samples for RT 1 and RT 2.

Three significant points emerge from this analysis: first, specific rock types are associated with distinctive capillary entry pressures results. Capillary entry pressures are highest for RT 3, also high for RT 4, and substantially lower for RT 1 and RT 2. Second, capillary entry pressures depend also on the fluid type present in the reservoir, where P_C oil < P_C gas, a consequence of the different surface tension of the two fluids in water. Finally, we observed systematic difference between the oil- and gas-producing wells, such that the capillary entry pressures for gas at 50 % of total pore volume intrusion are higher in the oil well than in the gas well for the same rock types (e.g. RT 3A and 3D from Figure 4.4.3e). This behavior was not observed for an oil composition neither at the oil well or the gas well.

- *Effect and relationship of rock types and hydrocarbon distribution in Septimus field.*

To comprehend the relationship between the hydrocarbon distribution in Septimus field and the four rock types identified is important to understand the origin of the hydrocarbons present in the Montney Formation. Previous studies had referred that hydrocarbon migration and charge of the WCSB involved vertical and lateral long-distance oil migration, multiple oil-mixing from different rock sources, oil degradation, and even per-descendum migration (Ducros et al., 2017). An example of this is the Montney Formation were hydrocarbons present migrated somewhere downdip from the Doig Formation.

Ducros (2017) studied the Montney Formation and conclude that hydrocarbon accumulations rather than correspond to a classical definition for accumulations, the Montney behaves more as a basin-center system characterized by an absence of downdip water contact, seal and conventional trap, very low reservoir permeabilities, and the proximity of a source rock (Law, 2002; Ramirez and Aguilera, 2012). Vertical migration in the Montney is difficult due to the overlaying Doig Phosphate layer that acts like a seal. Additionally, studies in the Montney infer that due to the very low permeabilities, hydrocarbons flow was only possible toward the east, mostly gas or condensates, and accumulate in the tight turbiditic reservoirs and which remained trap and experience secondary cracking (oil cracking into gas). From our petrophysical analysis, and the capillary entry pressure estimation in Septimus field, this model for the hydrocarbon distribution can be confirmed.

From the capillary entry pressure estimations analysis, the rock type properties (compositional and petrophysical) in conjunction with the hydrocarbon present, control capillary entry pressures, therefore hydrocarbon distribution. Rock types under the influence of a light oil (46 °API for our study) are expected to have lower capillary entry pressures as oil with lower surface tension area can invade more easily the pore space, in comparison to the capillary entry pressures estimated for a relatively wet gas, with a higher surface tension area.

Petrophysical analysis showed that mineral-assemblage and fabric, cements (mainly carbonates), and clays affect somehow the porosity-permeability relationship for each of the rock types. Additionally, samples analyzed showed that for our rock types, the different pore types present (except for the organic matter pores) are occluded either by these cements, detrital grains, and clays and/or organic matter, the latter present as a solid bitumen and one of the main factors that affects permeability.

In conclusion, our petrophysical analysis for the rock types, the capillary entry pressure estimations, according to fluid composition, in addition to our GOR map (Figure 3.1.1) validates the distribution of hydrocarbons in Septimus field, as less dense fluids are underlying more dense fluids, more important, our results validate our first assumption, were rock type can be used to map petrophysical properties and compared to fluid distribution at a field scale.

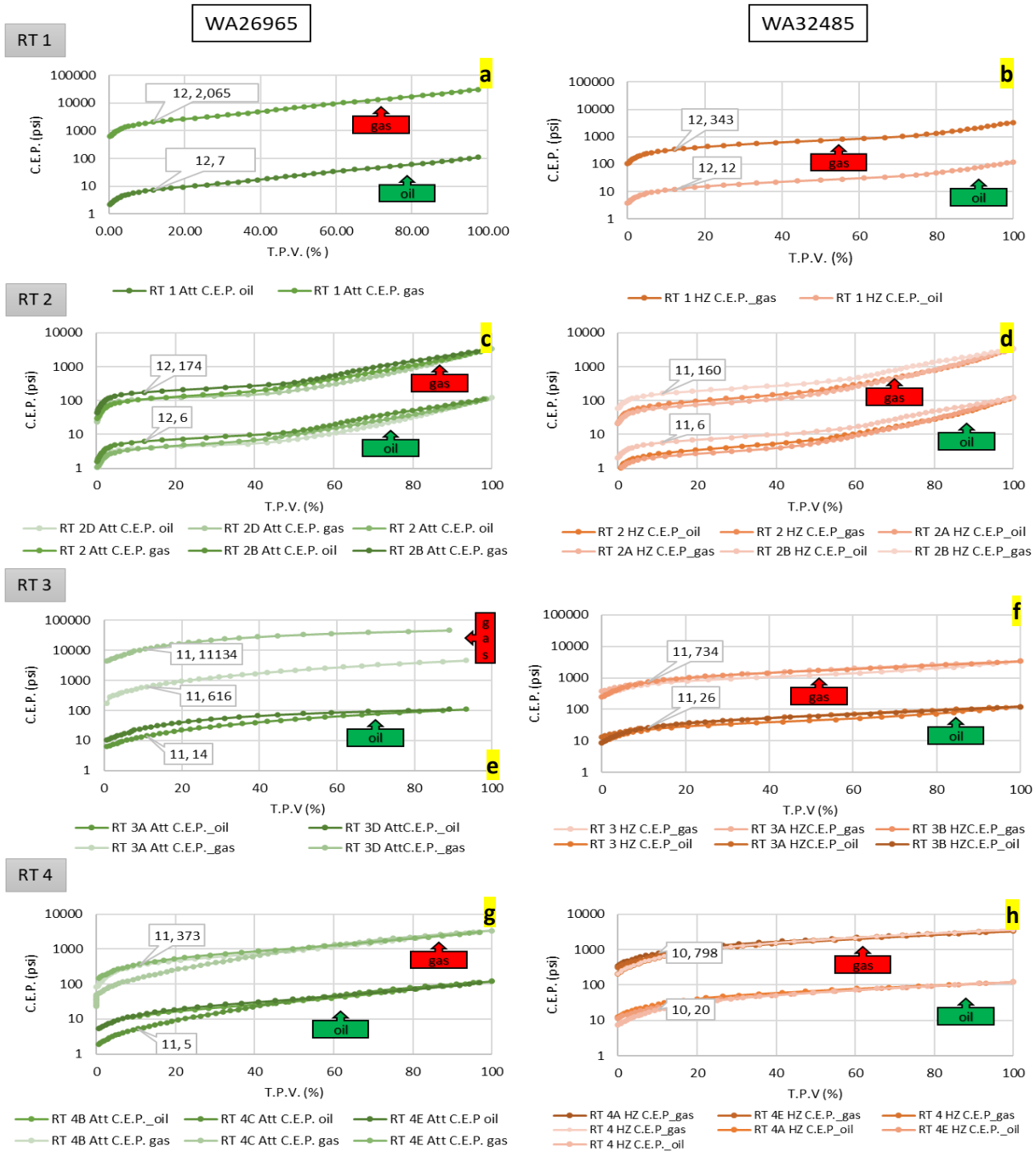

Figure 4.4.3 (a to h) C.E.P. (psi) vs T.P.V (%) plots for RT 1, RT 2, RT 3, and RT 4. Each plot represents a set of samples from the same rock type at different reservoir conditions. In green are represented the rock type samples from the oil well (100/04-09-084-22W6/00) and in orange rock type samples from the gas well (100/12-33-080-17W6/02).

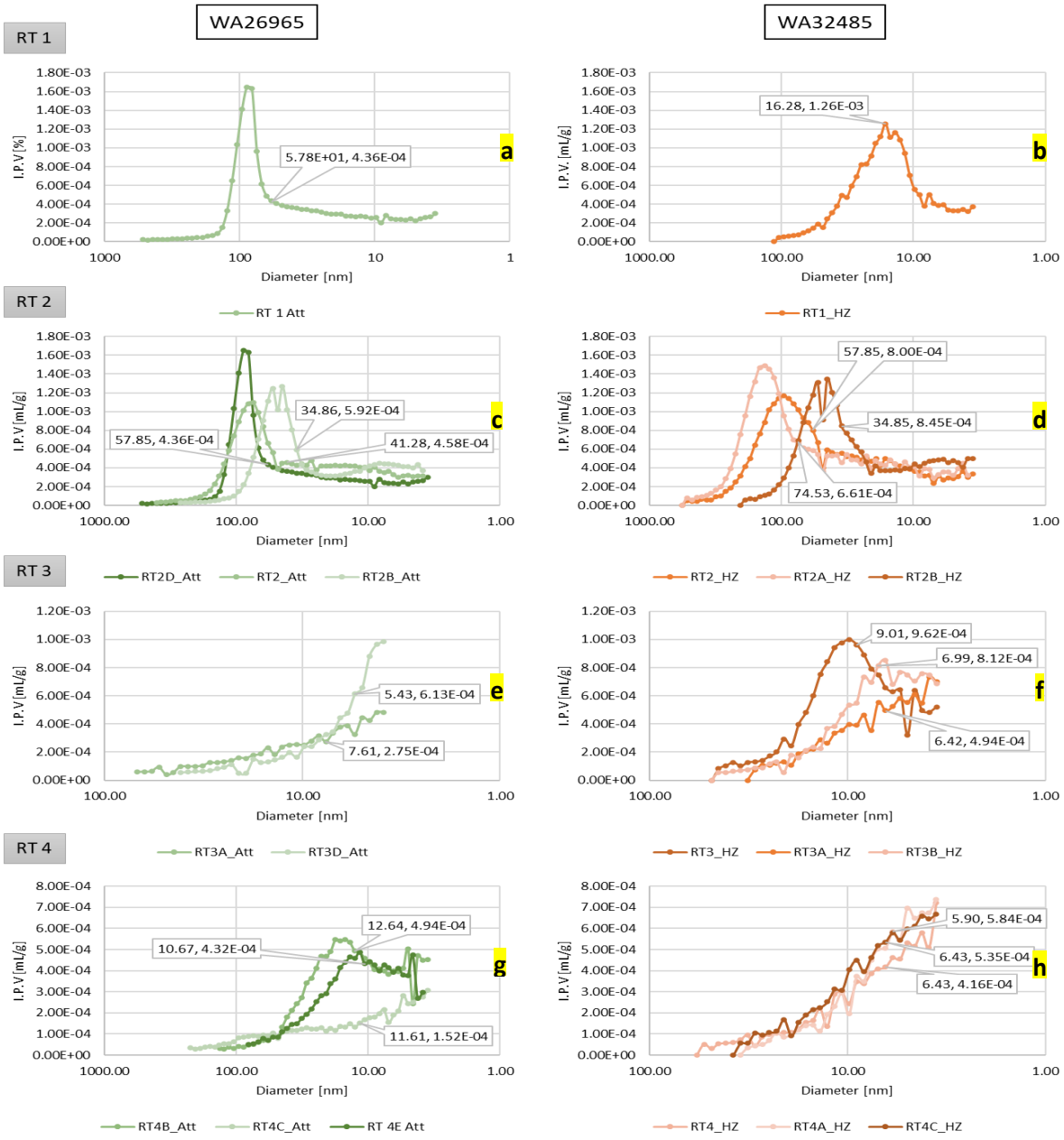

Figure 4.4.4 Cross-plots of pore throat diameter distribution (nm) versus I.P.V (mL/g) representing the different set of samples for each rock type. Cross-plots from the left represent samples from the oil well, the data represent the pore throat diameter and the I.PV. at 50% of mercury imbibition. Cross-plots from the right represent set of samples from the gas well. For RT 2 as e.g. we observed that intrusion varies even in the same rock type, which explains the differences on the capillary entry pressure curves depending on the reservoir conditions analyzed.

4.5 Conclusions

We investigate controls on fluid distributions in an unconventional Montney Formation hydrocarbon reservoir at Septimus field, applying a dataset that includes well logs and an extensive suite of core samples. Core samples were obtained from one well that produces oil and from two wells that produce gas.

To accomplish this analysis, we developed a workflow to define and map flow units in the Montney Formation. Our analysis shows that the Montney reservoir in Septimus field can be effectively classified from well logs as a combination of four rock type. We examined each rock type and demonstrated that:

(1) The differences between these four rock types mainly refers to the mineralogical proportion (%) of K-feldspar + plagioclase, quartz, and clays.

(2) Compositional differences observed in the four rock types are primarily attributed to diagenetic alteration of the original sediment rather than to depositional controls.

(3) Rock types (with distinctive mineralogical compositions) can be mapped with confidence across Septimus field. Pore systems and petrophysical properties can be associated with rock types, which can also be used to map petrophysical properties at a field scale.

(4) Interparticle and intraparticle pores are the most abundant, with subordinate organic-matter pores.

(5) Compositional variables (mineralogy), fabric, mineral assemblage, and TOC influence in the porosity loss of the rock types, moreover, the strong relationship between the median pore diameter and porosity reflected the strong impact of the bitumen saturation on the porosity loss; rock types can be in part distinguished on the basis of bitumen content.

(6) From the capillary entry pressure estimations analysis, the rock type properties (compositional and petrophysical) in conjunction with the hydrocarbon present, control capillary entry pressures. Rock types under the influence of a light oil are expected to have lower capillary entry pressures, whereas the same rock type under the influence of a gas are expected to have higher capillary entry pressures. This phenomena is explained as oil with a lower surface tension will invade first and more

easily the already occluded pore throats. In comparison to gas, with a higher surface tension, will require higher capillary entry pressures to penetrate the remanent pore space available. Comparison between well cores (oil and gas producer) confirmed this analysis as samples from the oil producer display fewer organic matter pores than samples from the gas producer.

References

- Adams, C. (2013): Summary of shale gas activity in Northeast British Columbia 2012; in Oil and Gas Reports 2013, British Columbia Ministry of Natural Gas Development, pages 1–27.

- Akai, T., Wood, J. M., (2018). Application of pore throat size distribution data to petrophysical characterization of Montney tight-gas siltstones. Bulletin of Canadian Petroleum Geology 2018;; 66 (2): 425–435.

- Al Rajaibi, I.M., Hollis, C., and Macquaker, J.H., (2015). Origin and variability of a terminal Proterozoic primary silica precipitate, Athel Silicilyte, South Oman Salt Basin, Sultanate of Oman. Sedimentology, 62(3), 793-825. https://doi.org/10.1111/sed.12173.

- Alvarez, J. O., and D. S. Schechter. (2016). Wettability, Oil and Rock Characterization of the Most Important Unconventional Liquid Reservoirs in the United States and the Impact on Oil Recovery. Paper presented at the SPE/AAPG/SEG Unconventional Resources Technology Conference, San Antonio, Texas, USA, August 2016.

- Anbari, A., Lowry, E., Piri, M., (2019). Estimation of Capillary Pressure in Unconventional Reservoirs Using Thermodynamic Analysis of Pore Images. JGR Solid Earth. Volume124, Issue11. November 2019. Pages 10893-10915.

- Ashoori, S., Abdideh, M., Alavi, A., (2015). 3D Geostatistical Modeling and Uncertainty Analysis of Clay Minerals Distribution in Reservoir Rocks. Geocarto International. 31. 1-25. 10.1080/10106049.2015.1047413.

- Bloch, S., Lander, R.H., and Bonnell, L., (2002). Anomalously high porosity and permeability in deeply buried sandstone reservoirs: Origin and predictability. American Association of Petroleum Geologists Bulletin, 86(2), 301-328.

- British Columbia Ministry of Natural Gas Development. (2013). The Ultimate Potential for Unconventional Petroleum from the Montney Formation of British Columbia and Alberta. November 2013.

- British Columbia Ministry of Natural Gas Development. (2016). Summary of Shale Gas Activity in Northeast British Columbia 2014. Upstream Development Division Tenure and Geoscience Branch. Oil and Gas Report 2016-1. 1-43.

- Brunauer, S., Emmett, P.H., and Teller, E., (1938). Adsorption of Gases in Multimolecular Layers. Journal of the American Chemical Society, 60 (2), 309-319.

- Cao, Z., Liu, G., Zhan, H., Li, C., You, Y., Yang, C., Jiang, H., (2016). Pore structure characterization of Chang-7 tight sandstone using MICP combined with N^2GA techniques and its geological control factors. Sci. Rep. 6, 36919.

- Caracciolo, L., Arribas, J., Ingersoll, R.V., and Critelli, S., (2014). The diagenetic destruction of porosity in plutoniclastic petrofacies: The Miocene Diligencia and Eocene Maniobra

formations, Orocopia Mountains, southern California, USA. Geological Society of London special publication, 386, 49–62. https://doi.org/10.1144/SP386.9.

- Chevrot, V., Hernandez, S., Harris, N. B., (2021): Example of fluid migration and distribution modelling in unconventional reservoirs from the Montney Formation, northeastern British Columbia (NTS 093P, 094A); in Geoscience BC Summary of Activities 2020: Energy and Water, Geoscience BC, Report 2021-02, p. 113–118.

- Clarkson, M.O., Kasemann, S.A., Wood, R.A., Lenton, T.M., Daines, S.J., Richoz, S., Ohnemueller, F., Meixner, A., Poulton, S.W., and Tipper, E.T., (2015). Ocean acidification and the Permo-Triassic mass extinction. Science, 348(6231), 229-232. https://doi.org/10.1126/science.aaa0193.

- Crombez, V., Baudin, F., Rohais, S., Riquier, L., Euzen, T., Pauthier, S., Ducros, M., Caron, B., Vaisblat, N., (2017). Basin scale distribution of organic matter in marine fine-grained sedimentary rocks: Insight from sequence stratigraphy and multi-proxies analysis in the Montney and Doig Formations. Marine and Petroleum Geology. Volume 83. 2017, Pages 382-401.

- Crombez, V., Rohais, S., Baudin, F., and Euzen, T., (2016). Facies, well-log patterns, geometries and sequence stratigraphy of a wave-dominated margin: insight from the Montney Formation (Alberta, British Columbia, Canada). Bulletin of Canadian Petroleum Geology, 64(4), 516-537.

- Cui, X., Nassichuk, B., (2018). Permeability of the Montney Formation in the Western Canada Sedimentary Basin: insights from different laboratory measurements. Bulletin of Canadian Petroleum Geology 2018; 66 (2): 394–424.

- Davies, G.R., Moslow, T.F., and Sherwin, M.D., (1997). The Lower Triassic Montney Formation, west-central Alberta. Bulletin of Canadian Petroleum Geology, 45(4), 474-505.

- Davies, G.R., Watson, N., Moslow, T.F., and Maceachern, J.A., (2018). Regional subdivisions, sequences, correlations and facies relationships of the Lower Triassic Montney Formation, west-central Alberta to northeastern British Columbia, Canada - With emphasis on role of paleostructure. Bulletin of Canadian petroleum geology, 66(1), 23-92.

- Descostes, M., Vitorge, P., Beaucaire, C., (2004). Pyrite dissolution in acidic media, Geochimica et Cosmochimica Acta. Volume 68, Issue 22, 2004, Pages 4559-4569.

- Dixon, J., (2000). Regional lithostratigraphic units in the Triassic Montney formation of Western Canada. Bulletin of Canadian Petroleum Geology, 48(1), 80–83.

- Dong, T., Harris, N. B., McMillan, J. M., Twemlow, C. E., Nassichuk, B. R., Bish, D. L., (2019). A model for porosity evolution in shale reservoirs: an example from the Upper Devonian Duvernay Formation, Western Canada Sedimentary Basin. AAPG Bull. 103, 1017–1044.

- Dong, T., Harris, N. B. (2020). The effect of thermal maturity on porosity development in the Upper Devonian –Lower Mississippian Woodford Shale, Permian Basin, US: Insights into the role of silica nanospheres and microcrystalline quartz on porosity preservation, International Journal of Coal Geology, Volume 217, 2020, 103346, ISSN 0166-5162.

- Edwards, D.E., Barclay, J.E., Gibson, D.W., Kvill, G.E., and Halton, E., (1994). Triassic strata of the Western Canada Sedimentary Basin, in: Mossop, G.D., and Shetsen, I. (Eds.). Geological Atlas of the Western Canada Sedimentary Basin. Canadian Society of Petroleum Geologists and Alberta Research Council, Calgary, pp. 259–275.

- Egbobawaye, E. I. (2016) Whole-Rock Geochemistry and Mineralogy of Triassic Montney Formation, Northeastern British Columbia, Western Canada Sedimentary Basin. International Journal of Geosciences, 7, 91-114.

- Eslinger, E., Burdick, Bernard., (1996). "GEOLOGIC ANALYSIS VIA MAXIMUM LIKELIHOOD (GAMLS): MODEL-BASED NEURAL SYSTEM FOR FLOW UNIT DELINEATION, RESERVOIR COMPARTMENTALIZATION, AND PREDICTION", Stratigraphic Analysis Utilizing Advanced Geophysical, Wireline and Borehole Technology for Petroleum Exploration and Production, Jory A. Pacht, Robert E. Sheriff, Bob F. Perkins.

- Euzen, T., Moslow, T.F., Crombez, V., and Rohais, S., 2018. Regional stratigraphic architecture of the Spathian deposits in western Canada - Implications for the Montney resource play. Bulletin of Canadian Petroleum Geology. 66(1), 175-192.

- Fanchi, J., (2018). Chapter 5 - Rock–Fluid Interaction., Principles of Applied Reservoir Simulation (Fourth Edition). Gulf Professional Publishing, 2018, (pp 81-99).

- Gegolick, A. E., Furlong, C.M., Playter, T. L., Prenoslo, D. T., Gingras, M. K. and Zonneveld, J-P. (2016): Facies analysis and ichnology of the upper Montney Formation in northeastern British Columbia; in Geoscience BC Summary of Activities 2015, Geoscience BC, Report 2016-1, p. 111–116.

- Ghanizadeh, A., Clarkson, C.R., Aquino, S., Ardakani, O.H. Sanei, H. (2015). Petrophysical and geomechanical characteristics of Canadian tight oil and liquid-rich gas reservoirs: I. Pore network and permeability characterization, Fuel. Volume 153. 2015, Pages 664-681/

- Golab, A., Knackstedt, M., Carnerup, A., Sok, R., Young, B., Riepe, L., (2013). Petrophysical Characterization Of Unconventional Reservoir Core At Multiple Scales. PETROPHYSICS. 54. 216-223.

- Győri, O., Haas, J., Hips, K., Lukoczki, G., Budai, T., Demény, A., Szőcs, E., (2020). Dolomitization of shallow-water, mixed siliciclastic-carbonate sequences: The Lower Triassic ramp succession of the Transdanubia Range, Hungary. Sedimentary Geology. Volume 395. 2020, 105549.

- Harris, N.B., Moghadam, A. and Dong, T., 2019. The effects of organic carbon content and thermal maturity on acoustic parameters in a black shale: Woodford Shale, Permian Basin, West Texas. Geophysics 84(6), D231-D248.

- Harris, N. B., Mnich, C. A., Selby, D., Korn, D., (2013), Minor and trace element and Re–Os chemistry of the Upper Devonian Woodford Shale, Permian Basin, west Texas: Insights into metal abundance and basin processes, Chemical Geology. Volume 356. 2013. Pages 76-93.

- Hemmesch, Nikki T., Nicholas B. Harris, Cheryl A. Mnich, and David Selby. "A sequence-stratigraphic framework for the upper Devonian Woodford Shale, Permian Basin, west Texas." AAPG Bulletin 98, no. 1 (2014): 23-47.

- Hofman, J., Slijkermail, W., Looyestijn, W., Volokitin, Y., (1999). "Constructing Capillary Pressure Curves From Nmr Log Data In The Presence Of Hydrocarbons." Paper presented at the SPWLA 40th Annual Logging Symposium, Oslo, Norway, May 1999.

- Iwuoha, S., Pedersen, P., Clarkson, C. (2018). Pore-scale variability and fluid distributions in Montney Formation: New insights from three-dimensional reservoir characterization and modeling.

- Jarvie, D., (2012). Shale Resource Systems for Oil and Gas: Part 1—Shale-gas Resource Systems. AAPG Mem.. 97. 10.1306/13321446M973489.

- Knapp, L. J., McMillan, J. M., Harris, N. B., (2017.), A depositional model for organic-rich Duvernay Formation Porosity Evolution in Shale Reservoirs of the Duvernay Formation mudstones: Sedimentary Geology. Volume. 347. Pages 160–182.

- Krause, F.F., Wiseman, A.C., Williscroft, K.R., Solano, N., Morris, N.J., Meyer, R., and Marr, R., (2012). Petrographic and petrophysical comparison of the Montney Formation in the Sturgeon Lake South area. In Site, Canadian Well Logging Society Magazine, 31, 6-9.

- Lai, J., Wang, G., Ran, Ye., Zhou, Z., Cui, Yufeng., (2016). Impact of diagenesis on the reservoir quality of tight oil sandstones: The case of Upper Triassic Yanchang Formation Chang 7 oil layers in Ordos Basin, China, Journal of Petroleum Science and Engineering. Volume 145. Pages 54-65,

- Lan, Q., Dehghanpour, H., Wood, J., Hamed, S. (215). Wettability of the Montney Tight Gas Formation. SPE Res Eval & Eng. 18 (2015): 417–431.

- Lan, Q., Xu, M., Binazadeh, M., Dehghanpour, H., Wood, J. M., (2015). A comparative investigation of shale wettability: The significance of pore connectivity. Journal of Natural Gas Science and Engineering. Volume 27. Part 2, 2015, Pages 1174-1188.

- LaMothe, J.T., (2008). Sedimentology, Ichnology, Stratigraphy and Depositional History of the Contact Between the Triassic Doig and Montney Formations in West-Central Alberta,

Canada- Presence of an Unconformity Bound Sand Wedge. MSc. Thesis, Department of Earth and Atmospheric Sciences, University of Alberta, Edmonton, Alberta, Canada.

- Liseroudi, M. H., Ardakani, O. H., Sanei, H., Pedersen, P. K., Wood, J. M., (2017). Late sulfate cements in the Lower Triassic Montney tight gas play and its relation to the origin of sulfate and H_2S. Abstracts of the 34th Annual Meeting of the Society of Organic Petrology, Calgary, Alberta, Canada. September 21-27, 2017.

- Lomando, AnthonyJ., (1992). The Influence of Solid Reservoir Bitumen on Reservoir Quality. AAPG Bulletin 1992;; 76 (8): 1137–1152.

- Loucks, R.G., Reed, R.M., Ruppel, S.C., and Hammes, U., (2012). Spectrum of pore types and networks in mudrocks and a descriptive classification for matrix-related mudrock pores. American Association of Petroleum Geologists Bulletin, 96, 1071-1098.

- Love, L., Coleman, M., & Curtis, C. (1983). Diagenetic pyrite formation and sulphur isotope fractionation associated with a Westphalian marine incursion, northern England. Transactions of the Royal Society of Edinburgh: Earth Sciences, 74(3), 165-182. doi:10.1017/S0263593300009822

- Lüning, S., and S. Kolonic. (2003). "Uranium spectral gamma-ray response as a proxy for organic richness in black shales: Applicability and limitations." Journal of petroleum geology 26, no. 2: 153-174.

- Machel, H.G., (2004). Concepts and models of dolomitization: a critical reappraisal. Geological. Society, London, Special Publications, 235(1), 7-63.

- Milliken, K.L., and Olson, T., 2017. Silica diagenesis, porosity evolution, and mechanical behavior in siliceous mudstones, Mowry Shale (Cretaceous), Rocky Mountains, U.S.A.. Journal of Sedimentary Research, 87(4): 366-387. doi: https://doi.org/10.2110/jsr.2017.24.

- Moore, D.M., 2000. Diagenesis of the Purington Shale in the Illinois Basin and implications for the diagenetic state of sedimentary rocks of shallow Paleozoic basins. Journal of Geology, 108(5), 553-567. https://doi.org/10.1086/314423.

- Mohnhoff, D., Littke, R., Krooss, B., Weniger, P. (2016). Flow-through extraction of oil and gas shales under controlled stress using organic solvents: Implications for organic matter-related porosity and permeability changes with thermal maturity, International Journal of Coal Geology, Volume 157, 2016, Pages 84-99.

- Moslow, T.F. (2000). Reservoir architecture of a fine-grained turbidite system: Lower Triassic Montney Formation, Western Canada Sedimentary Basin. In: Deep-water Reservoirs of the World, Conference Proceedings, Gulf Coast SEPM. P. Weimer, R.M. Slatt, J. Coleman, N.C. Rosen, H. Nelson, A.H. Bouma, M.J. Styzen, and D.T. Lawrence (eds.). p. 686–713.

- Nassichuk, B., (2000). Sedimentological, diagenesis and reservoir development of the lower Triassic Montney Formation, Northeastern British Columbia. (pp 1-95). The University of British Columbia. June 200.

- Ness, S.M., (2001). The application of basin analysis to the Triassic succession, Alberta Basin: an investigation of burial and thermal history and evolution of hydrocarbons in Triassic rocks. M.Sc.. Thesis, Department of Geology and Geophysics, University of Calgary, Calgary, Alberta, Canada.

- Nur Asyraf, Mr A., Gaafar, G., Saaid., I., (2015). Quantification of Clay Mineral and Log Response Toward Reservoir Rock Properties. DOI:10.1007/978-981-287-368-2_20

- Panek R., (2000). The Sedimentology and Stratigraphy of the Lower Triassic Montney Formation in the Subsurface of the Peace River Area, Northwestern Alberta. M. Sc. Thesis. Department of Geology and Geophysics, University of Calgary, Calgary, Alberta.

- Playter, T. L. 2013. Petrographic and X-ray Microtomographic Analysis of the Upper Montney Formation, Northeastern British Columbia, Canada. M.Sc. Thesis, University of Alberta, Canada.

- Prenoslo, D., (2017). The Sedimentology, Stratigraphy, and Reservoir Characterization of the Montney D1 and D2 Horizons, Greater Pouce Coupe Area, Alberta and British Columbia. M.Sc. Thesis, University of Alberta, Canada.

- Proverbs, I.P., Bann, K.L., Fratton, C.M., Frostad, C.J., Juska, A., (2018). Facies architecture and sequence stratigraphy of the Lower Triassic Montney Formation, NE British Columbia: Fundamental controls on the distribution of 'sweet spots' in a world-class unconventional reservoir. Bulletin of Canadian Petroleum Geology 2018;; 66 (1): 237–258.

- Pytte, A. M., and R. C. Reynolds (1989), The thermal transformation of smectite to illite, in Thermal Histories of Sedimentary Basins, edited by T. H. McCulloh and N. D. Naeser, pp. 133– 140, Springer, New York.

- Qi, Y., Ju, Y., Cai, J., Gao, Y., Zhu, H., Hunag, C., Wu, J., Meng, Chen, S. W., (2019). The effects of solvent extraction on nanoporosity of marine-continental coal and mudstone,
- Fuel. Volume 235. Pages 72-84.

- Raith, M.M., Raase, P., Reinhardt, J. (2012). Guide to thin section microscopy.

- Riediger, C.L., Fowler, M.G., Brooks, P.W., and Snowdon, L.R., 1990. Triassic oils and potential Mesozoic source rocks, Peace River Arch area, Western Canada Basin. Organic Geochemistry, 16(1-3), 295–305. https://doi.org/10.1016/0146-6380(90)90049-6.

- Revil, M., Cathles, L. (1999). Permeability of Shaly Sands. Water Resources Research. V. 35, No. 3, 651-662.

- Rohais, S., Crombez, V., Euzen, T., and Zonneveld, J.-P., 2018. Subsidence dynamics of the Montney Formation (Early Triassic, western Canada sedimentary basin): Insights for its geodynamic setting and wider implications. Bulletin of Canadian Petroleum Geology, 66(1), 128-160.

- Salimifard, B., Ruth, D. W., Nassichuk, B. (2015). A Study of Mercury Intrusion on Montney Formation Rocks and How It Relates to Permeability. Paper presented at the SPE/CSUR Unconventional Resources Conference, Calgary, Alberta, Canada, October 2015. 1-18.

- Sanei, H., Wood, J, M., Ardakani, O. H., Clarkson, C. R. Jiang, C., (2015). Characterization of organic matter fractions in an unconventional tight gas siltstone reservoir. International Journal of Coal Geology. Volumes 150–151. Pages 296-305.

- Seifert, M., Geol, P., Lenko, M., Eng, P., Lee, J., (2015). "Optimizing Completions within the Montney Resource Play." Paper presented at the SPE/AAPG/SEG Unconventional Resources Technology Conference, San Antonio, Texas, USA, July 2015.

- Sereda, R., John, F. (2017). The Lower Montney Turbidite Complex of Northwest Alberta and Northeast British Columbia: Evolution of an Oil and Gas Play From Conventional to Unconventional" Paper presented at the SPE/AAPG/SEG Unconventional Resources Technology Conference, Austin, Texas, USA, July 2017.

- Schettler, P.D., Parmely, C.R., and Lee, W.J., (1989). Gas Storage and Transport in Devonian Shales, SPE Formation Evaluation, 3(3), 371-376. http://doi.org/10.2118/17070-PA.

- Schowalter, T., (1979). Mechanics of Secondary Hydrocarbon Migration and Entrapment. AAPG Bulletin 1979;; 63 (5): 723–760.

- Scott, R., Meffre, S., Woodhead, J., Gilbert, S., Berry, R., Emsbo, P., (2009). Development of Framboidal Pyrite During Diagenesis, Low-Grade Regional Metamorphism, and Hydrothermal Alteration. Economic Geology. 104. 1143-1168. 10.2113/gsecongeo.104.8.1143.

- Soliman, A., Abdelfattah, M., Ahmed Yassin, M. (2015). Unconventional Reservoir: Definitions, Types and Egypt's Potential. 10.13140/RG.2.1.3846.0880.

- Sohail, G., Hawkes, M., Yasin, Qamar., (2020). An integrated petrophysical and geomechanical characterization of Sembar Shale in the Lower Indus Basin, Pakistan, using well logs and seismic data. Journal of Natural Gas Science and Engineering. Volume 78. 2020, 103327.

- Surdam, R.C., Crossey, L.J., (1987). Integrated diagenetic modeling: a process-oriented approach for clastic systems. Annu. Rev. Earth Planet. Sci. 15 (1), 141–170.

- Tada, R., Siever, R., (2003). Pressure Solution During Diagenesis. Annu. Rev. Earth Planet. Sci. 17. 89-118. 10.1146/annurev.ea.17.050189.000513.

- Tribovillard, N., Algeo, T.J., Lyons, T., and Riboulleau, A., (2006). Trace metals as paleo redox and paleo productivity proxies: An update. Chemical Geology, 232(1-2), 12-32. https://doi.org/10.1016/j.chemgeo.2006.02.012.

- Vaisblat, N., (2020). Control on Reservoir Quality in the Lower Triassic Montney Formation. PhD. Thesis, University of Alberta, 2020.

- Vaisblat, N., Harris, N. B., Ayranci, K., Power, Matthew., DeBhur, C., Bish, D.L., Chalaturnyk, R., Krause, F., Crombez, V., Euzen, T., Rohais, S., Compositional and diagenetic evolution of a siltstone, with implications for reservoir quality; an example from the Lower Triassic Montney Formation in western Canada. Marine and Petroleum Geology. Volume 129. 2021, 105066.

- Velde, B., Vasseur, G., (1992). Estimation of the diagenetic smectite to illite transformation in time-temperature space. American Mineralogist 1992; 77 (9-10): 967–976.

- Vidence., (2020). Automated mineralogy – Methods summary., 2020., pp. 1-13.

- Vishkai, M., and Gates, I.D., 2018. Geomechanical Characterization of Naturally Fractured Formation, Montney, Alberta. 52nd U.S. Rock Mechanics/Geomechanics Symposium, June 17-20, Seattle, Washington.

- Wang, Y., Liu, L., Cheng, H. Pore structure of Triassic Yanchang mudstone, Ordos Basin: Insights into the impact of solvent extraction on porosity in lacustrine mudstone within the oil window. (2020) Journal of Petroleum Science and Engineering, 195, art. no. 107944.

- Wilkin, R.T., Barnes, H.L., Brantley, S.L., (1996). The size distribution of framboidal pyrite in modern sediments: An indicator of redox conditions. Geochimica et Cosmochimica Acta. Volume 60, Issue 20. Pages 3897-3912.

- Wood, J. M., Curtis, M. E., Ardakani, O. H., Sanei, H., (2021). Movement of native fluids during scanning electron microscopy imaging of petroliferous siltstones: Evidence from the Montney Formation, western Canada, Fuel. Volume 290. 2021, 120020.

- Wood, J., Sanei, H., Curtis, M., Clarkson C. (2015). Solid bitumen as a determinant of reservoir quality in an unconventional tight gas siltstone play. International Journal of Coal Geology. Volumes 150–151. 2015. 287-295.

- Wood, M. J., Euzen, T., Sharp, L., Leroux, S. (2021). Phase separation and secondary migration of methane-rich gas accompanying uplift of an unconventional tight-hydrocarbon system, Montney Formation, western Canada, Marine and Petroleum Geology, Volume 124, 2021, 104808.

- Wang, Y., Liu, L., Cheng, H. (2020). Pore structure of Triassic Yanchang mudstone, Ordos Basin: Insights into the impact of solvent extraction on porosity in lacustrine mudstone within the oil window. Journal of Petroleum Science and Engineering. Volume 195,2020,107944.

- Wüst, R.A.J., and Cui, X., (2018). From X-ray Fluorescence (XRF) to Mechanical Profiling for Better Well Completion. Valuable Analytics for the Exploration Toolbox! Recorder 43, 22-28.

- Yang, Y., Aplin, A., (2010). A permeability–porosity relationship for mudstones. Marine and Petroleum Geology. 27. 1692-1697. 10.1016/j.marpetgeo.2009.07.001.

- Yao, S., Jiao, K., Zhang, K., Hu, W., Ding, H., Li, M., Pei, W. (2011). An atomic force microscopy study of coal nanopore structure. Chinese Science Bulletin. 56. 2706-2712.
- Yang, Y., Aplin, A. (2007). Permeability and petrophysical properties of 30 natural mudstones. Journal of Geophysical Research. 112. 10.1029/2005JB004243.

- Yuan, G,. Cao, Y., Schulz, Hans-Martin., Hao, F., Gluyas, J., Liu, K., Yang, T., Wang, Y., Xi, K., Li, Fulai., (2019). A review of feldspar alteration and its geological significance in sedimentary basins: From shallow aquifers to deep hydrocarbon reservoirs. Earth-Science Reviews. Volume 191. Pages 114-140.

- Zonneveld, J.-P., Moslow, T.F., 2018. Paleogeographic setting, lithostratigraphy, and sedimentary framework of the Lower Triassic Montney Formation of western Alberta and northeastern British Columbia. Bulletin of Canadian Petroleum Geology, 66(1), 93-127.

- Zonneveld, J-P., Moslow, T.F, Golding, M. L, Orchard, M. J., Playter, T. L., Wilson, N. (2011). Depositional Framework of the Lower Triassic Montney Formation, West-central Alberta and Northeastern British Columbia.

- Zonneveld, J.-P., Beatty, T.W., MacNaughton, R.B., Pemberton, S.G., Utting, J., and Henderson, C.M., (2010). Sedimentology and ichnology of the Lower Triassic Montney Formation in the Pedigree-Ring/Border-Kahntah River area, northwestern Alberta and northeastern British Columbia. Bulletin of Canadian Petroleum Geology, 58(2), 115–140. https://doi.org/10.2113/gscpgbull.58.2.115.

- Zhang, J., Liu, G., Torsaeter, O., Tao, S., Jiang, M. Li, G. Zhang, S., (2020). Pore-throat structure characteristics and its effect on flow behavior in Gaotaizi tight siltstone reservoir, northern Songliao Basin. Marine and Petroleum Geology. Volume 122, 2020, 104651.

- Zhang, Y., Shao, D., Yan, J., Jia, X., Li, Y., Yu, P., Zhang, T., (2016). The pore size distribution and its relationship with shale gas capacity in organic-rich mudstone of Wufeng-Longmaxi Formations, Sichuan Basin, China. Journal of Natural Gas Geoscience. Volume 1, Issue 3. Pages 213-220.

- Zorski, T., Ossowski, A., Środoń, J., Kawiak, T. (2011). Evaluation of mineral composition and petrophysical parameters by the integration of core analysis data and wireline well log data: the Carpathian Foredeep case study. Clay Minerals 2011; 46 (1): 25–45.

Appendix 1: Whole Rock Characterization

Table 1A. Bureau Veritas standard SO-18 – Whole rock characterization

	Method	WGHT	LF200	LF200	LF200	LF200	LF200	LF200	LF200	LF200	LF200	LF200	LF200	LF200	LF200	LF200	LF200	LF200	LF200	LF200
	Analyte	Wgt	SiO2	Al2O3	Fe2O3	MgO	CaO	Na2O	K2O	TiO2	P2O5	MnO	Cr2O3	Ba	Ni	Sc	LOI	Sum	Be	Co	Cs
	Unit	kg	%	%	%	%	%	%	%	%	%	%	%	ppm	ppm	ppm	%	%	ppm	ppm	ppm
	MDL	0.01	0.01	0.01	0.04	0.01	0.01	0.01	0.01	0.01	0.01	0.01	0.002	1	20	1	-5.1	0.01	1	0.2	0.1
Reference Materials																					
STD GS311-1	Standard																				
STD GS910-4	Standard																				
STD SO-19	Standard		60.50	13.89	7.46	2.91	5.92	4.10	1.30	0.70	0.32	0.13	0.500	454	472	26	1.9	99.79	14	24.0	4.3
STD SO-19	Standard		60.76	13.79	7.38	2.88	5.90	4.09	1.29	0.70	0.32	0.13	0.495	456	466	26	1.9	99.78	14	23.6	4.4
STD SO-19	Standard		60.33	14.03	7.45	2.93	5.93	4.08	1.31	0.70	0.32	0.13	0.510	482	478	27	1.9	99.78	21	23.6	4.0
STD SO-19	Standard		60.17	14.03	7.60	2.94	5.94	4.07	1.31	0.70	0.32	0.13	0.511	477	488	27	1.9	99.77	16	23.8	4.2
STD GS311-1 Expected																					
STD GS910-4 Expected																					
STD SO-19 Expected			61.13	13.95	7.47	2.88	6	4.11	1.29	0.69	0.32	0.13	0.5	486	470	27			20	24	4.5
BLK	Blank																				
BLK	Blank		<0.01	<0.01	<0.04	<0.01	<0.01	<0.01	<0.01	<0.01	<0.01	<0.01	<0.002	1	<20	<1	0.0	<0.01	<1	<0.2	<0.1
BLK	Blank		0.01	<0.01	<0.04	<0.01	<0.01	<0.01	<0.01	<0.01	<0.01	<0.01	<0.002	<1	<20	<1	0.0	0.02	<1	<0.2	<0.1
Prep Wash																					
ROCK-VAN	Prep Blank		71.11	14.13	2.89	0.85	2.28	4.65	1.85	0.34	0.10	0.08	<0.002	768	<20	7	1.6	99.93	1	3.6	0.2
ROCK-VAN	Prep Blank		71.39	14.04	2.83	0.84	2.27	4.67	1.86	0.34	0.09	0.08	<0.002	757	<20	7	1.5	99.93	<1	3.6	0.3

	Method	LF200	LF200	LF200	LF200	LF200	LF200	LF200	LF200	LF200	LF200	LF200	LF200	LF200	LF200	LF200	LF200	LF200	LF200	LF200	LF200
	Analyte	Ga	Hf	Nb	Rb	Sn	Sr	Ta	Th	U	V	W	Zr	Y	La	Ce	Pr	Nd	Sm	Eu	Gd
	Unit	ppm	ppm	ppm	ppm	ppm	ppm	ppm	ppm	ppm	ppm	ppm	ppm	ppm	ppm	ppm	ppm	ppm	ppm	ppm	ppm
	MDL	0.5	0.1	0.1	0.1	1	0.5	0.1	0.2	0.1	8	0.5	0.1	0.1	0.1	0.1	0.02	0.3	0.05	0.02	0.05
Reference Materials																					
STD GS311-1	Standard																				
STD GS910-4	Standard																				
STD SO-19	Standard	15.4	3.0	68.4	19.3	18	308.7	4.6	13.0	20.2	166	9.4	106.1	35.2	73.1	159.2	18.92	74.1	12.97	3.62	10.01
STD SO-19	Standard	15.2	3.2	70.4	20.1	18	320.7	4.8	13.6	20.5	164	9.6	110.7	35.7	72.8	157.9	18.88	73.9	13.00	3.60	10.37
STD SO-19	Standard	15.3	3.1	68.7	19.0	18	316.9	4.6	13.5	19.3	172	9.0	111.7	34.9	71.6	159.0	19.43	73.7	12.98	3.50	10.26
STD SO-19	Standard	16.5	2.9	69.3	18.8	18	314.8	4.4	13.1	19.6	172	9.7	107.7	34.8	71.9	160.3	19.26	75.8	12.99	3.66	10.07
STD GS311-1 Expected																					
STD GS910-4 Expected																					
STD SO-19 Expected		17.5	3.1	68.5	19.5	19	317.1	4.9	13	19.4	165	9.8	112	35.5	71.3	161	19.4	75.7	13.7	3.81	10.53
BLK	Blank																				
BLK	Blank	<0.5	<0.1	<0.1	<0.1	<1	<0.5	<0.1	<0.2	<0.1	<8	<0.5	0.1	<0.1	<0.1	<0.1	<0.02	<0.3	<0.05	<0.02	<0.05
BLK	Blank	<0.5	<0.1	<0.1	<0.1	<1	<0.5	<0.1	<0.2	<0.1	<8	<0.5	0.5	<0.1	<0.1	<0.1	<0.02	<0.3	<0.05	<0.02	<0.05
Prep Wash																					
ROCK-VAN	Prep Blank	11.8	3.5	5.5	32.0	<1	208.6	0.4	3.2	1.3	31	0.5	131.5	17.2	15.4	27.8	3.12	12.0	2.56	0.73	2.67
ROCK-VAN	Prep Blank	11.7	3.3	5.5	31.4	<1	203.6	0.4	3.2	1.5	34	2.9	129.7	17.4	15.3	27.4	3.10	12.5	2.42	0.69	2.70

Table 1B. Bureau Veritas standard SO-18 – Whole rock characterization

		Method	LF200	LF200	LF200	LF200	LF200	LF200	LF200	TC000	TC000
		Analyte	Tb	Dy	Ho	Er	Tm	Yb	Lu	TOT/C	TOT/S
		Unit	ppm	ppm	ppm	ppm	ppm	ppm	ppm	%	%
		MDL	0.01	0.05	0.02	0.03	0.01	0.05	0.01	0.02	0.02
Reference Materials											
STD GS311-1	Standard									1.06	2.40
STD GS910-4	Standard									2.76	8.32
STD SO-19	Standard	1.32	7.20	1.32	3.69	0.52	3.37	0.50			
STD SO-19	Standard	1.34	7.43	1.36	3.66	0.54	3.34	0.51			
STD SO-19	Standard	1.38	7.04	1.34	3.76	0.55	3.35	0.51			
STD SO-19	Standard	1.35	7.02	1.32	3.85	0.54	3.24	0.51			
STD GS311-1 Expected										1.02	2.35
STD GS910-4 Expected										2.65	8.27
STD SO-19 Expected		1.41	7.5	1.39	3.78	0.55	3.55	0.53			
BLK	Blank									<0.02	<0.02
BLK	Blank	<0.01	<0.05	<0.02	<0.03	<0.01	<0.05	<0.01			
BLK	Blank	<0.01	<0.05	<0.02	<0.03	<0.01	<0.05	<0.01			
Prep Wash											
ROCK-VAN	Prep Blank	0.46	2.84	0.61	1.94	0.31	2.20	0.34	0.09	<0.02	
ROCK-VAN	Prep Blank	0.42	2.71	0.61	2.07	0.30	2.11	0.35	0.09	<0.02	

Appendix 2: Core cleaning

Evidence of plugs from the oil well producer prior and after oil extraction through a solution made of 30% acetone, 23% methanol, and 47% chloroform

Time: 0

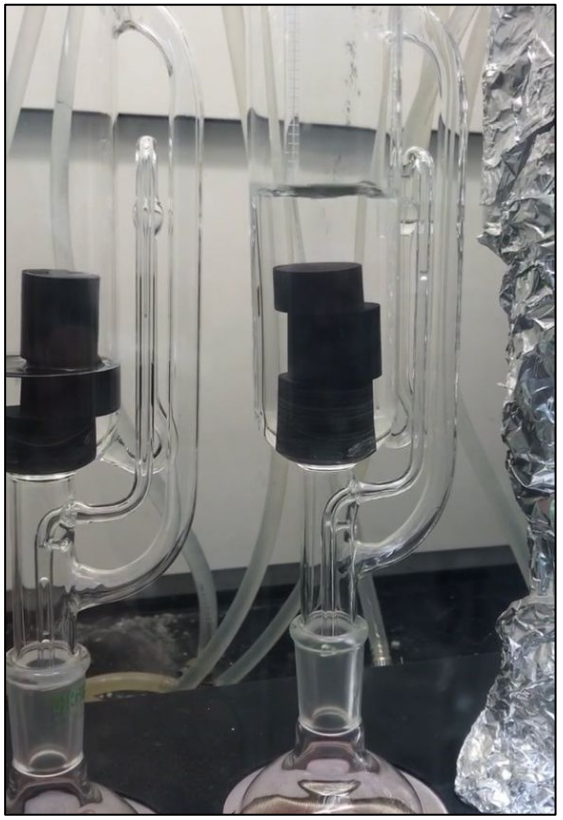

Time: after 12 hrs

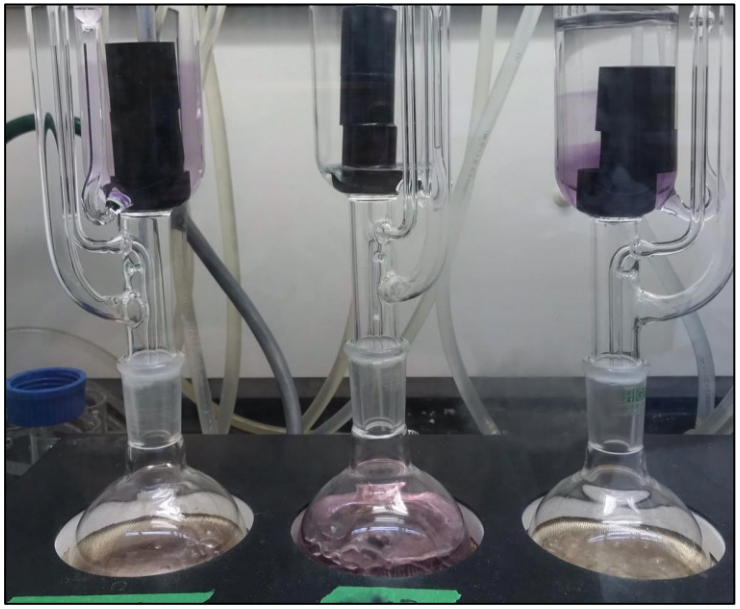

Time: after 8 hrs

Appendix 3: Core log description

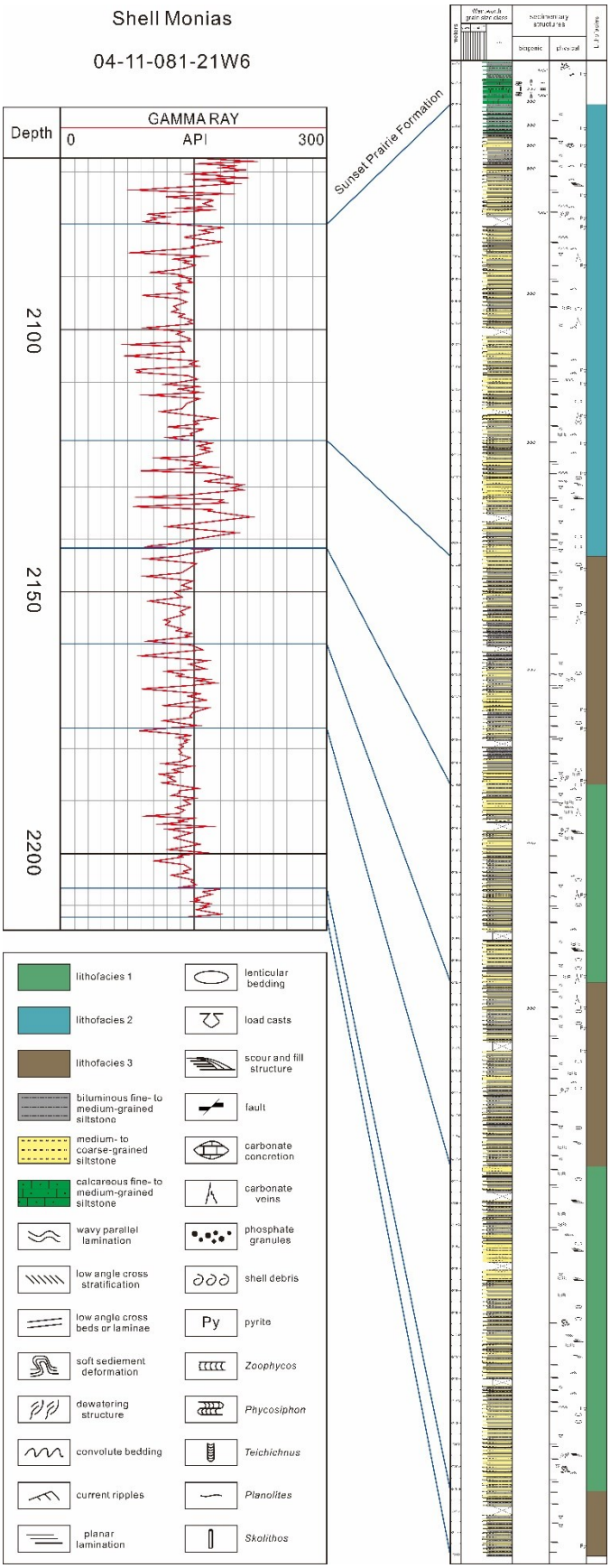
Shell Monias
04-11-081-21W6
Depth
GAMMA RAY
0
API
300
2100
2150
2200
Sunset Prairie Formation
lithofacies 1
lithofacies 2
lithofacies 3
bituminous fine- to medium-grained siltstone
medium- to coarse-grained siltstone
calcareous fine- to medium-grained siltstone
wavy parallel lamination
low angle cross stratification
low angle cross beds or laminae
soft sediement deformation
dewatering structure
convolute bedding
current ripples
planar lamination
lenticular bedding
load casts
scour and fill structure
fault
carbonate concretion
carbonate veins
phosphate granules
shell debris
Py
pyrite
Zoophycos
Phycosiphon
Teichichnus
Planolites
Skolithos

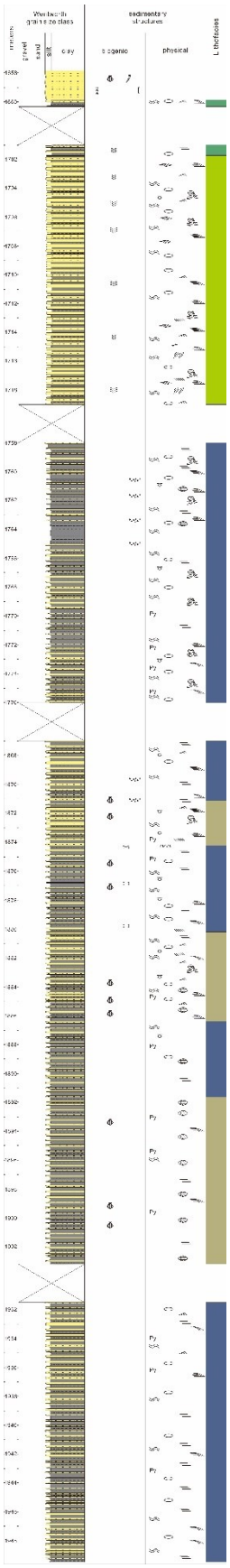

4-9-84-22W6

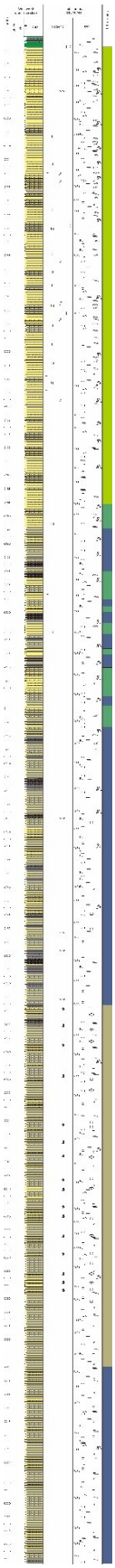

16-6-81-17W6

Legend

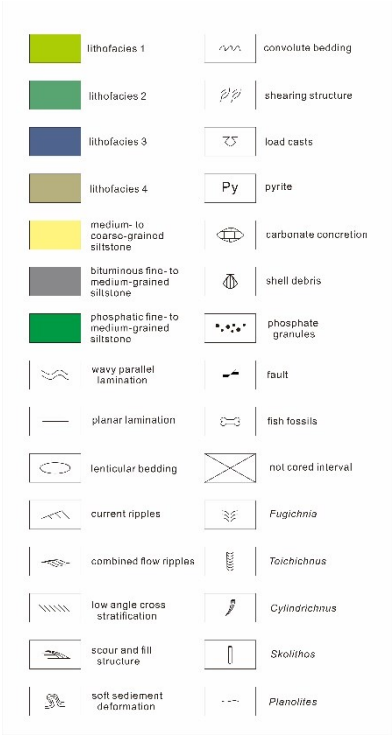

Appendix 4: Student-T results

Student-T calculations

Formulas used to calculate “t”

Two samples

$$t = \frac{(\sum D)/N}{\sqrt{\frac{\sum D^2 - \left(\frac{(\sum D)^2}{N}\right)}{(N-1)(N)}}}$$

One sample

$$t = \frac{\bar{x} - \mu}{\frac{s}{\sqrt{n}}}$$

RT 1 - RT 2					
CA-Dol	D	D^2	N	t=	p-value
	7.75	93.78	26	1.919299997	**0.07**
KFS-PLG	142.67	6095.953	26	0.794595171	**0.43**

Media Qtz	34.10
Pooled media Qtz	32
standar dev	7.125720174
num obs	26
n-1	25
t=	1.499834801
p-value=	**0.15**

RT 1 - RT 3					
Ca- Dol	D	D^2	N	t	p-value
	186.5	6829.075	28	2.450180773	**0.02**
Kfs - Plgs	14.528	194.232	28	1.044103296	**0.31**

Media Qtz	31.85
Pooled media Qtz	30
standar dev	6.709728083
num obs	28
n-1	27
t=	1.456365008
p-value=	**0.16**

Media Ill+Ill-smec	12.31
Media Ill+Ill-smec agrupada	13.05
standar dev	5.307627117
num obs	28
n-1	27
t=	-0.740487877
p-value=	**0.47**

Media Fe-Ill+Ill-smect	0.46
Pooled media Qtz	0.54
standar dev	0.338673985
num obs	28
n-1	27
t=	-1.302793578
p-value=	**0.20**

RT 1 - RT 4					
Ca- Dol	D	D^2	N	t	p-value
	8.02	17086.44	21	0.059881525	**0.95**
Kfs - Plgs	14.528	194.232	21	1.044692092	**0.39**

Media Qtz	30.04
Media Qtz agrupada	27.18
standar dev	9.404107386
num obs	21
n-1	20
t=	1.392030971
p-value=	**0.18**

Media Ill+Ill-smec	11.98
Media Ill+Ill-smec agrupada	11.48
standar dev	6.234143154
num obs	21
n-1	20
t=	0.363988365
p-value=	**0.72**

Media Fe-Ill+Ill-smect	0.56
Pooled Media Fe-Ill+Ill-smect	0.76
standar dev	0.672185554
num obs	21
n-1	20
t=	-1.334232611
p-value=	**0.20**

Student-T calculations

RT 2 - RT 3					
Ca- Dol	**D**	**D^2**	**N**	**t**	**p-value**
	-127.61	1336.44	30	-4.453630192	**0.0001**
Kfs - Plgs	18.68	173.43	30	1.443869298	**0.16**

Media Qtz	34.52
Pooled Media Qtz agrupada	33.28
standar dev	4.54758122
num obs	30
n-1	29
t=	1.491600209
p-value=	**0.15**

Media Ill+Ill-smec	10.70
Pooled Media Ill+Ill-smec	11.8
standar dev	4.667818073
num obs	30
n-1	29
t=	-1.295812624
p-value=	**0.20**

Media Fe-Ill+Ill-smect	0.49
Pooled Media Fe-Ill+Ill-smect	0.53
standar dev	0.275439649
num obs	30
n-1	29
t=	-0.844843365
p-value=	**0.40**

RT 3 - RT 4					
Ca- Dol	**D**	**D^2**	**N**	**t**	**p-value**
	134.27	1837.86	21	4.187091483	**0.0005**
Kfs - Plgs	14.528	194.232	21	1.044692092	**0.0010**

Media Qtz	31.78
Pooled Media Qtz	30.59
standard dev	5.377882829
num obs	21
n-1	20
t=	1.010259922
p-value=	**0.32**

Media Ill+Ill-smec	13.91
Pooled Media Ill+Ill-smec	14.89
standar dev	4.156924458
num obs	21
n-1	20
t=	-1.078602399
p-value=	**0.29**

Media Fe-Ill+Ill-smect	0.58
Pooled Media Fe-Ill+Ill-smect	0.77
standar dev	0.514670448
num obs	21
n-1	20
t=	-1.669592838
p-value=	**0.11**

RT 2 - RT 4					
Ca- Dol	**D**	**D^2**	**N**	**t**	**p-value**
	60.7	12930.24	23	0.525339315	**0.55**
Kfs - Plgs	14.528	194.232	23	1.044485517	**0.55**

Media Qtz	35.49
Media Qtz agrupada	31.7
standar dev	8.466036843
num obs	23
n-1	22
t=	2.149196863
p-value=	**0.04**

Media Ill+Ill-smec	9.63
Pooled Media Ill+Ill-smec	9.98
standar dev	4.91151746
num obs	23
n-1	22
t=	-0.343045013
p-value=	**0.73**

Media Fe-Ill+Ill-smect	0.49
Pooled Media Fe-Ill+Ill-smect	0.73
standar dev	0.616098772
num obs	23
n-1	22
t=	-1.866922363
p-value=	**0.07**

Appendix 5: Porosity-permeability related to mineralogy

Porosity-permeability relationship associated to mineralogical composition (QEMSCAN)

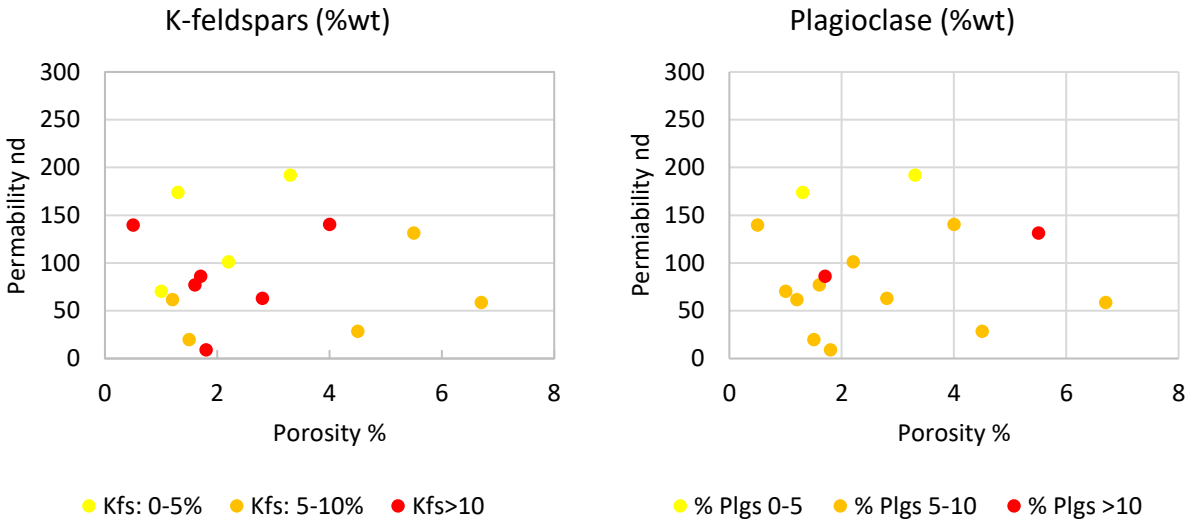

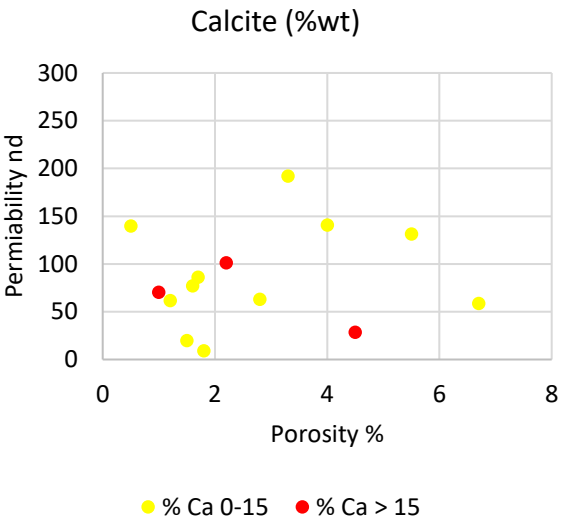

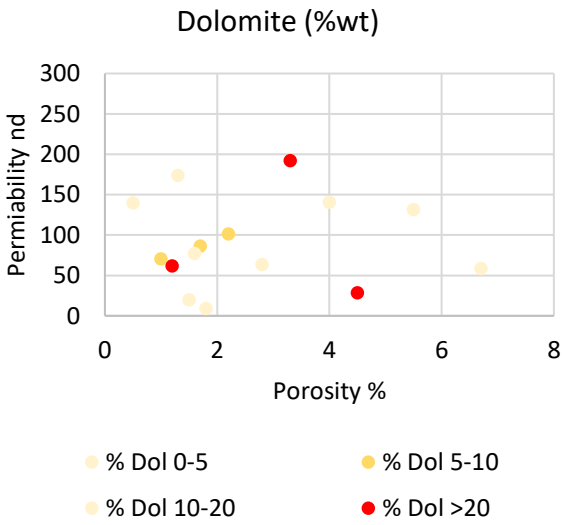

Appendix 6: Cores analyses results

Petrography and analyses

RT 1D – WA25261
Depth: 2074.57 (m)

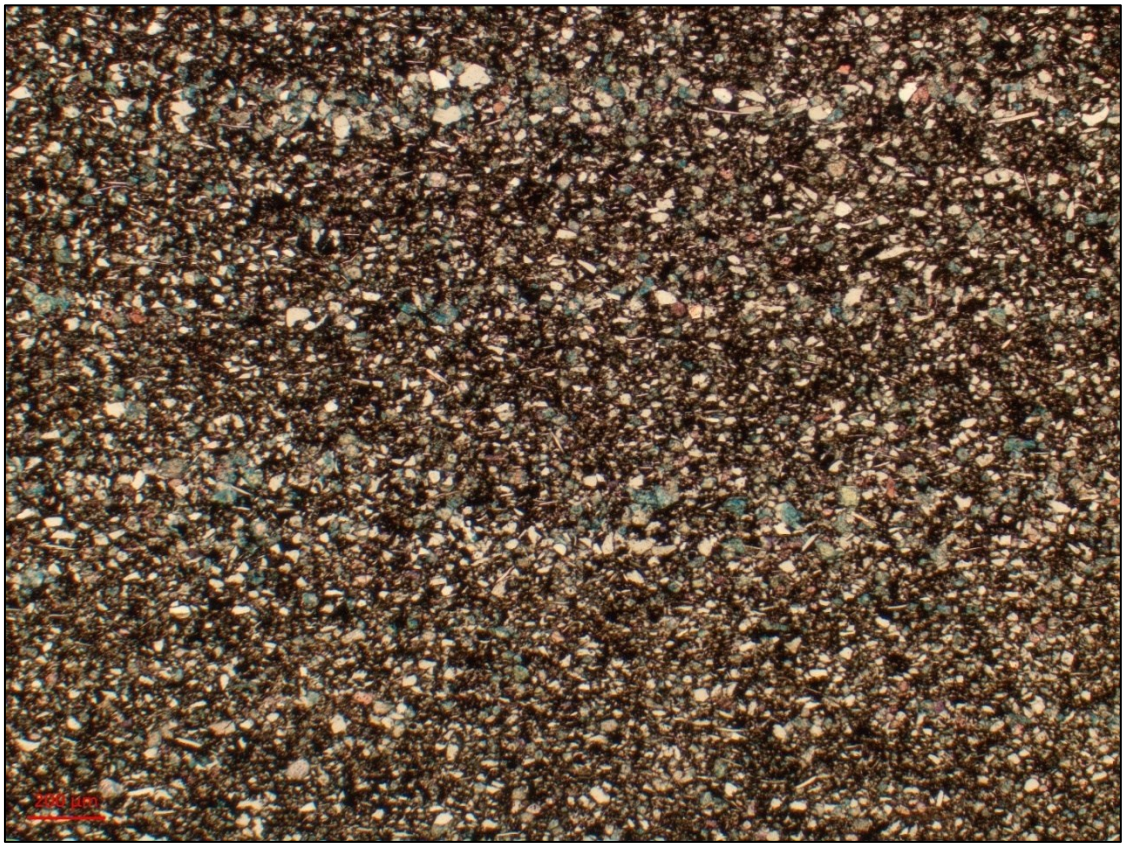

Thin section description:

Faintly laminated, slightly argillaceous dolomitic, calcareous siltstone. Slight vertical variations in calcite and dolomite cement, and clays. Grains are sub-angular to sub-rounded, well sorted and with a matrix mainly of a mixture of detrital clays and bitumen.

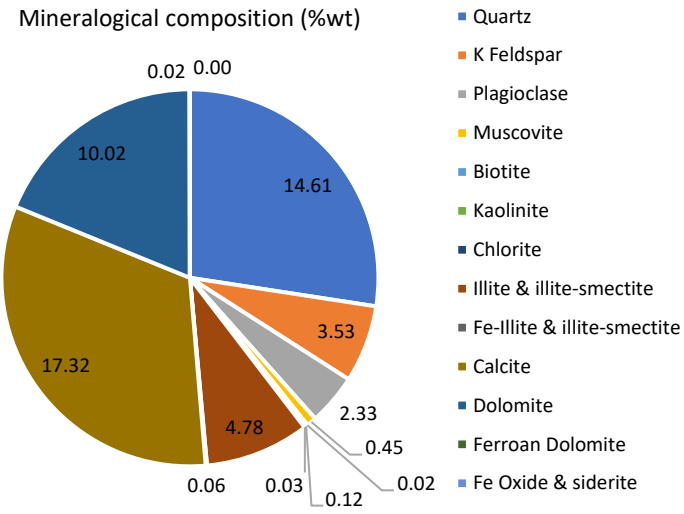

Additional images – RT 1D

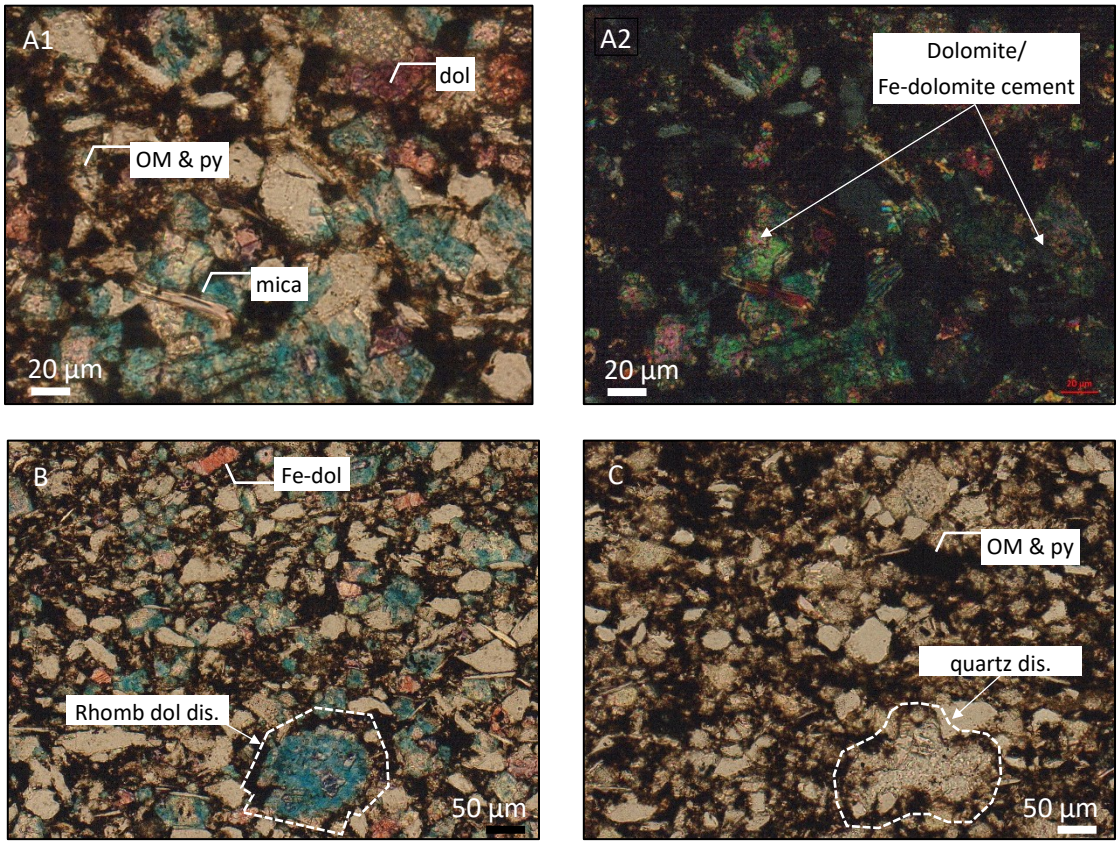

Mineralogical composition – data is in (%wt) – QEMSCAN analysis

Block Code	Pyrite	Sphalerite	Barite	Anhydrite	Halite	Rutile & Ti Silicates	Tourmaline	Chromite	Apatite	Zircon	Monazite	K2O
A	1.90	0.00	0.07	0.07	0.00	0.18	0.01	0.00	44.47	0.03	0.00	1.0

Macroporosity Estimate (Area %)	Grain Density (g/cm³)	Bulk Density (g/cm³)
1.0	2.904	2.885

RT 1 – WA25261
Depth: 2088.12 (m)

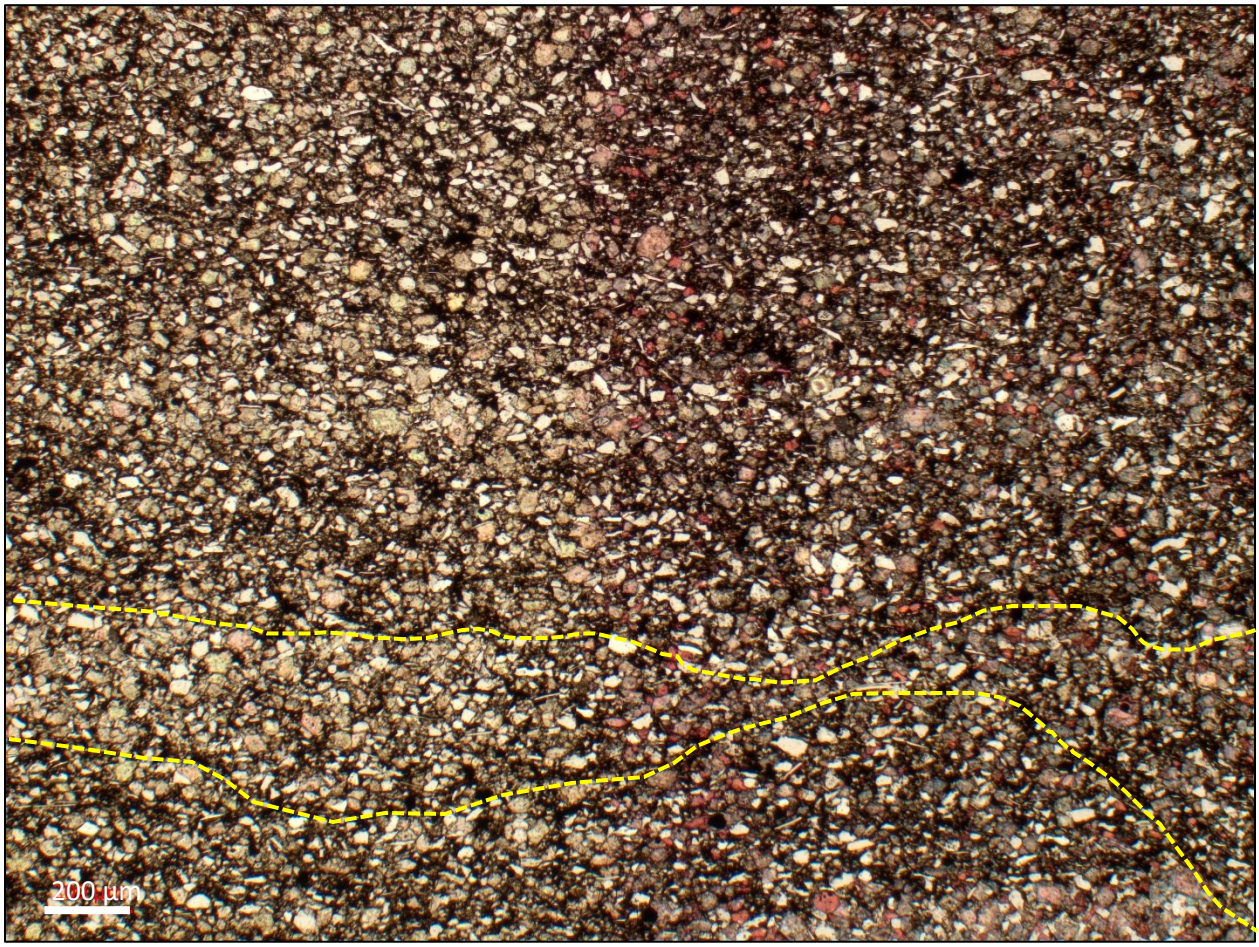

Thin section description:

Faintly laminated, moderately bioturbated, slightly argillaceous dolomitic, calcareous siltstone. Slight vertical variations are defined by variations in grain size, in calcite and dolomite cement, and clays. Grains are sub-angular to sub-rounded, well sorted and with a matrix mainly of a mixture of detrital clays and bitumen. Detrital framework grains include quartz and dolomite with a minor amount of micas.

%TOC: 1.23 (%wt)

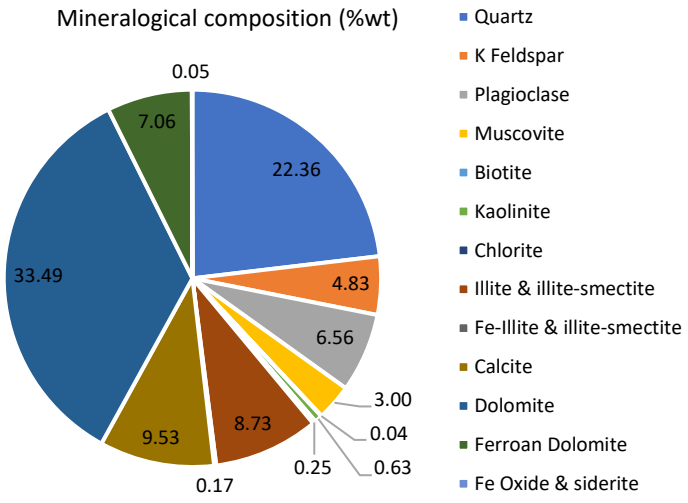

Additional images – RT 1

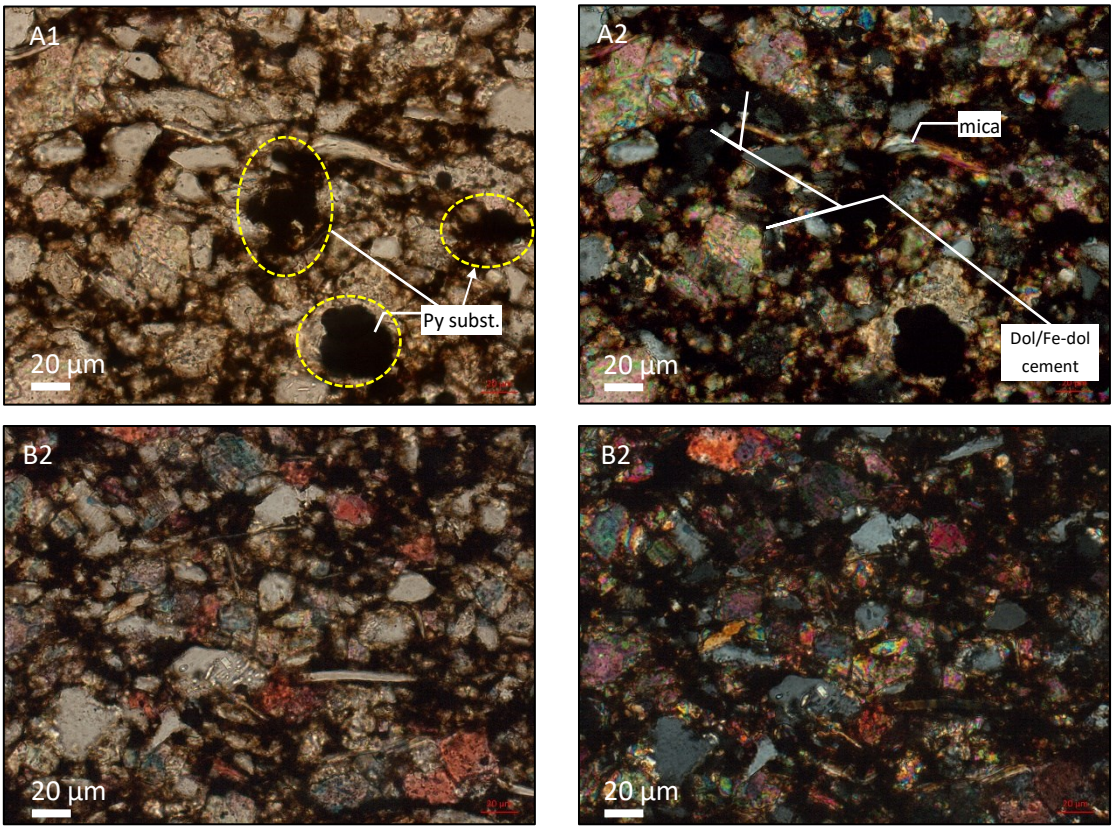

Mineralogical composition – data is in (%wt) – QEMSCAN analysis

Block Code	Pyrite	Sphalerite	Barite	Anhydrite	Halite	Rutile & Ti Silicates	Tourmaline	Chromite	Apatite	Zircon	Monazite	Macroporosity Estimate (Area %)	Grain Density (g/cm³)	Bulk Density (g/cm³)
A	2.49	0.00	0.07	0.07	0.00	0.33	0.03	0.00	0.29	0.02	0.01	3.0	2.770	21.765
B	2.34	0.00	0.05	0.08	0.00	0.30	0.02	0.00	0.32	0.04	0.00	3.3	2.766	23.559
C	2.49	0.00	0.05	0.09	0.00	0.38	0.03	0.00	0.39	0.03	0.00	3.5	2.753	20.769

ICP/ICP-MS

Wgt	SiO2	Al2O3	Fe2O3	MgO	CaO	Na2O	K2O	TiO2	P2O5	MnO	Cr2O3	Ba	Ni	Sc	LOI	Sum
0.08	39.17	6.56	3.78	6.91	17.49	0.95	2.34	0.45	0.17	0.08	0.005	376	23	7	21.9	99.79

- data is in [%wt]

Be	Co	Cs	Ga	Hf	Nb	Rb	Sn	Sr	Ta	Th	U	V	W	Zr	Y	La	Ce	Pr	Nd	Sm	Eu	Gd	Tb	Dy	Ho	Er	Tm	Yb	Lu	TOT/C	TOT/S
2	10	1.9	5.7	5.2	7.9	52.6	1	146	0.5	5.6	6	117	1.2	207.8	22.8	22.5	39	5	18.9	3.77	0.77	3.71	0.58	3.41	0.71	2.62	0.33	2.29	0.35	7.48	1.22

Data is in [ppm]

MICP

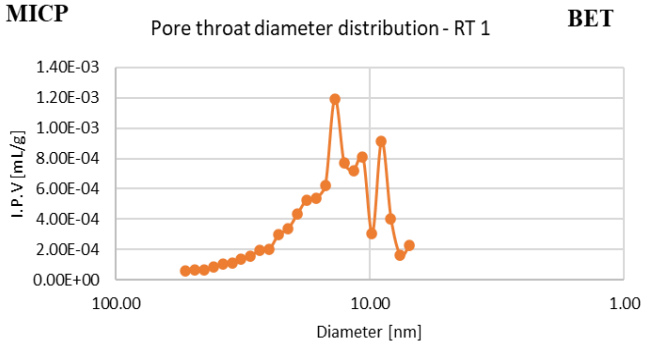

BET

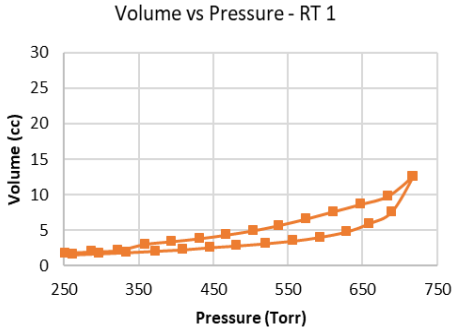

RT 1A – WA25261
Depth: 2093.22 (m)

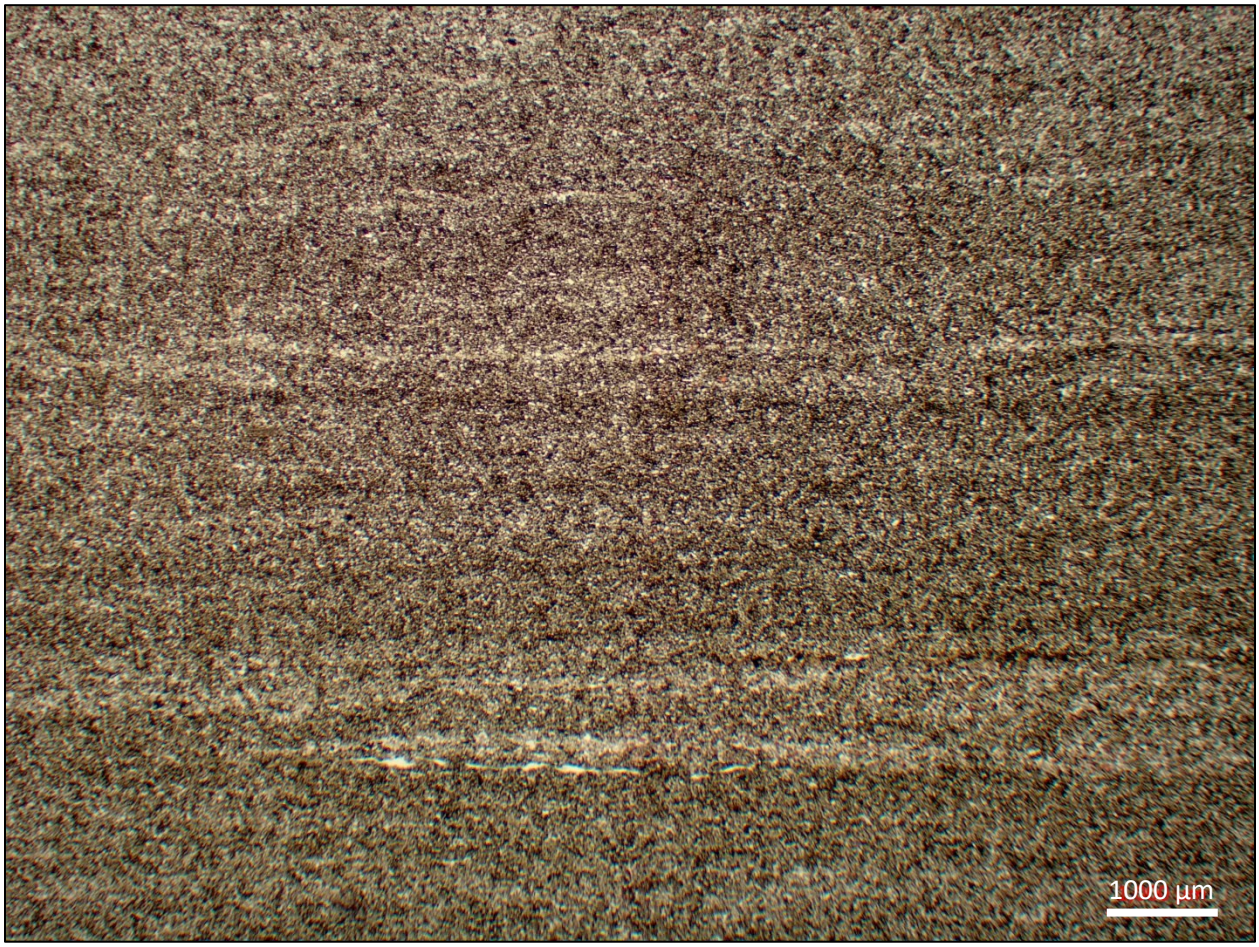

Thin section description:

Laminated to faintly laminated, slightly argillaceous calcareous siltstone. Vertical variations are defined by variations in grain size, in calcite, dolomite and quartz cement, and clays. Grains are sub-angular to sub-rounded, moderately sorted and with a matrix mainly of a mixture of detrital clays and extensive organic matter. Detrital framework grains include quartz and dolomite with a minor amount of micas. Pyrite and phosphate are consistent for this sample.

%TOC: 1.82 (%wt)

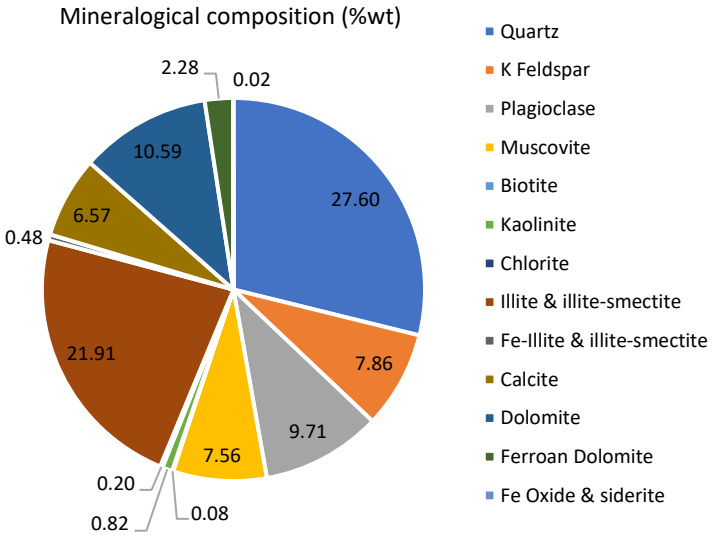

Additional images – RT 1A

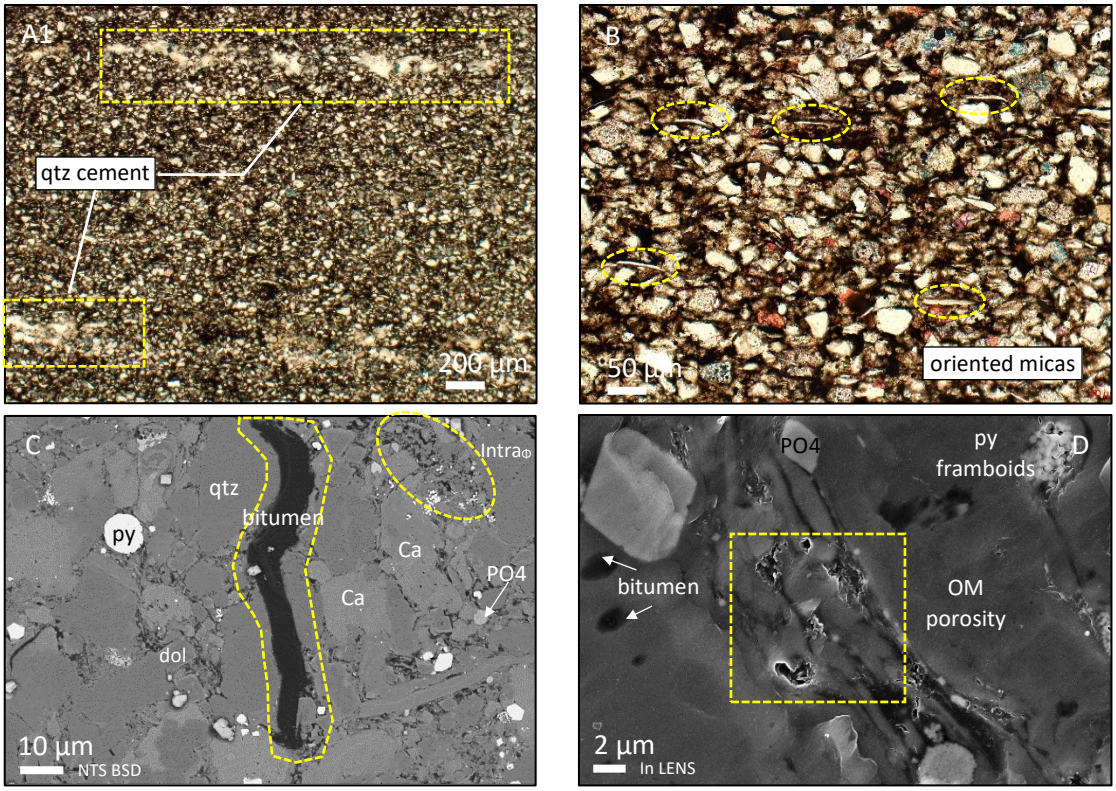

Mineralogical composition – data is in (%wt) – QEMSCAN analysis

Block Code	Pyrite	Sphalerite	Barite	Anhydrite	Halite	Rutile & Ti Silicates	Tourmaline	Chromite	Apatite	Zircon	Monazite	K2O	Macroporosity Estimate (%)	Grain Density (g/cm³)	Bulk Density (g/cm³)
A	2.40	0.00	0.07	0.12	0.00	0.48	0.04	0.00	0.54	0.02	0.01	3.64	3.7	2.713	29.710
B	2.14	0.00	0.06	0.10	0.00	0.50	0.03	0.00	0.53	0.05	0.01	3.47	4.6	2.714	30.803
C	2.97	0.00	0.08	0.18	0.00	0.52	0.03	0.00	0.52	0.03	0.00	3.98	3.1	2.718	26.878

ICP/ICP-MS

Wgt	SiO2	Al2O3	Fe2O3	MgO	CaO	Na2O	K2O	TiO2	P2O5	MnO	Cr2O3	Ba	Ni	Sc	LOI	Sum
0.14	56.44	10.01	2.98	2.73	9.14	1.41	3.6	0.67	0.48	0.03	0.009	546	35	9	12.3	99.82

- data is in [%wt]

Be	Co	Cs	Ga	Hf	Nb	Rb	Sn	Sr	Ta	Th	U	V	W	Zr	Y	La	Ce	Pr	Nd	Sm	Eu	Gd	Tb	Dy	Ho	Er	Tm	Yb	Lu	TOT/C	TOT/S
3	10.5	3.5	11.1	7.7	10.3	78.7	2	142.8	0.9	8.3	5.8	167	1.3	282.2	36.4	36.1	65.5	8.63	33.3	6.84	1.54	6.87	1.02	6.06	1.18	3.6	0.47	3.09	0.45	4.47	1.36

Data is in [ppm]

MICP

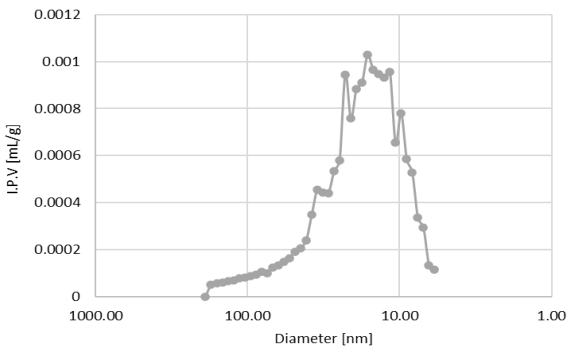

BET

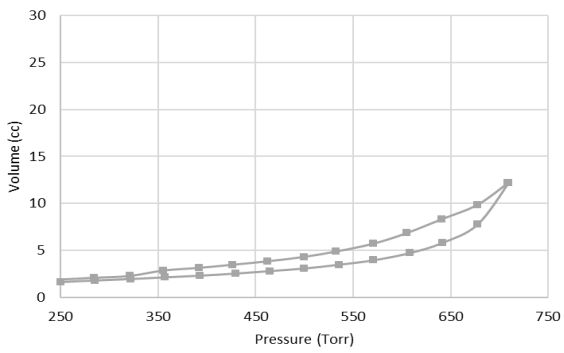

EDS image – mineralogical composition for RT 1A

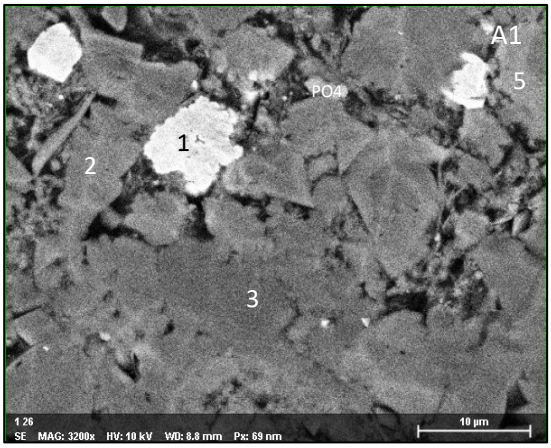

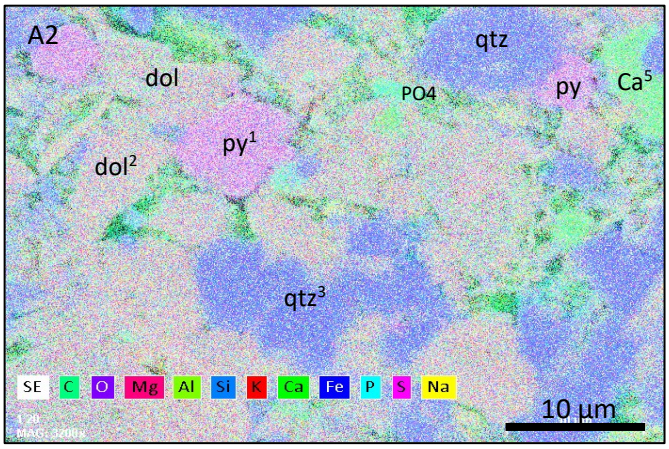

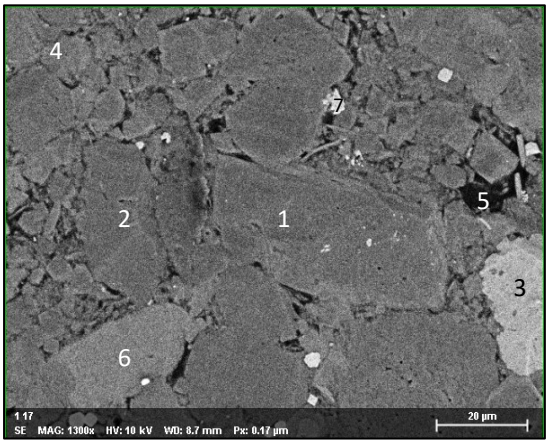

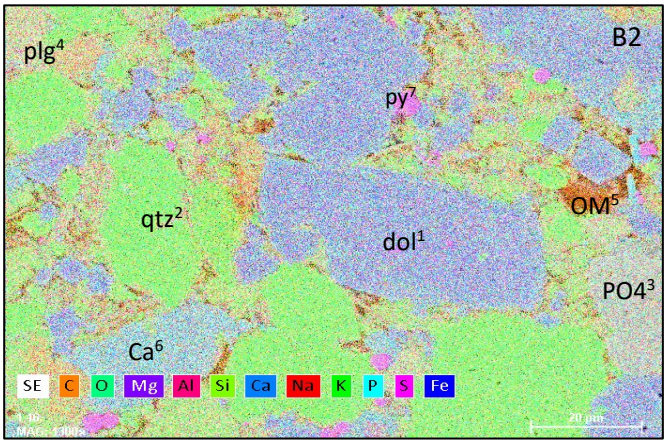

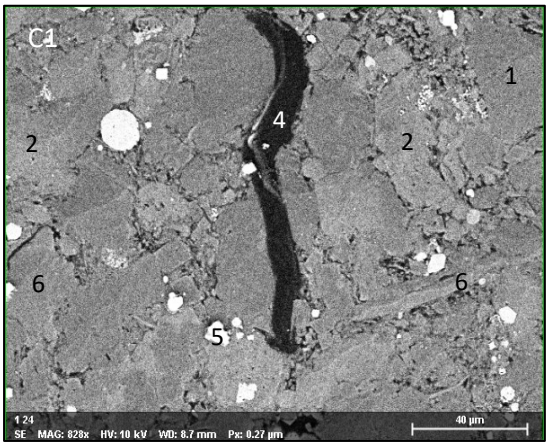

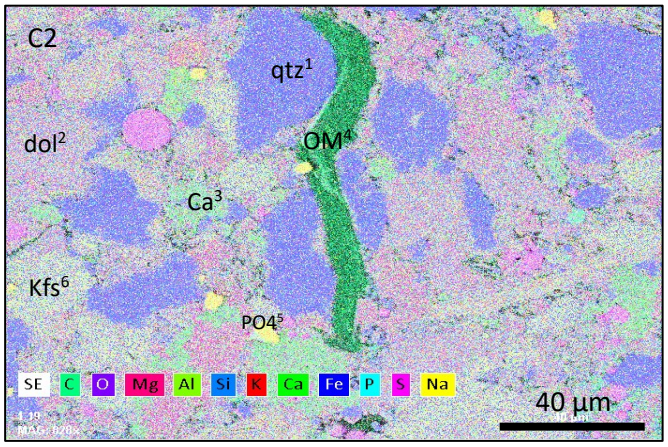

RT 1C – WA25261
Depth: 2096.62 (m)

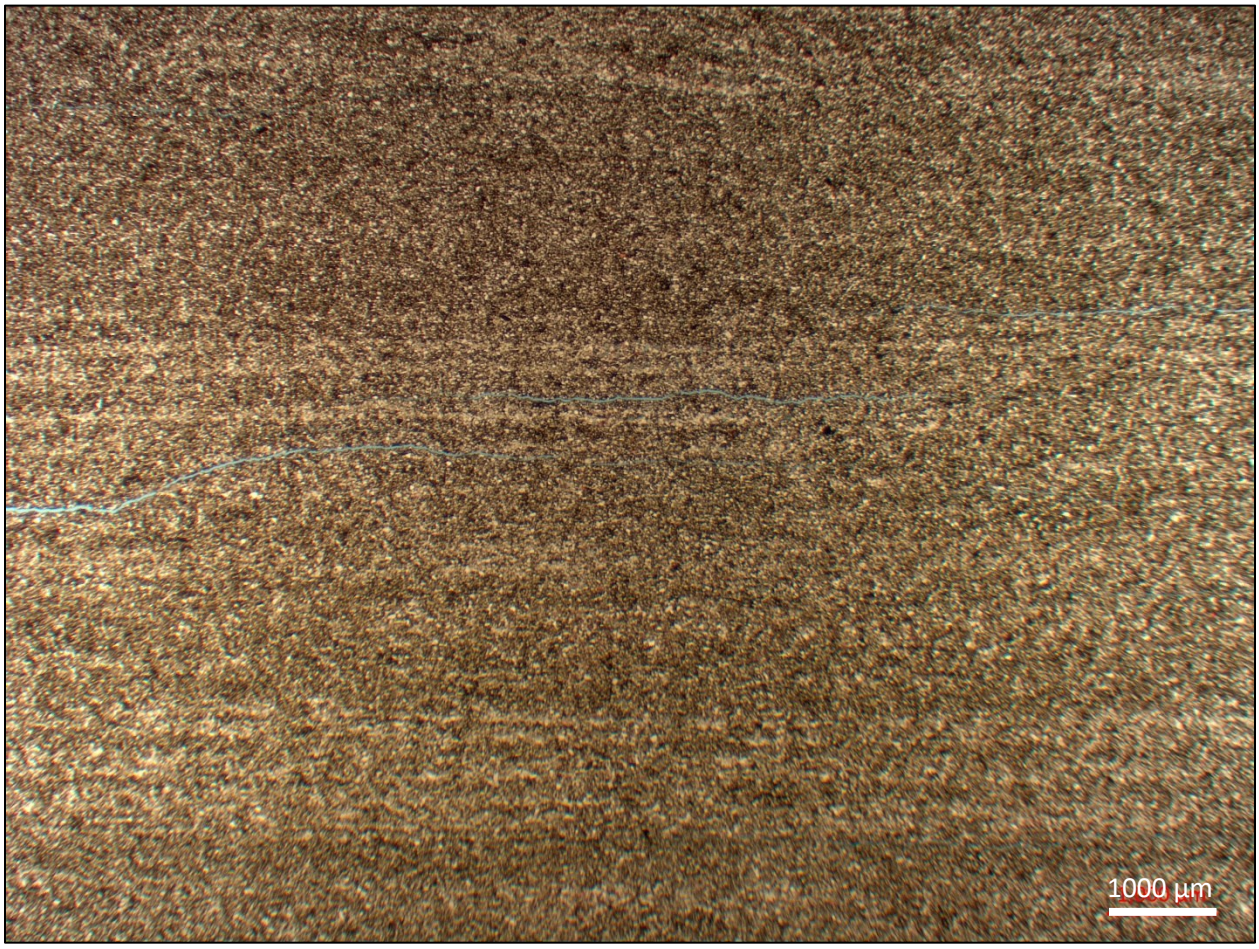

Thin section description:

Laminated to faintly laminated, slightly argillaceous calcareous siltstone. Vertical variations are defined by variations in grain size, in calcite, dolomite and quartz cement, and clays. Grains are sub-angular to sub-rounded, moderately sorted and with a matrix mainly of a mixture of detrital clays and extensive organic matter. Detrital framework grains include quartz and dolomite with a minor amount of micas. Pyrite and phosphate are consistent for this sample.

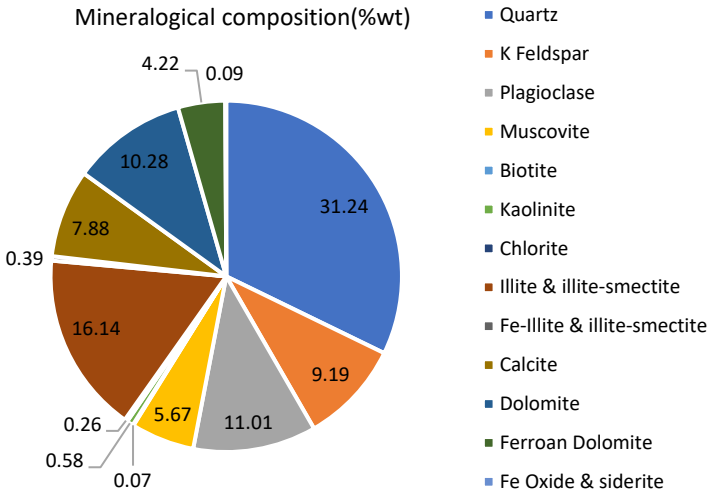

%TOC: 1.32 (%wt)

Additional images – RT 1C

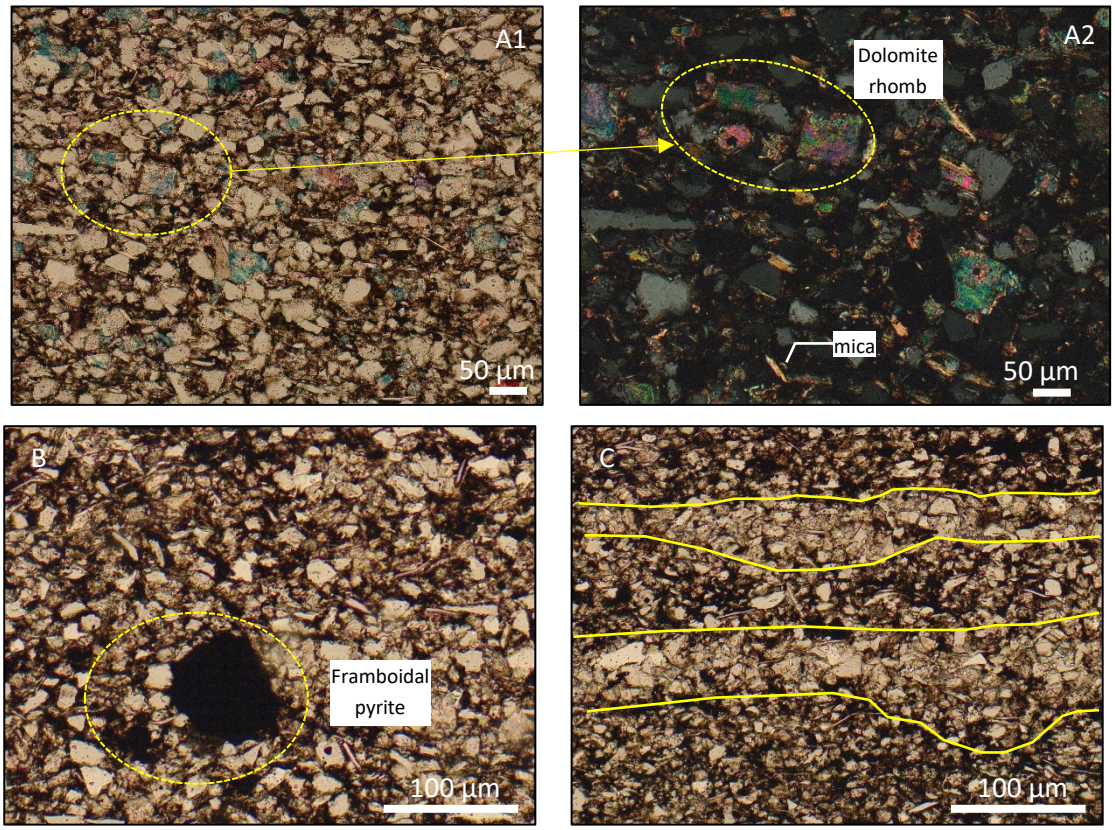

Mineralogical composition – data is in (%wt) - QEMSCAN analysis

Block Code	Pyrite	Sphalerite	Barite	Anhydrite	Halite	Rutile & Ti Silicates	Tourmaline	Chromite	Apatite	Zircon	Monazite	Total	K2O	Macroporosity Estimate (%)	Grain Density (g/cm³)	Bulk Density (g/cm³)
A	1.73	0.03	0.09	0.06	0.00	0.48	0.05	0.00	0.32	0.06	0.00	100.00	3.53	3.7	2.711	29.710
B	1.87	0.03	0.12	0.07	0.00	0.48	0.04	0.00	0.34	0.03	0.00	100.00	3.64	4.6	2.710	30.803
C	1.73	0.00	0.12	0.07	0.00	0.51	0.03	0.00	0.36	0.03	0.00	100.00	3.40	4.4	2.711	26.878

SiO2	Al2O3	Fe2O3	MgO	CaO	Na2O	K2O	TiO2	P2O5	MnO	Cr2O3	Ba	Ni	Sc	LOI	Sum
56.45	9.57	2.97	3	9.26	1.44	3.45	0.64	0.2	0.04	0.008	785	22	9	12.7	99.85

- data is in [%wt]

Be	Co	Cs	Ga	Hf	Nb	Rb	Sn	Sr	Ta	Th	U	V	W	Zr	Y	La	Ce	Pr	Nd	Sm	Eu	Gd	Tb	Dy	Ho	Er	Tm	Yb	Lu	TOT/C	TOT/S
<1	8.8	3	11.2	7.4	11	75.7	2	134	0.8	8.3	3.8	186	1.4	273.6	26	29.1	50.8	6.38	24.4	4.77	0.95	4.68	0.74	4.43	0.92	2.73	0.38	2.72	0.41	4.36	0.97

data is in [ppm]

MICP -

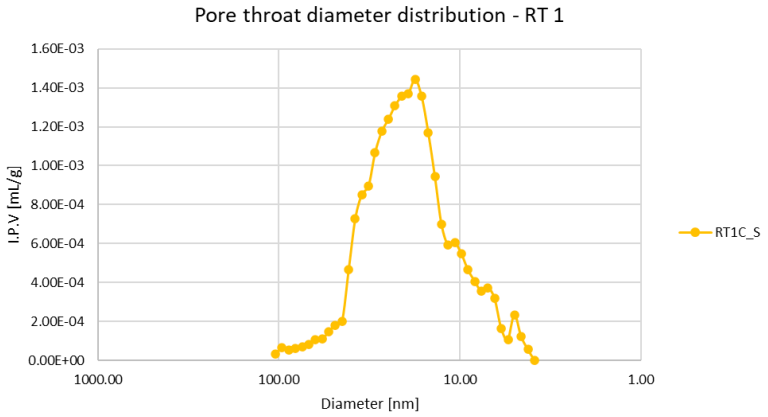

RT 3D – WA25261
Depth: 2100.4 (m)

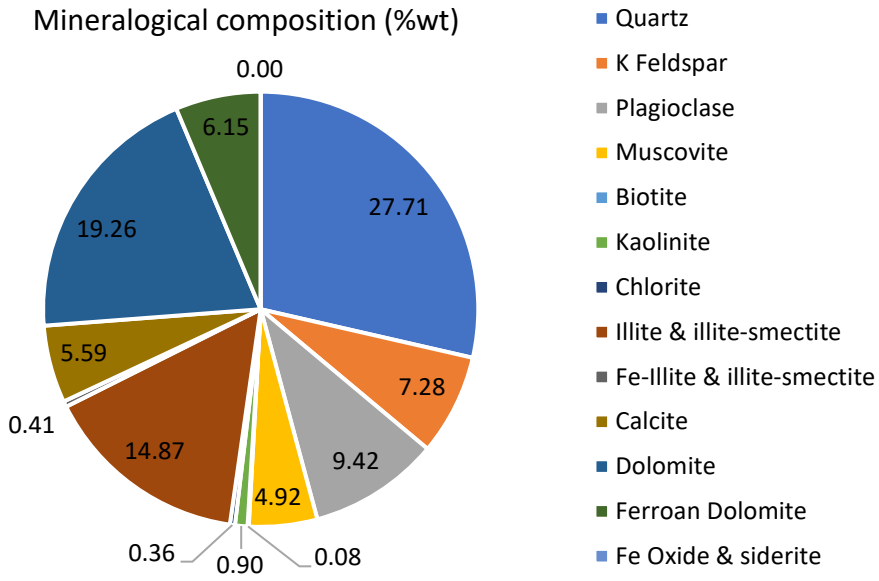

Sample Name	Block Code	Pyrite	Sphalerite	Barite	Anhydrite	Halite	Rutile & Ti Silicates	Tourmaline	Chromite	Apatite	Zircon	Monazite	Total	K2O	Macroporosity Estimate (%)	Grain Density (g/cm³)	Bulk Density (g/cm³)
M3D	A	2.07	0.01	0.07	0.09	0.00	0.49	0.04	0.00	0.38	0.04	0.01	100.00	3.6	3.9	2.720	2.652
M3D	B	1.92	0.01	0.06	0.09	0.00	0.44	0.04	0.00	0.45	0.04	0.01	100.00	3.2	3.5	2.734	2.673

RT 3E – WA25261
Depth: 2158.79 (m)

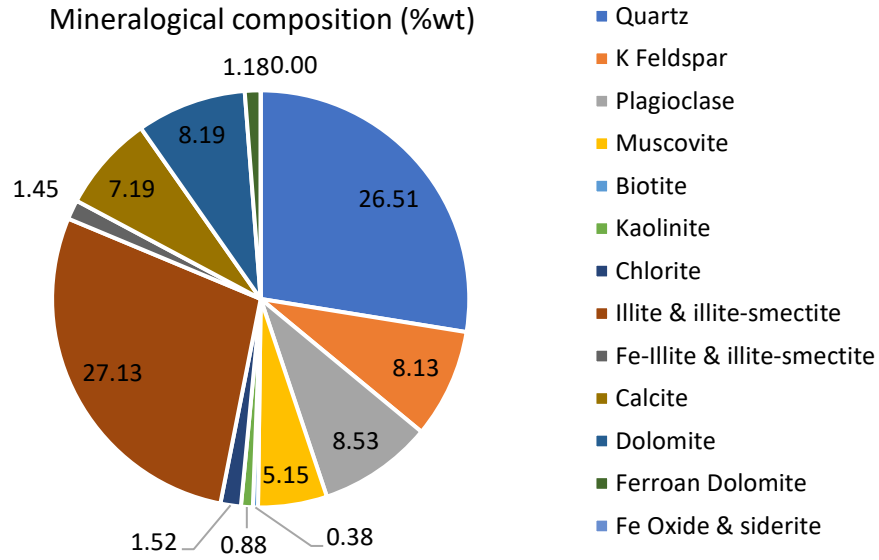

Sample Name	Block Code	Pyrite	Sphalerite	Barite	Anhydrite	Halite	Rutile & Ti Silicates	Tourmaline	Chromite	Apatite	Zircon	Monazite	Total	K2O	Macroporosity Estimate (%)	Grain Density (g/cm³)	Bulk Density (g/cm³)
M3E	A	2.62	0.06	0.08	0.13	0.00	0.42	0.02	0.00	0.64	0.03	0.01	100.00	4.2	3.1	2.712	2.660
M3E	B	2.52	0.02	0.08	0.16	0.00	0.39	0.03	0.00	0.53	0.02	0.01	100.00	4.3	2.8	2.711	2.663

RT 3A – WA25261
Depth: 2125.35 (m)

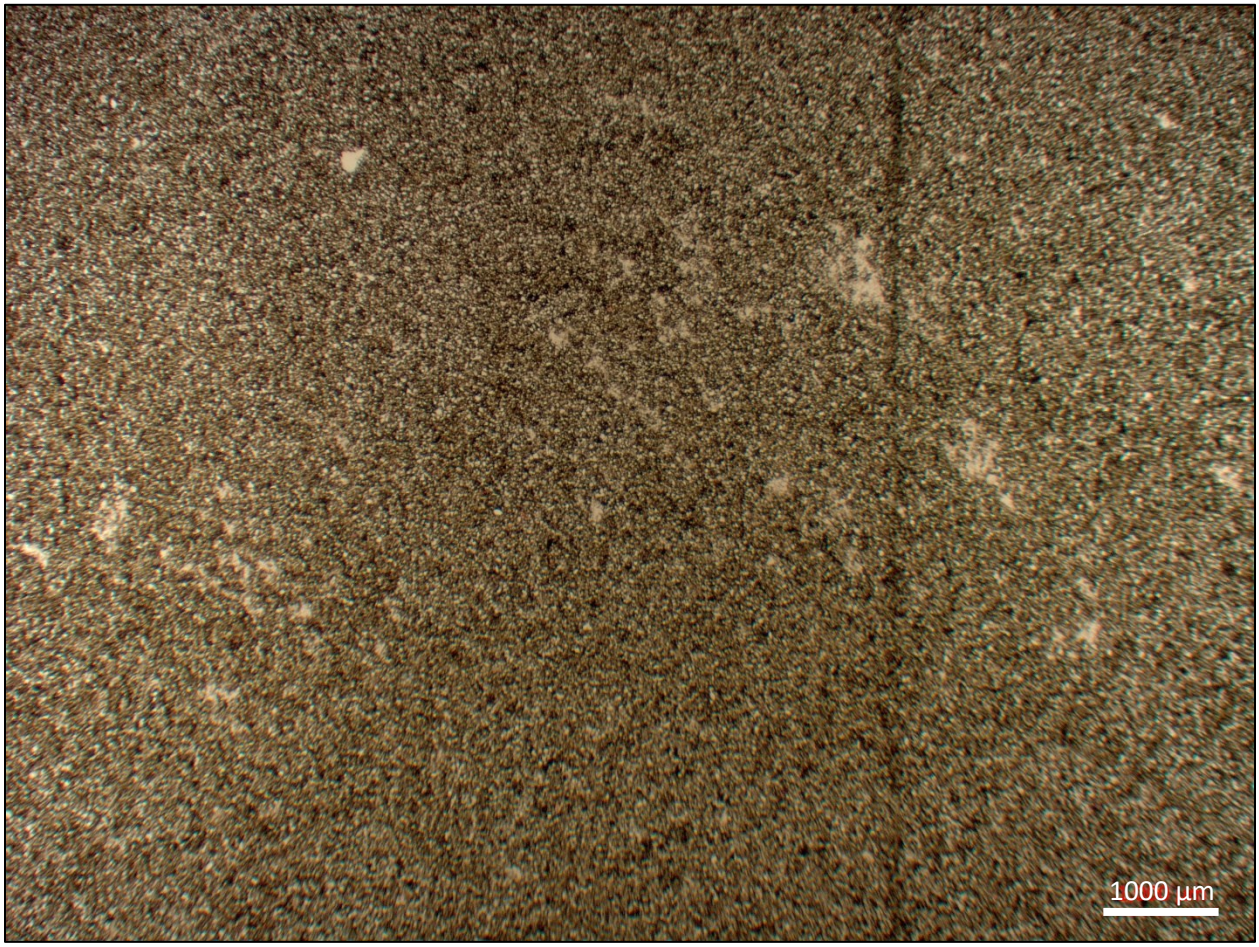

Thin section description:

Massive, slightly argillaceous siltstone. Moderately sorted sample, the framework grains include quartz, plagioclase, K-feldspar, and micas. Quartz cement is consistent at this sample with less calcite and dolomite/Fe-dolomite. Most of the interparticle space is infilled with abundant detrital clays and organics.

Framboidal pyrite, pyrite substitution, quartz "patches" and quartz overgrowth were observed.

%TOC: 2.4 (%wt)

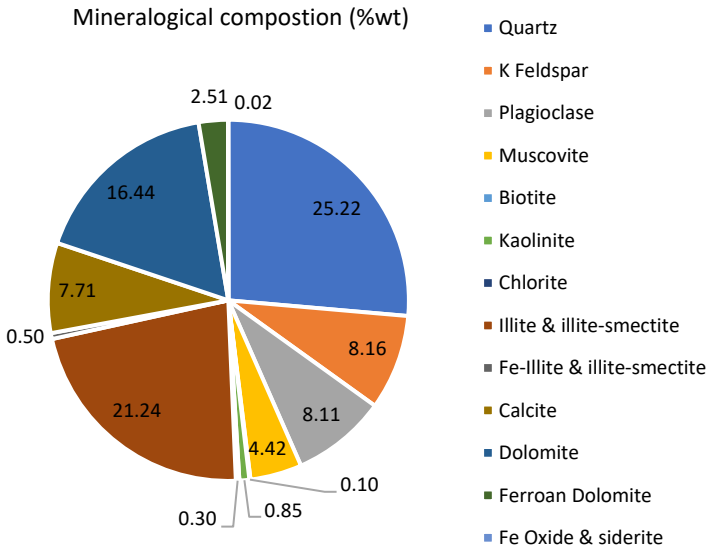

Additional images – RT 3A

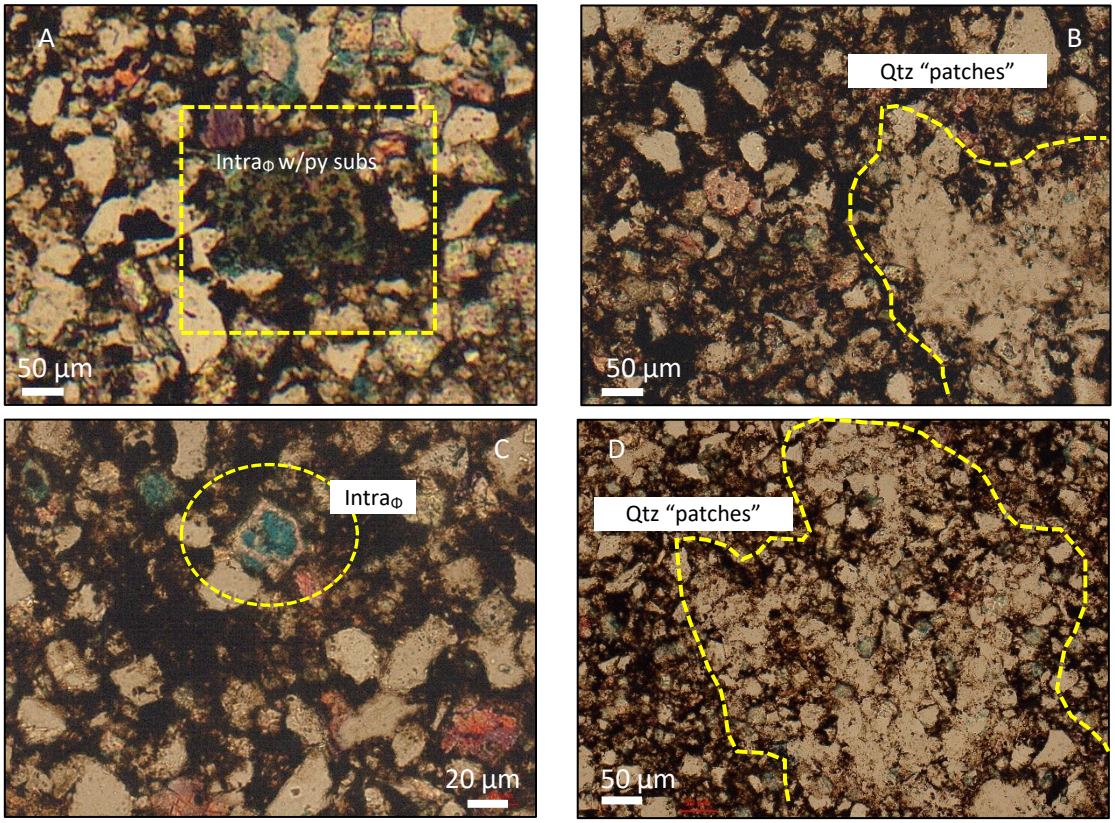

Mineralogical composition – data is in (%wt) – QEMSCAN analysis

Block Code	Pyrite	Sphalerite	Barite	Anhydrite	Halite	Rutile & Ti Silicates	Tourmaline	Chromite	Apatite	Zircon	Monazite	Total	K2O	Macroporosity Estimate (%)	Grain Density (g/cm³)	Bulk Density (g/cm³)
A	3.16	0.01	0.07	0.18	0.00	0.44	0.03	0.00	0.67	0.02	0.00	100.00	3.56	5.8	2.730	31.735
B	2.68	0.01	0.10	0.14	0.00	0.41	0.02	0.00	0.67	0.02	0.00	100.00	3.59	5.8	2.723	30.037
C	3.07	0.00	0.08	0.17	0.00	0.43	0.03	0.00	0.62	0.02	0.00	100.00	3.65	4.8	2.728	31.511

ICP/ ICP-MS

SiO2	Al2O3	Fe2O3	MgO	CaO	Na2O	K2O	TiO2	P2O5	MnO	Cr2O3	Ba	Ni	Sc	LOI	Sum
52.38	8.83	3.66	3.42	10.57	1.1	3.39	0.58	0.4	0.05	0.007	480	39	9	15.4	99.85

- data is in [%wt]

Be	Co	Cs	Ga	Hf	Nb	Rb	Sn	Sr	Ta	Th	U	V	W	Zr	Y	La	Ce	Pr	Nd	Sm	Eu	Gd	Tb	Dy	Ho	Er	Tm	Yb	Lu	TOT/C	TOT/S
2	12.7	3.5	9.7	6.6	9.9	70.3	2	133.1	0.7	7.9	7.1	184	1.1	240.9	28	27.8	51.4	6.41	24.6	4.85	0.99	4.76	0.74	4.3	0.93	2.86	0.39	2.56	0.4	5.84	1.43

└ data is in [ppm]

MICP -

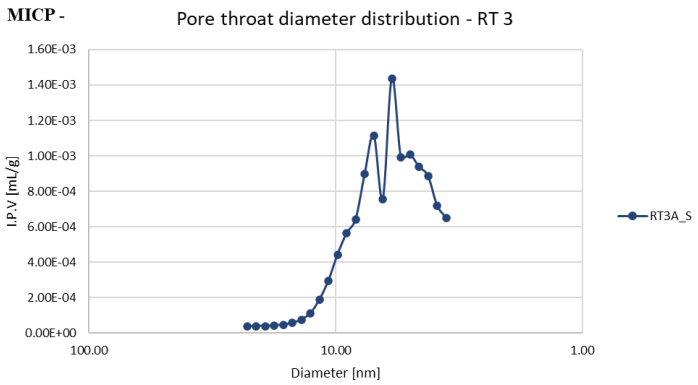

RT 3C -WA25261
Depth: 2127.23 (m)
%TOC: 2.0 (%wt)

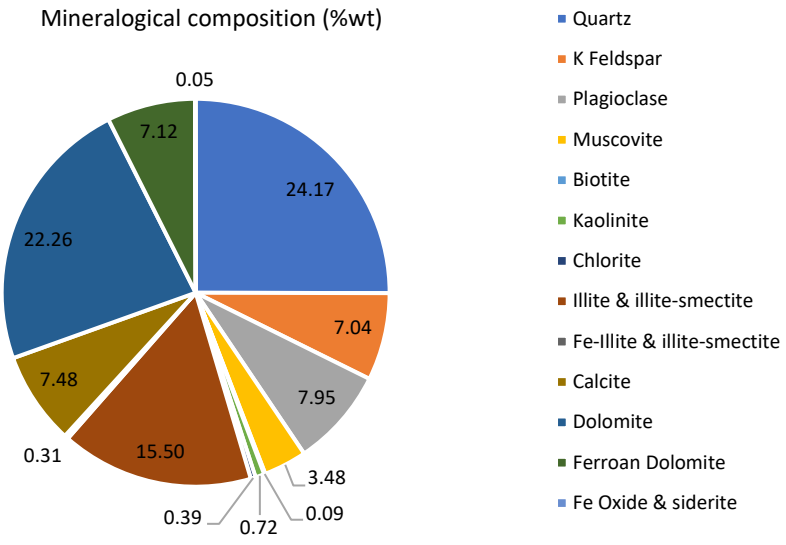

Block Code	Pyrite	Sphalerite	Barite	Anhydrite	Halite	Rutile & Ti Silicates	Tourmaline	Chromite	Apatite	Zircon	Monazite	Total	K2O	Macroporosity Estimate (%)	Grain Density (g/cm³)	Bulk Density (g/cm³)
A	1.91	0.00	0.19	0.09	0.00	0.36	0.03	0.00	0.63	0.04	0.00	100.00	2.93	5.45	2.75	31.19
B	2.08	0.00	0.24	0.10	0.00	0.39	0.02	0.00	0.60	0.02	0.00	100.00	2.97	6.15	2.75	30.42
C	1.57	0.00	0.22	0.07	0.00	0.32	0.02	0.00	0.60	0.02	0.00	100.00	2.61	5.37	2.76	31.63

ICP/ ICP-MS

SiO2	Al2O3	Fe2O3	MgO	CaO	Na2O	K2O	TiO2	P2O5	MnO	Cr2O3	Ba	Ni	Sc	LOI	Sum
45.19	7.95	3.84	5.28	13.71	1.03	3.03	0.52	0.27	0.07	0.009	1078	37	7	18.8	99.79

- data is in [%wt]

Be	Co	Cs	Ga	Hf	Nb	Rb	Sn	Sr	Ta	Th	U	V	W	Zr	Y	La	Ce	Pr	Nd	Sm	Eu	Gd	Tb	Dy	Ho	Er	Tm	Yb	Lu	TOT/C	TOT/S
3	8.3	3.1	6.6	5.7	8.2	64.4	1	151.9	0.4	6.6	4.9	79	1.1	211.4	23.5	23.9	46.3	5.59	22.6	4.23	0.94	4.2	0.67	4.04	0.85	2.58	0.33	2.44	0.33	6.74	1

data is in [ppm]

MICP -

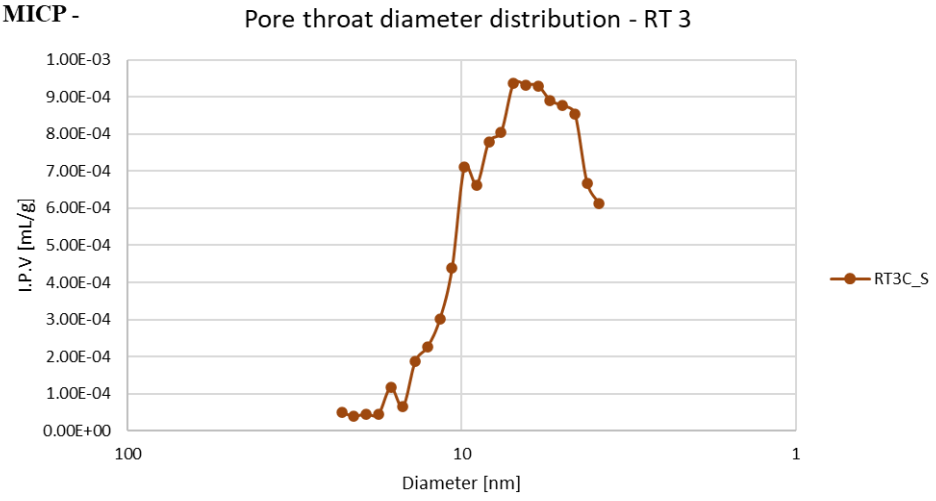

RT 3 – WA25261
Depth: 2133.09 (m)

Thin section description:

Massive appearing, slightly argillaceous, siltstone. Detrital matrix clays and organics are observed infilling interstitial areas. Framework grains are primarily comprised of quartz, plagioclase, K-feldspar, and micas. Pyrite is noted throughout the sample. Cements include dolomite-Fe-dolomite, calcite, and quartz overgrowths.

%TOC: 2.34 (%wt)

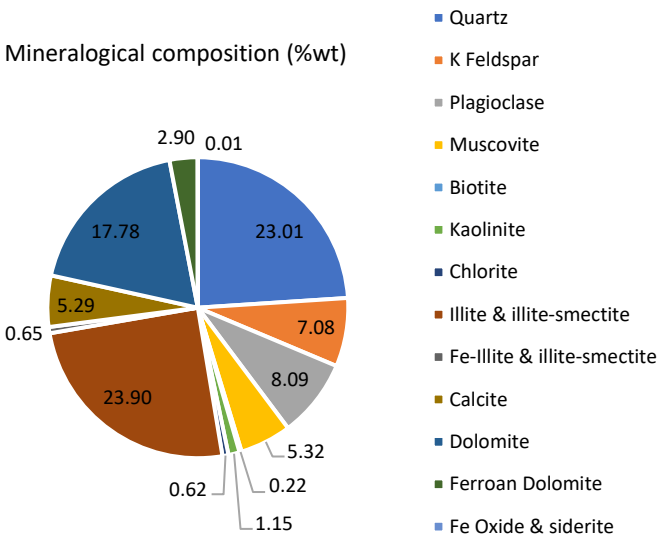

Additional images – RT 3

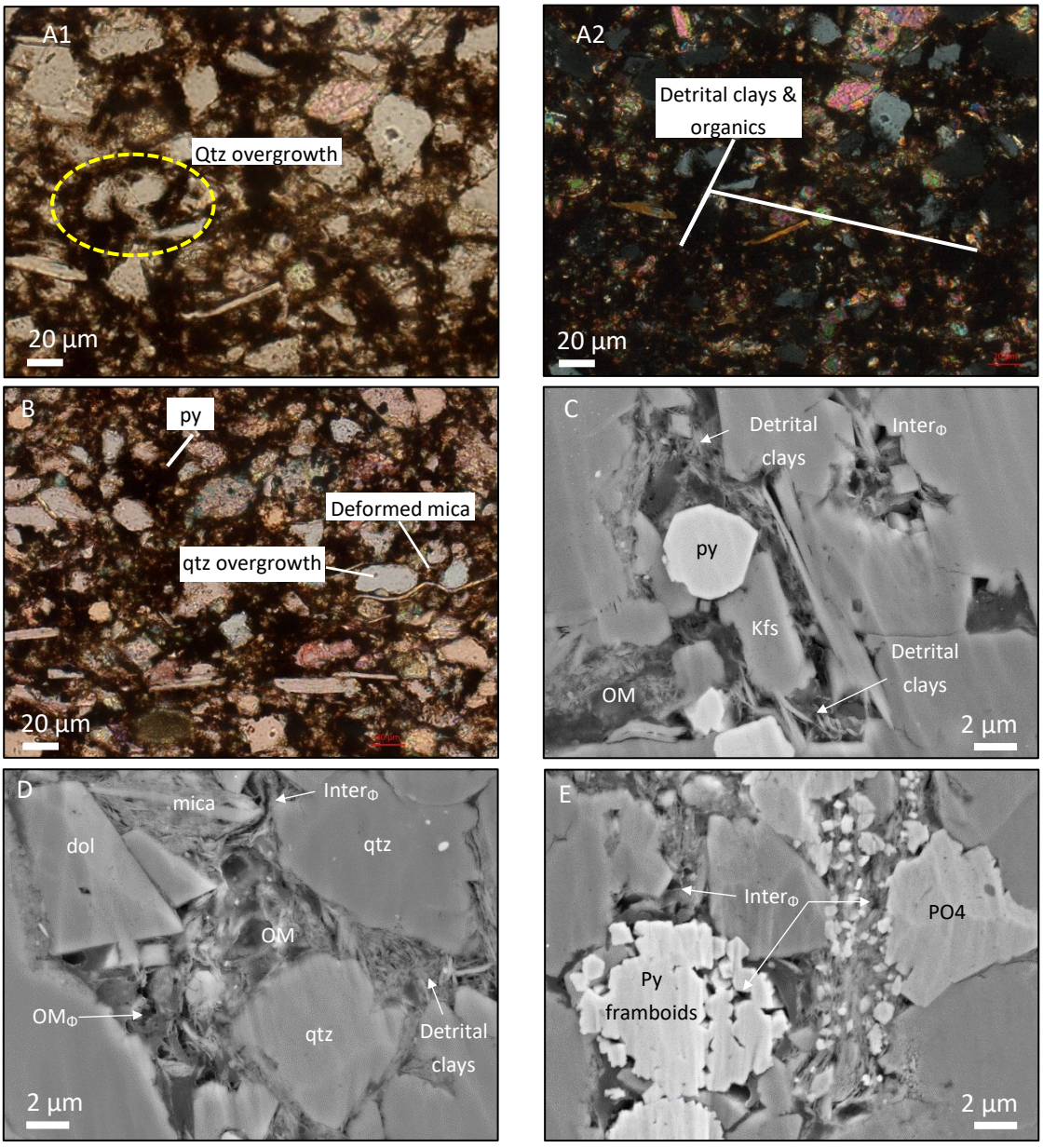

Mineralogical composition – data is in (%wt) – QEMSCAN analysis

Block Code	Pyrite	Sphalerite	Barite	Anhydrite	Halite	Rutile & Ti Silicates	Tourmaline	Chromite	Apatite	Zircon	Monazite	Total	K2O	Macroporosity Estimate (%)	Grain Density (g/cm³)	Bulk Density (g/cm³)
A	2.84	0.00	0.07	0.17	0.00	0.38	0.02	0.00	0.48	0.02	0.00	100.00	3.85	3.11	2.73	31.73
B	2.56	0.00	0.10	0.12	0.00	0.41	0.03	0.00	0.51	0.03	0.01	100.00	3.77	4.17	2.73	30.04
C	2.48	0.00	0.15	0.12	0.00	0.38	0.04	0.00	0.46	0.02	0.01	100.00	3.38	3.75	2.74	31.51

ICP/ ICP-MS

SiO2	Al2O3	Fe2O3	MgO	CaO	Na2O	K2O	TiO2	P2O5	MnO	Cr2O3	Ba	Ni	Sc	LOI	Sum
52.51	9.74	3.45	3.64	9.67	1.24	3.73	0.62	0.32	0.05	0.009	754	40	9	14.8	99.82

- data is in [%wt]

Be	Co	Cs	Ga	Hf	Nb	Rb	Sn	Sr	Ta	Th	U	V	W	Zr	Y	La	Ce	Pr	Nd	Sm	Eu	Gd	Tb	Dy	Ho	Er	Tm	Yb	Lu	TOT/C	TOT/S
2	14	3.8	11.1	6.6	9.9	85.8	1	140.2	0.8	8.6	11	129	1.5	241.7	27	31.2	58.3	6.94	26.5	5.33	1.12	4.82	0.77	4.59	0.95	3	0.43	2.71	0.41	5.94	1.33

data is in [ppm]

EDS images – R3

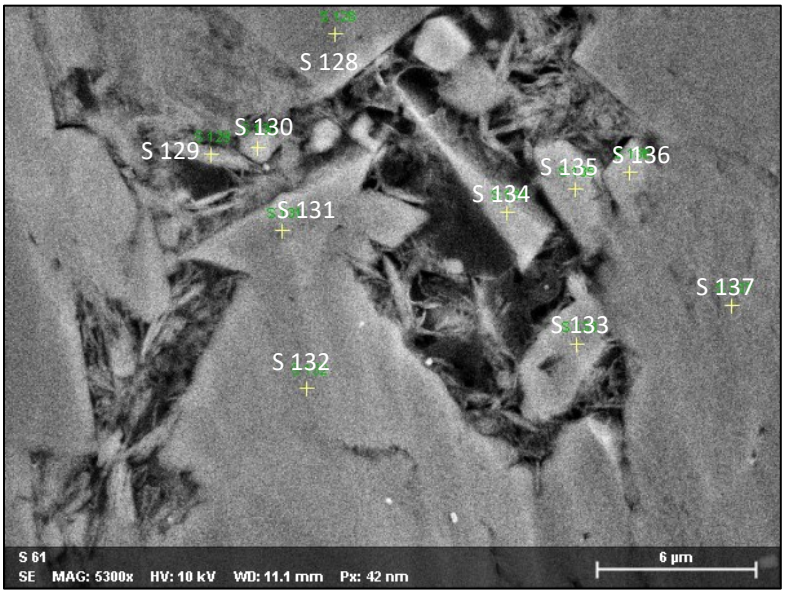

Atomic concentration [%]

Spectrum	C	O	Na	Mg	Al	Si	K	Ca	Fe	As
S 128	20.6	59.3		7.9				11.2	1.0	
S 129	24.9	50.5	0.1	1.0	6.4	14.7	1.9		0.6	
S 130		67.3	0.1	0.9	6.6	21.2	3.8		0.1	
S 131	16.3	62.8		4.6	1.3	6.2	0.7	7.0	0.6	0.5
S 132	10.2	60.4			4.7	21.1	3.6			
S 133	16.6	57.5	0.1		4.1	18.1	3.5			
S 134	23.6	59.8		5.9	0.1	0.2		9.1	1.3	
S 135		66.5			5.5	22.8	5.3			
S 136	19.9	54.7		0.2	1.4	4.4	0.6	18.7		
S 137	15.8	56.7	0.1	0.6	8.7	15.4	2.2		0.4	
Mean	**18.5**	**59.5**	**0.1**	**3.0**	**4.3**	**13.8**	**2.7**	**11.5**	**0.7**	**0.5**
Sigma	**4.7**	**5.1**	**0.0**	**3.1**	**2.9**	**8.2**	**1.6**	**5.1**	**0.4**	**0.0**
SigmaMean	**1.5**	**1.6**	**0.0**	**1.0**	**0.9**	**2.6**	**0.5**	**1.6**	**0.1**	**0.0**

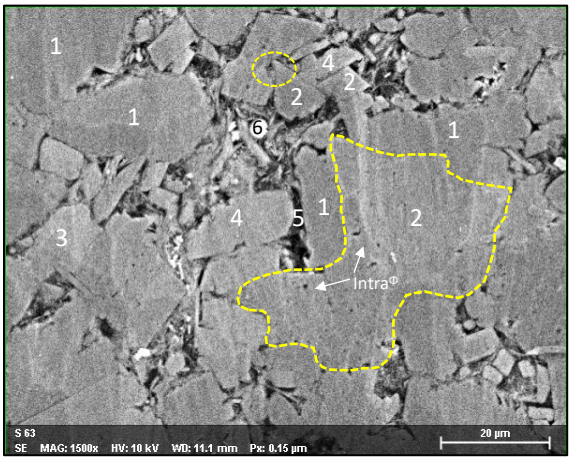

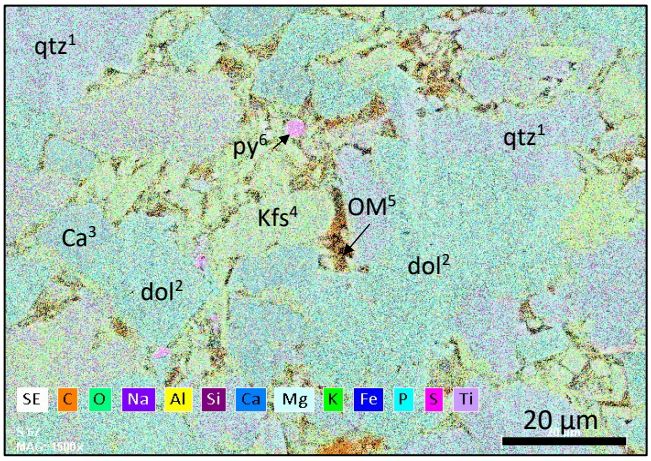

MICP - Pore throat diameter distribution - RT 3

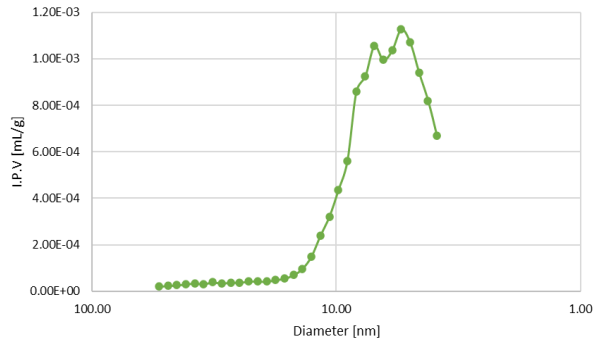

BET - Volume vs Pressure - RT 3

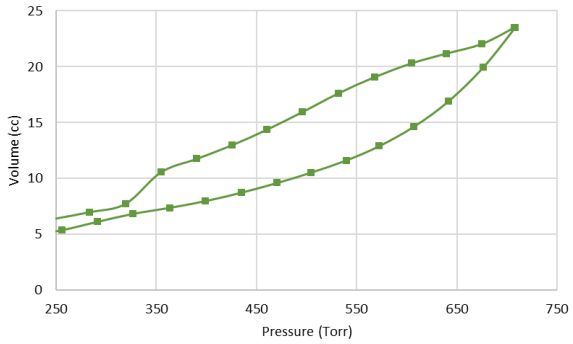

RT 2 – WA25261
Depth: 2136.37 (m)

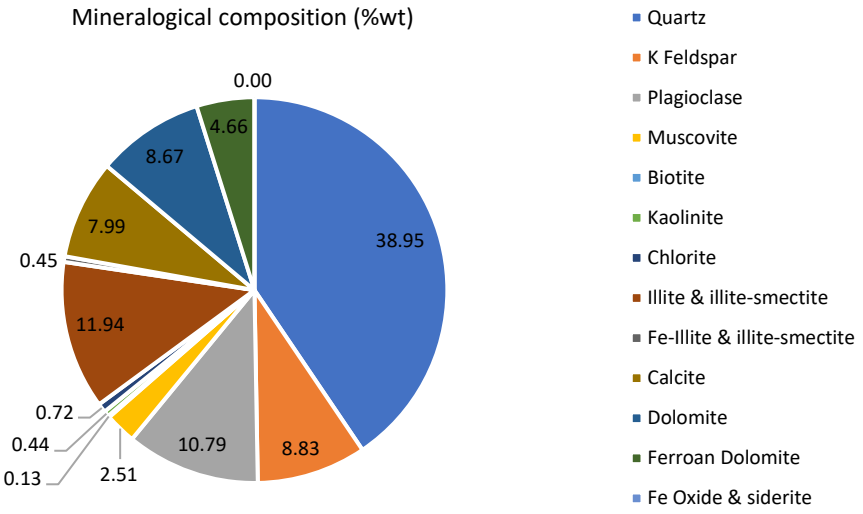

Mineralogical composition – data is in (%wt) – QEMSCAN analysis

Block Code	Pyrite	Sphalerite	Barite	Anhydrite	Halite	Rutile & Ti Silicates	Tourmaline	Chromite	Apatite	Zircon	Monazite	Total	K2O	Macroporosity Estimate (%)	Grain Density (g/cm³)	Bulk Density (g/cm³)
A	2.45	0.00	0.28	0.11	0.00	0.45	0.04	0.00	0.68	0.01	0.01	100.00	3.19	4.76	2.71	2.63
B	2.23	0.05	0.40	0.10	0.00	0.39	0.03	0.00	0.67	0.04	0.00	100.00	2.98	4.45	2.71	2.64

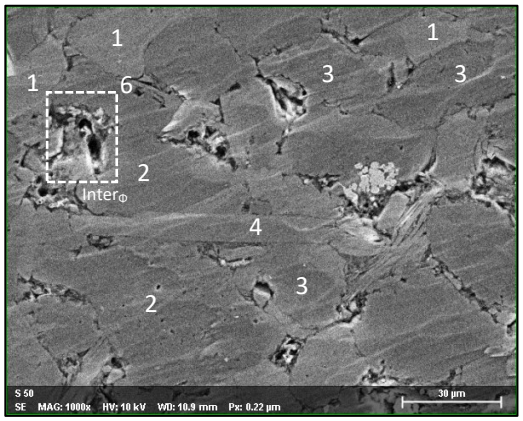

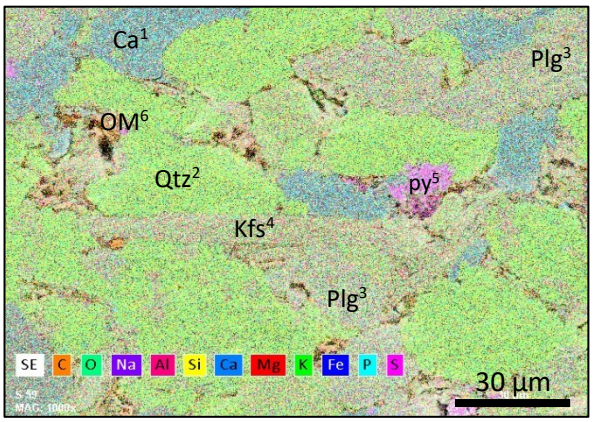

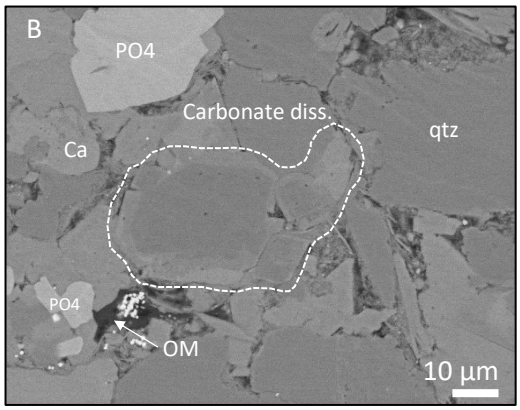

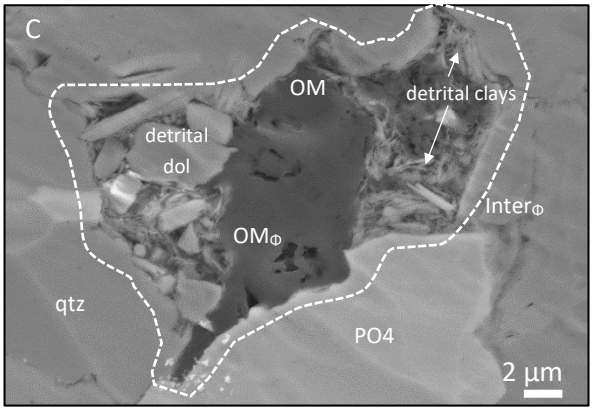

RT 1B – WA25261
Depth: 2174.01 (m)

Thin section description:

Massive appearing, slightly argillaceous, calcareous siltstone. This sample show some burrowing (cryptic bioturbation). Detrital matrix clays and organics are observed infilling interstitial space. Framework grains are primarily quartz, plagioclase, K-feldspar, and micas. Pyrite substitution and pyrite framboids are noted. Cements include dolomite-Fe-dolomite, calcite, and quartz overgrowths.

%TOC: 1.1 (%wt)

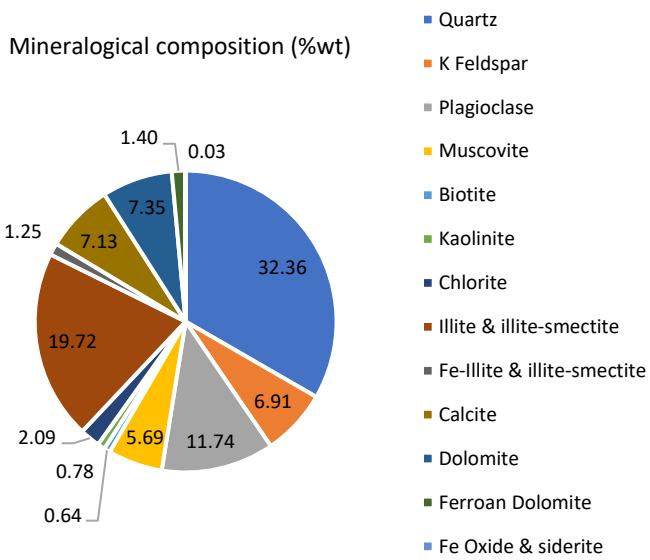

Additional images – RT 1B

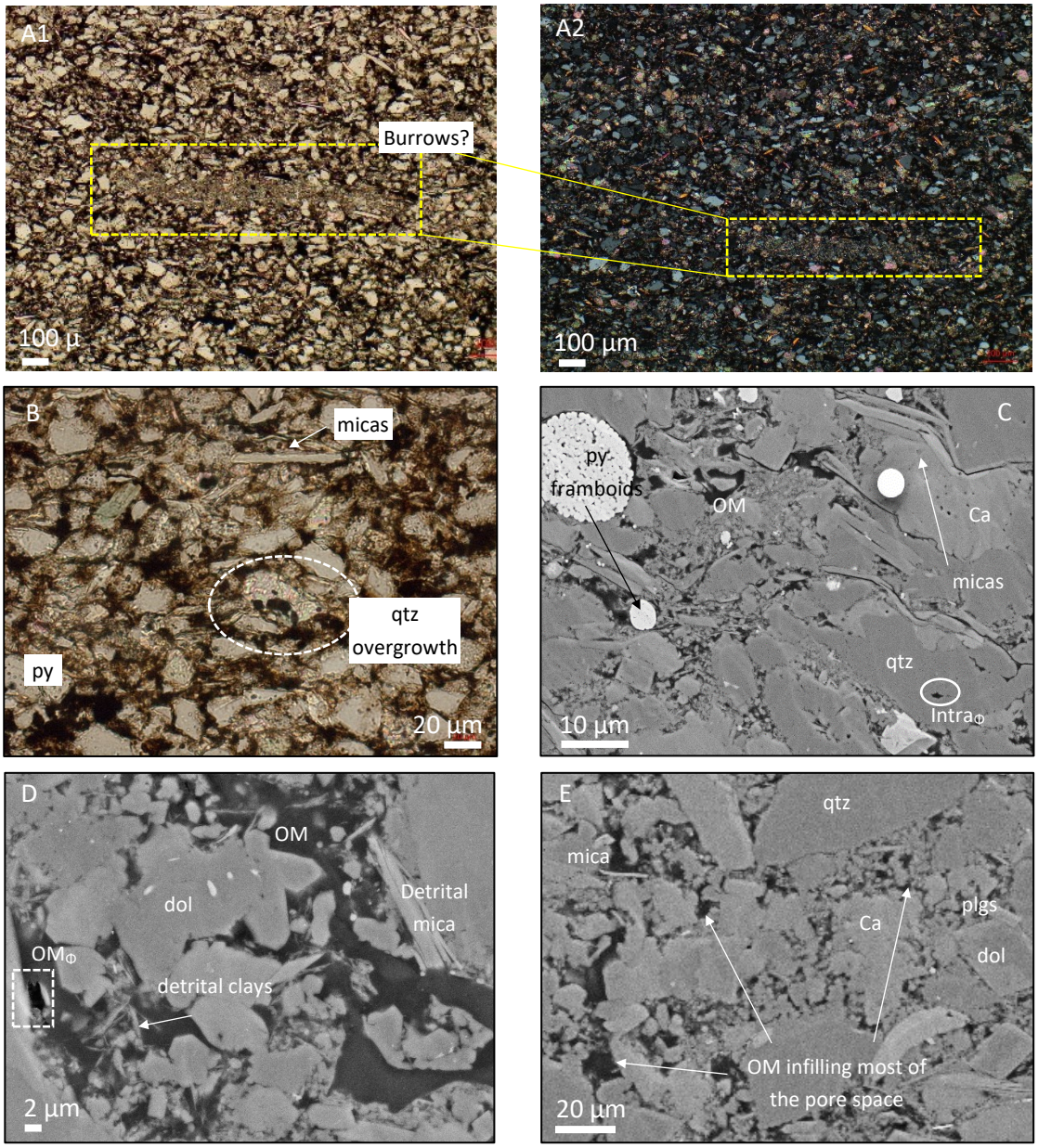

Mineralogical composition – data is in (%wt) – QEMSCAN analysis

Block Code	Pyrite	Sphalerite	Barite	Anhydrite	Halite	Rutile & Ti Silicates	Tourmaline	Chromite	Apatite	Zircon	Monazite	Total	K2O	Macroporosity Estimate (%)	Grain Density (g/cm³)	Bulk Density (g/cm³)
A	1.837	0.034	0.062	0.073	1.18E-03	0.424	0.026	0.0000	0.282	0.030	0.003	100	3.722	2.142	2.704	30.420
B	2.098	0.036	0.082	0.061	6.98E-05	0.390	0.032	0.0014	0.283	0.032	0.008	100	3.927	3.014	2.708	31.193
C	1.971	0.041	0.061	0.063	0.00E+00	0.420	0.036	0.0008	0.301	0.018	0.003	100	3.667	3.165	2.706	31.626

ICP/ ICP-MS

SiO2	Al2O3	Fe2O3	MgO	CaO	Na2O	K2O	TiO2	P2O5	MnO	Cr2O3	Ba	Ni	Sc	LOI	Sum
59.76	10.75	3.4	2.36	6.98	1.47	3.47	0.68	0.16	0.04	0.01	470	57	10	10.6	99.71

- data is in [%wt]

Be	Co	Cs	Ga	Hf	Nb	Rb	Sn	Sr	Ta	Th	U	V	W	Zr	Y	La	Ce	Pr	Nd	Sm	Eu	Gd	Tb	Dy	Ho	Er	Tm	Yb	Lu	TOT/C	TOT/S
2	11.8	3.9	12	6.5	10.1	90.6	2	130.7	0.9	8.2	6.5	708	1.8	243.8	24.5	29.4	53	6.39	24.2	4.81	0.98	4.37	0.68	4.32	0.86	2.71	0.38	2.46	0.36	3.24	1.03

└ data is in [ppm]

Mercury Injection analysis – RT 1B – WA25261

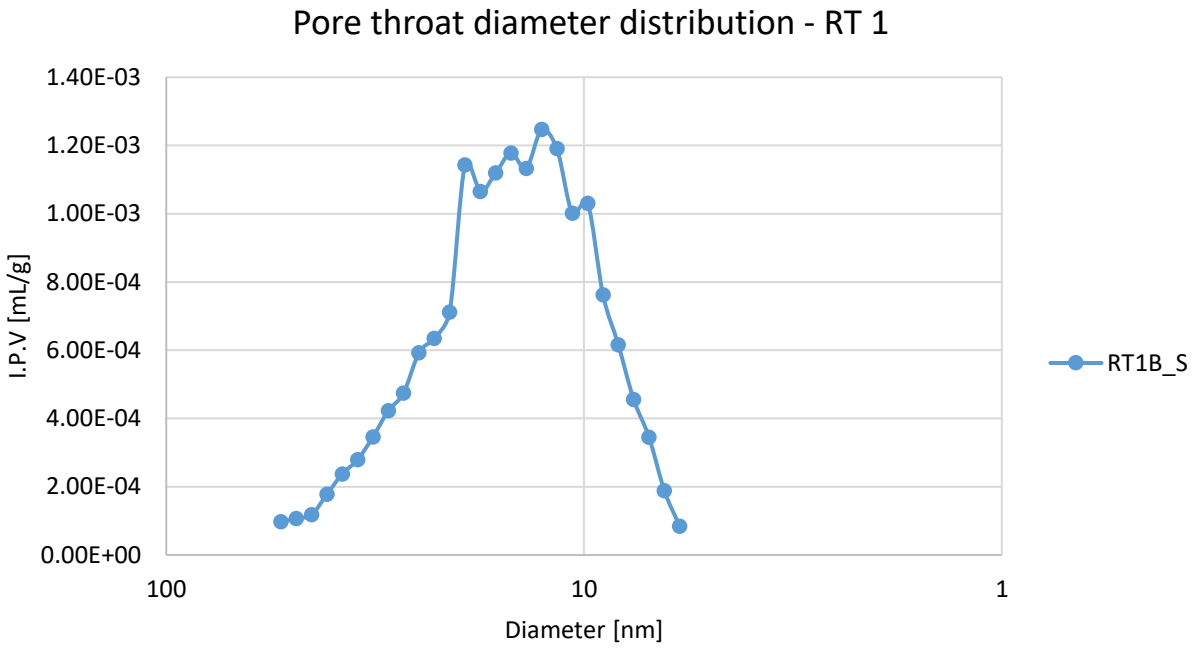

BET Analysis – RT 1B – WA25261

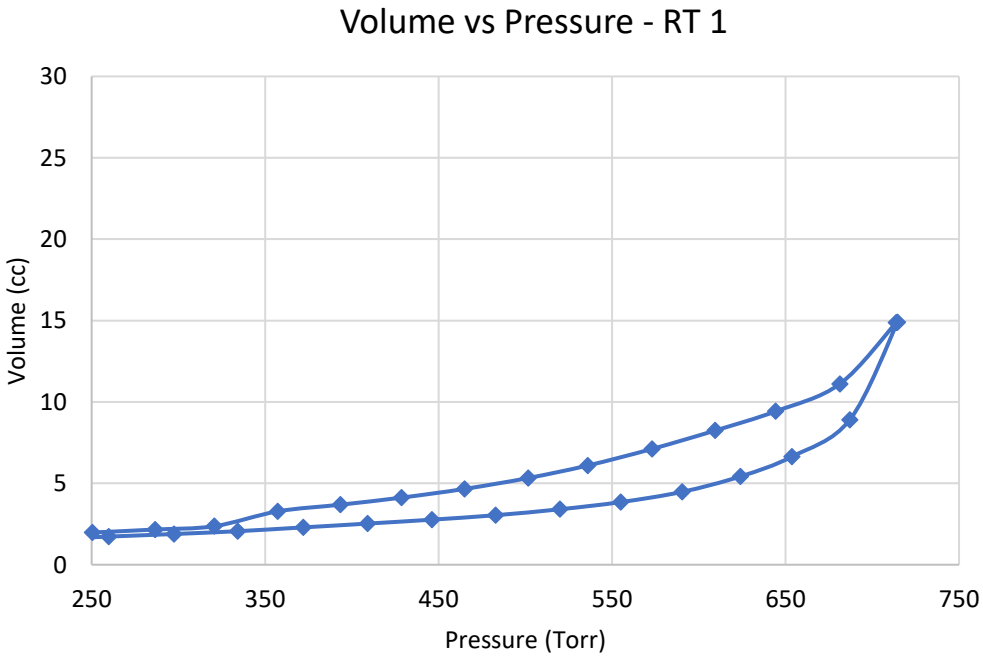

RT 3B – WA25261
Depth: 2195.8 (m)

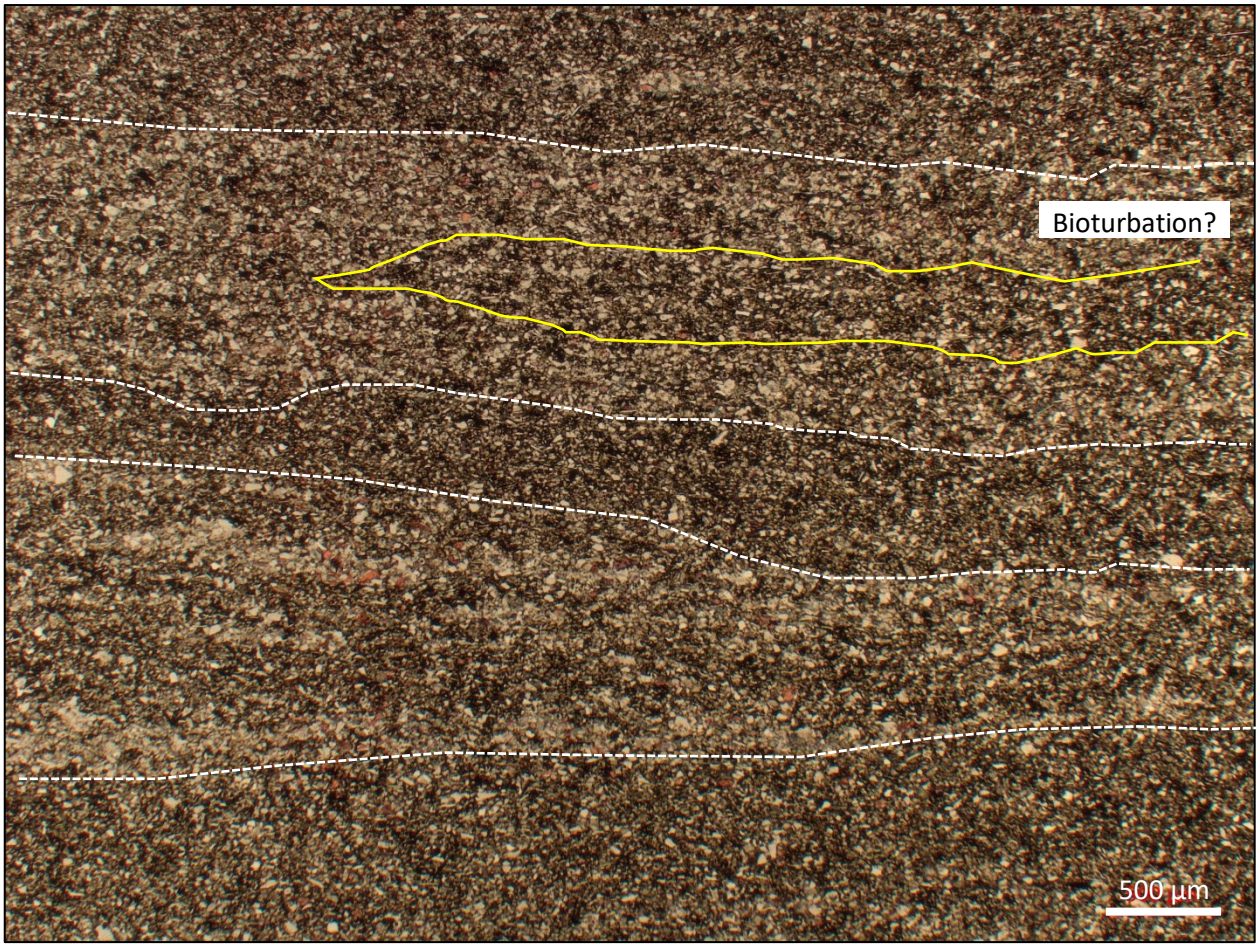

Thin section description:

Well laminated, bioturbated, argillaceous, calcareous siltstone. Laminations are sharp based and are normally graded. Detrital framework grains are sub rounded to sub angular and are mainly quartz and plagioclase with minor K-feldspar and micas. Main cements are dolomite/Fe-dolomite with minor calcite. Most of the pore space is occluded by detrital matrix clays and organics.

%TOC: 2.36 (%wt)

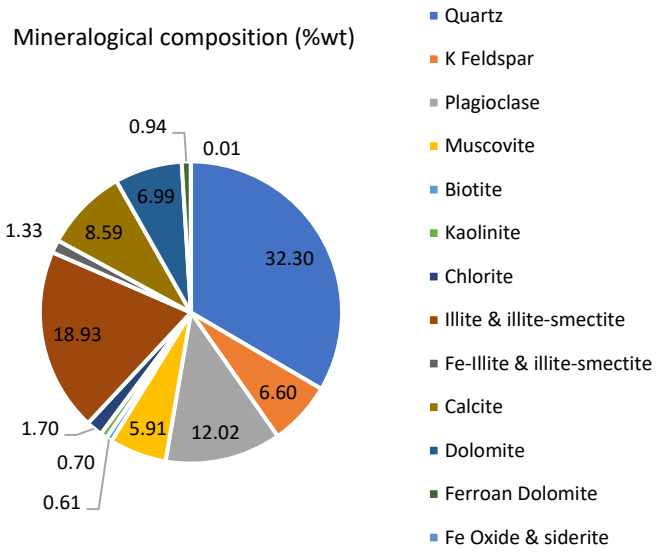

Additional images – RT 3B

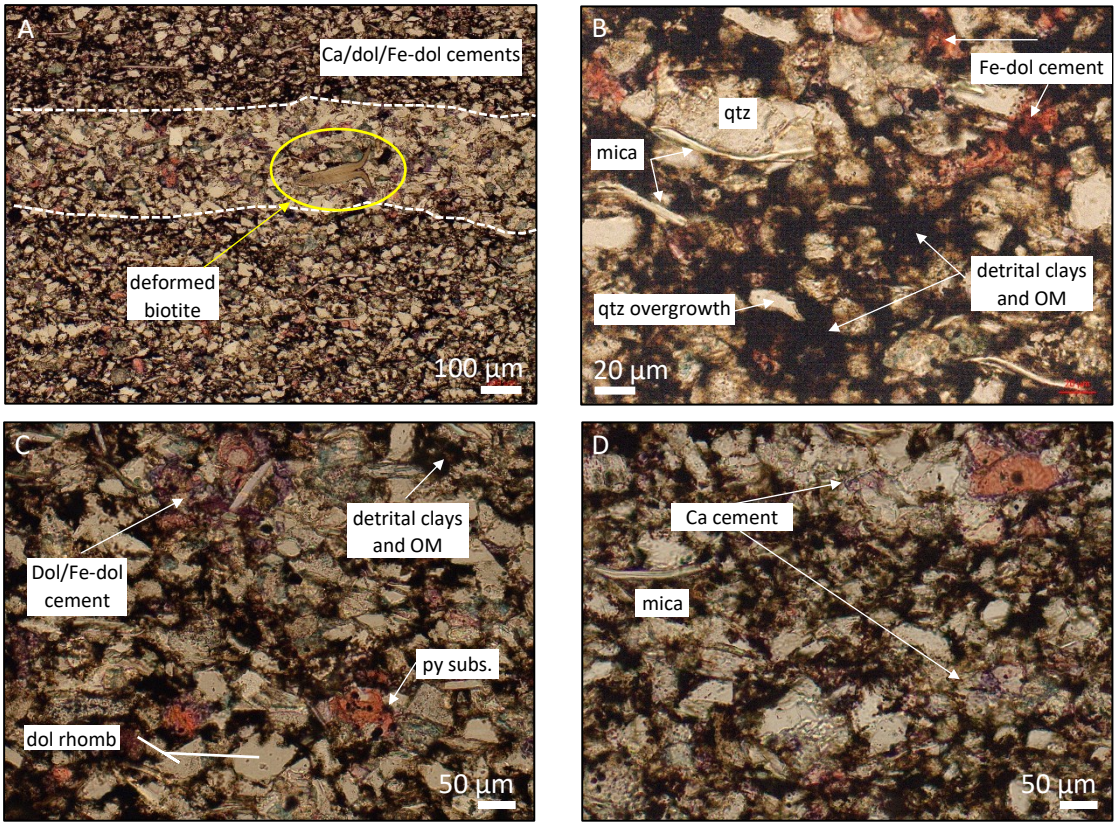

Mineralogical composition – data is in (%wt) – QEMSCAN analysis

Block Code	Pyrite	Sphalerite	Barite	Anhydrite	Halite	Rutile & Ti Silicates	Tourmaline	Chromite	Apatite	Zircon	Monazite	Total	K2O	Macroporosity Estimate (%)	Grain Density (g/cm³)	Bulk Density (g/cm³)
A	2.222	0.027	0.053	0.081	1.81E-02	0.444	4.46E-02	0	0.410	0.054	0.002	100	3.275	4.832	2.707	21.765
B	2.131	0.030	0.056	0.073	0.00E+00	0.463	3.28E-02	0.0010874	0.390	0.037	0.006	100	3.337	3.675	2.707	20.769
C	2.262	0.024	0.069	0.079	0.00E+00	0.511	3.16E-02	0.001398	0.383	0.029	0.003	100	3.479	3.611	2.706	23.559

ICP/ ICP-MS

SiO2	Al2O3	Fe2O3	MgO	CaO	Na2O	K2O	TiO2	P2O5	MnO	Cr2O3	Ba	Ni	Sc	LOI	Sum
57.12	10.67	3.35	2.47	7.7	1.52	3.26	0.72	0.18	0.04	0.01	424	78	10	12.6	99.64

- data is in [%wt]

Be	Co	Cs	Ga	Hf	Nb	Rb	Sn	Sr	Ta	Th	U	V	W	Zr	Y	La	Ce	Pr	Nd	Sm	Eu	Gd	Tb	Dy	Ho	Er	Tm	Yb	Lu	TOT/C	TOT/S
<1	11.6	3.9	10.2	7.8	11.8	89.5	2	117.7	0.8	8.8	7	1087	1.2	291.2	27	30	53.4	6.65	23.2	4.83	0.94	4.39	0.72	4.56	0.92	2.74	0.4	3.02	0.42	4.46	1.18

data is in [ppm]

MICP -

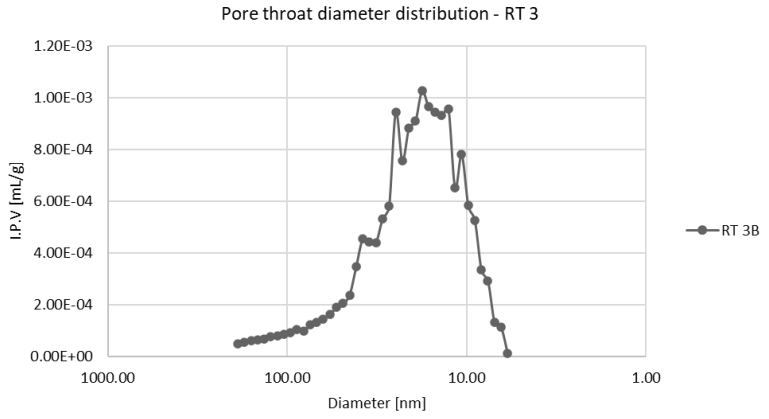

RT 1 – WA32485
Depth: 2068.03 (m)

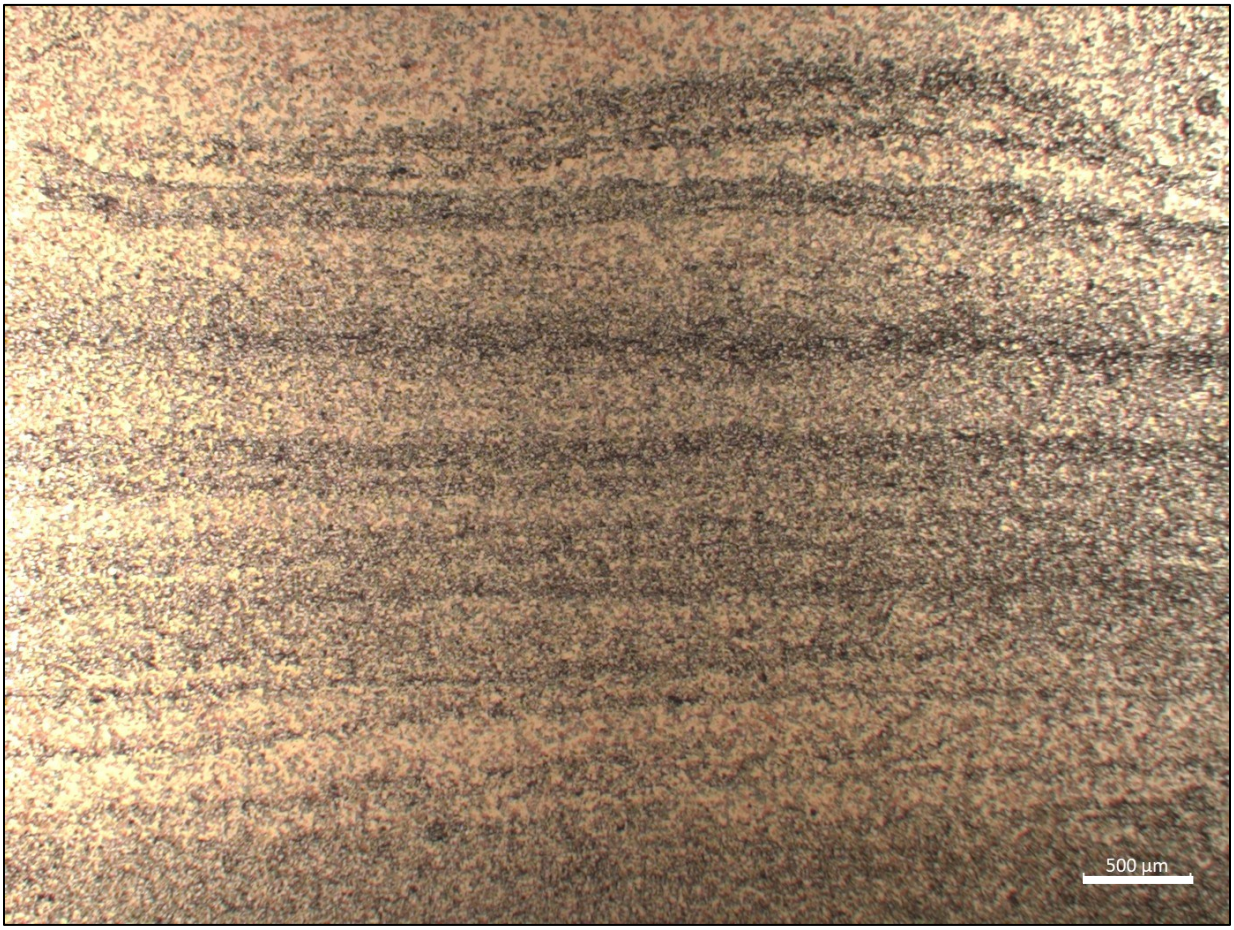

Thin section description

Well laminated to laminated (minor ripples), slightly argillaceous dolomitic, calcareous siltstone. Laminae have sharp basal contacts and are normally graded. Framework grains include quartz and plagioclase with minor K-feldspar and micas. Minor phosphate and replacement pyrite is noted.

%TOC: 1.07 (%wt)

Porosity: 4 (%)

Permeability: 6.1887x10^{-5} (md)

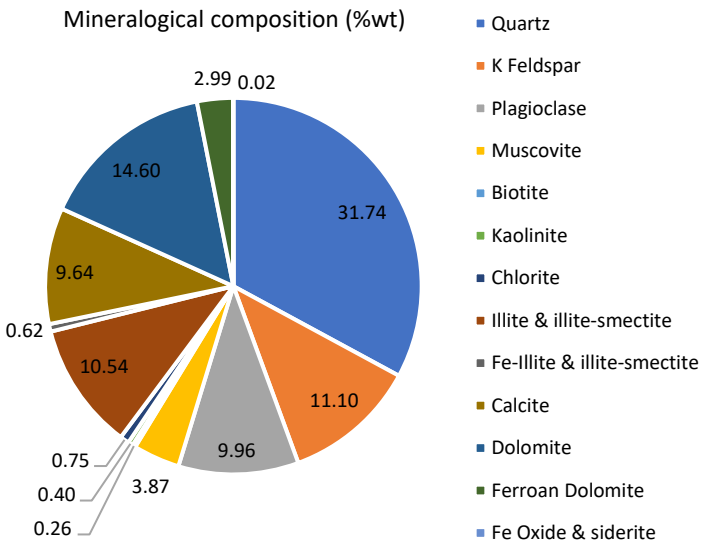

Additional images – RT 1

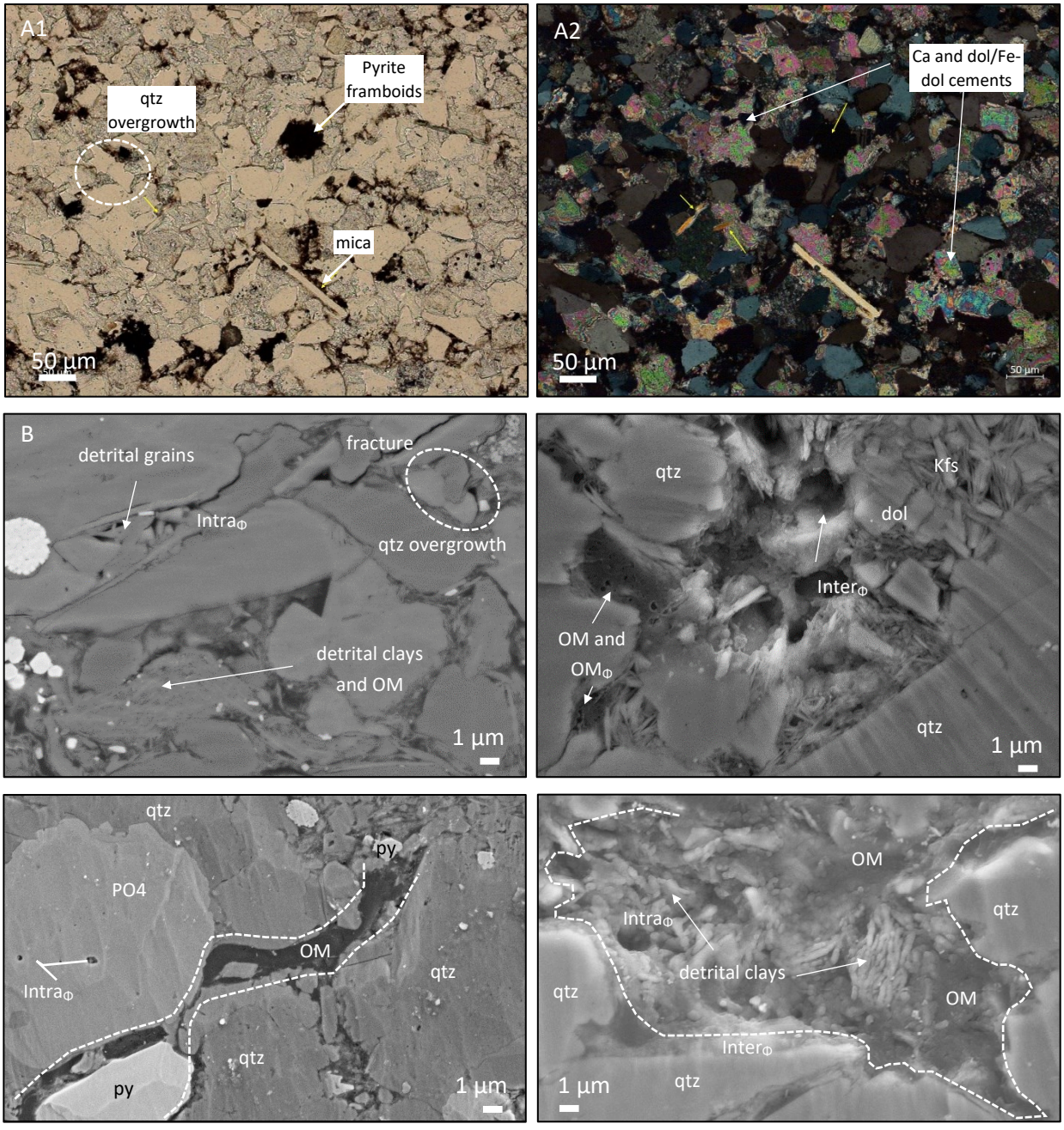

Mineralogical composition – data is in (%wt) – QEMSCAN analysis

Block Code	Pyrite	Sphalerite	Barite	Anhydrite	Halite	Rutile & Ti Silicates	Tourmaline	Chromite	Apatite	Zircon	Monazite	Total	Macroporosity (%)	Grain Density (g/cm³)	Bulk Density (g/cm³)
A	2.53	0.000	0.0224	0.0221	0.0053	0.4209	0.0284	0.0013	0.4130	0.0535	0.0047	100	3.33	2.72	2.66

ICP/ICP-MS

SiO2	Al2O3	Fe2O3	MgO	CaO	Na2O	K2O	TiO2	P2O5	MnO	Cr2O3	Ba	Ni	Sc	LOI	Sum
54.68	8.71	3.02	3.51	10.76	1.38	3.32	0.59	0.22	0.05	0.007	285	<20	8	13.6	99.85

- data is in [%wt]

Be	Co	Cs	Ga	Hf	Nb	Rb	Sn	Sr	Ta	Th	U	V	W	Zr	Y	La	Ce	Pr	Nd	Sm	Eu	Gd	Tb	Dy	Ho	Er	Tm	Yb	Lu	TOT/C	TOT/S
3	9.2	2.8	8.9	8.5	10.1	68.8	2	110.7	0.7	8.1	5	69	1.5	317.5	24	28.3	51.2	6.06	22.7	4.49	0.9	4.16	0.68	4.19	0.88	2.56	0.37	2.52	0.41	4.41	1.04

data is in [ppm]

MICP -

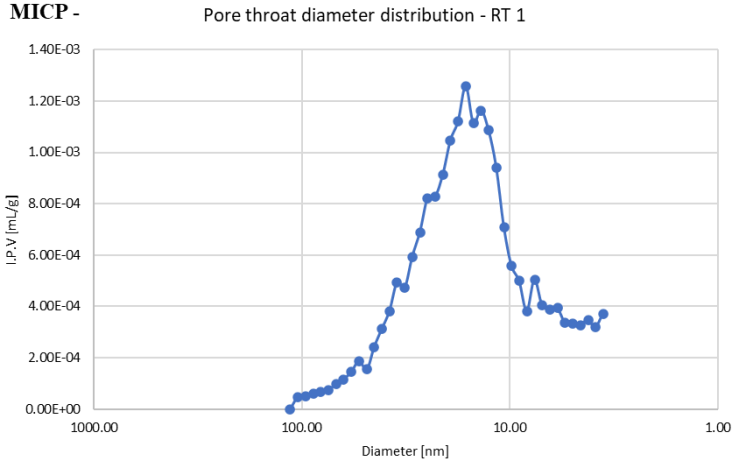

BET -

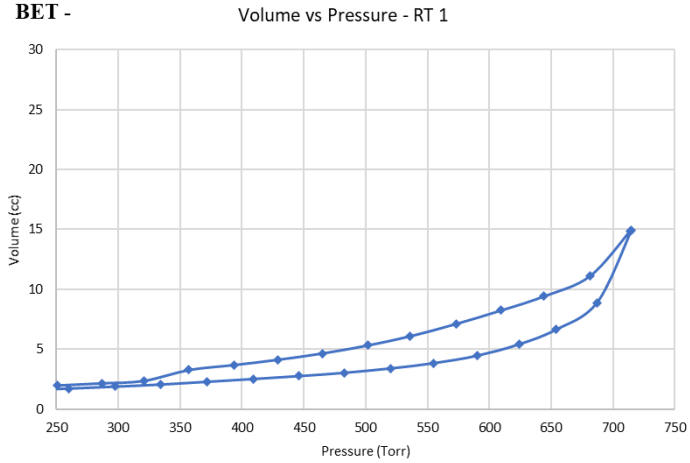

RT 2E – WA32485
Depth: 2124.46 (m)

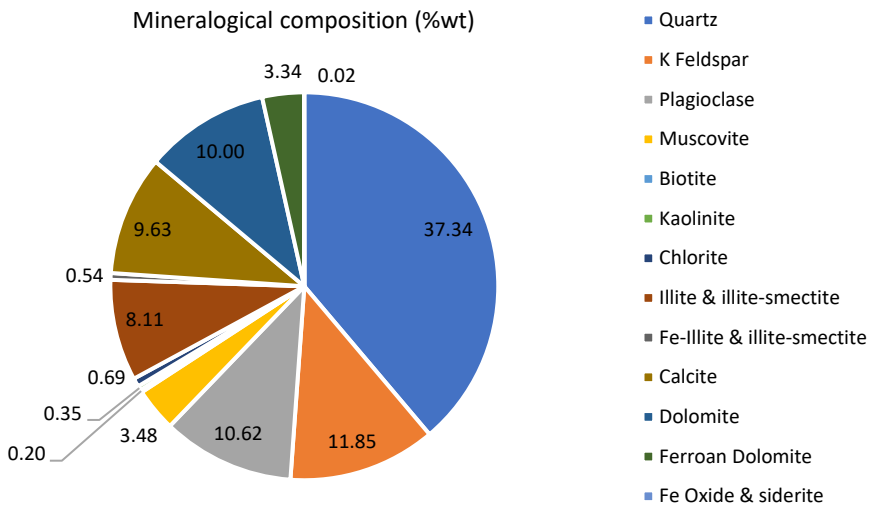

Block Code	Pyrite	Sphalerite	Barite	Anhydrite	Halite	Rutile & Ti Silicates	Tourmaline	Chromite	Apatite	Zircon	Monazite	Total	Macroporosity (%)	Grain Density (g/cm³)	Bulk Density (g/cm³)
A	2.79	0	0.06	0.02	6.53E-04	0.49	0.05	0	0.35	0.06	0.013	100.00	5.47	2.71	2.62

RT 2D – WA32485
Depth: 2179.47 (m)

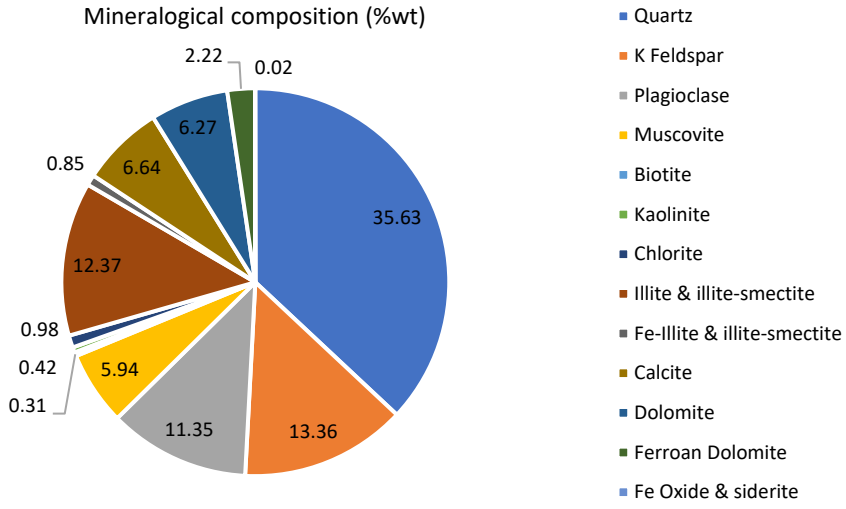

Block Code	Pyrite	Sphalerite	Barite	Anhydrite	Halite	Rutile & Ti Silicates	Tourmaline	Chromite	Apatite	Zircon	Monazite	Total	Macroporosity (%)	Grain Density (g/cm³)	Bulk Density (g/cm³)
A	2.6	0	0.056	0.0582	7.29126E-05	0.510	0.032	6.44E-04	0.33	5.78E-02	6.7E-03	100	5.59	2.70	2.61

RT 3E – WA32485
Depth: 2196.39 (m)

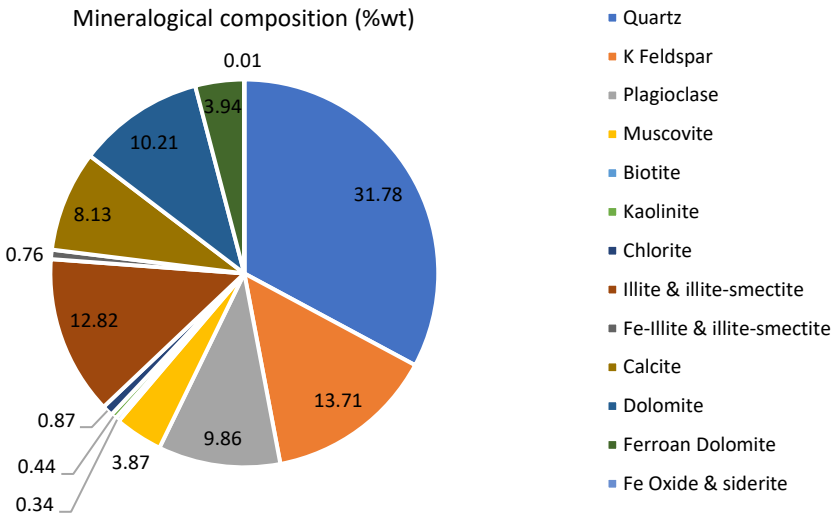

Block Code	Pyrite	Sphalerite	Barite	Anhydrite	Halite	Rutile & Ti Silicates	Tourmaline	Chromite	Apatite	Zircon	Monazite	Total	Macroporosity (%)	Grain Density (g/cm³)	Bulk Density (g/cm³)
A	2.267	0	0.056	0.117	0	0.3789155	0.0175185	0.00262	0.368	0.05468	1E-03	100	1.6	2.7	2.7

RT 4C – WA32485
Depth: 2200.2 (m)

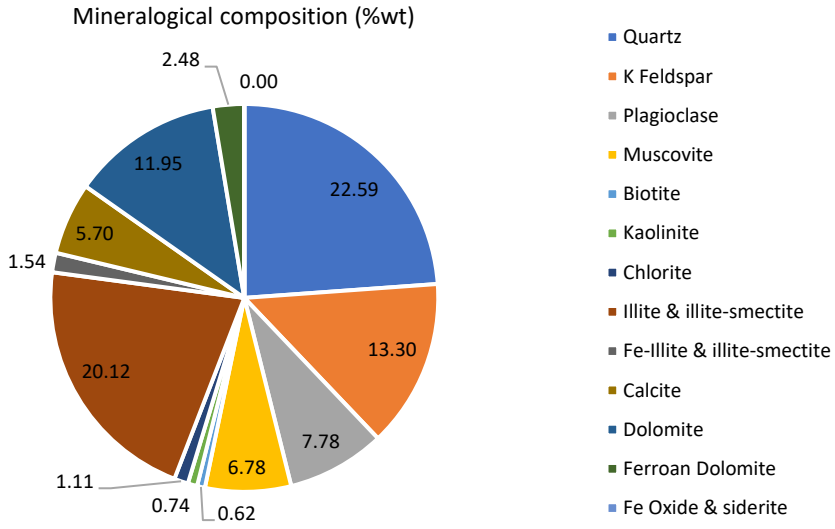

Block Code	Pyrite	Sphalerite	Barite	Anhydrite	Halite	Rutile & Ti Silicates	Tourmaline	Chromite	Apatite	Zircon	Monazite	Total	Macroporosity (%)	Grain Density (g/cm³)	Bulk Density (g/cm³)
A	4.083	0	0.08	0.15	0	0.31	0.02	0.0011	0.6	0.02	0.002126	100	1.18	2.73	2.71

RT 2 – WA32485
Depth: 2096.37 (m)

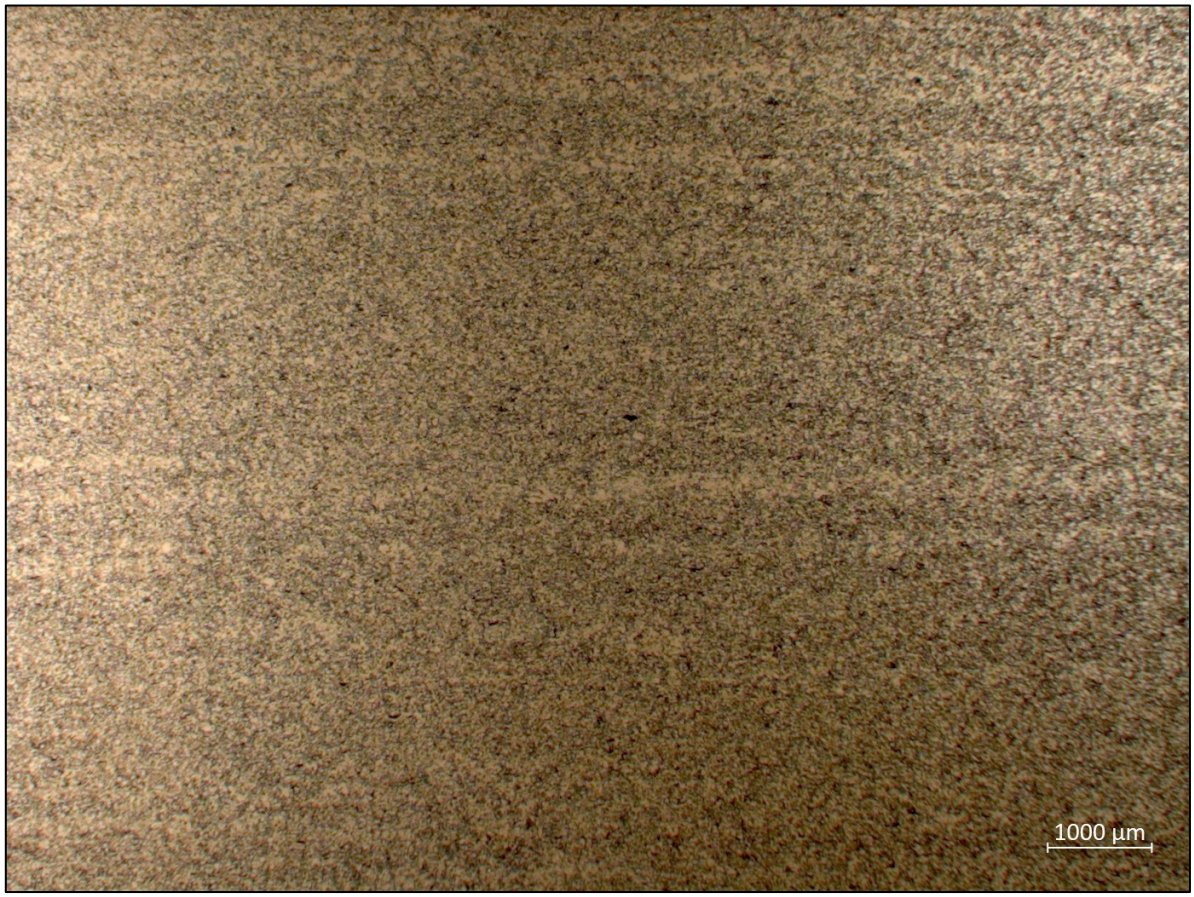

Thin section description:

Very faintly laminated, argillaceous, dolomitic, calcareous siltstone. At higher magnification, the sample appears massive. The dominant framework grains include quartz with minor plagioclase, K-feldspar, and micas. Pore spaces is occluded by matrix clays and cements (dolomite/Fe-dolomite with minor calcite, and quartz overgrowths)

%TOC: 0.46 (%wt)

Porosity: 6.7 (%)

Permeability: 3.503x10^{-4} (md)

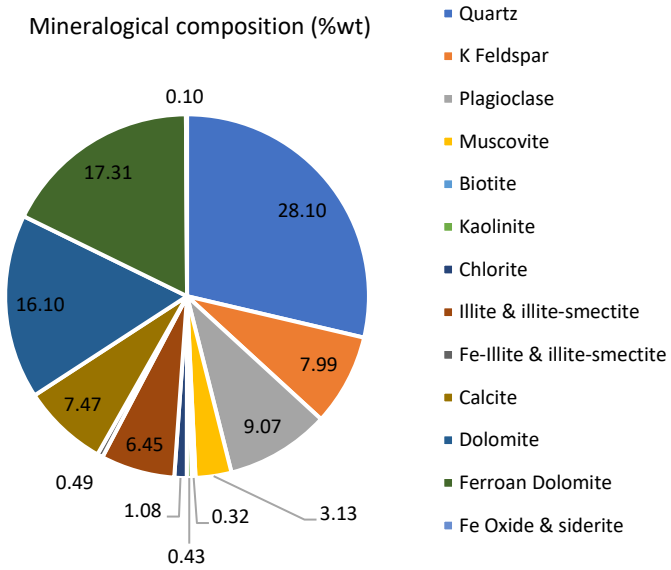

Additional images – RT 2

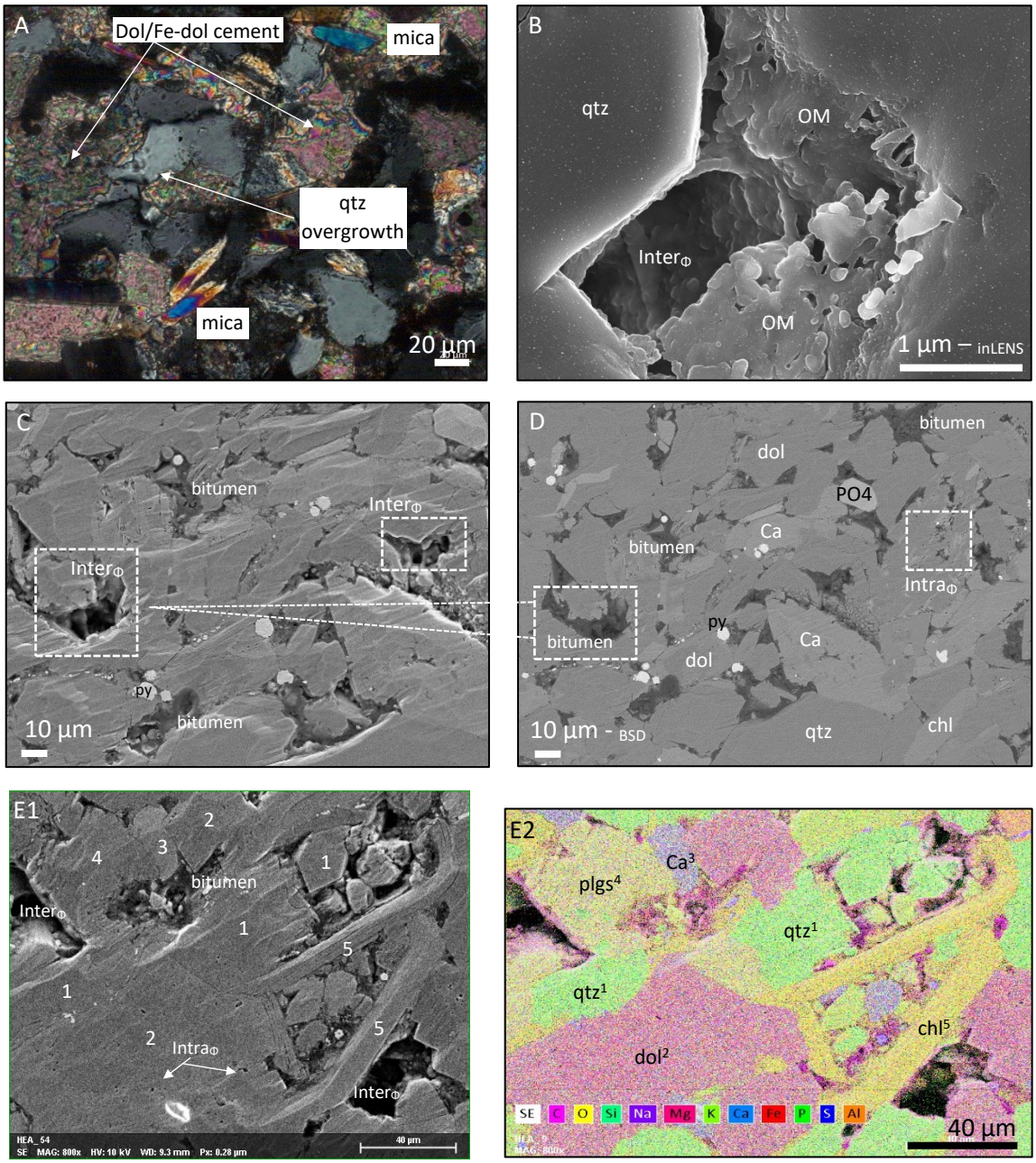

Mineralogical composition – data is in (%wt) – QEMSCAN analysis

Block Code	Pyrite	Sphalerite	Barite	Anhydrite	Halite	Rutile & Ti Silicates	Tourmaline	Chromite	Apatite	Zircon	Monazite	Total	Macroporosity (%)	Grain Density (g/cm³)	Bulk Density (g/cm³)
A	1.109	0.00248	0.025	0.01671	0.0006	0.3476359	0.04030355	0.004482	0.3326	0.057	0.009959	100	3.517238482	2.7576	2.6958

Complementary data – RT 2

ICP/ICP-MS

SiO2	Al2O3	Fe2O3	MgO	CaO	Na2O	K2O	TiO2	P2O5	MnO	Cr2O3	Ba	Ni	Sc	LOI	Sum
43.76	6.17	3.7	6.31	15.63	1.18	2.21	0.45	0.13	0.11	0.004	242	24	6	20.1	99.78

- data is in (%wt)

Be	Co	Cs	Ga	Hf	Nb	Rb	Sn	Sr	Ta	Th	U	V	W	Zr	Y	La	Ce	Pr	Nd	Sm	Eu	Gd	Tb	Dy	Ho	Er	Tm	Yb	Lu	TOT/C	TOT/S
2	4.7	1.4	5.8	6.5	7.7	44.9	1	107.7	0.6	6	4.2	226	0.8	247.9	27.5	23.8	46.4	5.93	23.8	5.08	1.15	4.93	0.74	4.78	0.94	2.93	0.4	2.36	0.38	5.83	0.41

data is in (ppm)

MICP

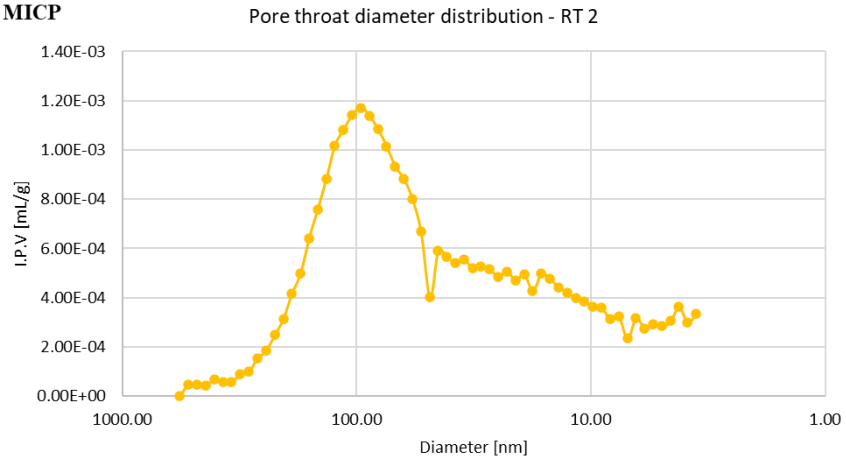

BET

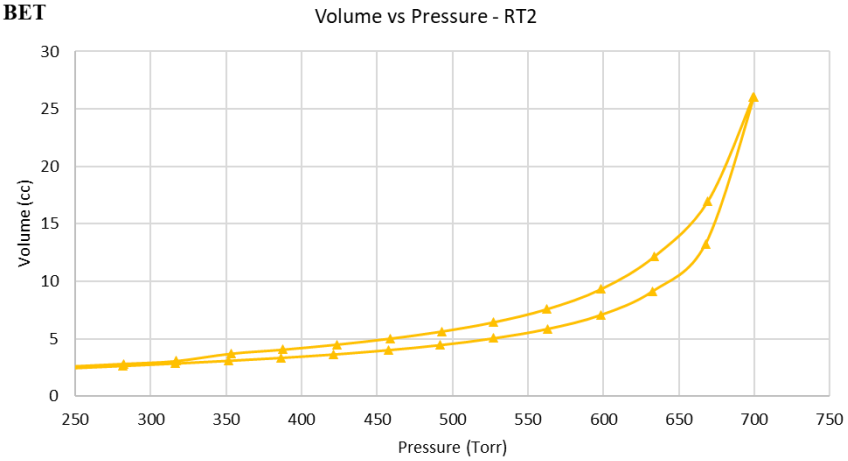

RT 1A – WA32485
Depth: 2106.47 (m)

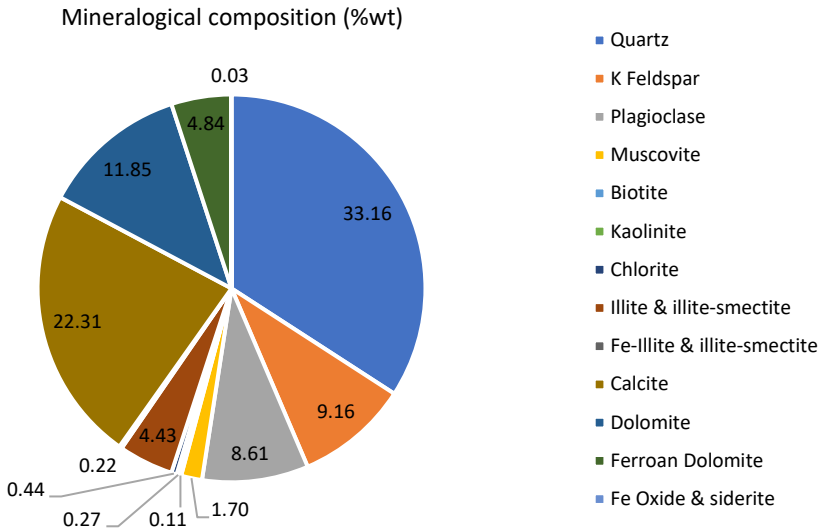

Block Code	Pyrite	Sphalerite	Barite	Anhydrite	Halite	Rutile & Ti Silicates	Tourmaline	Chromite	Apatite	Zircon	Monazite	Total	Macroporosity (%)	Grain Density (g/cm³)	Bulk Density (g/cm³)
A	1.753	0	0.05	0.093677	6E-04	0.2928088	0.0265182	0.002513	0.5784	0.07	0.000506	100	3.68	2.72	2.65

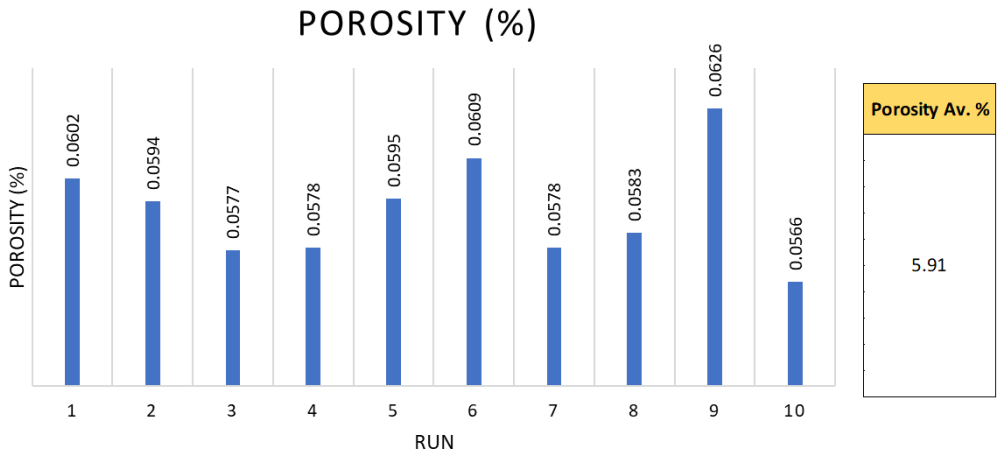

RT 2A – WA32485
Depth: 2109.18 (m)

Thin section description:

Very faintly laminated to massive appearing dolomitic siltstone. At amplified magnification images are more massive due to possible bioturbation observed. Most of the pore space is occluded with dolomite/Fe-dolomite and less calcite cements, and minor matrix clays. Detrital framework grains include quartz with minor plagioclase, K-feldspar, and micas.

%TOC: 0.65 (%wt)

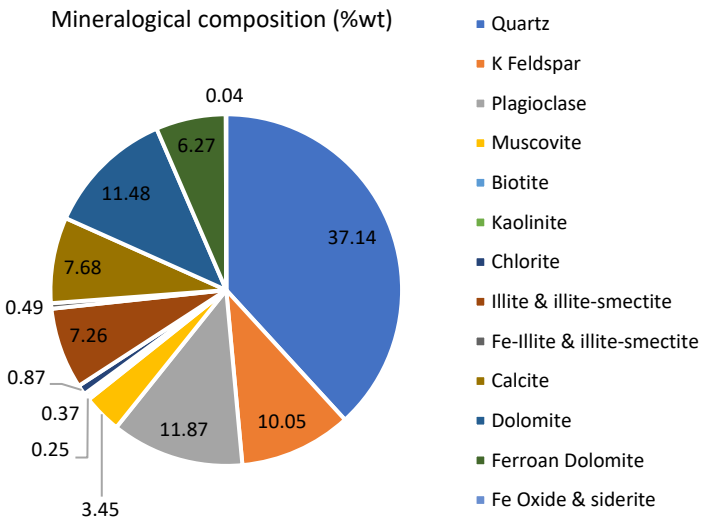

Additional images – RT 2A

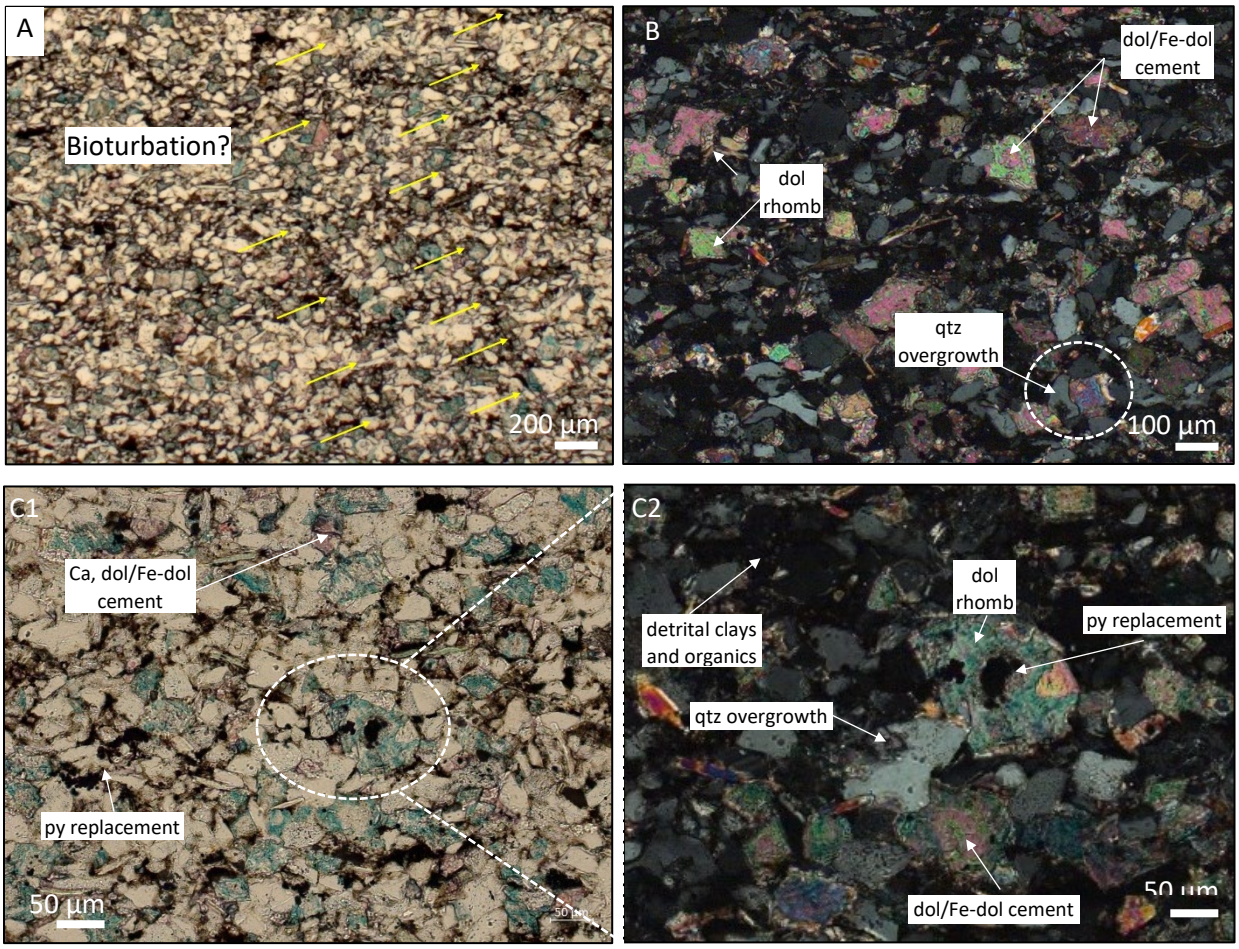

EDS images – RT 2A

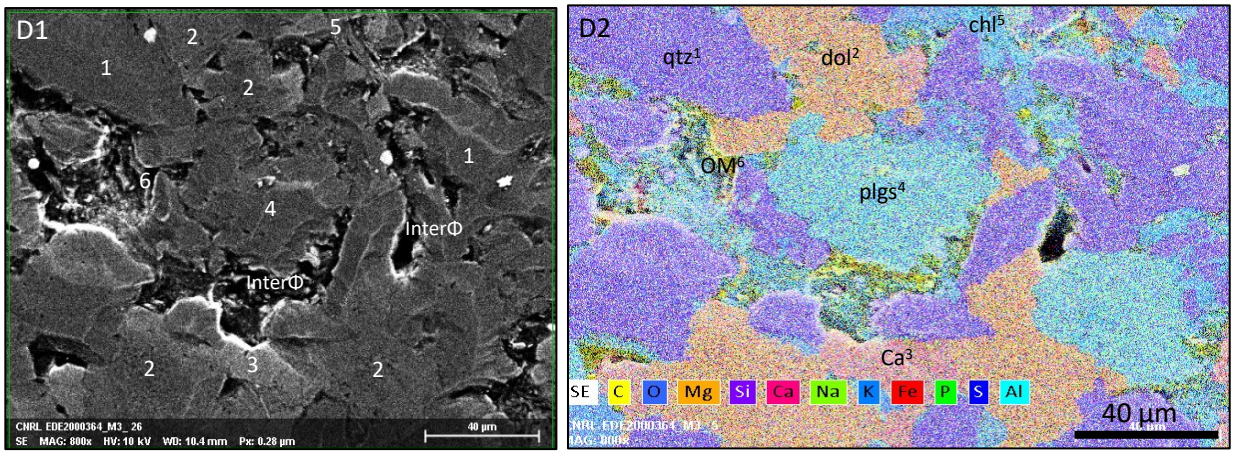

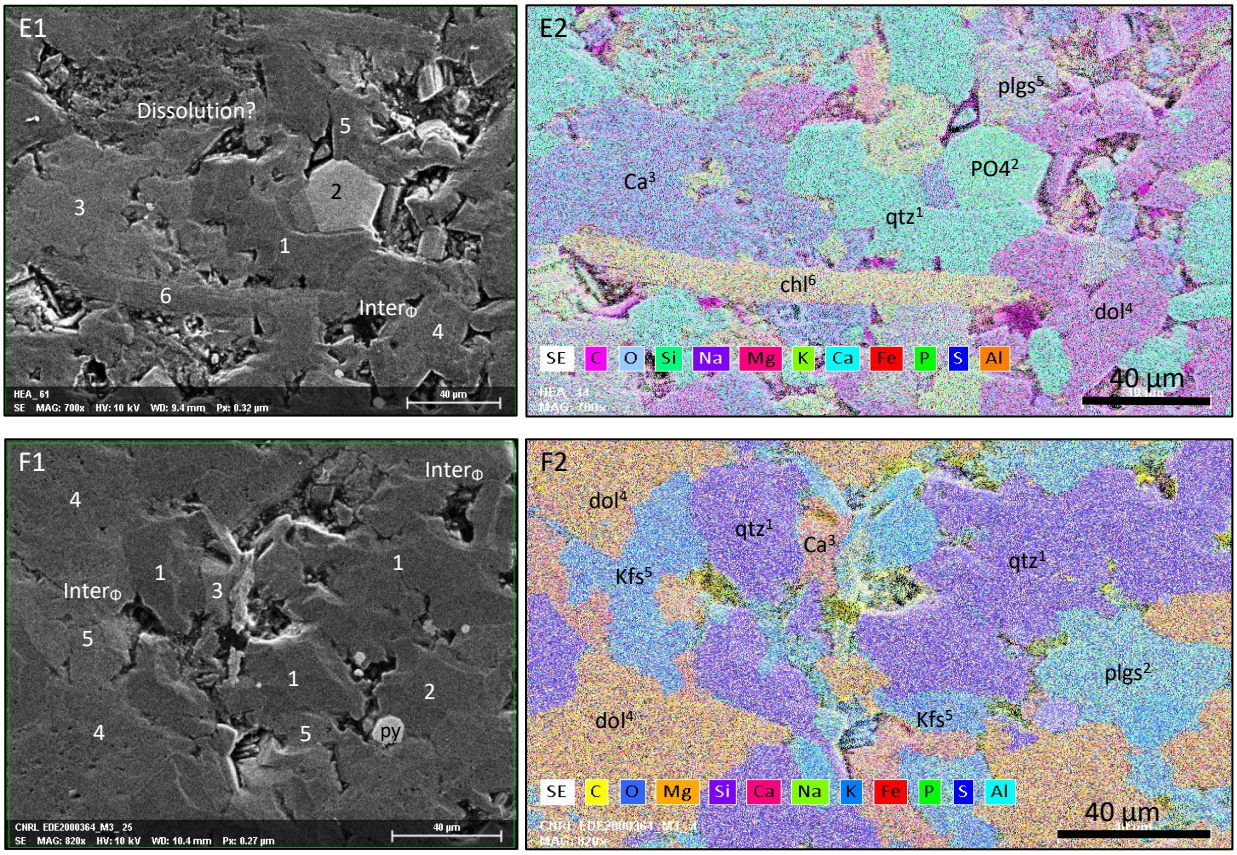

Mineralogical composition – data is in (%wt) – QEMSCAN analysis

Block Code	Pyrite	Sphalerite	Barite	Anhydrite	Halite	Rutile & Ti Silicates	Tourmaline	Chromite	Apatite	Zircon	Monazite	Total	Macroporosity (%)	Grain Density (g/cm³)	Bulk Density (g/cm³)
A	1.664	0	0.052	0.012697	1E-04	0.5062208	0.0321909	0.002845	0.4175	0.078	0.006282	100	4.21	2.72	2.64

ICP/ICP-MS

SiO2	Al2O3	Fe2O3	MgO	CaO	Na2O	K2O	TiO2	P2O5	MnO	Cr2O3	Ba	Ni	Sc	LOI	Sum
57.26	8.23	2.83	3.5	9.93	1.62	2.89	0.63	0.23	0.08	0.007	289	36	8	12.5	99.78

- data is in (%wt)

Be	Co	Cs	Ga	Hf	Nb	Rb	Sn	Sr	Ta	Th	U	V	W	Zr	Y	La	Ce	Pr	Nd	Sm	Eu	Gd	Tb	Dy	Ho	Er	Tm	Yb	Lu	TOT/C	TOT/S
1	7	2.1	7.8	10.3	10.6	60.3	1	104.7	0.7	8.5	6.8	305	1.3	382.2	29.3	32.5	57.3	7.25	28.1	5.41	1.12	5.39	0.82	4.94	1.02	3.09	0.45	2.83	0.44	3.83	0.72

└ data is in (ppm)

Pore throat diameter distribution - RT 2

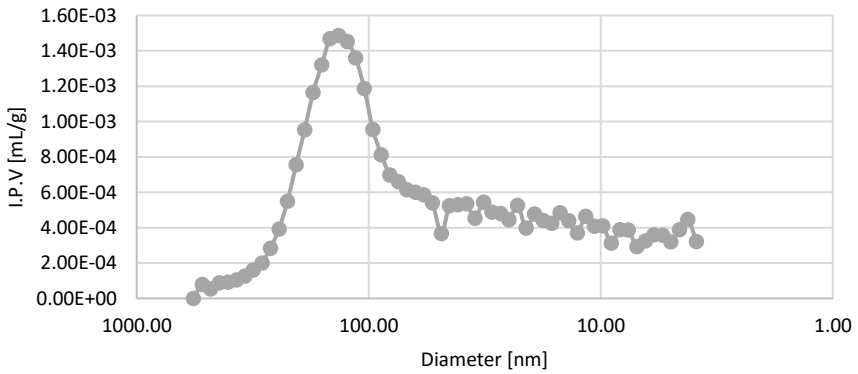

RT 3 – WA32485
Depth: 2136.24 (m)

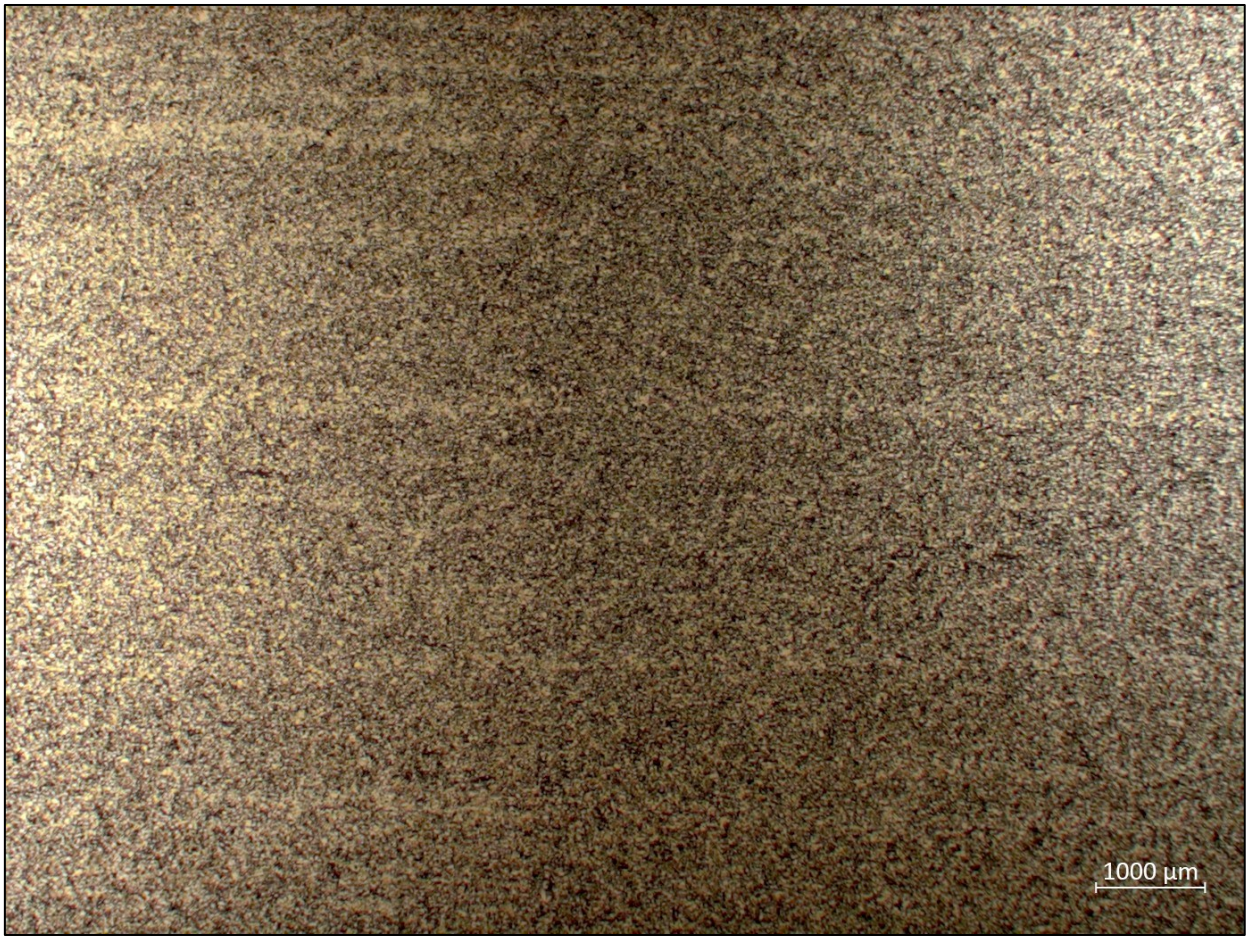

Thin section description:

Very faintly laminated to massive appearing dolomitic siltstone. Most of the pore space is occluded with matrix clay and organic matter and in less amount dolomite/Fe-dolomite and less calcite cements. Detrital framework grains include quartz with minor plagioclase, K-feldspar, and micas. Framboidal pyrite and pyrite substitution were consistent for this sample.

%TOC: 1.3 (%wt)

Porosity: 1.9 (%)

Permeability: 1.27x10^{-3} (md)

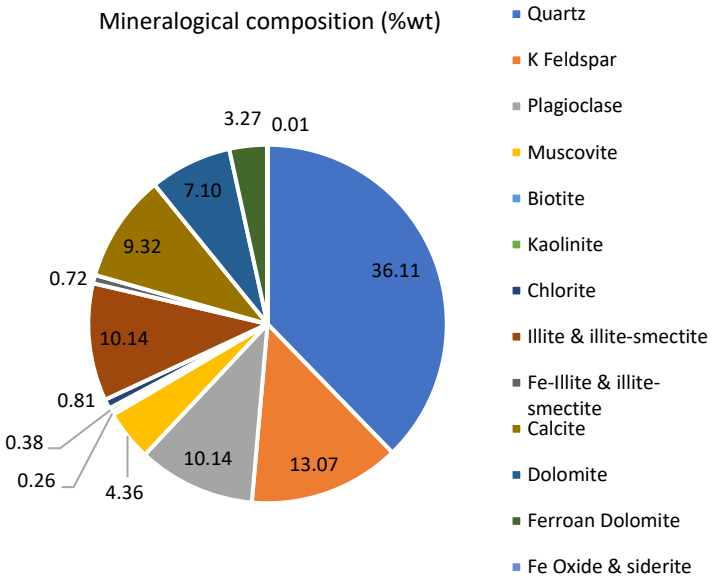

Additional images -RT 3

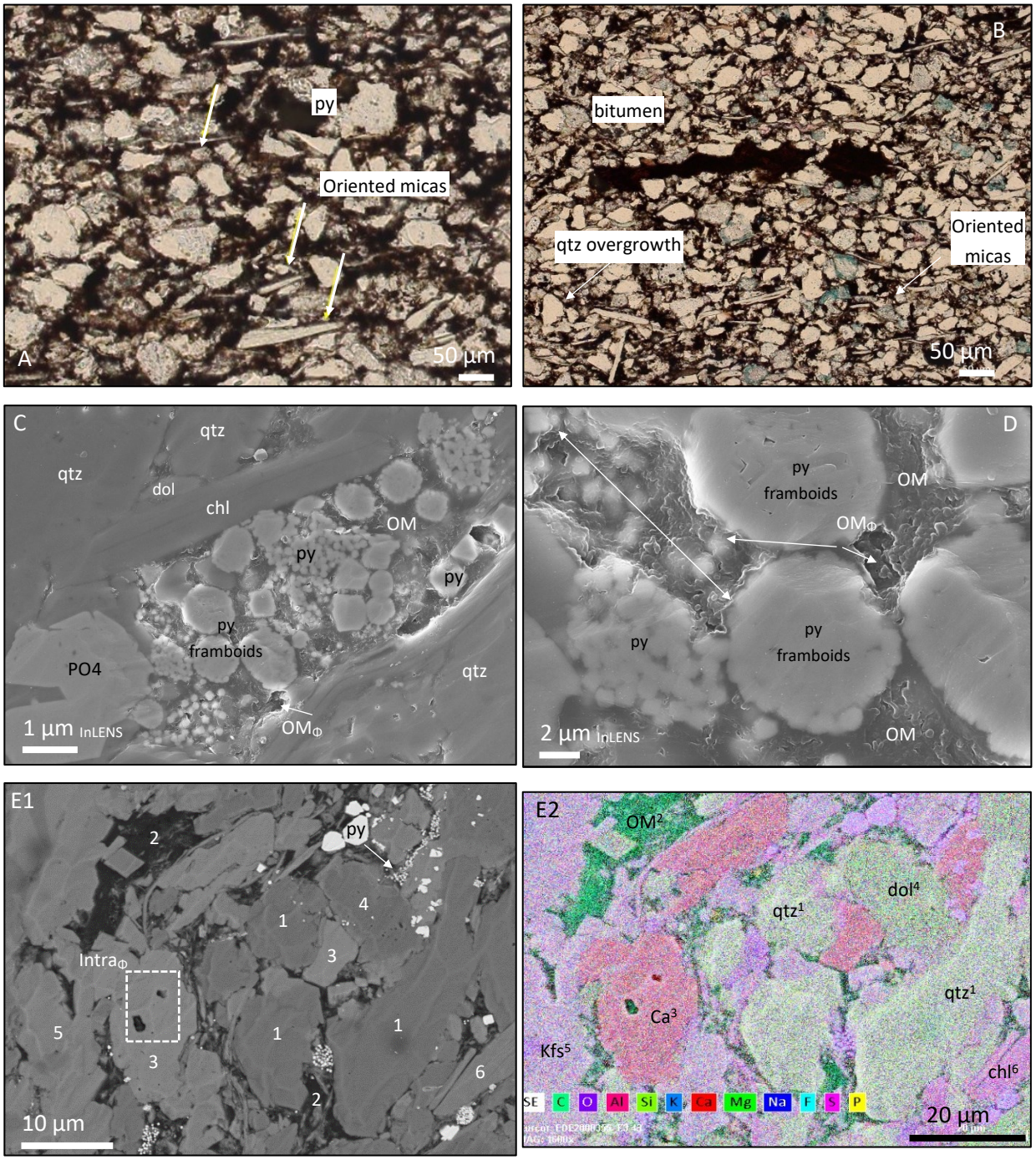

Mineralogical composition – data is in (%wt) – QEMSCAN analysis

Block Code	Pyrite	Sphalerite	Barite	Anhydrite	Halite	Rutile & Ti Silicates	Tourmaline	Chromite	Apatite	Zircon	Monazite	Total	Macroporosity (%)	Grain Density (g/cm³)	Bulk Density (g/cm³)
A	2.684	0.218179	0.0906	0.240447	0.0232	0.5049552	0.045959	0.002374	0.4557	0.0495	0.00425	100	4.12	2.71	2.64

Complementary data – RT 3

ICP/ICP-MS

SiO2	Al2O3	Fe2O3	MgO	CaO	Na2O	K2O	TiO2	P2O5	MnO	Cr2O3	Ba	Ni	Sc	LOI	Sum
58.5	9.33	3.28	2.15	8	1.32	3.7	0.66	0.2	0.05	0.009	310	35	9	12.6	99.83

- data is in (%wt)

Be	Co	Cs	Ga	Hf	Nb	Rb	Sn	Sr	Ta	Th	U	V	W	Zr	Y	La	Ce	Pr	Nd	Sm	Eu	Gd	Tb	Dy	Ho	Er	Tm	Yb	Lu	TOT/C	TOT/S
<1	12.2	2.8	9.5	8.9	11.6	72.9	2	94.5	0.9	8.5	17.3	128	1.3	335.1	29.2	31.4	56.9	6.99	26.9	5.13	1.01	5.07	0.81	4.82	1.05	2.97	0.44	2.8	0.43	5.18	1.24

└ data is in (ppm)

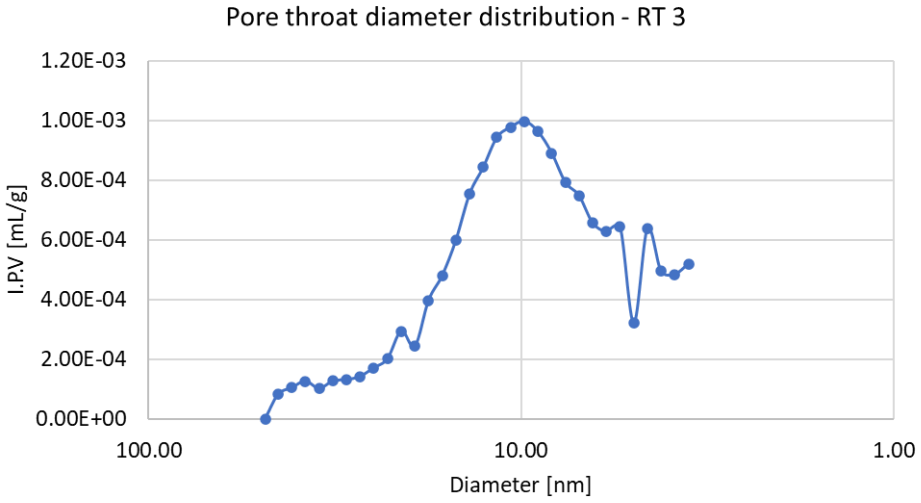

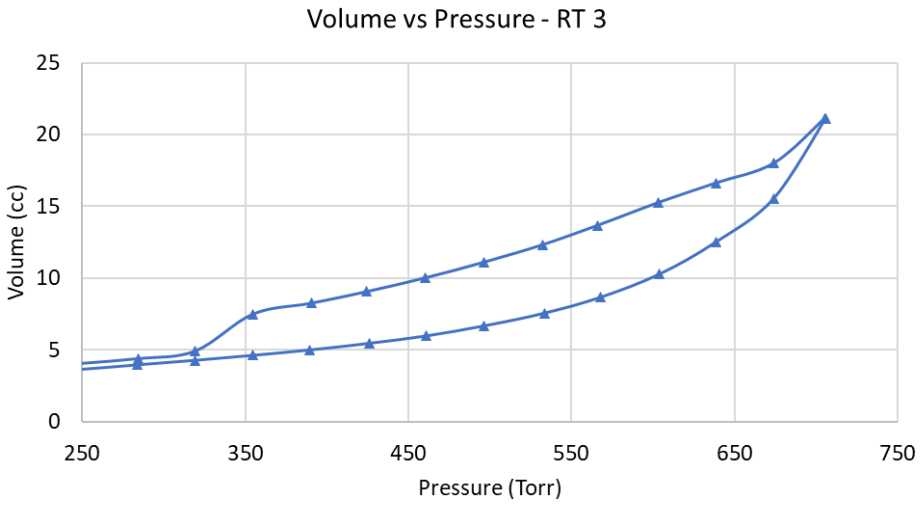

RT 3C – WA32485
Depth: 2151.13 (m)
% TOC: 3.6 (%wt)

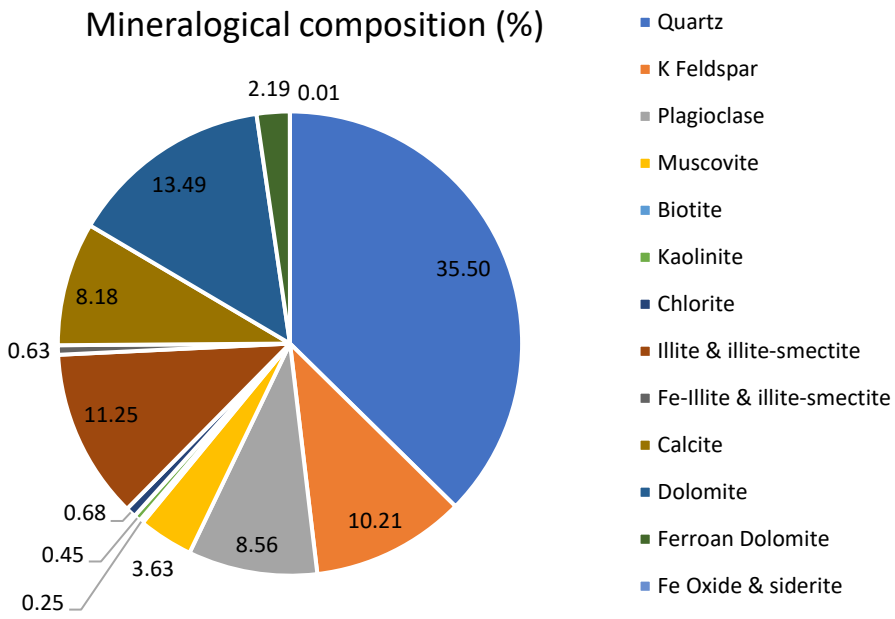

Mineralogical composition – data is in (%wt) – QEMSCASN analysis

Block Code	Pyrite	Sphalerite	Barite	Anhydrite	Halite	Rutile & Ti Silicates	Tourmaline	Chromite	Apatite	Zircon	Monazite	Total	Macroporosity (%)	Grain Density (g/cm³)	Bulk Density (g/cm³)
A	2.976	0.590793	0.0255	0.062972	0.0013	0.4355618	0.0567157	0.006309	0.7898	0.0612	0.001605	100	9.019	2.728	2.572

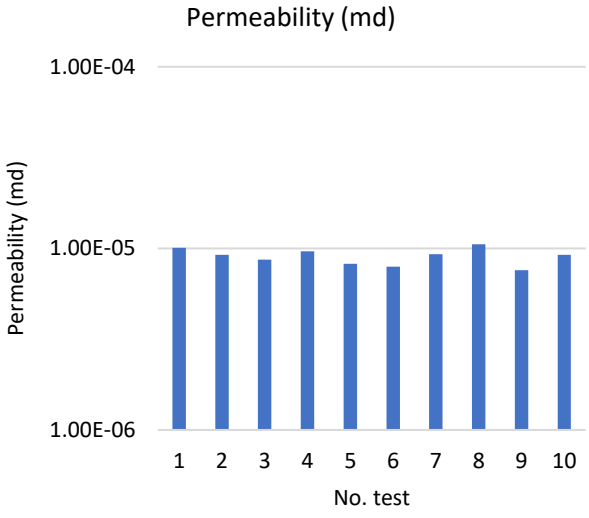

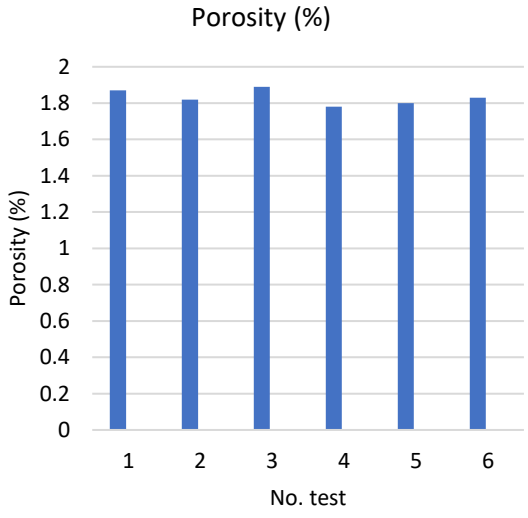

RT 3A – WA32485
Depth: 2165.25 (m)

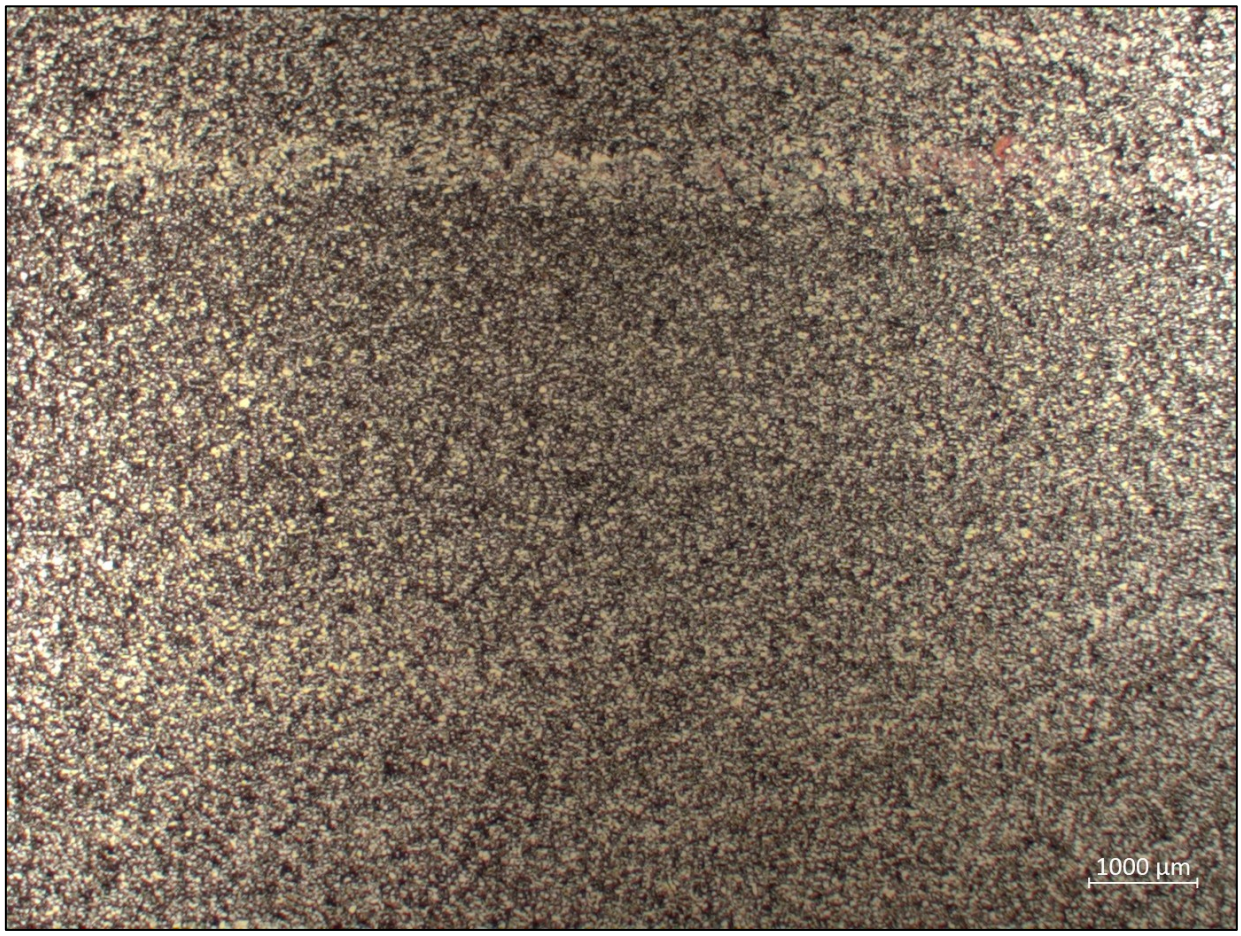

Thin section analysis:

Faintly laminated to massive appearing dolomitic siltstone. Most of the pore space is occluded with matrix clay and organic matter and in less amount dolomite/Fe-dolomite and less calcite cements. Detrital framework grains include quartz with minor plagioclase, K-feldspar, and micas.

%TOC: 2.7 (%wt)

Porosity: 1.6 (%)

Permeability: 8.55x10^{-5} (md)

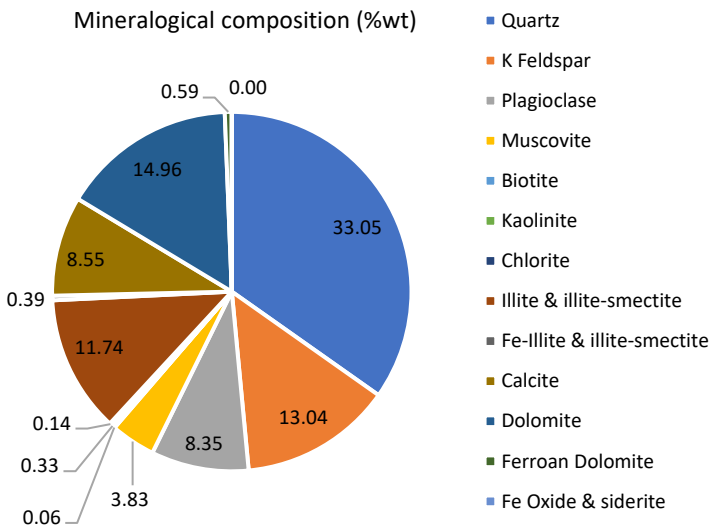

Additional images – R 3A

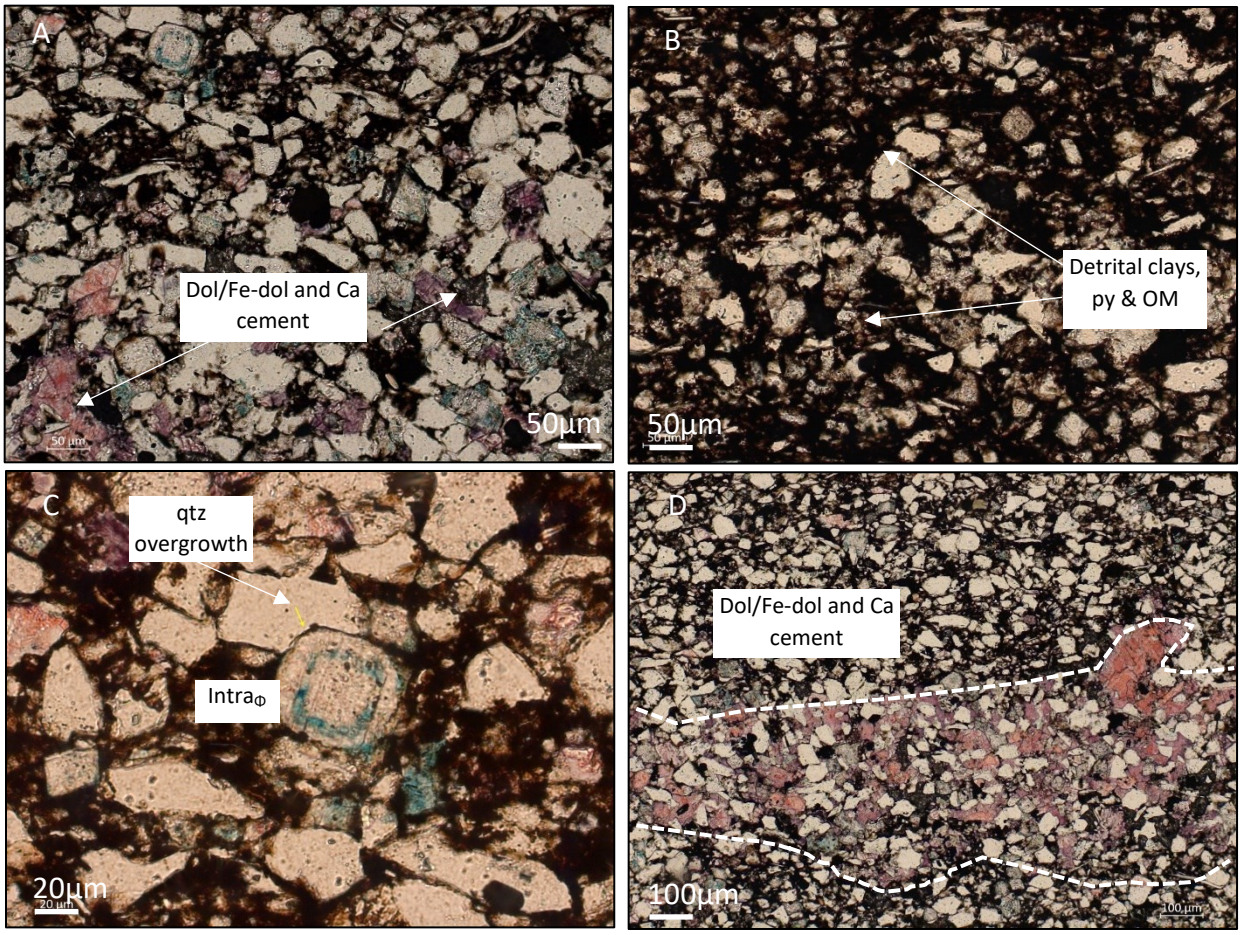

Mineralogical composition – data is in (%wt) – QEMSCAN analysis

Block Code	Pyrite	Sphalerite	Barite	Anhydrite	Halite	Rutile & Ti Silicates	Tourmaline	Chromite	Apatite	Zircon	Monazite	Total	Macroporosity (%)	Grain Density (g/cm³)	Bulk Density (g/cm³)
A	3.688	0.02282	0.0414	0.058403	0	0.432782	0.0351882	0	0.6563	0.0365	0.005736	100	3.82	2.72	2.66

ICP/ ICP-MS

SiO2	Al2O3	Fe2O3	MgO	CaO	Na2O	K2O	TiO2	P2O5	MnO	Cr2O3	Ba	Ni	Sc	LOI	Sum
56.88	8.6	3.03	2.72	8.67	1.11	3.74	0.58	0.3	0.06	0.008	290	37	8	14.1	99.82

- data is in (%wt)

Be	Co	Cs	Ga	Hf	Nb	Rb	Sn	Sr	Ta	Th	U	V	W	Zr	Y	La	Ce	Pr	Nd	Sm	Eu	Gd	Tb	Dy	Ho	Er	Tm	Yb	Lu	TOT/C	TOT/S
2	12.1	2.9	8	9.1	10.4	69.1	2	107.3	0.6	8.3	13.1	99	1.3	341.4	26.9	28.4	50.3	6.41	24.6	4.94	0.99	4.74	0.72	4.41	0.91	2.72	0.4	2.67	0.42	6.33	1.84

data is in (ppm)

Complementary data – RT 3A

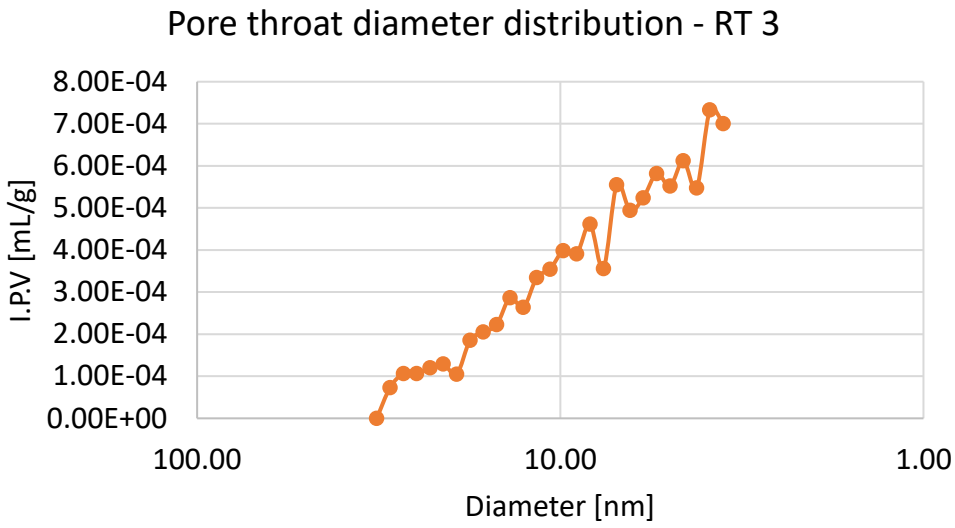

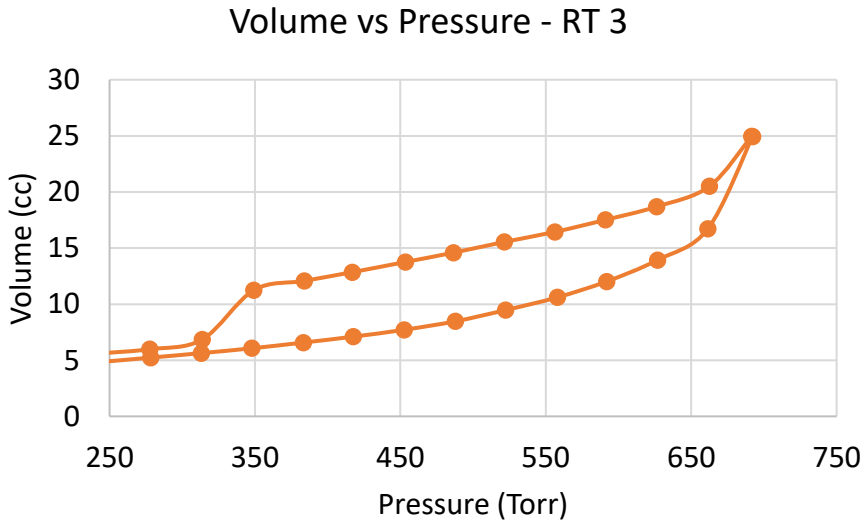

RT 3D – WA32485
Depth: 2168.19 (m)

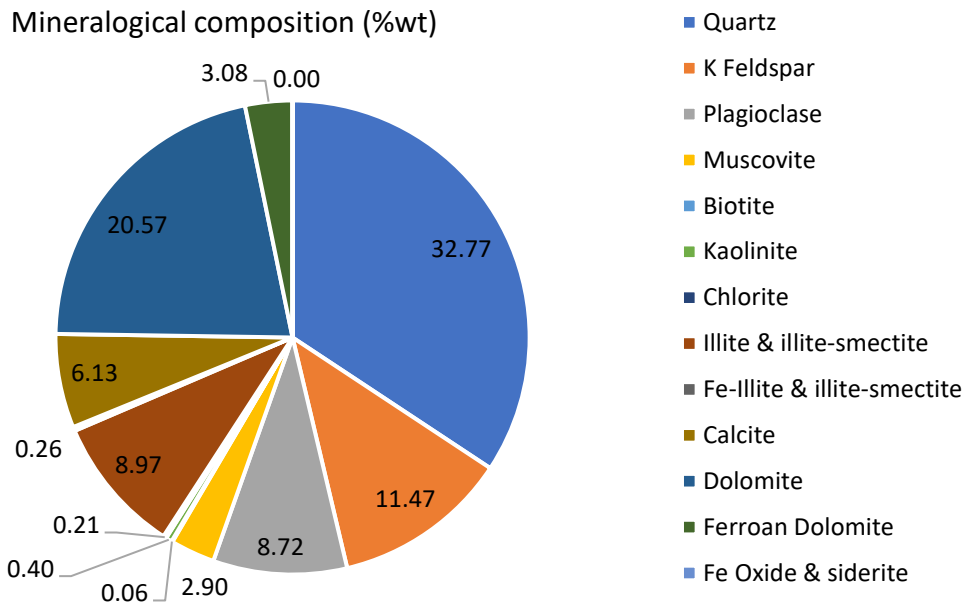

Mineralogical composition – data is in (%wt) – QEMSCAN analysis

Block Code	Pyrite	Sphalerite	Barite	Anhydrite	Halite	Rutile & Ti Silicates	Tourmaline	Chromite	Apatite	Zircon	Monazite	Total
A	2.787	0	0.0389	0.070543	0.0002	0.4133386	0.0325248	0.002243	1.0179	0.0901	0.003098	100

Macroporosity (%)	Grain Density (g/cm³)	Bulk Density (g/cm³)
6.01	2.73	2.63

RT 2B – WA32485
Depth: 2177.36 (m)

Thin section analysis:

Massive appearing slightly argillaceous dolomitic, calcareous siltstone. Minor bioturbation was observed in this sample. Detrital framework grains are sub rounded to sub angular and comprised of quartz with minor plagioclase, K-feldspar, and micas. Main cements include dolomite/Fe-dolomite and minor calcite. Some of the pore space is occluded by detrital matrix clays, organics and pyrite.

%TOC: 1.35 (%wt)

Porosity: 3.4 (%)

Permeability: 7.34 x10^{-5} (md)

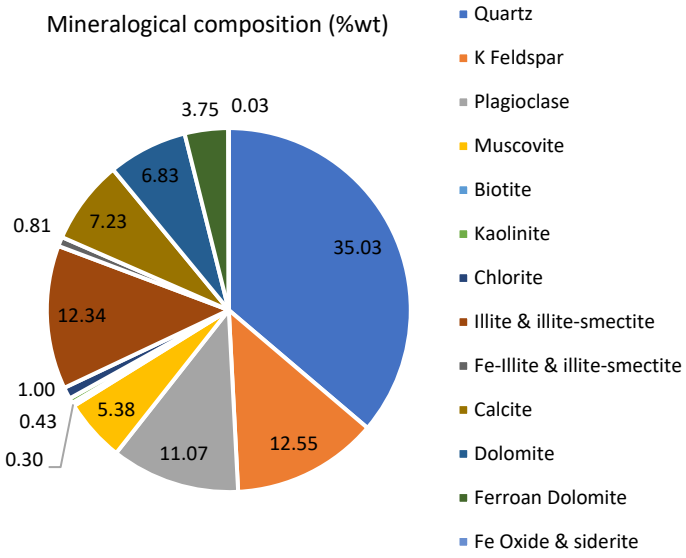

Additional images – RT 2B

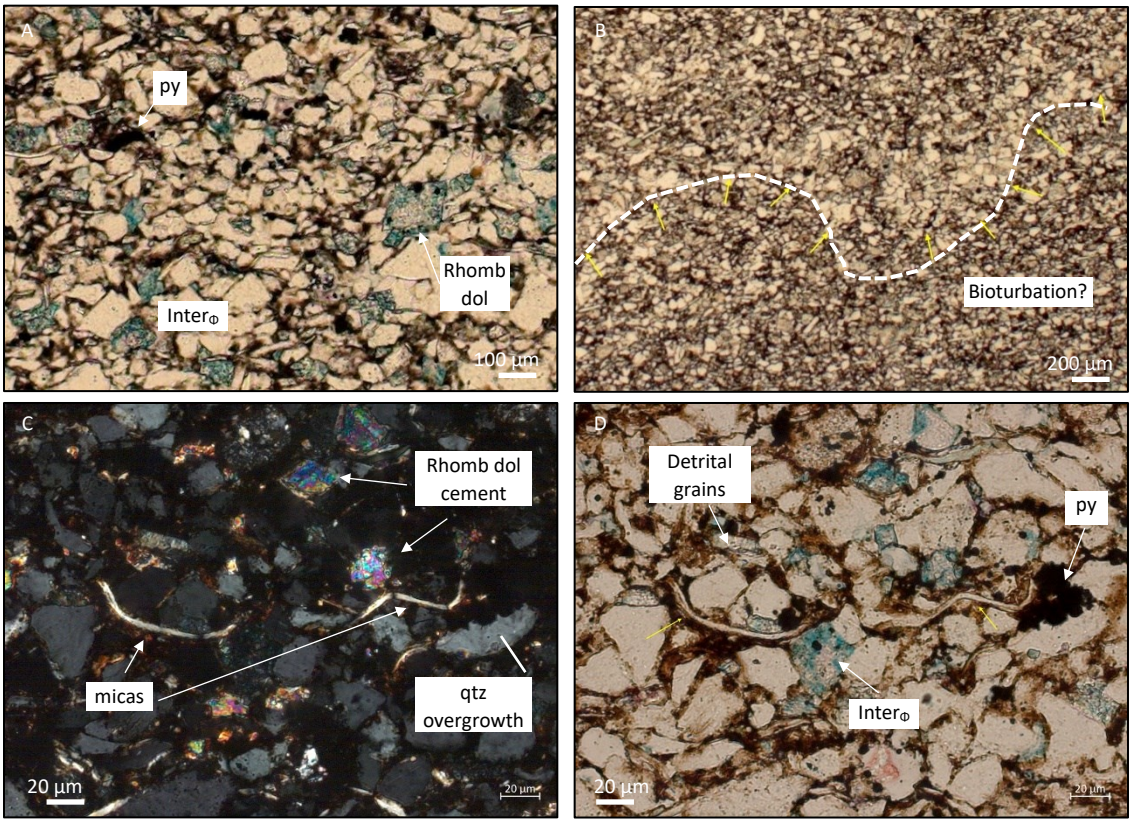

Mineralogical composition – data is in (%wt) – QEMSCAN analysis

Block Code	Pyrite	Sphalerite	Barite	Anhydrite	Halite	Rutile & Ti Silicates	Tourmaline	Chromite	Apatite	Zircon	Monazite	Total	Macroporosity (%)	Grain Density (g/cm³)	Bulk Density (g/cm³)
A	2.21	0.033245	0.07	0.029717	0	0.4744448	0.0437427	0.006223	0.3245	0.056	0.006851	100	2.33	2.71	2.67

ICP/ ICP-MS

SiO2	Al2O3	Fe2O3	MgO	CaO	Na2O	K2O	TiO2	P2O5	MnO	Cr2O3	Ba	Ni	Sc	LOI	Sum
60.82	9.44	2.71	1.97	8.06	1.39	3.72	0.67	0.88	0.05	0.01	322	47	9	10.1	99.82

- data is in (%wt)

Be	Co	Cs	Ga	Hf	Nb	Rb	Sn	Sr	Ta	Th	U	V	W	Zr	Y	La	Ce	Pr	Nd	Sm	Eu	Gd	Tb	Dy	Ho	Er	Tm	Yb	Lu	TOT/C	TOT/S
3	8.9	2.7	7.6	8.4	12.2	72.6	2	105.6	0.9	9.2	4.4	154	1.3	327.5	47.5	43.5	80.6	11.3	45.5	9.3	1.96	9.2	1.37	7.71	1.5	4.14	0.53	3.35	0.49	3.82	0.83

data is in (ppm)

MICP

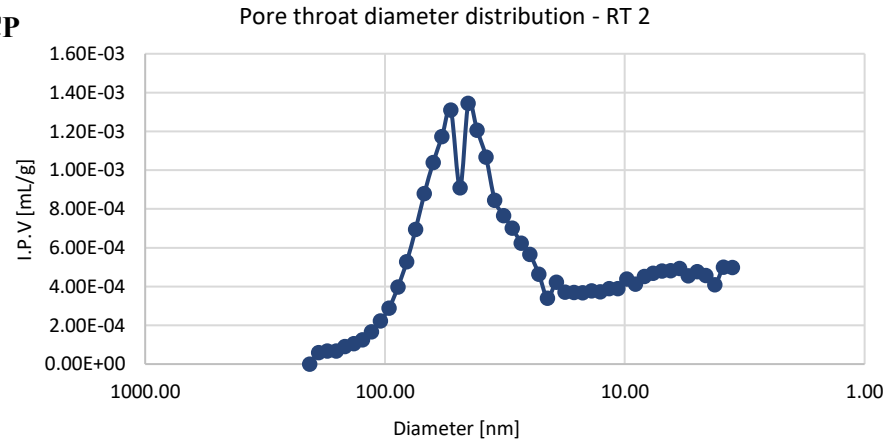

RT 3B – WA32485
Depth: 2186.01 (m)

Thin section analysis:

Massive appearing, argillaceous dolomitic, calcareous siltstone. The main framework grain is comprised of quartz, with minor K-feldspar, plagioclase, and micas. The main cements present were dolomite/Fe-dolomite and in less amount calcite. Pyrite cement, detrital clays, and organics are noted occluding most of the pore space.

%TOC: 3.7 (%wt)

Porosity: 1.7 (%)

Permeability: 8.2 x10^{-5} (md)

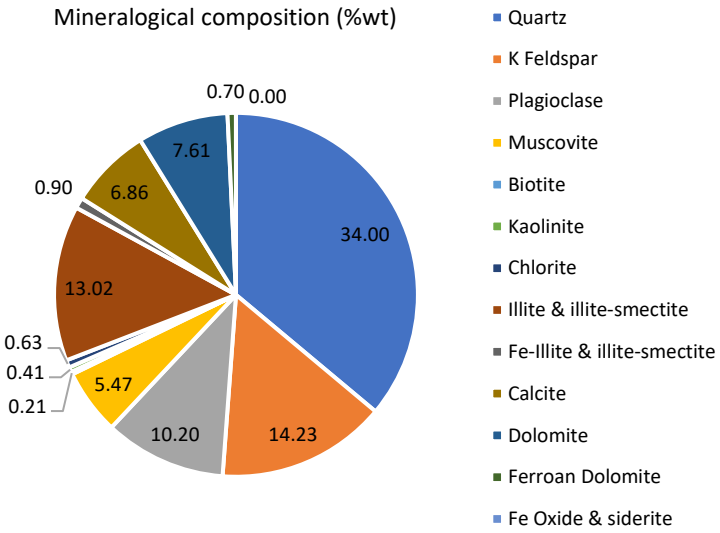

Additional images – RT 3B

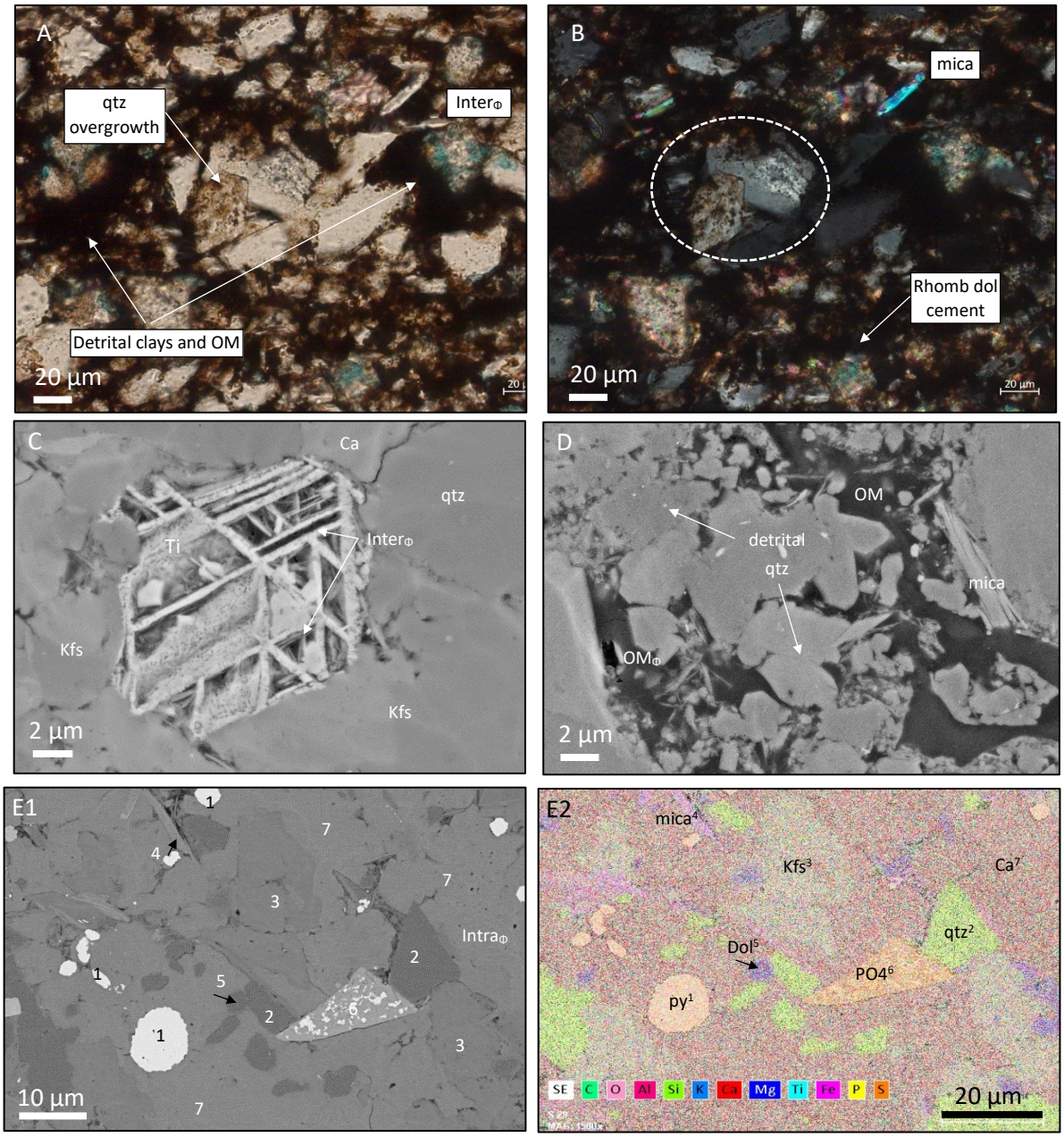

Mineralogical composition - data is in (%wt) – QEMSCAN analysis.

Block Code	Pyrite	Sphalerite	Barite	Anhydrite	Halite	Rutile & Ti Silicates	Tourmaline	Chromite	Apatite	Zircon	Monazite	Total	Macroporosity (%)	Grain Density (g/cm³)	Bulk Density (g/cm³)
A	4.052	0	0.0759	0.198297	7.25224E-05	0.418959	0.0352669	0.00016	0.9052	0.0646	0.00654	100	5.45	2.71	2.62

ICP/ ICP-MS

SiO2	Al2O3	Fe2O3	MgO	CaO	Na2O	K2O	TiO2	P2O5	MnO	Cr2O3	Ba	Ni	Sc	LOI	Sum
55.71	8.79	5.35	2.18	7.95	1.2	3.65	0.59	0.78	0.07	0.008	372	58	9	13.5	99.83

- data is in (%wt)

Be	Co	Cs	Ga	Hf	Nb	Rb	Sn	Sr	Ta	Th	U	V	W	Zr	Y	La	Ce	Pr	Nd	Sm	Eu	Gd	Tb	Dy	Ho	Er	Tm	Yb	Lu	TOT/C	TOT/S
<1	11.2	3	7.1	9.3	10.7	70.3	2	120.5	0.7	8.8	18.7	129	1.5	348.3	44.5	40.1	80.5	11.29	45.9	9.3	1.83	8.62	1.3	7.28	1.41	3.82	0.51	3.17	0.5	5.57	3.39

data is in (ppm)

RT 1B – WA32485
Depth 2189.56 (m)

Thin section analysis:

Very faintly to faintly laminated slightly argillaceous dolomitic, calcareous siltstone. Most of the pore space is occluded with matrix clay and organic matter and in less amount dolomite/Fe-dolomite and less calcite cements. Detrital framework grains include quartz, K-feldspar with minor plagioclase, and micas. In this sample at amplified scale some of the pore space is occluded by micritic mud.

%TOC: 1.07 (%wt)

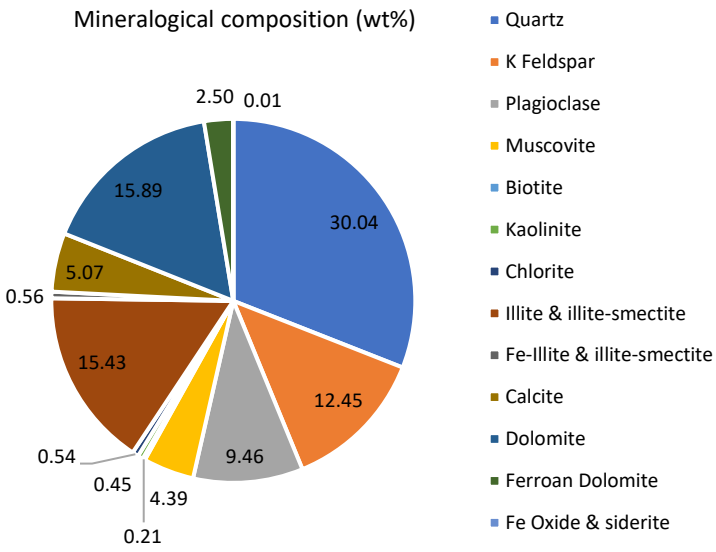

Additional images – RT 1B

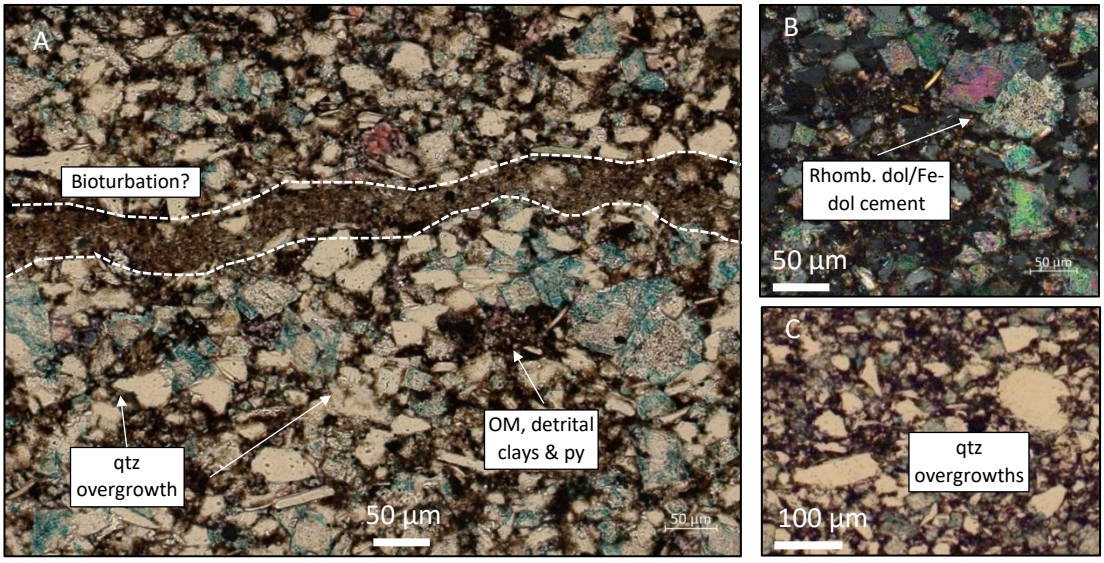

Mineralogical composition – data is in (%wt) – QEMSCAN analysis

Block Code	Pyrite	Sphalerite	Barite	Anhydrite	Halite	Rutile & Ti Silicates	Tourmaline	Chromite	Apatite	Zircon	Monazite	Total
A	2.076	0.000776	0.0455	0.03501	0	0.382327	0.0295745	0.003828	0.3713	0.0522	0.003947	100

Macroporosity (%)	Grain Density (g/cm³)	Bulk Density (g/cm³)
1.06	2.71	2.70

ICP/ICP-MS

SiO2	Al2O3	Fe2O3	MgO	CaO	Na2O	K2O	TiO2	P2O5	MnO	Cr2O3	Ba	Ni	Sc	LOI	Sum
53.68	9.2	3.27	3.92	9.65	1.19	3.66	0.62	0.23	0.2	0.008	309	25	8	14.2	99.83

- data is in (%wt)

Be	Co	Cs	Ga	Hf	Nb	Rb	Sn	Sr	Ta	Th	U	V	W	Zr	Y	La	Ce	Pr	Nd	Sm	Eu	Gd	Tb	Dy	Ho	Er	Tm	Yb	Lu	TOT/C	TOT/S
2	10.4	3.2	9.4	8.7	11.5	78	2	114.7	0.8	8.7	4.2	75	1.4	321.3	25.2	31.7	59	6.83	26.1	5.24	1.02	4.76	0.73	4.59	0.9	2.86	0.4	2.74	0.42	4.62	1.1

└ data is in (ppm)

RT 4 – WA32485
Depth: 2206.28 (m)

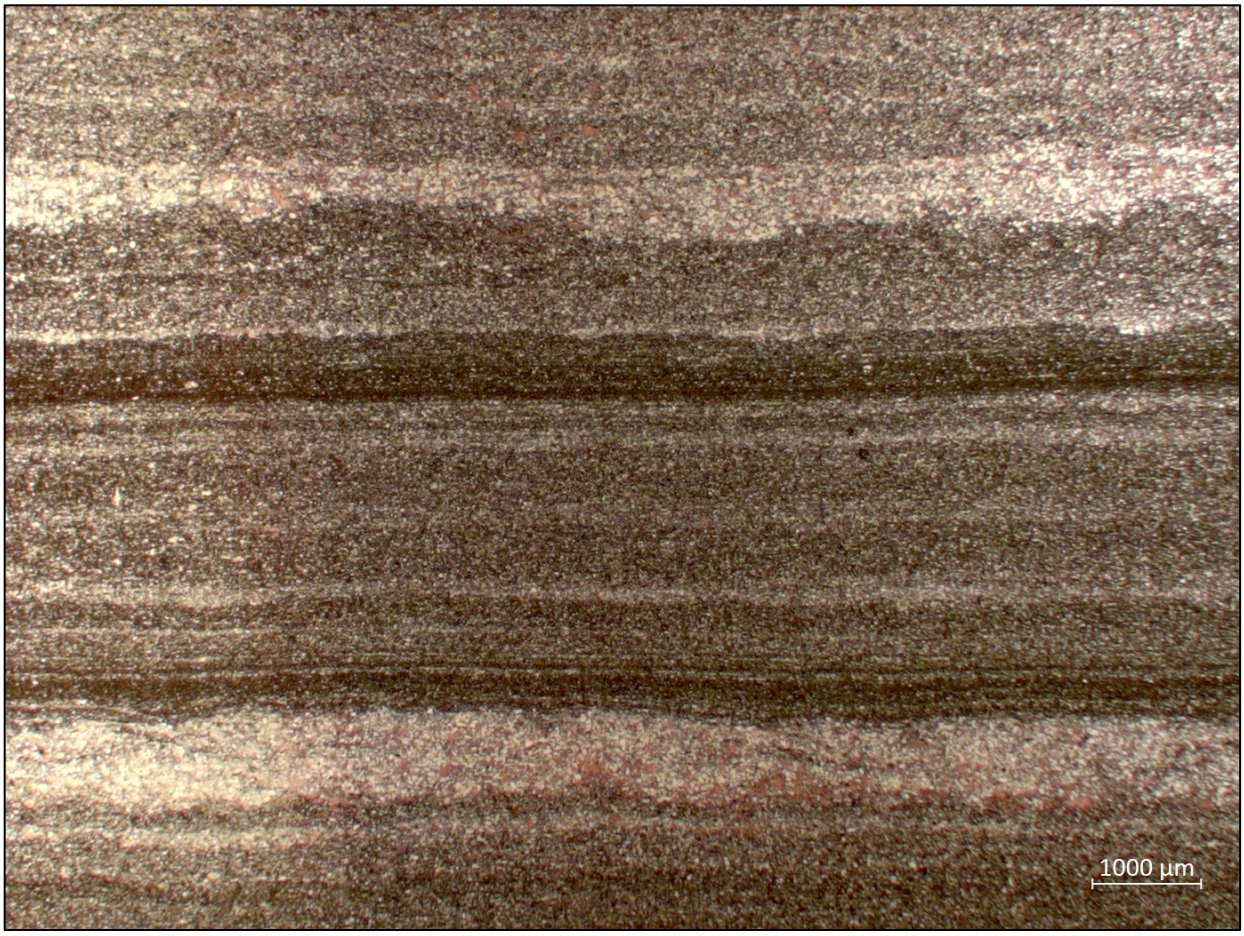

Thin section analysis:

Well laminated to ripple laminated, argillaceous, dolomitic, calcareous siltstone. Individual laminations are sharp based, and are defined by vertical variations in clay content, grain size and content of cement. This sample is well cemented, mainly with dolomite/Fe-dolomite cement. Minor to moderate bioturbation.

%TOC: 1.2 (%wt)

Porosity: 1.2 (%)

Permeability: 1.22 x10^{-4} (md)

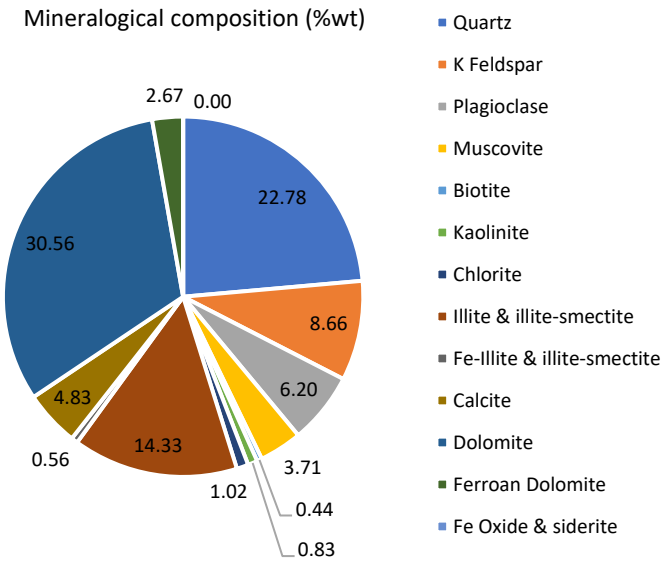

Additional images – RT 4

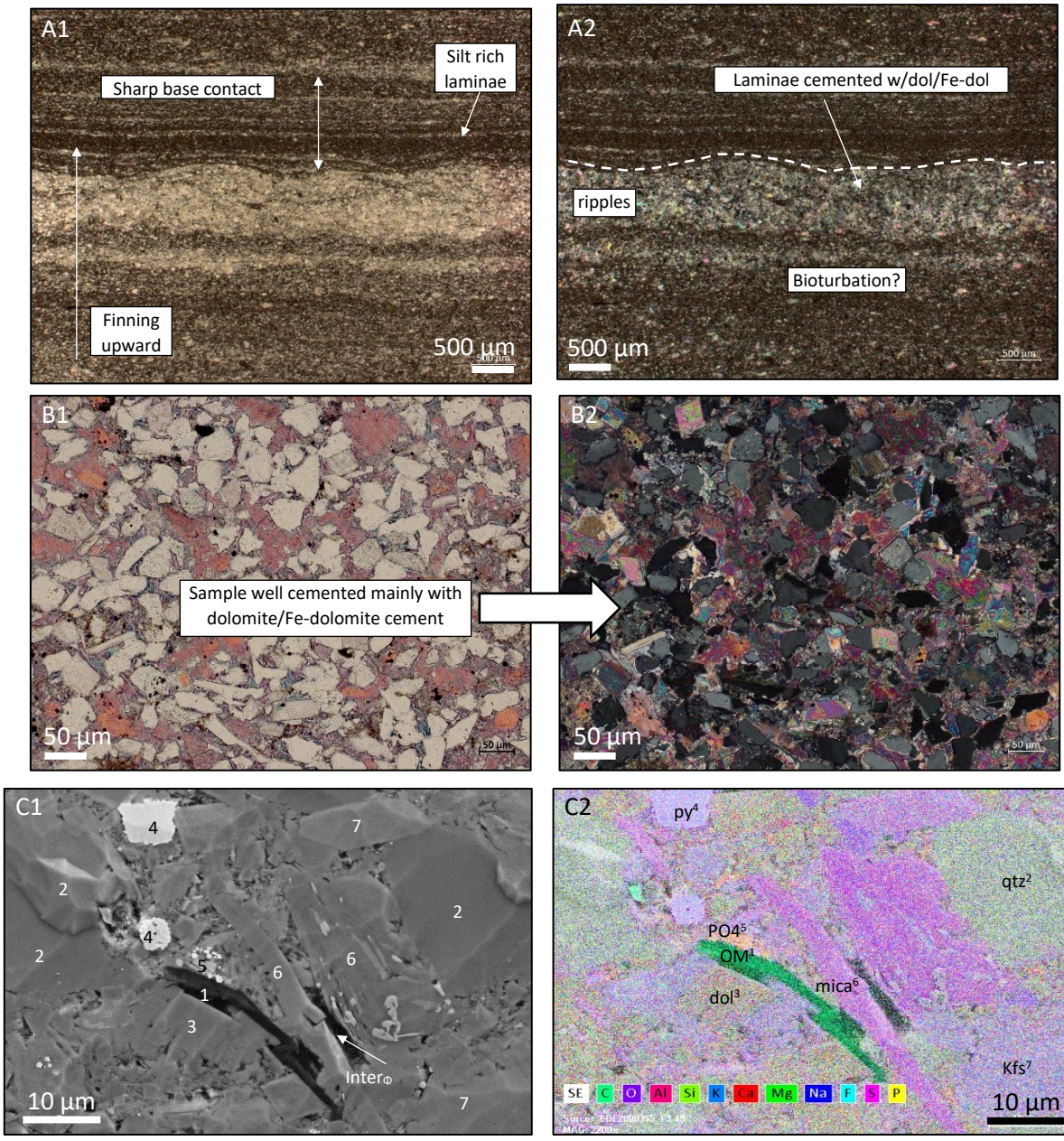

Mineralogical composition – data is in (%wt) – QEMSCAN analysis

Block Code	Pyrite	Sphalerite	Barite	Anhydrite	Halite	Rutile & Ti Silicates	Tourmaline	Chromite	Apatite	Zircon	Monazite	Total
A	2.559	0.000127	0.0479	0.068497	0	0.3202309	0.0166778	0.001052	0.3724	0.0187	0.003711	100

Macroporosity (%)	Grain Density (g/cm³)	Bulk Density (g/cm³)
0.45	2.75	2.74

Additional data – R4

ICP/ICP-MS

SiO2	Al2O3	Fe2O3	MgO	CaO	Na2O	K2O	TiO2	P2O5	MnO	Cr2O3	Ba	Ni	Sc	LOI	Sum
45.08	9.26	3.62	5.45	12.96	0.83	3.92	0.55	0.36	0.44	0.008	478	38	9	17.3	99.8

- data is in (%wt)

Be	Co	Cs	Ga	Hf	Nb	Rb	Sn	Sr	Ta	Th	U	V	W	Zr	Y	La	Ce	Pr	Nd	Sm	Eu	Gd	Tb	Dy	Ho	Er	Tm	Yb	Lu	TOT/C	TOT/S
2	13.9	4.3	10.1	5	9.7	86.1	2	139.5	0.7	7.7	5.6	160	1.3	181.3	24.1	28.2	52.5	6.4	24.2	4.92	0.94	4.53	0.68	4	0.87	2.53	0.36	2.29	0.36	5.4	1.11

data is in (ppm)

MICP -

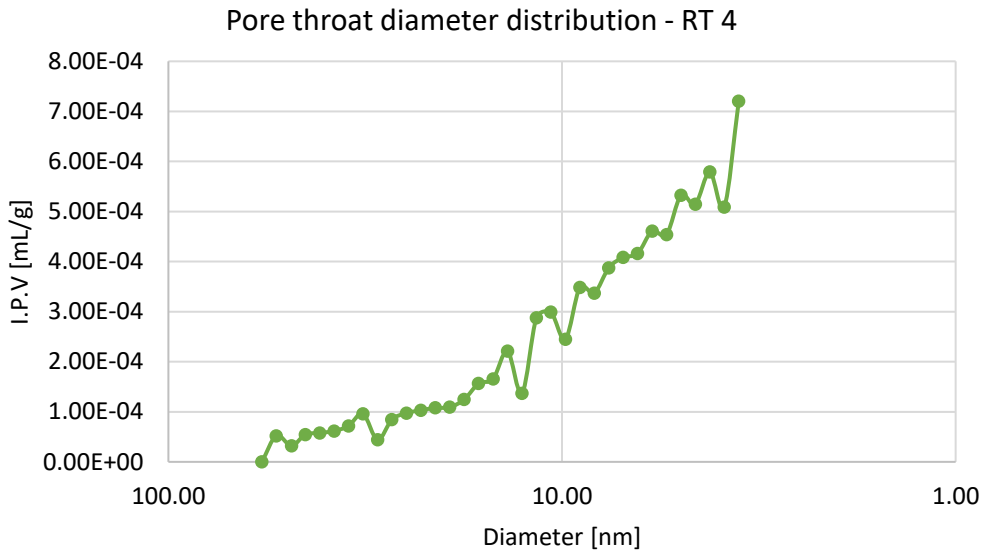

BET -

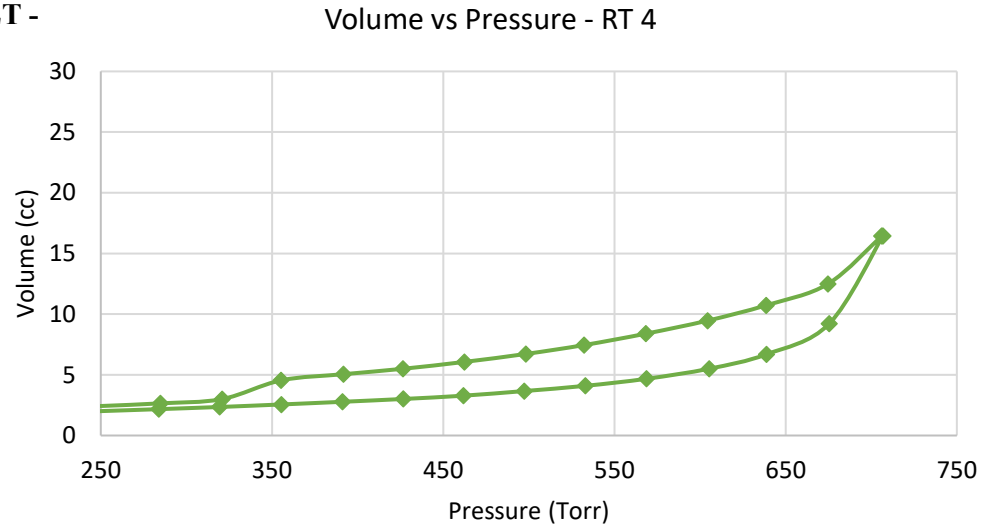

RT 4A – WA32485
Depth: 2241.64 (m)

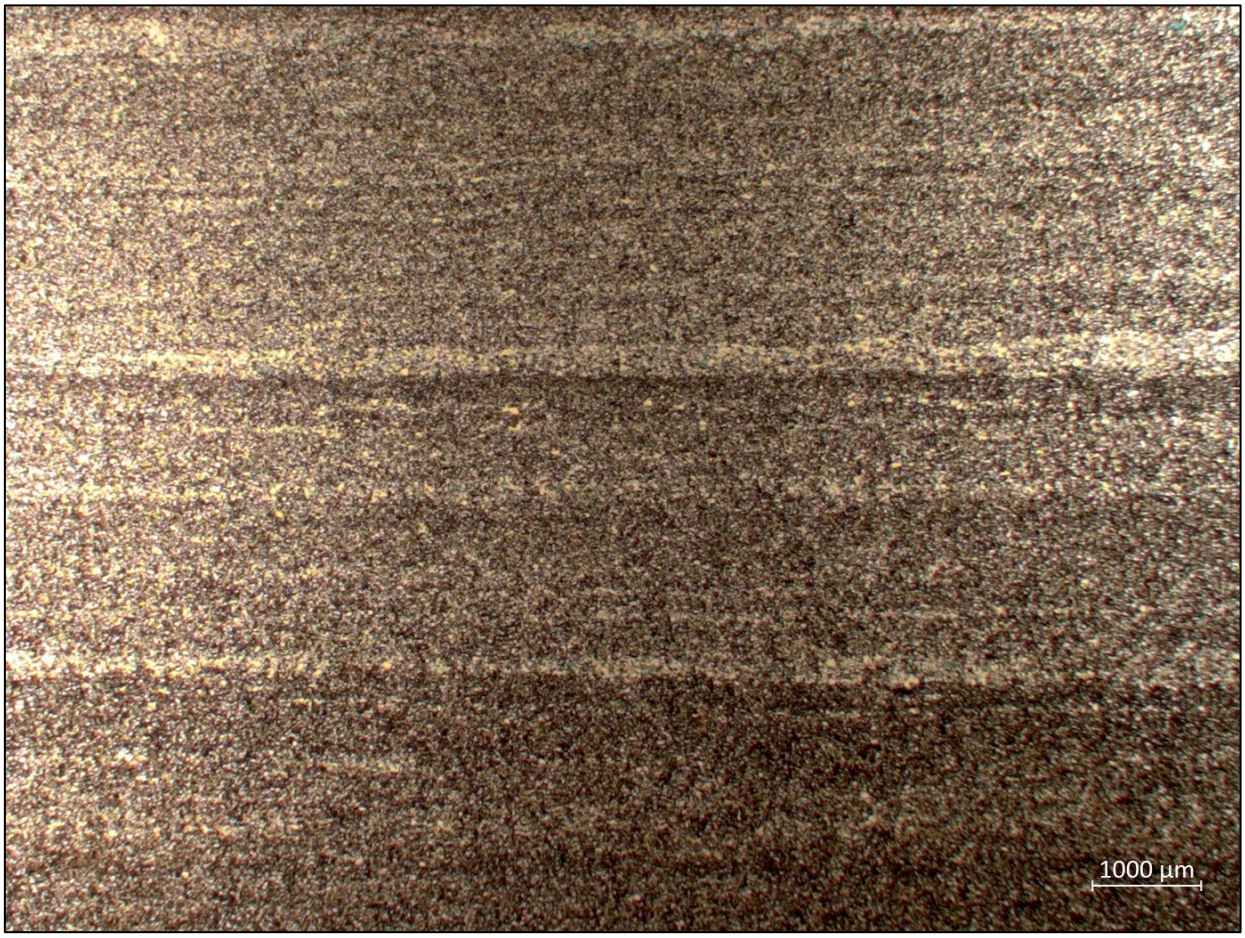

Thin section analysis:

Laminated to well laminated, argillaceous, dolomitic, calcareous siltstone. Interparticle porosity is noted within clay-lean, cemented areas as the clays reduce and occlude the rest of the pore space. Dominant cement types include dolomite/Fe-dolomite, calcite and minor quartz overgrowths, Framework grains are quartz with minor K-feldspar, plagioclase and micas. Pyrite replacement is noted.

%TOC: 0.88 (%wt)

Porosity: 2.8 (%)

Permeability: 2.7 x10^{-5} (md)

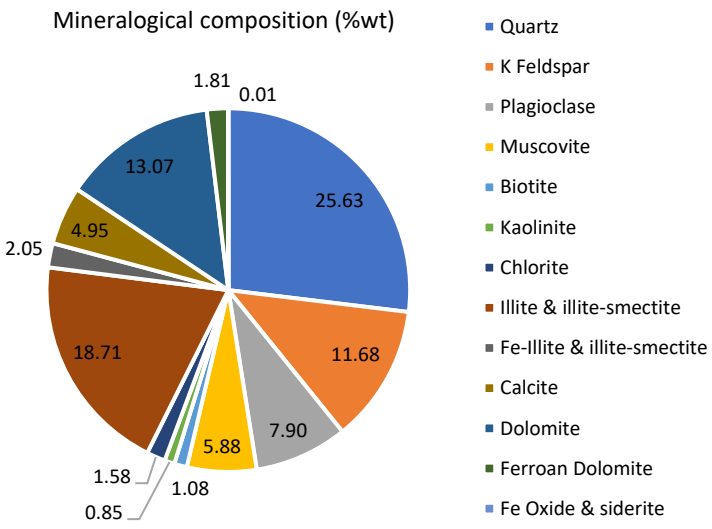

Additional images – RT4A

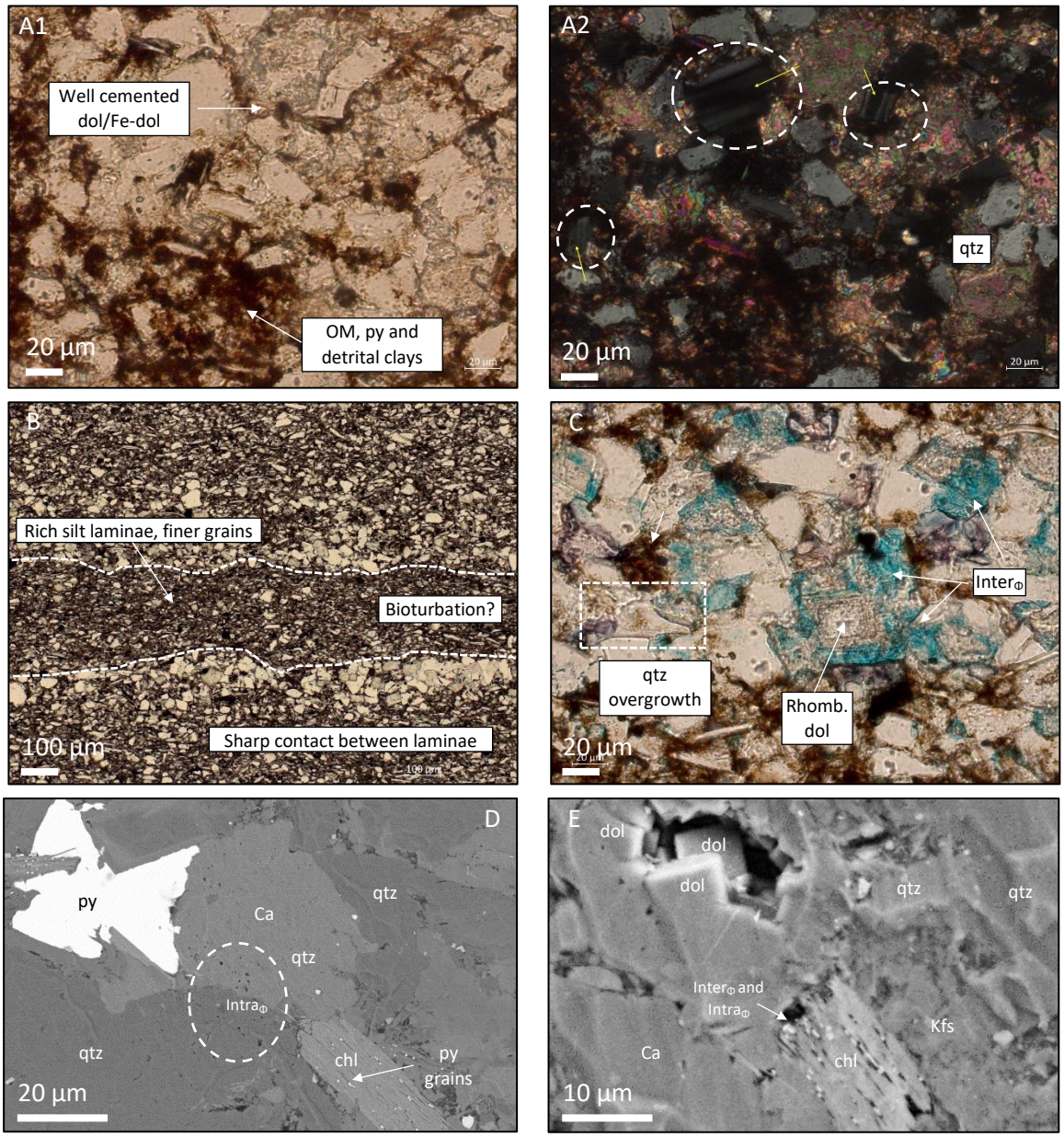

Mineralogical composition – data is in (%wt) – QEMSCAN analysis

Block Code	Pyrite	Sphalerite	Barite	Anhydrite	Halite	Rutile & Ti Silicates	Tourmaline	Chromite	Apatite	Zircon	Monazite	Total
A	3.608	0	0.0546	0.142415	0.0002	0.3778489	0.0168765	0.004836	0.5605	0.0316	0.002921	100

Macroporosity (%)	Grain Density (g/cm³)	Bulk Density (g/cm³)
0.37	2.73	2.72

Additional data – R4A

ICP/ICP-MS

SiO2	Al2O3	Fe2O3	MgO	CaO	Na2O	K2O	TiO2	P2O5	MnO	Cr2O3	Ba	Ni	Sc	LOI	Sum
54.99	10.34	3.88	3.26	8.46	1.1	4.21	0.64	0.34	0.12	0.009	1114	30	10	12.4	99.84

- data is in (%wt)

Be	Co	Cs	Ga	Hf	Nb	Rb	Sn	Sr	Ta	Th	U	V	W	Zr	Y	La	Ce	Pr	Nd	Sm	Eu	Gd	Tb	Dy	Ho	Er	Tm	Yb	Lu	TOT/C	TOT/S
6	13.7	4.4	11.4	6.5	11.2	94.4	2	141.2	0.8	8.9	7.3	87	1	249	27.2	31.1	59.6	7.01	26.5	5.35	1.11	5.07	0.76	4.42	0.95	2.68	0.4	2.46	0.38	4.07	1.29

data is in (ppm)

MICP –

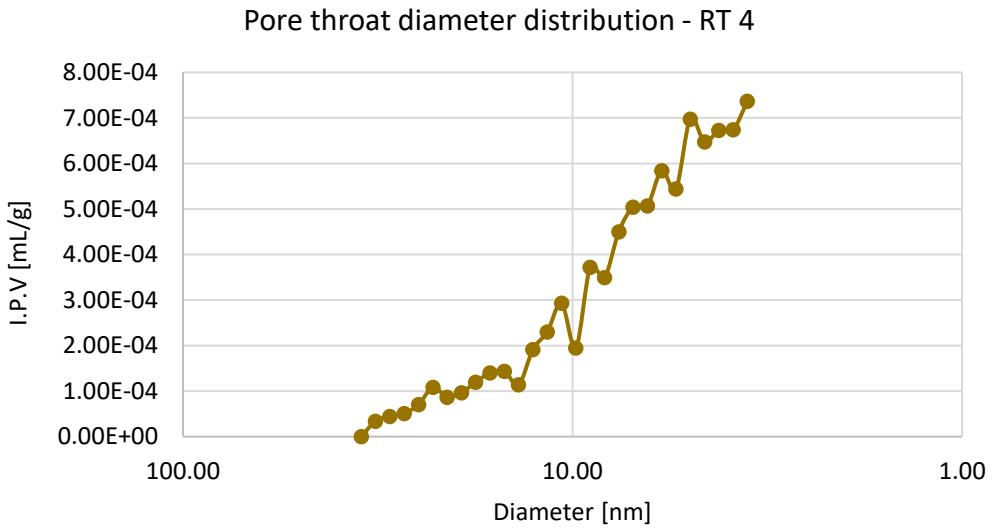

RT 1C – WA32485
Depth: 2249.42 (m)

Thin section analysis:

Laminated, argillaceous, dolomitic, calcareous siltstone. Observed at Macro, some burrows are observed. Laminations are defined by vertical variations in clay content, cement, and grain size. Framework grains are comprised by quartz with minor K-feldspar, plagioclase, and micas. Detrital grains are well cemented by dolomite/Fe-dolomite and calcite.

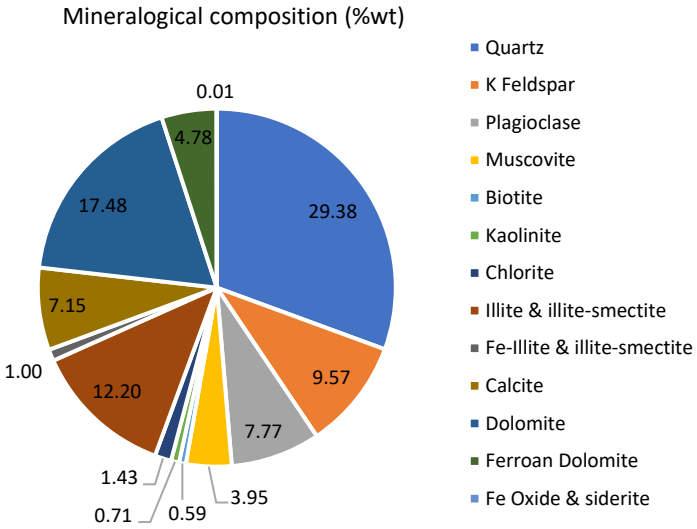

Additional images – RT 1C

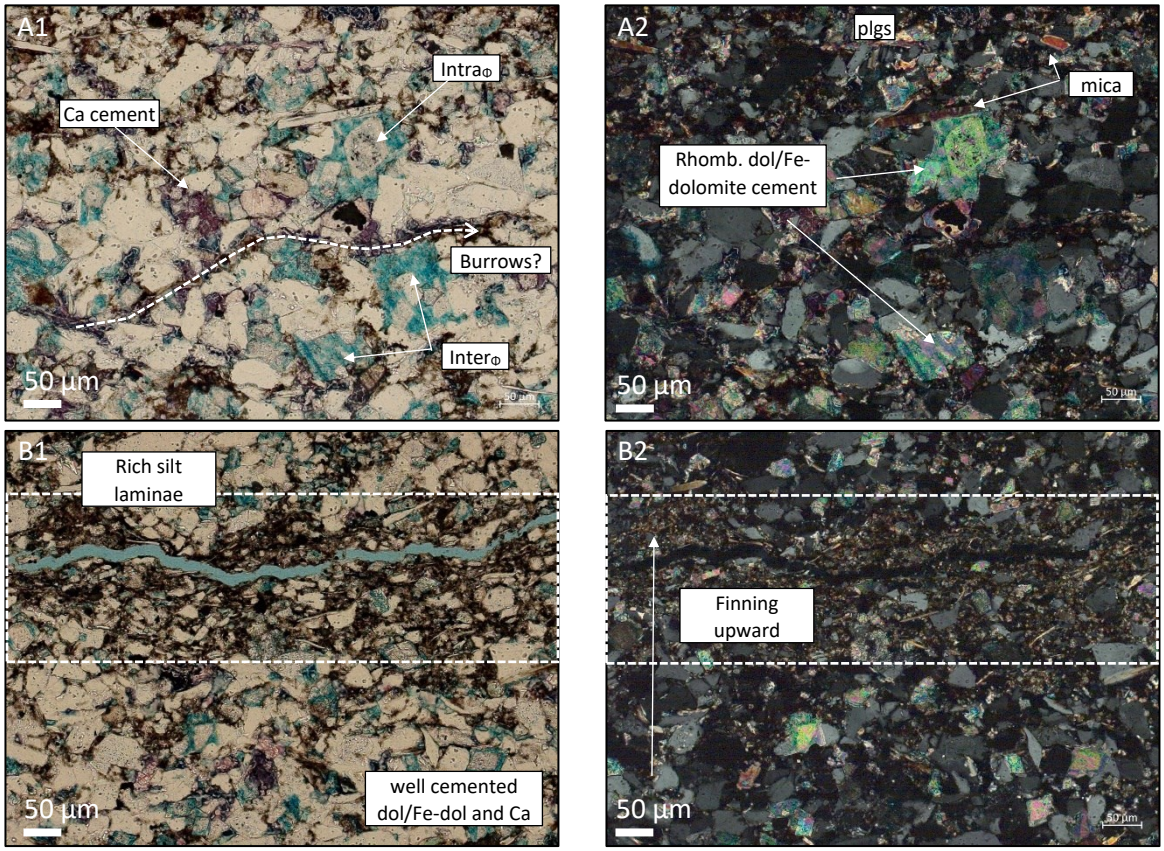

Mineralogical composition – data is in (%wt) – QEMSCAN analysis

Block Code	Pyrite	Sphalerite	Barite	Anhydrite	Halite	Rutile & Ti Silicates	Tourmaline	Chromite	Apatite	Zircon	Monazite	Total
A	2.758	0	0.169	0.069676	6.82264E-05	0.378901	0.0184211	0.003769	0.5514	0.0341	0.0034	100

Macroporosity (%)	Grain Density (g/cm³)	Bulk Density (g/cm³)
0.38	2.74	2.73

ICP/ICP-MS

SiO2	Al2O3	Fe2O3	MgO	CaO	Na2O	K2O	TiO2	P2O5	MnO	Cr2O3	Ba	Ni	Sc	LOI	Sum
33.79	6.08	2.89	2.67	26.77	0.79	2.28	0.39	0.22	0.25	0.005	280	22	6	23.7	99.88

- data is in (%wt)

Be	Co	Cs	Ga	Hf	Nb	Rb	Sn	Sr	Ta	Th	U	V	W	Zr	Y	La	Ce	Pr	Nd	Sm	Eu	Gd	Tb	Dy	Ho	Er	Tm	Yb	Lu	TOT/C	TOT/S
<1	7	2.4	7	3.6	7.4	49.2	<1	197.1	0.5	5.1	4.4	54	1.4	145.8	19.9	21.7	40.2	4.68	17.5	3.58	0.71	3.25	0.51	3.07	0.64	1.87	0.26	1.62	0.26	7.42	0.73

data is in (ppm)

RT 4B – WA32485
Depth: 2256.65 (m)

Thin section analysis:

Faintly laminated to laminated argillaceous, dolomitic, calcareous siltstone. Changes in grain size and clay content help define individual laminae. Slight bioturbation is observed at Macro scale as micritic mud. Framework grains are composed of quartz, with minor K-feldspar, plagioclase, and micas. Framboidal pyrite is noted

%TOC: 0.94 (%wt)

Porosity: 1.5 (%)

Permeability: 3.4 x10^{-5} (md)

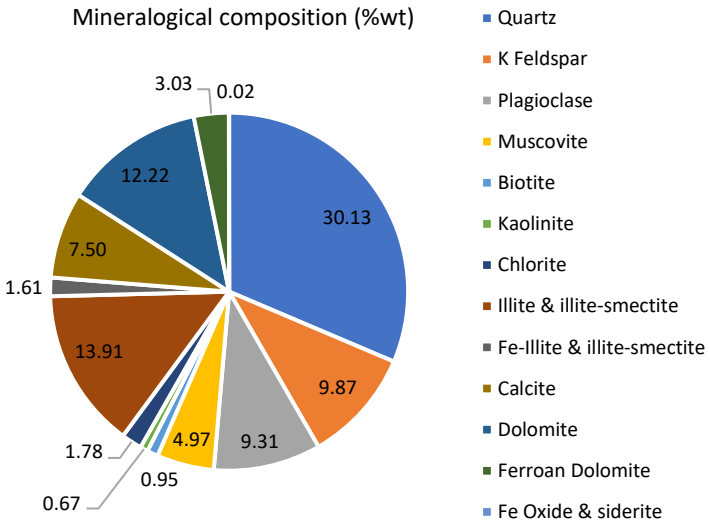

Additional images – RT 4B

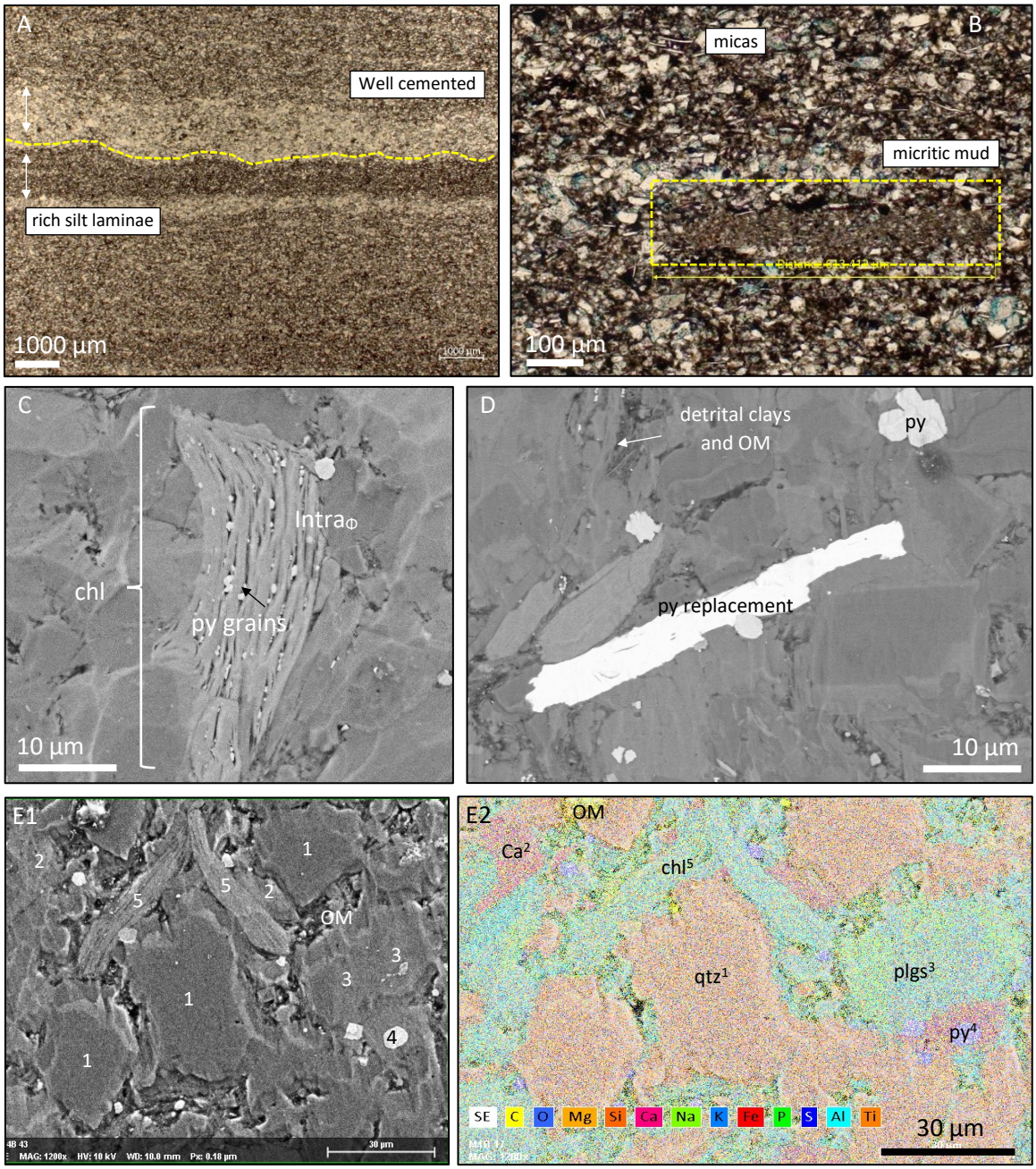

Mineralogical composition – data is in (%wt) – QEMSCAN analysis

Block Code	Pyrite	Sphalerite	Barite	Anhydrite	Halite	Rutile & Ti Silicates	Tourmaline	Chromite	Apatite	Zircon	Monazite	Total	Macroporosity (%)	Grain Density (g/cm³)	Bulk Density (g/cm³)
A	2.979	0.000512	0.0715	0.058679	0.000137249	0.3807316	0.0292871	0.004852	0.4414	0.0357	0.00228	100	0.58	2.73	2.72

Additional data – RT 4B

ICP/ICP-MS

SiO2	Al2O3	Fe2O3	MgO	CaO	Na2O	K2O	TiO2	P2O5	MnO	Cr2O3	Ba	Ni	Sc	LOI	Sum
54.72	10.17	4.04	3.27	9.27	1.22	3.71	0.65	0.31	0.1	0.009	538	45	10	12.3	99.84

- data is in (%wt)

Be	Co	Cs	Ga	Hf	Nb	Rb	Sn	Sr	Ta	Th	U	V	W	Zr	Y	La	Ce	Pr	Nd	Sm	Eu	Gd	Tb	Dy	Ho	Er	Tm	Yb	Lu	TOT/C	TOT/S
2	12.2	4.4	10.9	6.8	11.4	90.4	2	132.1	0.8	8.1	5.3	105	1.6	244.3	25	28.6	54.7	6.47	25.1	4.74	1.01	4.53	0.71	4.45	0.92	2.61	0.39	2.44	0.37	3.8	1.25

data is in (ppm)

MICP -

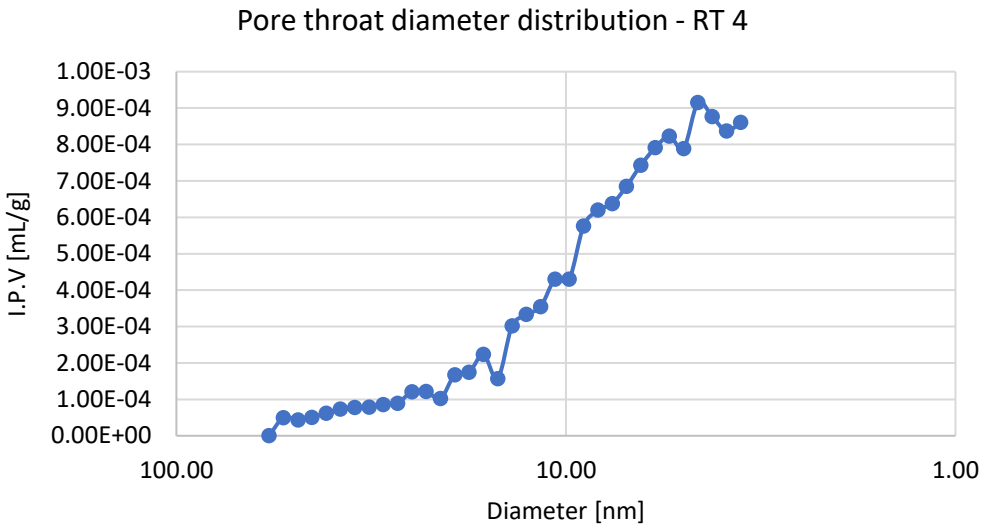

RT 2E – WA26965
Depth: 1656.2 (m)

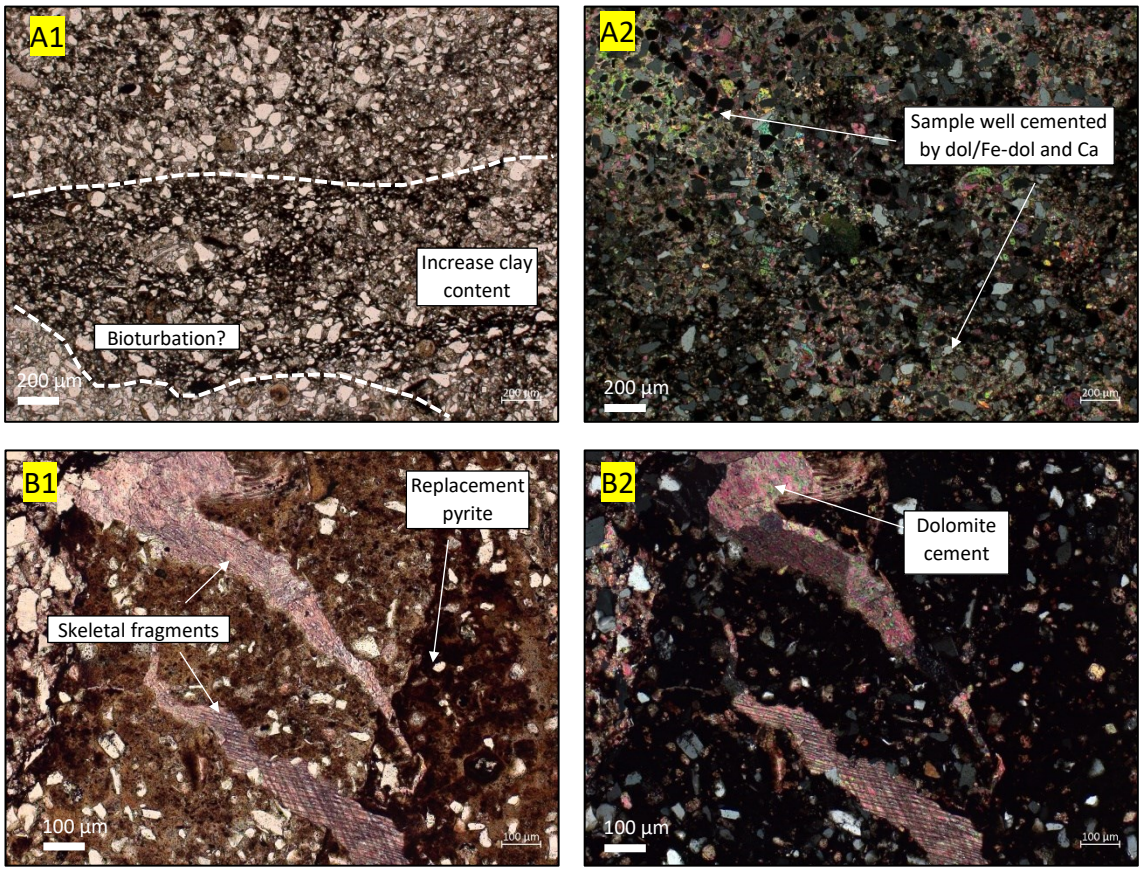

Thin section description:

Laminated to massive appearing skeletal-rich silty calcareous siltstone. Skeletal fragments are present in this sample. Basal contacts are sharp. Silt size detrital grains include quartz, feldspar, and micas. Minor matrix clays are observed as much of the matrix has been cemented by calcite and in less amount Fe-dol/dolomite cement. Abundant replacement pyrite is noted within skeletal-rich areas.

%TOC: 1.6 (wt)

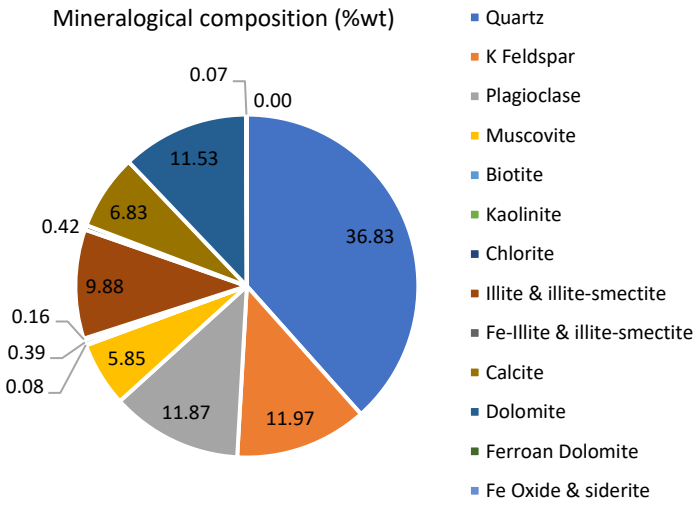

Additional data – RT 2E

Mineralogical composition – data is in (%wt) – QEMSCAN analysis

Block Code	Pyrite	Sphalerite	Barite	Anhydrite	Halite	Rutile & Ti Silicates	Tourmaline	Chromite	Apatite	Zircon	Monazite	Total
A	2.737	0.000137	0.0835	0.034391	0.002058508	0.5881601	0.0542137	0.000487	0.4904	0.1381	0.002966	100

Macroporosity (%)	Grain Density (g/cm³)	Bulk Density (g/cm³)
7.231935273	2.70868	2.58511

- **MICP**

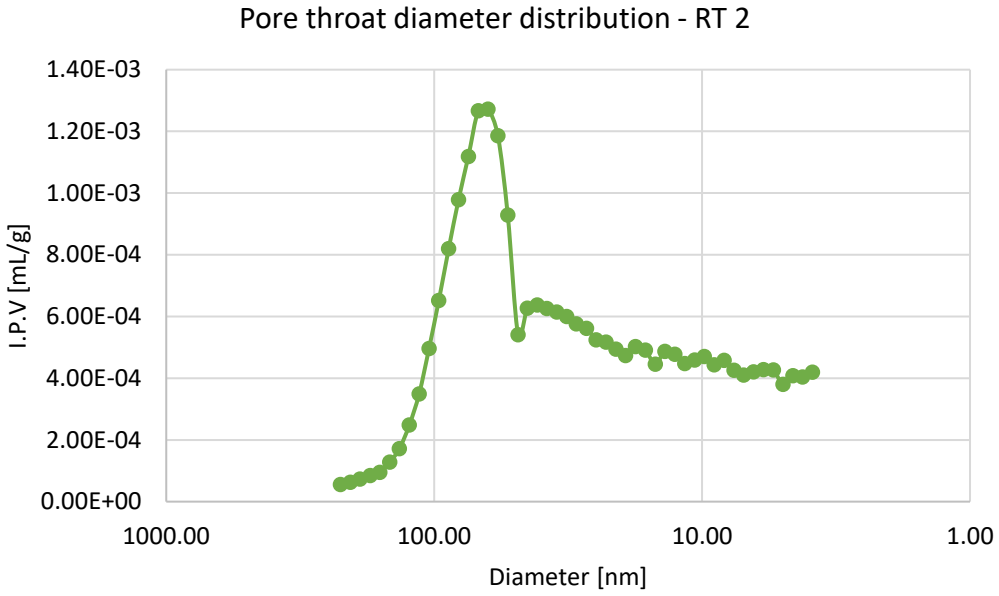

RT 2D – WA26965
Depth: 1659.2 (m)

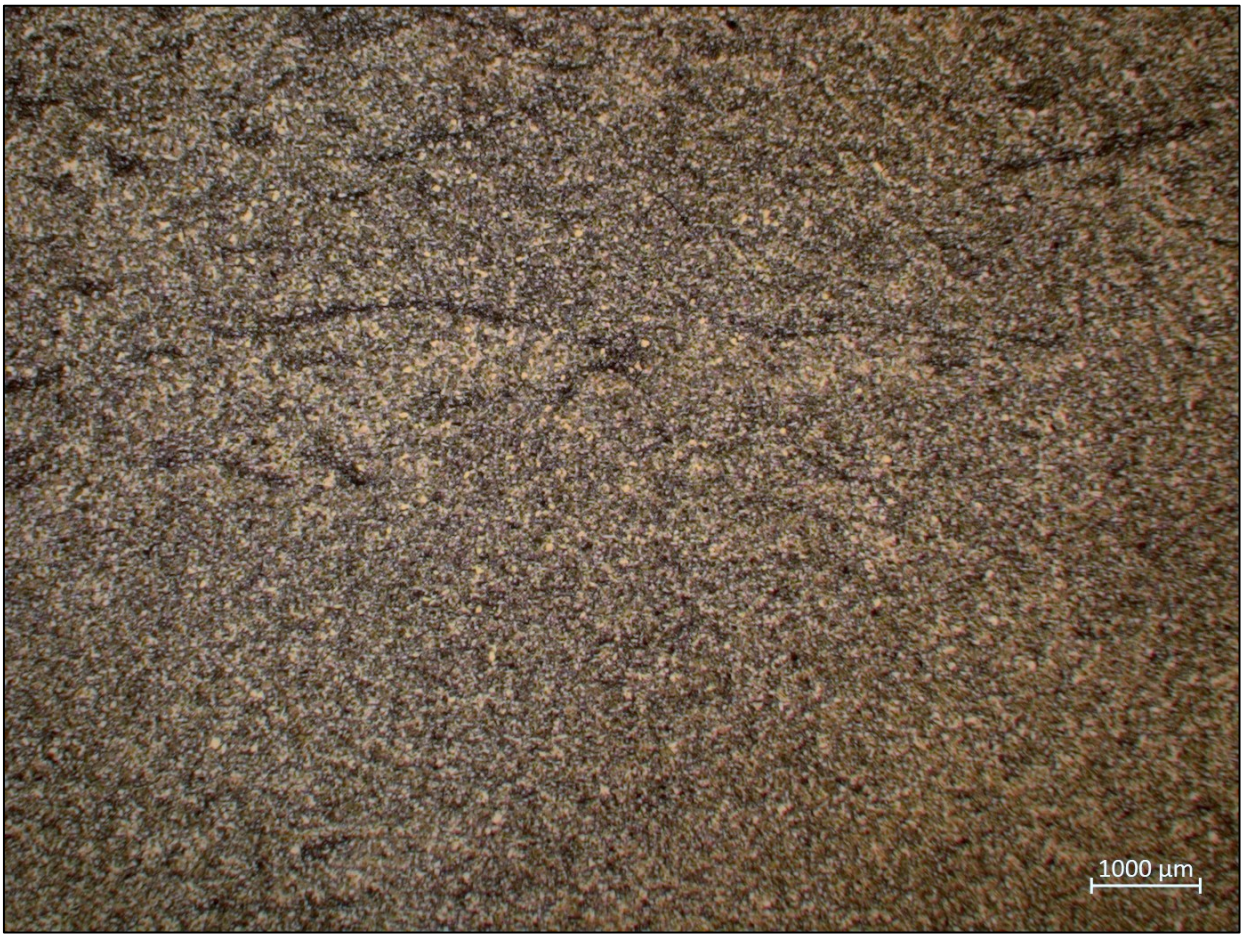

Thin section description:

Massive, moderately bioturbated argillaceous dolomitic, calcareous siltstone. Higher magnifications reveal a more massive appearance due to pervasive cryptic bioturbation. This sample is very well cemented (dolomite/Fe-dol and calcite) and in minor proportion by clays and organics. Quartz, with minor K-feldspar, plagioclase and micas are the main detrital framework grains. Replacement pyrite is observed throughout the sample.

%TOC: 0.65 (%wt)

Porosity = 4.50 (%)

Permeability = 28.581 (nd)

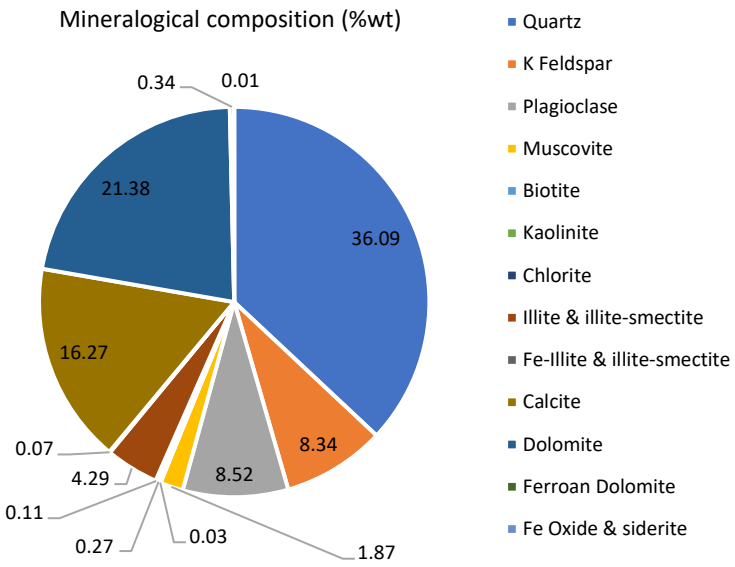

Additional images – RT 2D

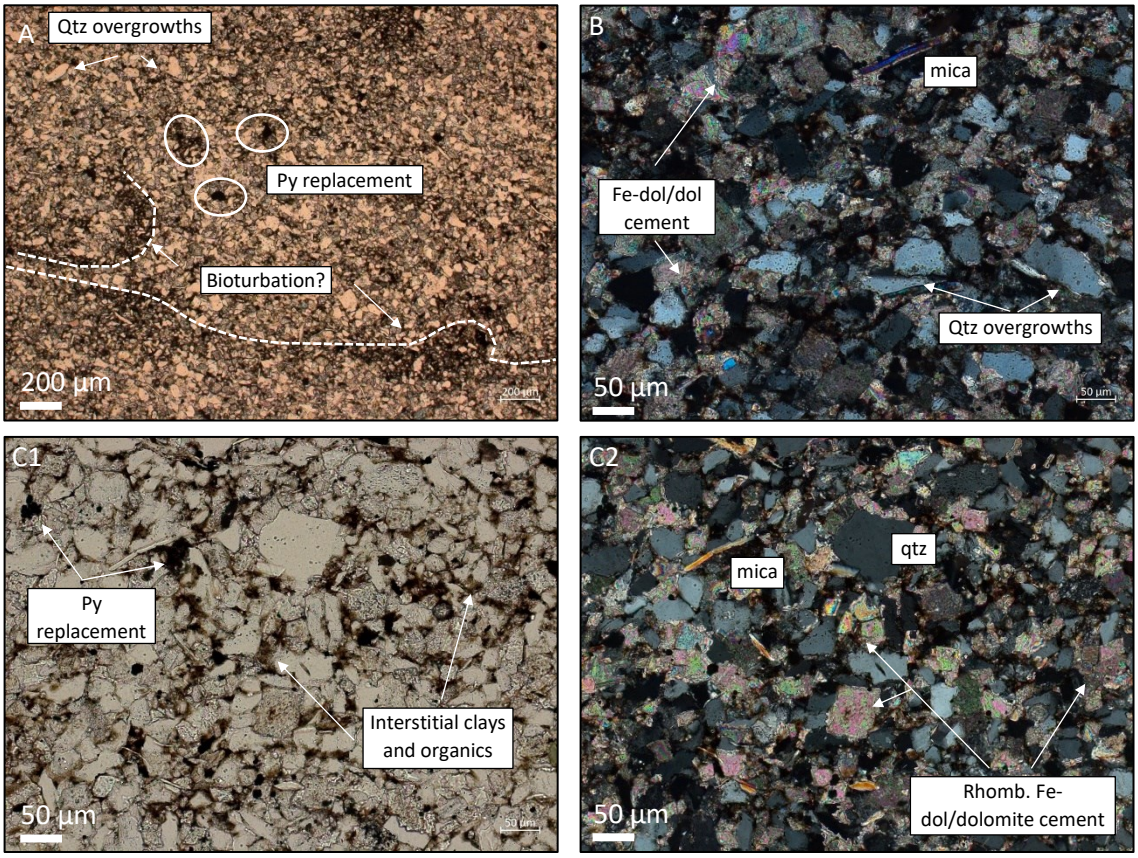

Mineralogical composition – data is in (%wt) – QEMSCAN analysis

Block Code	Pyrite	Sphalerite	Barite	Anhydrite	Halite	Rutile & Ti Silicates	Tourmaline	Chromite	Apatite	Zircon	Monazite	Total
A	1.321	0	0.0386	0.023879	0.000141117	0.3497337	0.0298052	0.00421	0.5447	0.0951	0.004689	100

Macroporosity (%)	Grain Density (g/cm³)	Bulk Density (g/cm³)
3.60	2.72	2.65

- **MICP**

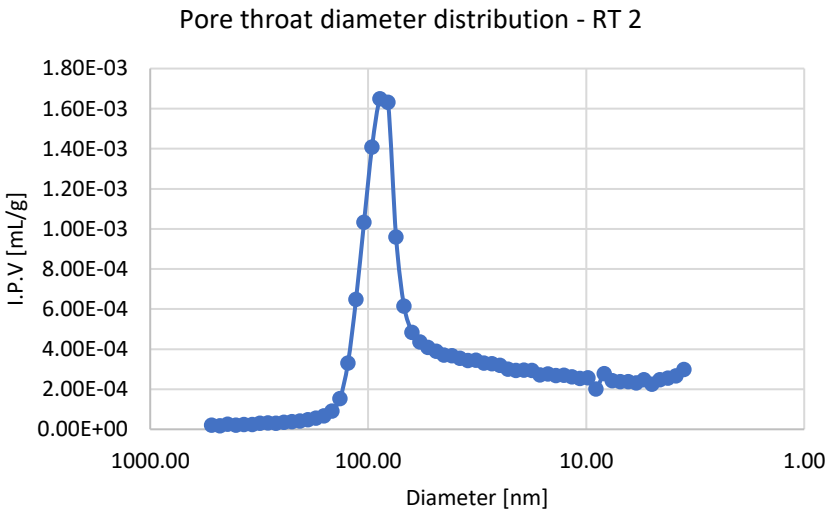

RT 1A – WA26965
Depth: 1703.4 (m)

Thin section description:

Faintly to massive argillaceous dolomitic calcareous siltstone. Moderate to well sorted sample. The grain fabric is supported by Fe-dolomite/dolomite and in less amount calcite cement. Quartz, and in les amount K-feldspar, plagioclase and micas are the main framework grains. Micas are shown to have random orientations. Pyrite replacement is observed throughout the sample.

%TOC: 1.6 (%wt)

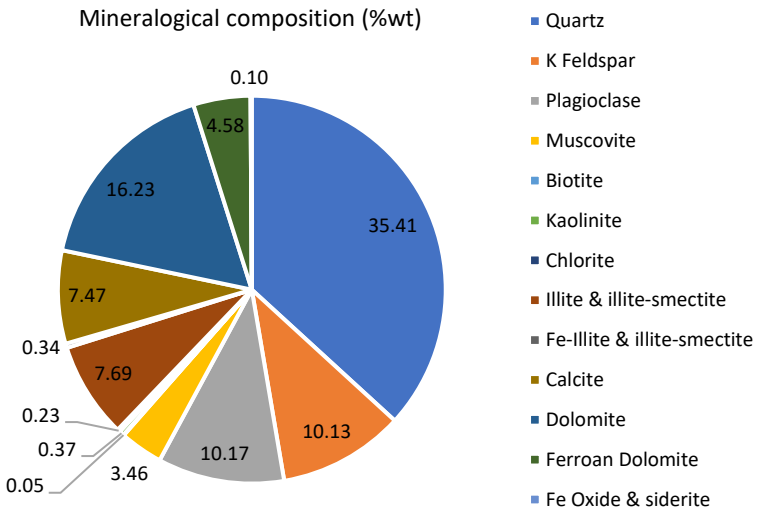

Additional images – RT 1A

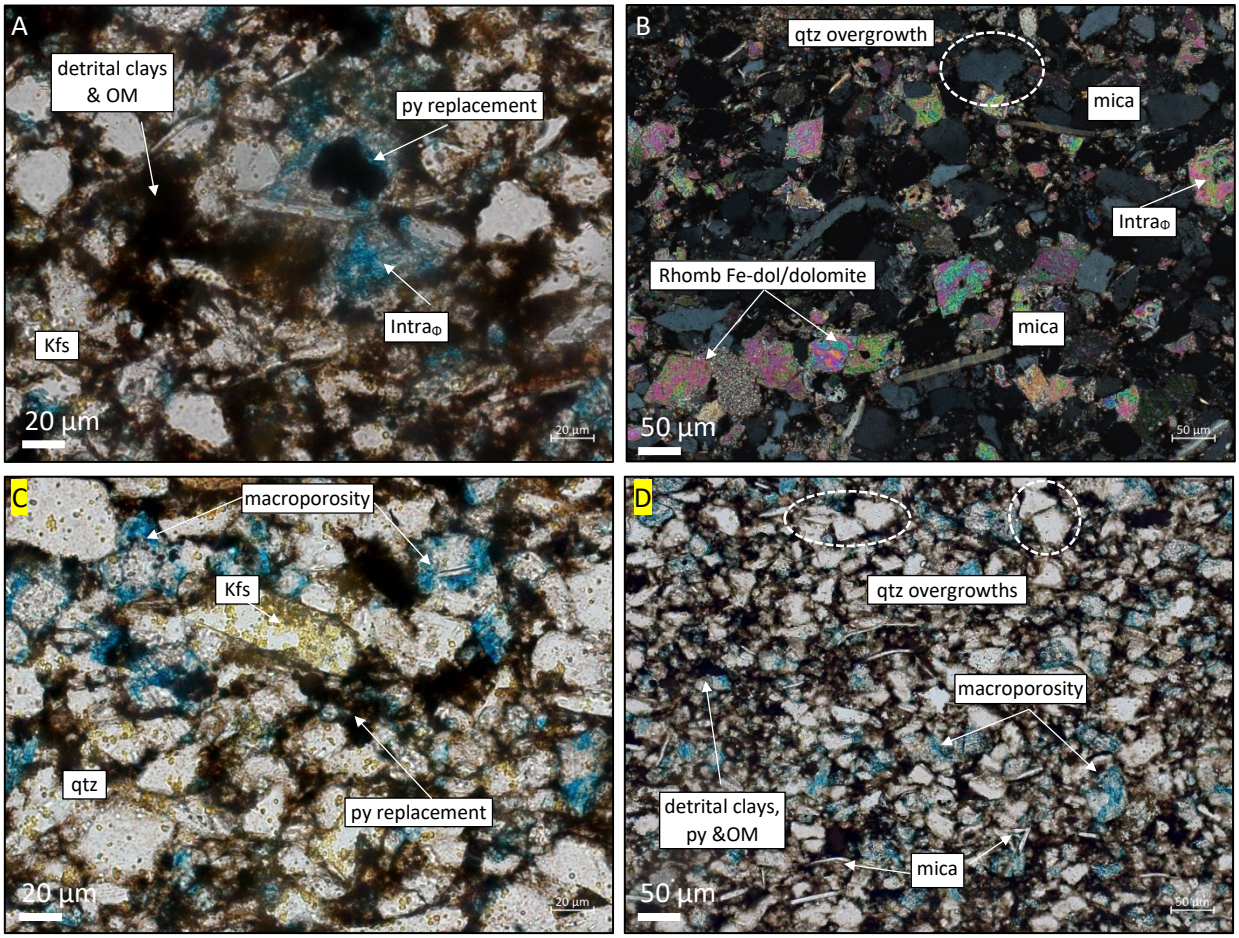

Mineralogical composition – data is in (%wt) – QEMSCAN analysis.

Block Code	Pyrite	Sphalerite	Barite	Anhydrite	Halite	Rutile & Ti Silicates	Tourmaline	Chromite	Apatite	Zircon	Monazite	Total
A	2.735	0	0.058	0.05985	0.00271	0.4232509	0.0340227	0.001133	0.4066	0.0414	0.004693	100

Macroporosity (%)	Grain Density (g/cm³)	Bulk Density (g/cm³)
7.49	2.73	2.60

RT 2F – WA26965
Depth: 1704.2 (m)

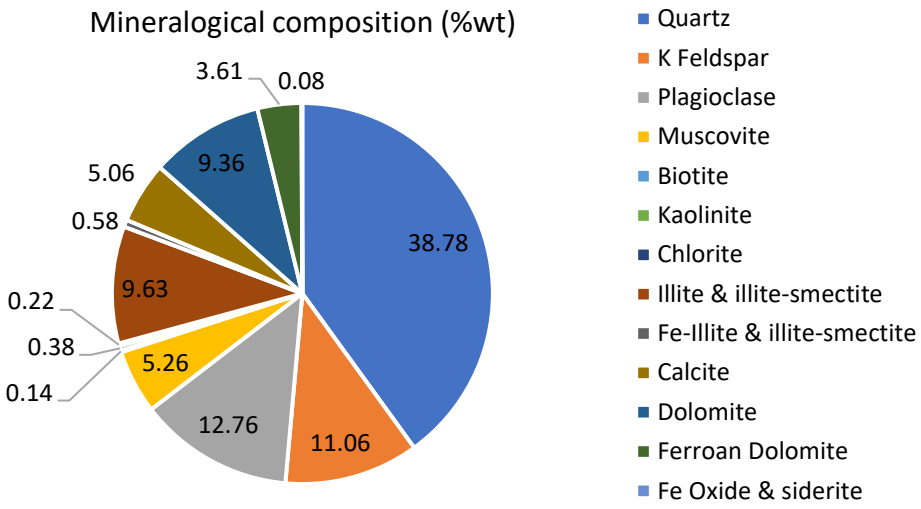

Block Code	Pyrite	Sphalerite	Barite	Anhydrite	Halite	Rutile & Ti Silicates	Tourmaline	Chromite	Apatite	Zircon	Monazite	Total
A	2.047	0	0.0698	0.032753	0.002947799	0.4730871	0.0346715	0.000162	0.3617	0.0593	0.010291	100

Macroporosity (%)	Grain Density (g/cm³)	Bulk Density (g/cm³)
7.07	2.71	2.58

RT 3A – WA26965
Depth: 1765.2 (m)

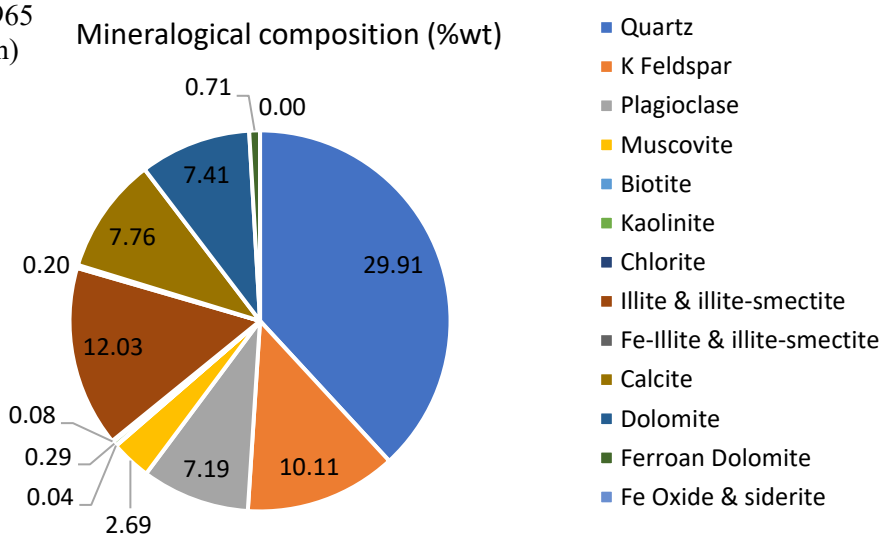

Block Code	Pyrite	Sphalerite	Barite	Anhydrite	Halite	Rutile & Ti Silicates	Tourmaline	Chromite	Apatite	Zircon	Monazite	Total	Macroporosity (%)	Grain Density (g/cm³)	Bulk Density (g/cm³)
A	1.472	0.006845	0.0446	0.06324	0.000143825	0.3886434	0.0207735	0.000159	19.527	0.0458	0.003413	100	7.24	2.77	2.64

RT 2 – WA26965
Depth: 1713.4 (m)

Thin section analysis:

Well to faintly, bioturbated, slightly argillaceous, dolomitic, calcareous siltstone. Very fine silt to very fine upper sand sizes framework grains include quartz, and in less amount K-feldspar, plagioclase, and micas. Higher magnifications show that the detrital very fine sand size quartz and feldspars grains are heavily cemented by Fe-dolomite/dolomite and in less amount calcite and were grains are very fine silt size the clay content increases. Pyrite replacement was observed within the silty matrix or locally replaces carbonaceous detritus.

%TOC: 1.3 (%wt)

Porosity = 5.5 (%)

Permeability = 131.488 (nd)

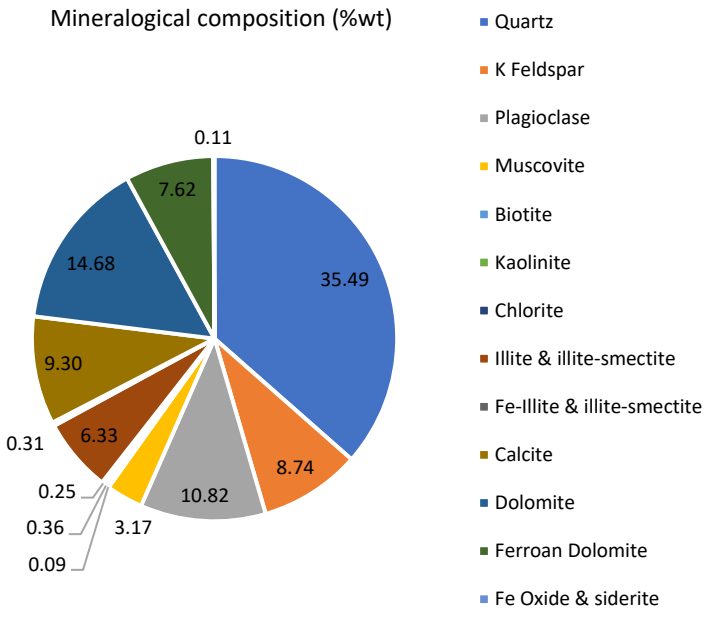

Additional images – RT 2

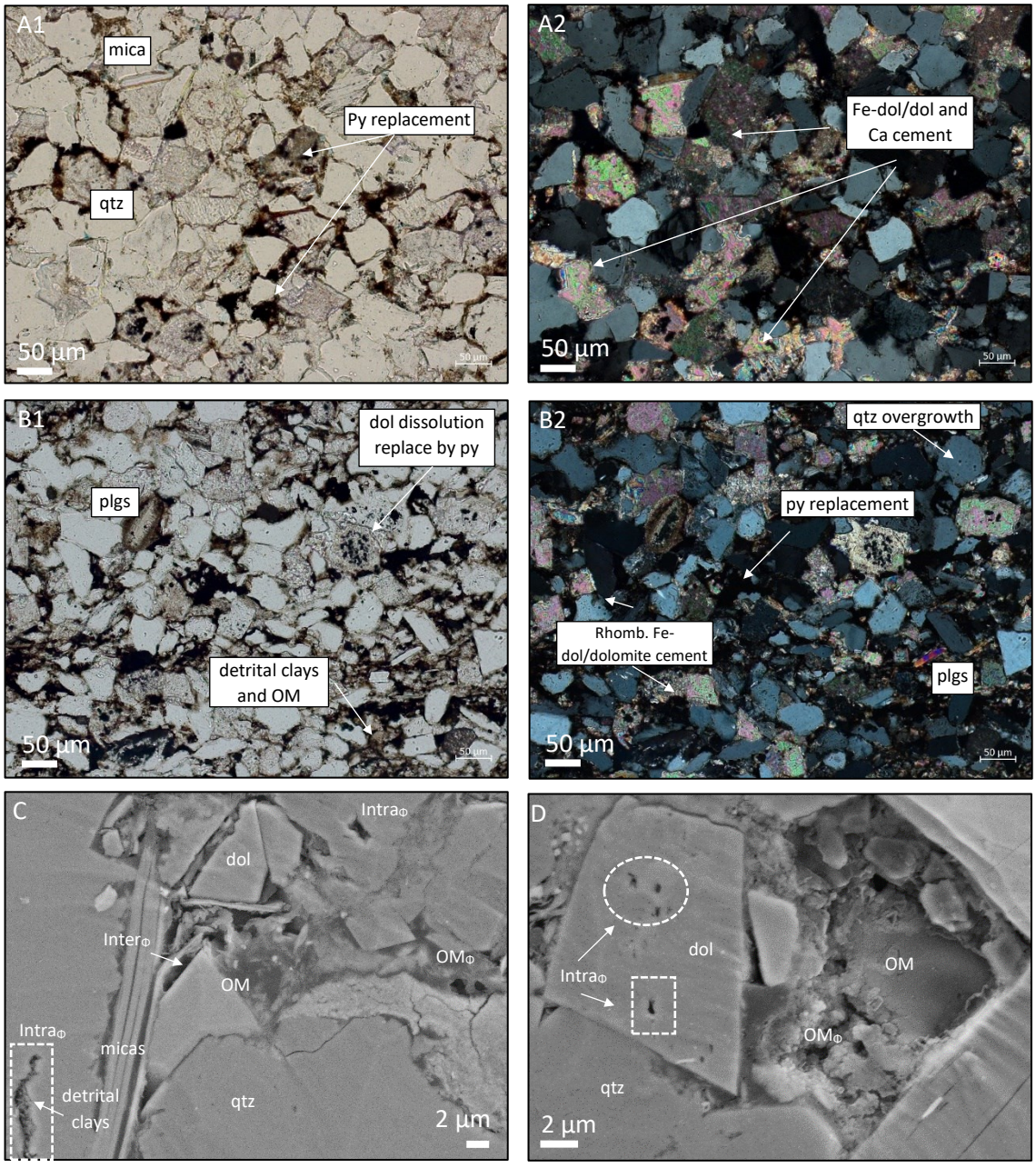

Mineralogical composition – data is in (%wt) – QEMSCAN analysis

Block Code	Pyrite	Sphalerite	Barite	Anhydrite	Halite	Rutile & Ti Silicates	Tourmaline	Chromite	Apatite	Zircon	Monazite	Total
A	1.662	0	0.0816	0.028705	0.001306569	0.4827363	0.0369088	0.00016	0.3673	0.0706	0.007736	100

Macroporosity (%)	Grain Density (g/cm³)	Bulk Density (g/cm³)
6.51	2.73	2.62

Additional data – RT 2

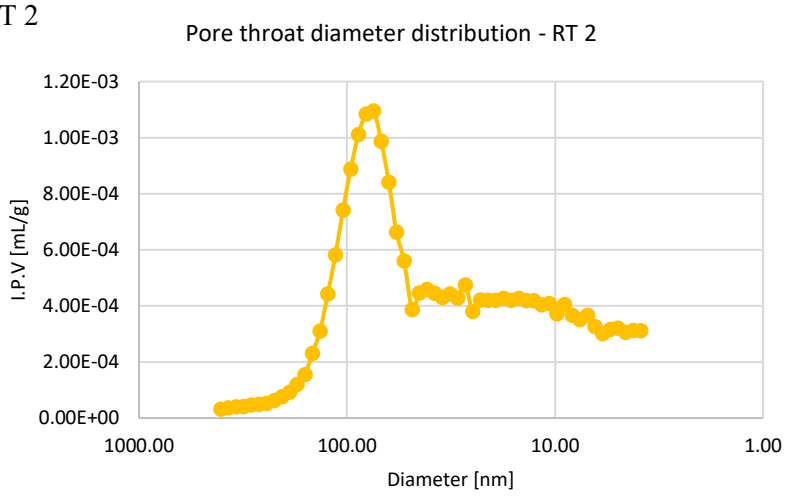

RT 2C – WA26965
Depth: 1716 (m)

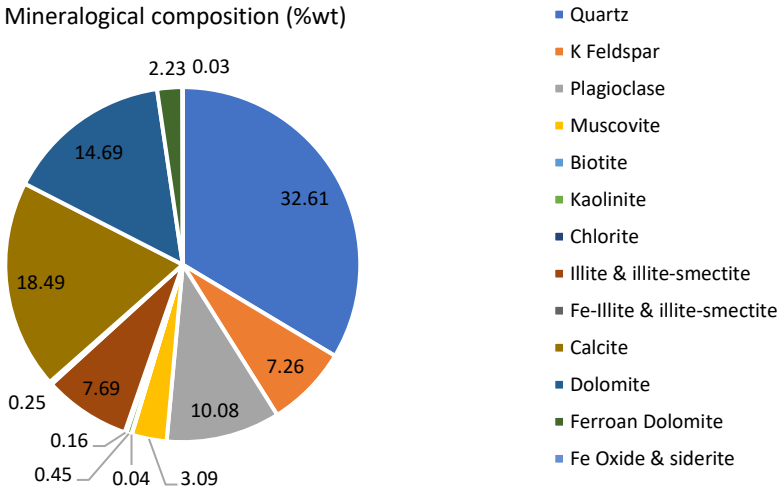

Block Code	Pyrite	Sphalerite	Barite	Anhydrite	Halite	Rutile & Ti Silicates	Tourmaline	Chromite	Apatite	Zircon	Monazite	Total	Macroporosity (%)	Grain Density (g/cm³)	Bulk Density (g/cm³)
A	1.753	0.006529	0.1053	0.068615	0.017211613	0.4455331	0.0494614	0	0.4128	0.072	0.010959	100	2.79	2.72	2.67

- **MICP**

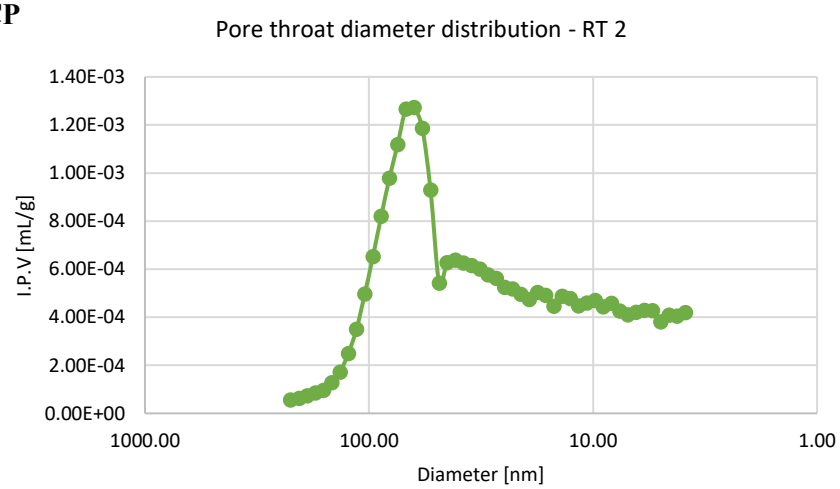

RT 3C -WA26965
Depth: 1763.2 (m)
%TOC= 3.6 (%wt)
Porosity= 1.8 (%)
Permeability= 139.733 (nd)

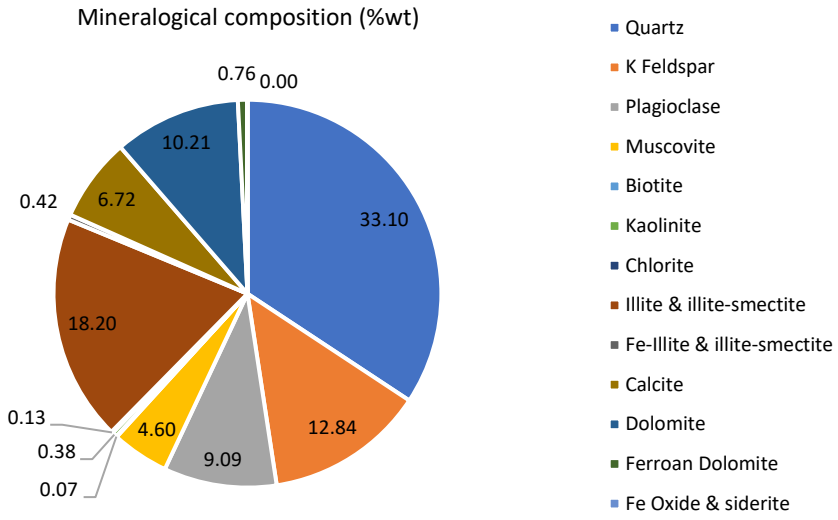

Mineralogical composition – data is in (%wt) – QEMSCAN analysis

Block Code	Pyrite	Sphalerite	Barite	Anhydrite	Halite	Rutile & Ti Silicates	Tourmaline	Chromite	Apatite	Zircon	Monazite	Total	Macroporosity (%)	Grain Density (g/cm³)	Bulk Density (g/cm³)
A	2.111	0.060028	0.0364	0.095554	7.53238E-05	0.3927103	0.0342237	0.000166	0.6788	0.0555	0.000179	100	9.18	2.70	2.55

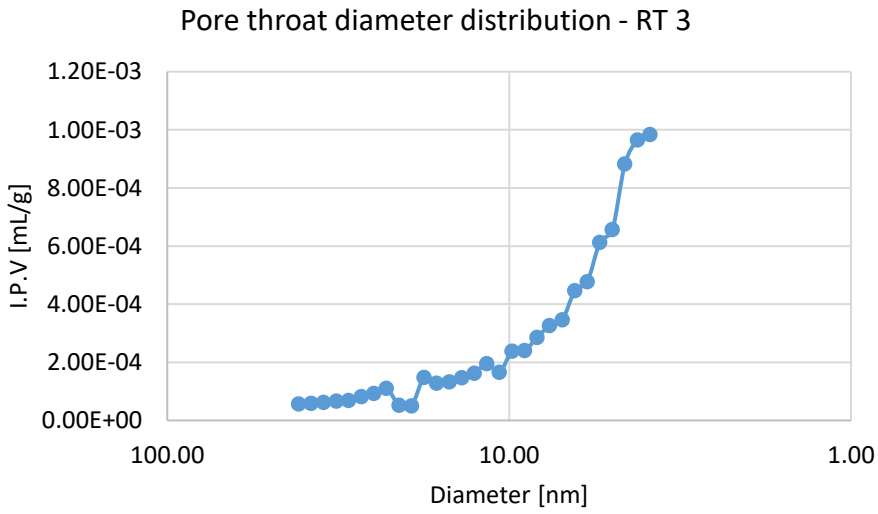

RT 2A – WA26965
Depth: 1768 (m)

Thin section analysis:

Faintly to very faintly, slightly argillaceous, dolomitic, calcareous siltstone. Very fine silt to very fine sand sizes framework grains include quartz, K-feldspar, plagioclase, and in less amount micas. Higher magnifications show that grains are cemented by Pyrite replacement, and it was observed within the silty matrix

%TOC: 3.7 (%wt)

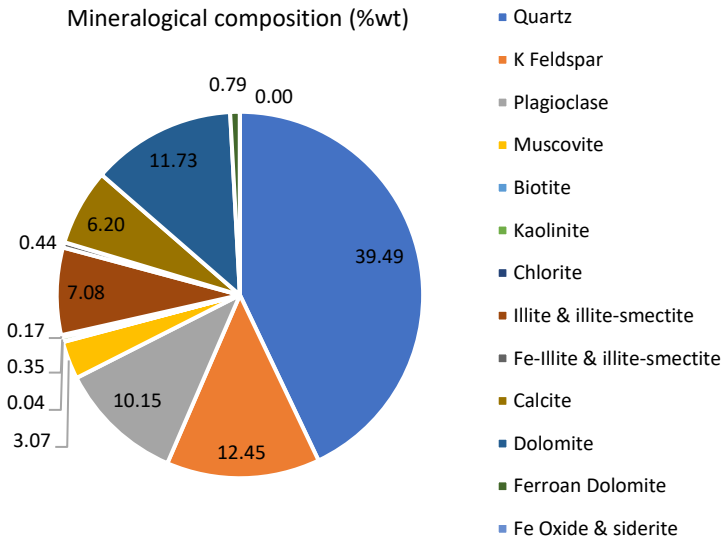

Additional images – RT 2A

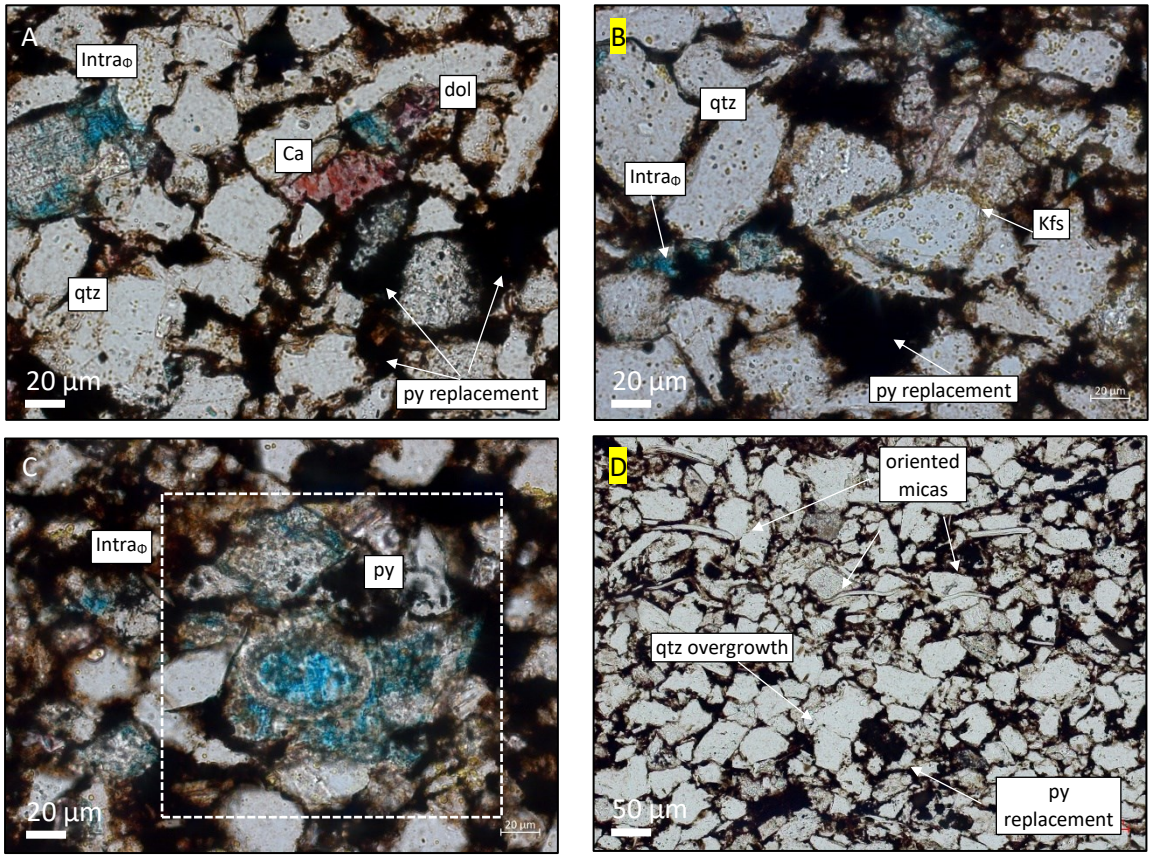

Mineralogical composition – data is in (%wt) – QEMSCAN analysis

Block Code	Pyrite	Sphalerite	Barite	Anhydrite	Halite	Rutile & Ti Silicates	Tourmaline	Chromite	Apatite	Zircon	Monazite	Total
A	6.163	0	0.0872	0.199674	0.000370791	0.4264634	0.0274633	0.005368	1.0216	0.0947	0.010308	100

Macroporosity (%)	Grain Density (g/cm³)	Bulk Density (g/cm³)
8.50	2.74	2.60

RT 1 – WA26965
Depth: 1770 (m)
%TOC: 1.4 (%wt)
Porosity: 3.3 (%)
Permeability: 192.029 (nd)

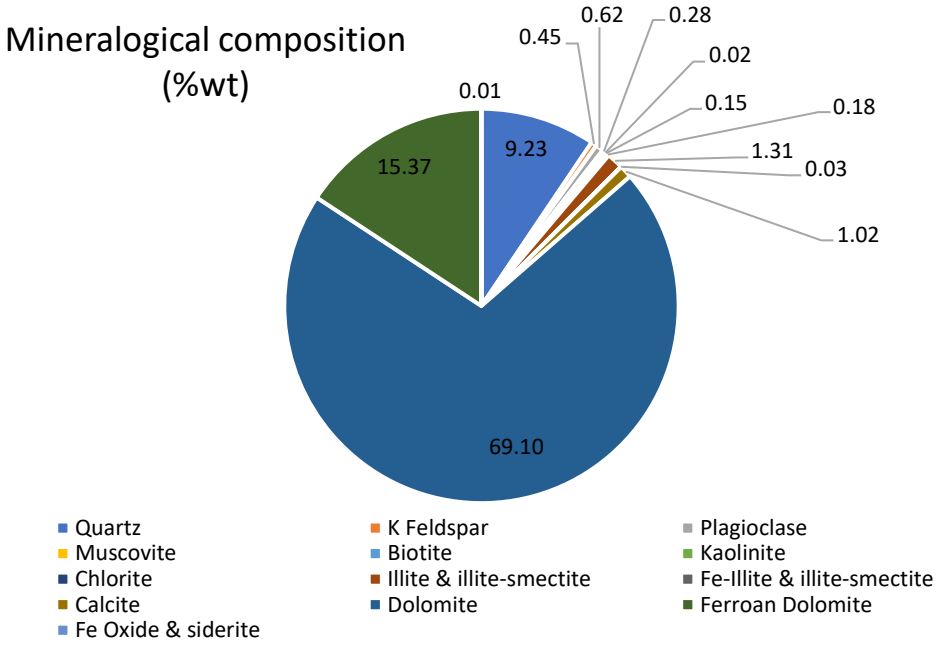

Mineralogical composition – data is in (%wt) – QEMSCAN analysis:

Block Code	Pyrite	Sphalerite	Barite	Anhydrite	Halite	Rutile & Ti Silicates	Tourmaline	Chromite	Apatite	Zircon	Monazite	Total
A	2.065	0.005413	0.0407	0.009228	0.000263645	0.0542648	0.0014352	0.00233	0.0483	0.0078	0	100

Macroporosity (%)	Grain Density (g/cm³)	Bulk Density (g/cm³)
2.25	2.87	2.82

RT 3 – WA2695
Depth: 1770.865 (m)

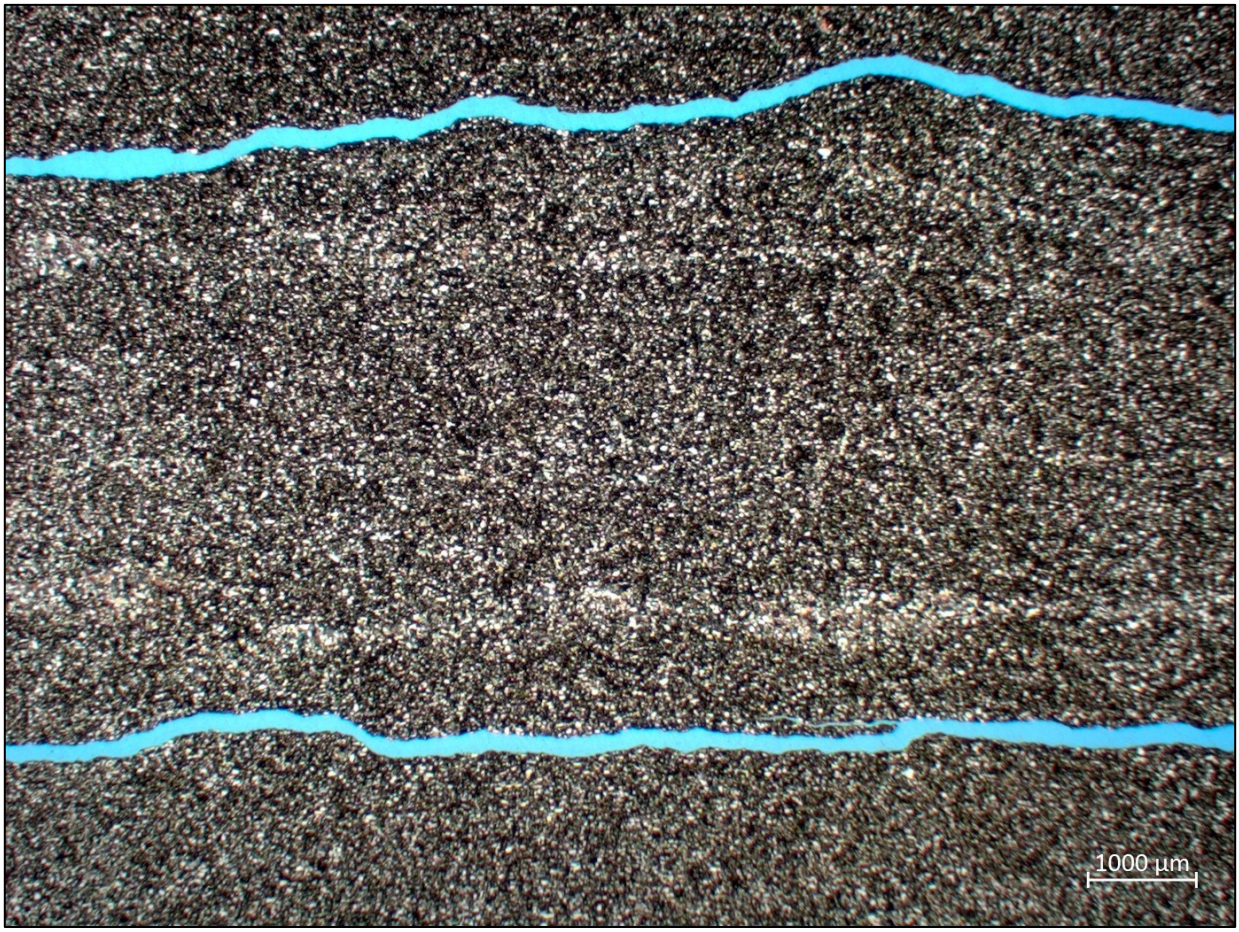

Thin section analysis:

Faintly to massive appearing dolomitic, calcareous siltstone. Pervasively occluded with a matrix clay and organic matter. At cleaner areas, it is cemented by Fe-dolomite/dolomite and in less amount calcite cement. Detrital framework grains include quartz, K-feldspar, and in less amount plagioclase and micas.

%TOC: 3.88 (%wt)

Permeability: 196.640 (nd)

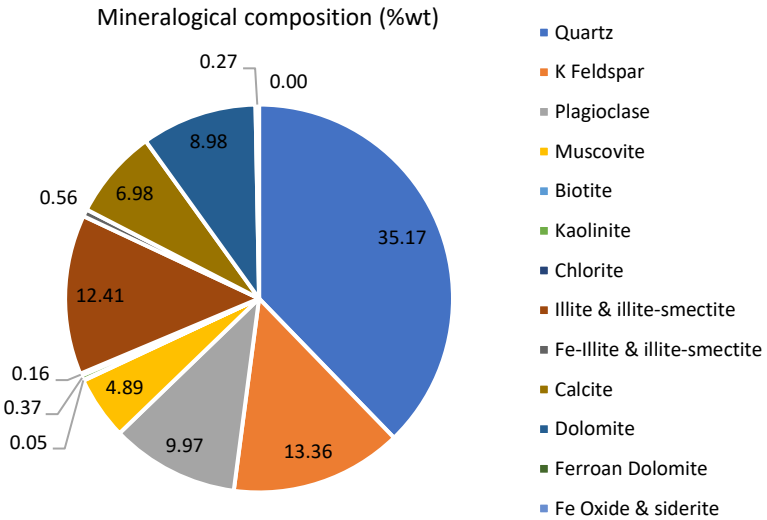

Additional images – RT 3

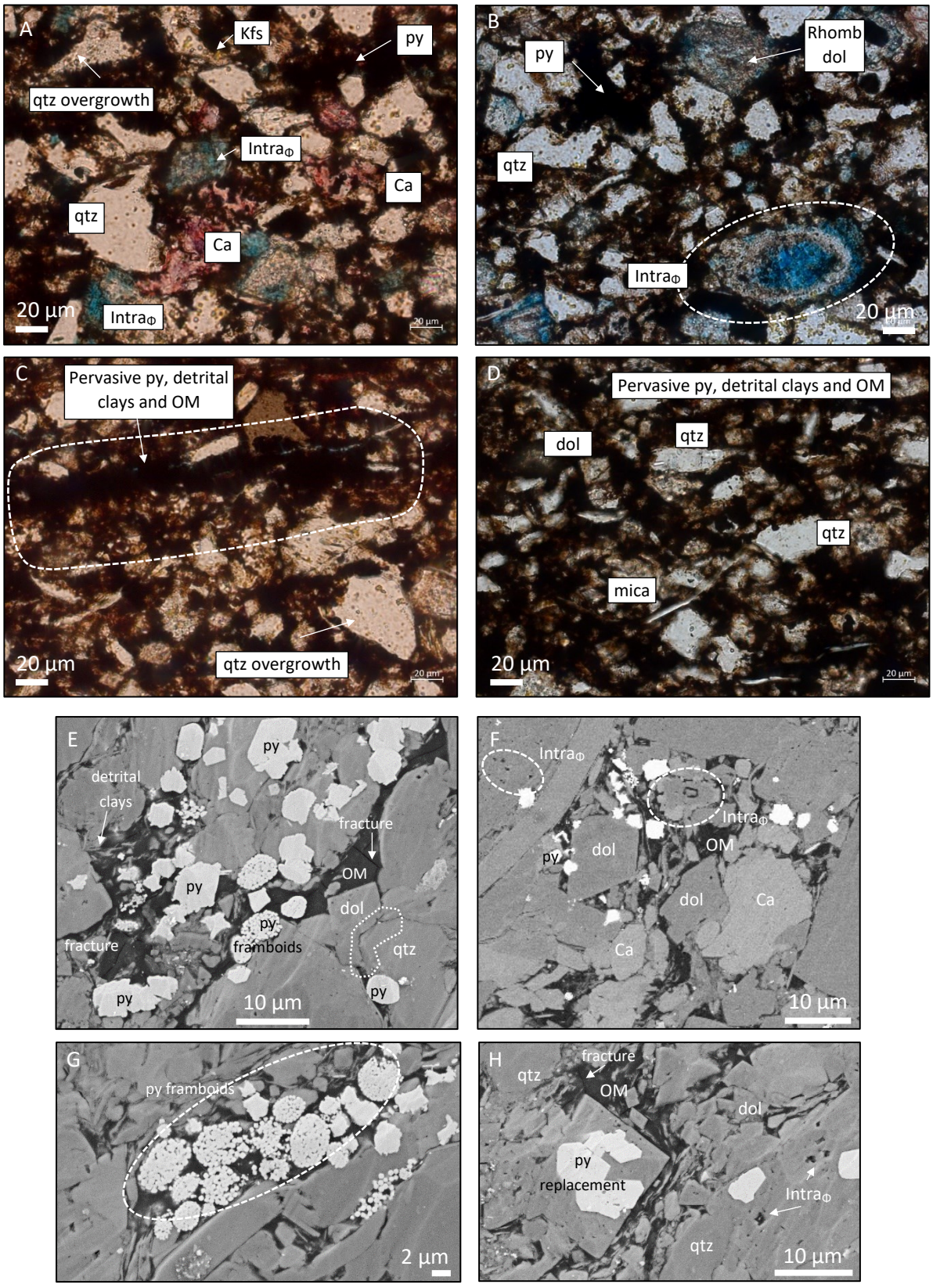

Mineralogical composition – data is in (%wt) – QEMSCAN analysis.

Block Code	Pyrite	Sphalerite	Barite	Anhydrite	Halite	Rutile & Ti Silicates	Tourmaline	Chromite	Apatite	Zircon	Monazite	Total
A	5.421	0.00462	0.0725	0.198259	0	0.4277143	0.0351459	0	0.595	0.0593	0.005875	100

Macroporosity (%)	Grain Density (g/cm³)	Bulk Density (g/cm³)
12.39	2.73	2.51

- **MICP**

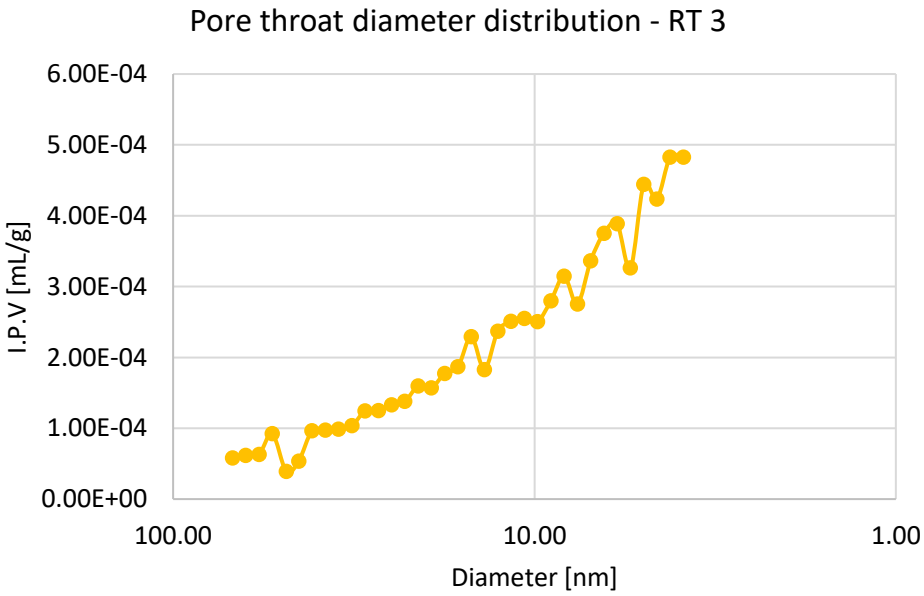

RT 3B – WA26965
Depth: 1776 (m)

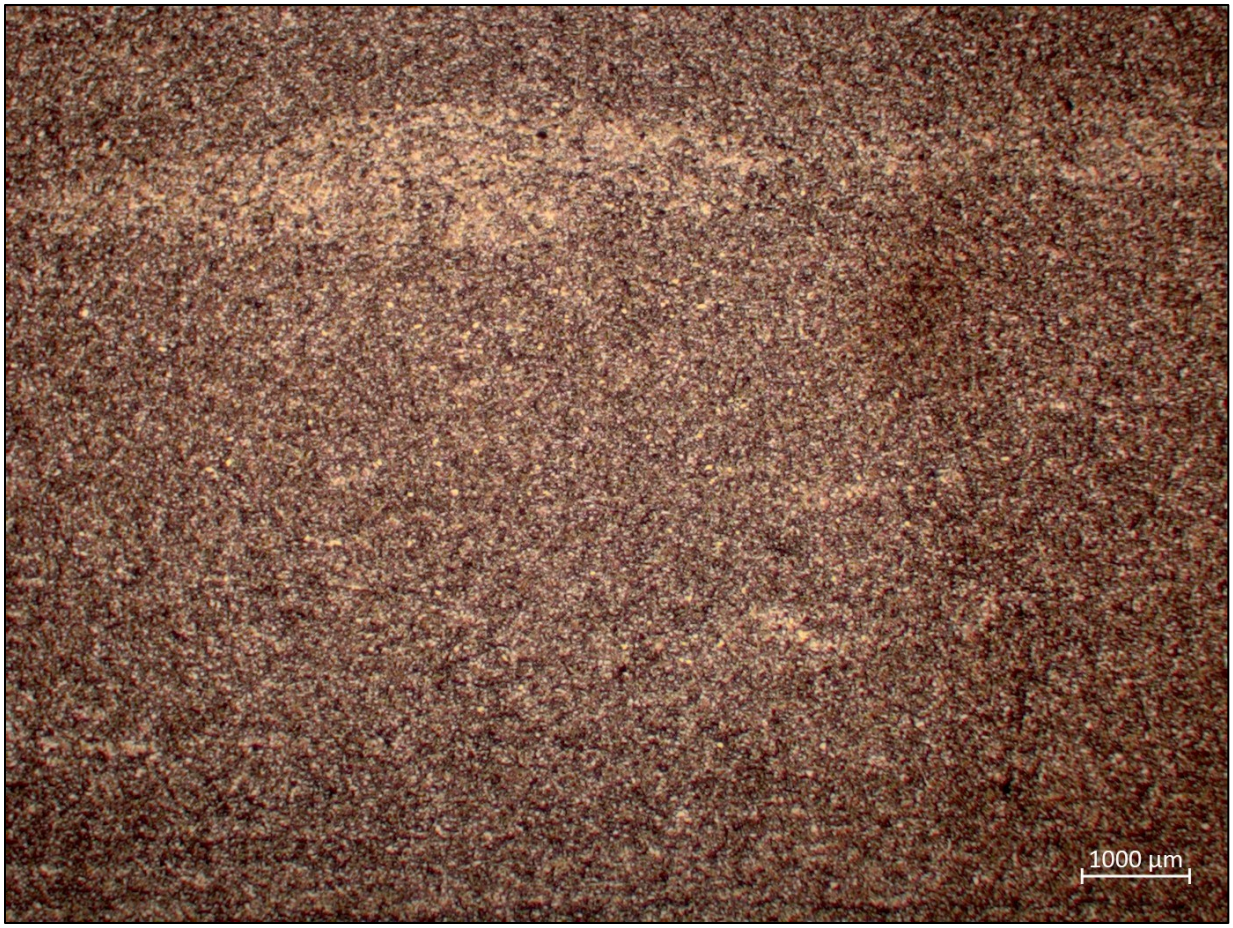

Thin section analysis:

Massive appearing, argillaceous dolomitic, calcareous siltstone. The main framework grain is comprised of quartz, with minor K-feldspar, plagioclase, and micas. The main cements present were dolomite/Fe-dolomite and in less amount calcite. Pyrite cement, detrital clays, and organics are noted occluding most of the pore space.

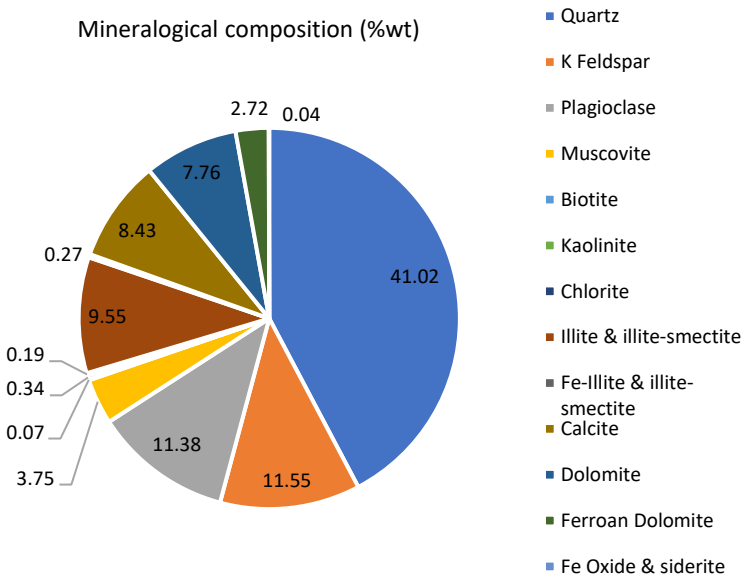

Additional images – RT 3B

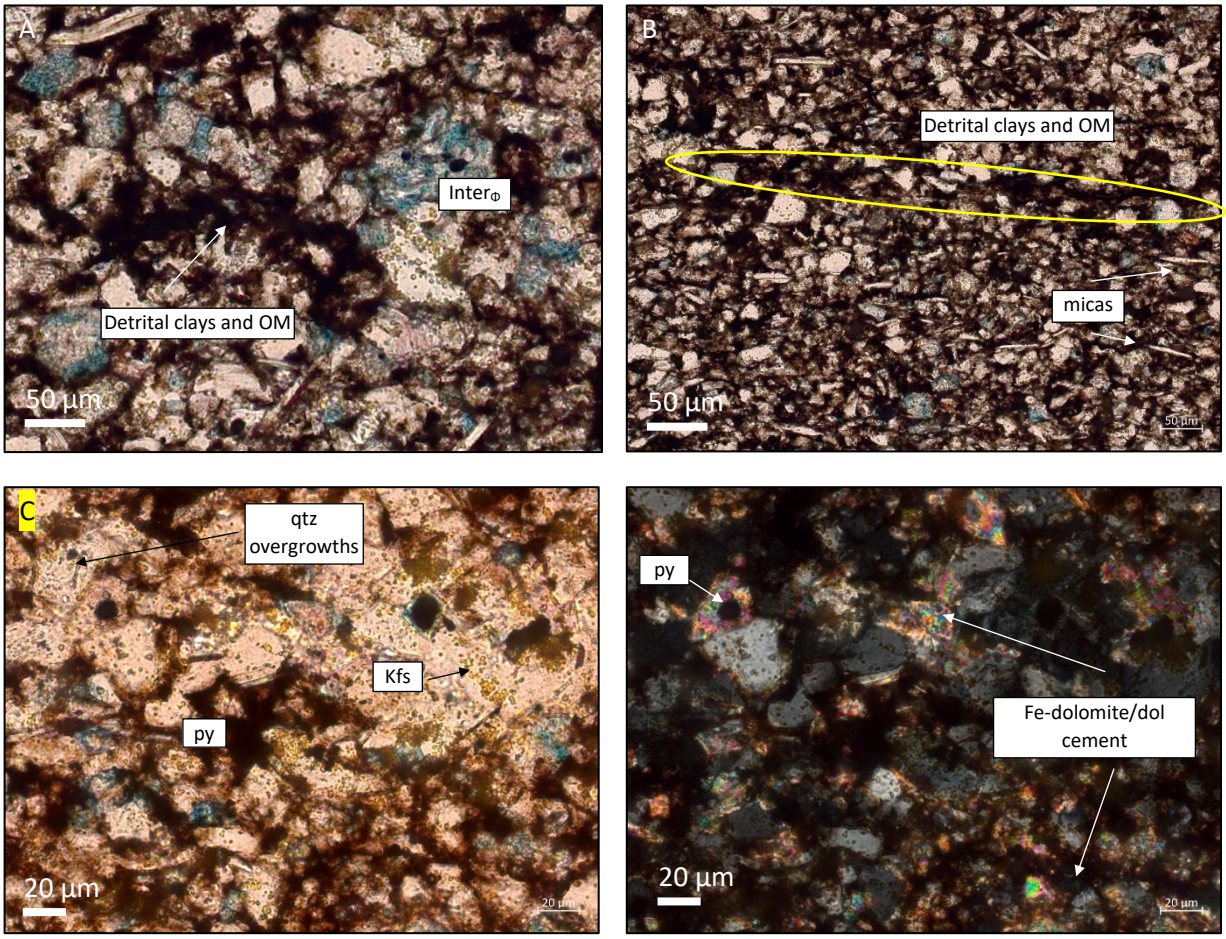

Mineralogical composition – data is in (%wt) – QEMSCAN analysis

Block Code	Pyrite	Sphalerite	Barite	Anhydrite	Halite	Rutile & Ti Silicates	Tourmaline	Chromite	Apatite	Zircon	Monazite	Total
A	1.509	0.000824	0.08	0.042254	0.002059797	0.4502171	0.0339582	0.001951	0.7454	0.0663	0.005936	100

Macroporosity (%)	Grain Density (g/cm³)	Bulk Density (g/cm³)
6.824	2.695	2.579

RT 4B – WA26965
Depth: 1867 (m)

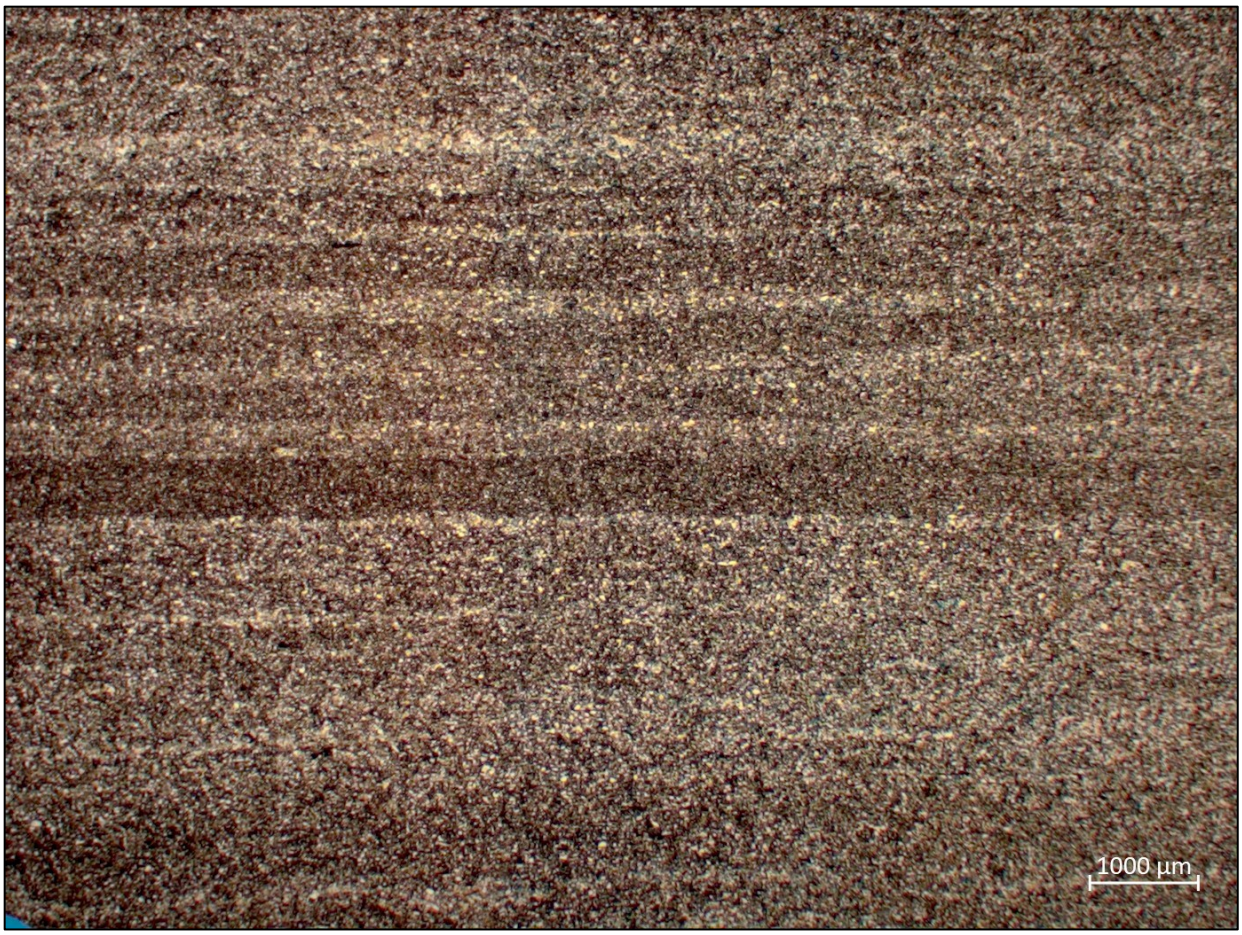

Thin section analysis:

Laminated to well laminated, argillaceous, dolomitic, calcareous siltstone. Interparticle porosity is noted within clay-lean, cemented areas as the clays reduce and occlude the rest of the pore space. Dominant cement types include dolomite/Fe-dolomite, calcite and minor quartz overgrowths, Framework grains are quartz with minor K-feldspar, plagioclase and micas. Pyrite replacement is noted.

%TOC: 1.02 (%wt)

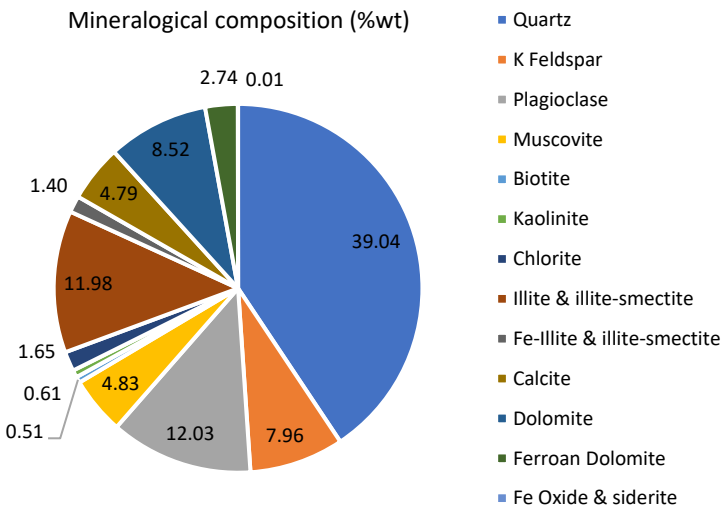

Additional images - RT 4B

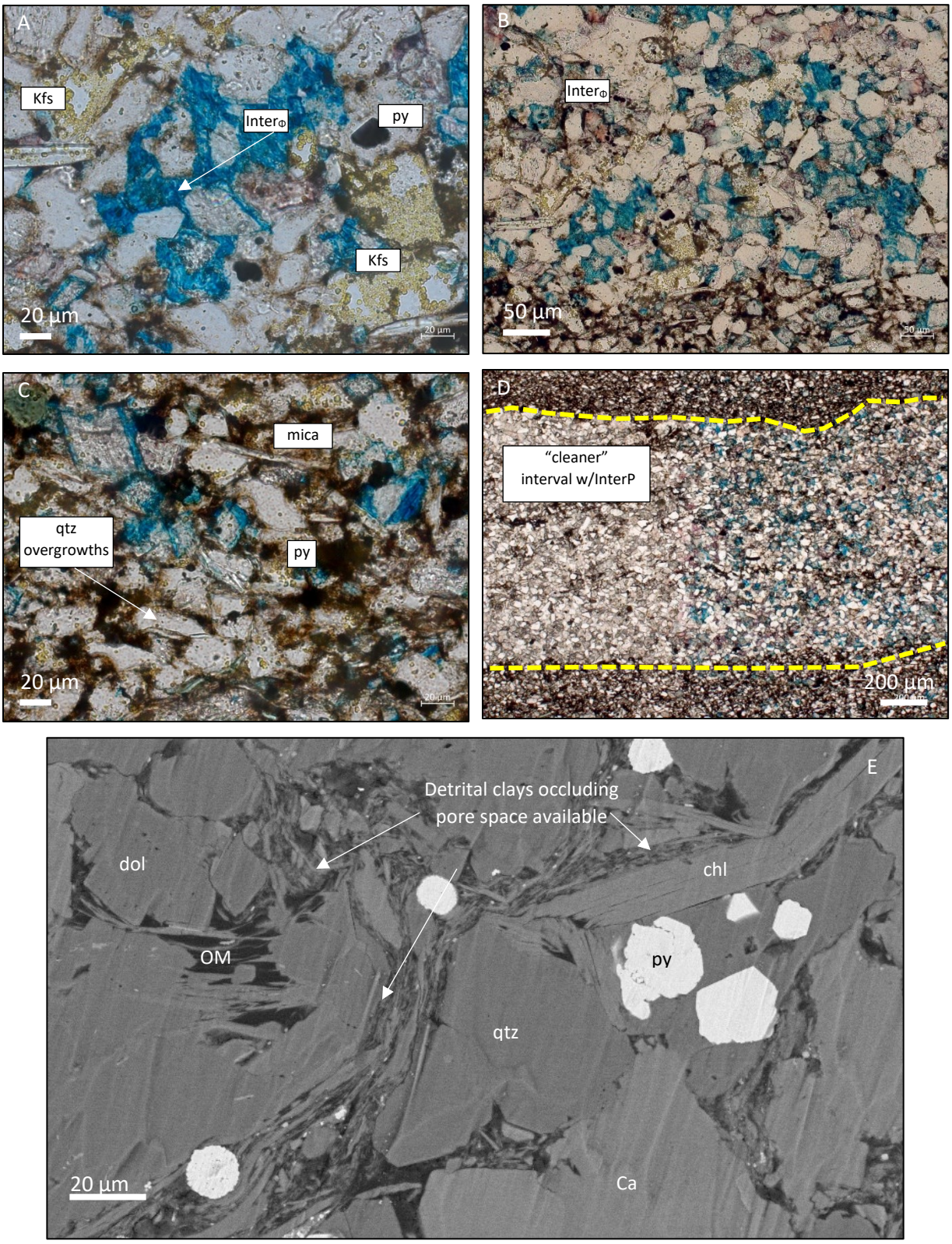

Additional data – RT 4B

Mineralogical composition – data is in (%wt) – QEMSCAN analysis

Block Code	Pyrite	Sphalerite	Barite	Anhydrite	Halite	Rutile & Ti Silicates	Tourmaline	Chromite	Apatite	Zircon	Monazite	Total
A	2.878	0	0.0713	0.04032	0	0.4907298	0.0471942	0.001696	0.3271	0.0581	0.006954	100

Macroporosity (%)	Grain Density (g/cm³)	Bulk Density (g/cm³)
2.5664	2.7181	2.6740

- **MICP**

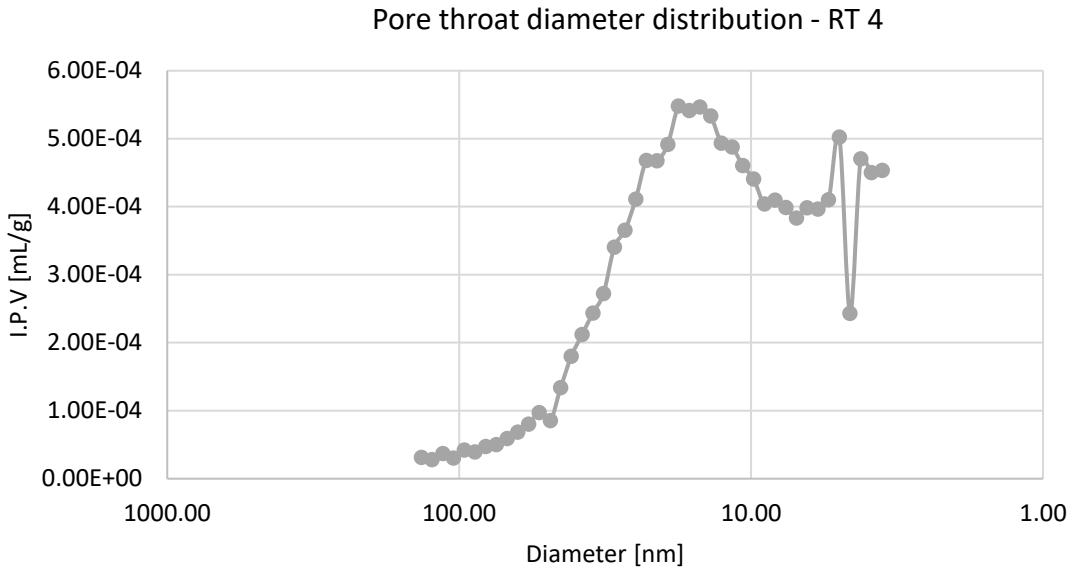

RT 4 – WA26965
Depth: 1870.4 (m)

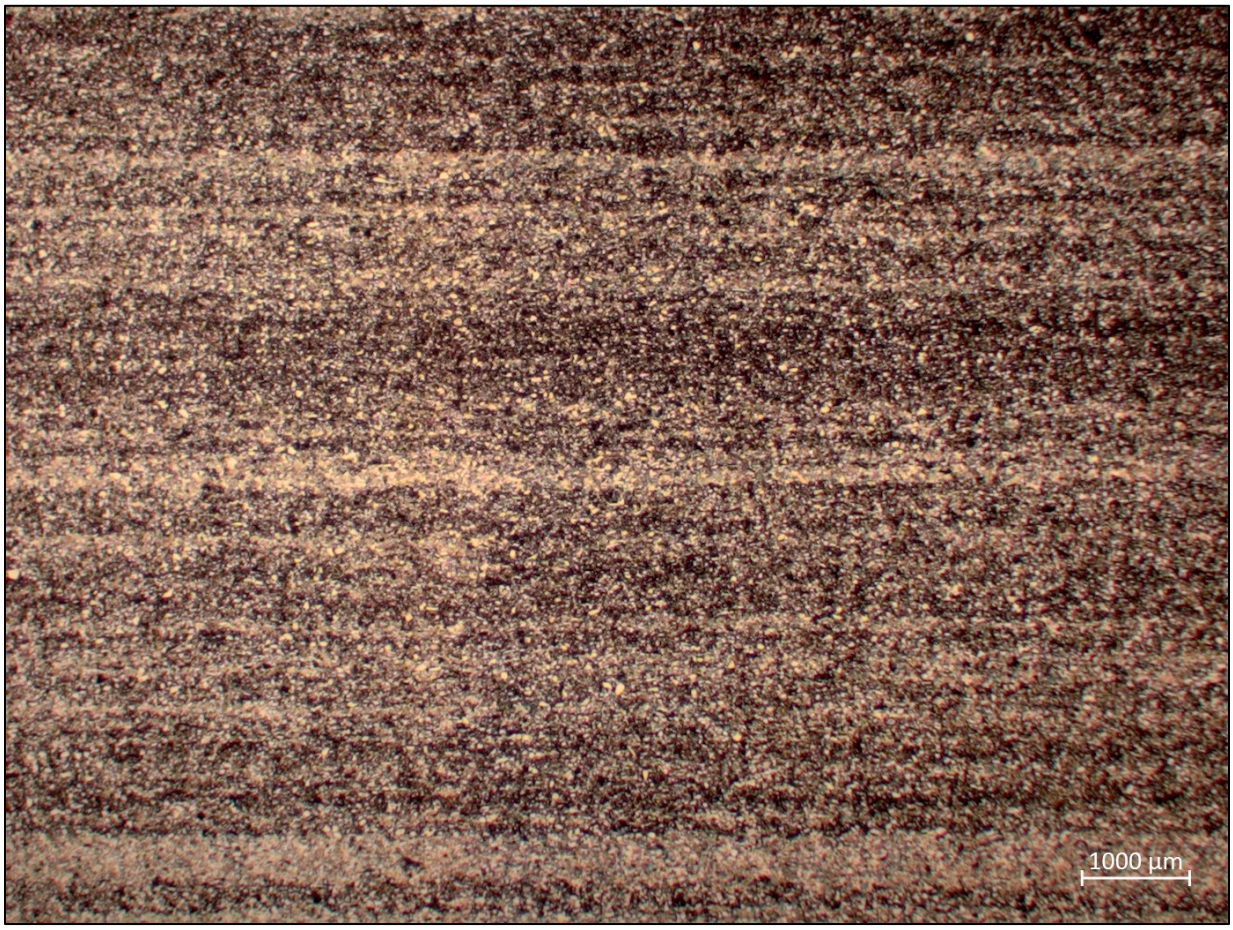

Thin section analysis:

Faintly laminated to laminated argillaceous, dolomitic, calcareous siltstone. Changes in grain size and clay content help define individual laminae. Slight bioturbation is observed at Macro scale as micritic mud. Framework grains are composed of quartz, with minor K-feldspar, plagioclase, and micas. Framboidal pyrite is noted

%TOC: 1.27 (%wt)

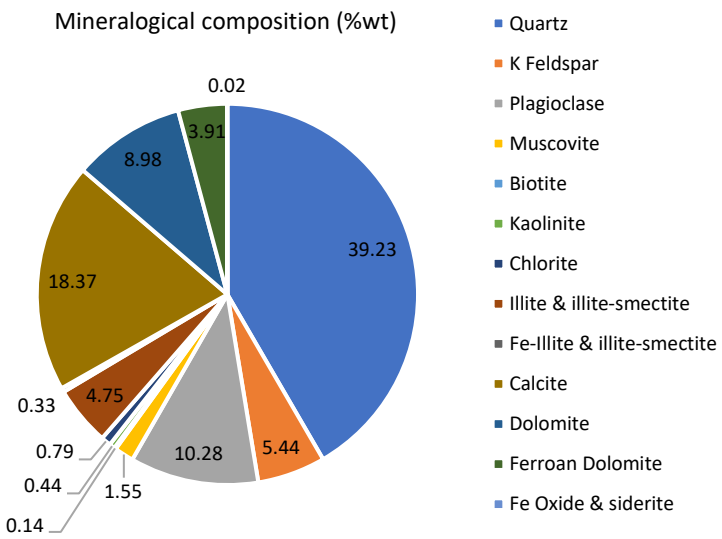

Additional images – RT 4

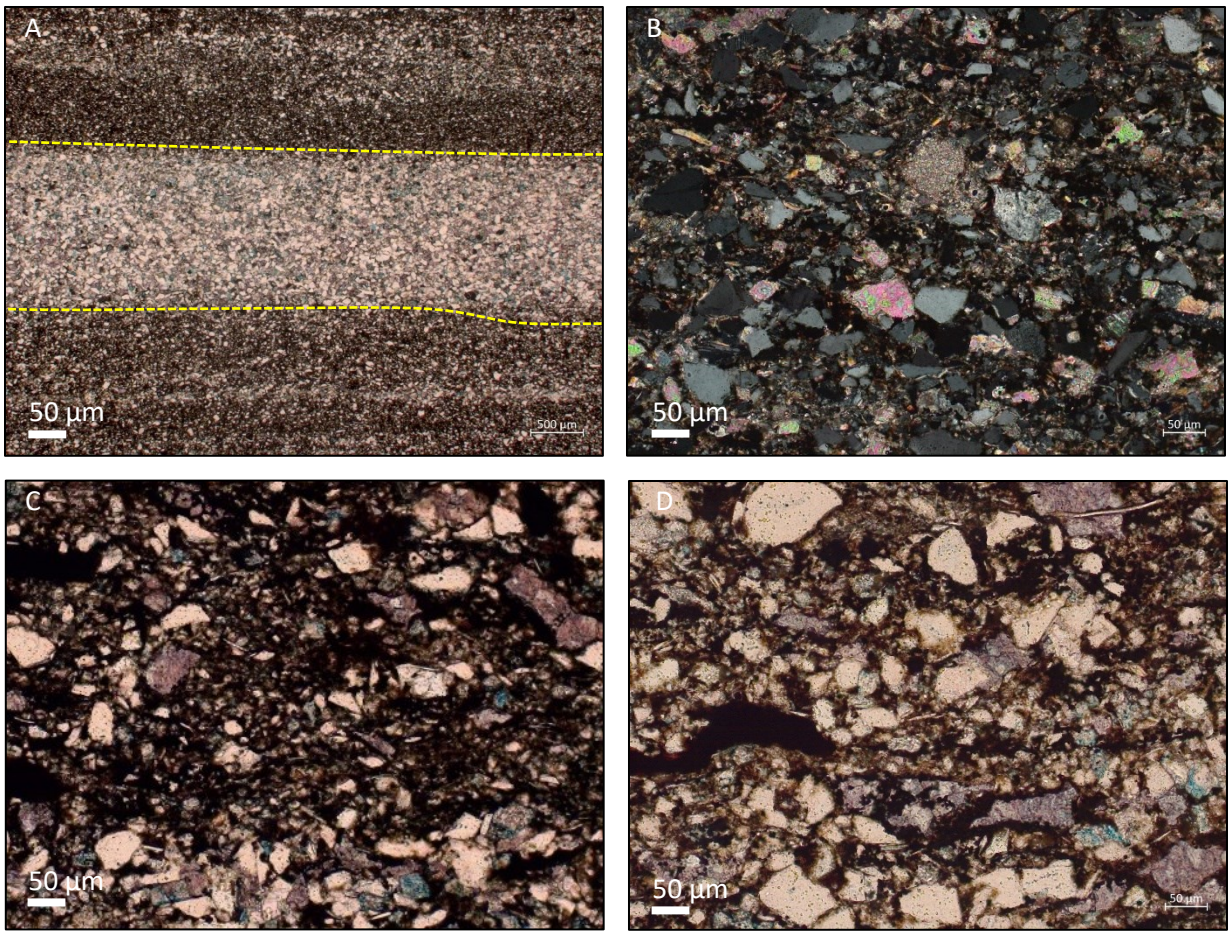

Mineralogical composition - data is in (%wt) – QEMSCAN analysis.

Block Code	Pyrite	Sphalerite	Barite	Anhydrite	Halite	Rutile & Ti Silicates	Tourmaline	Chromite	Apatite	Zircon	Monazite	Total	Macroporosity (%)	Grain Density (g/cm³)	Bulk Density (g/cm³)
A	4.364	0	0.0534	0.074805	6.86782E-05	0.3082288	0.0356905	0.004553	0.8874	0.0348	0.002119	100	1.838	2.742	2.710

- **MICP**

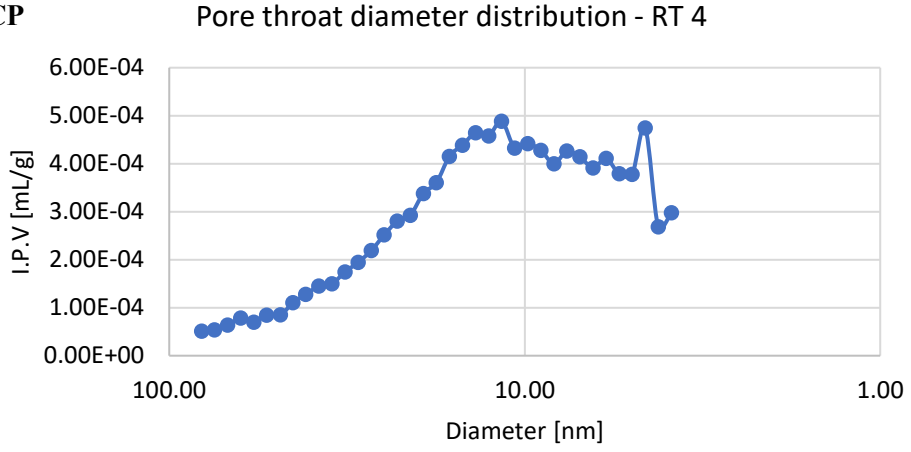

RT 4C – WA26965
Depth: 1873.4 (m)

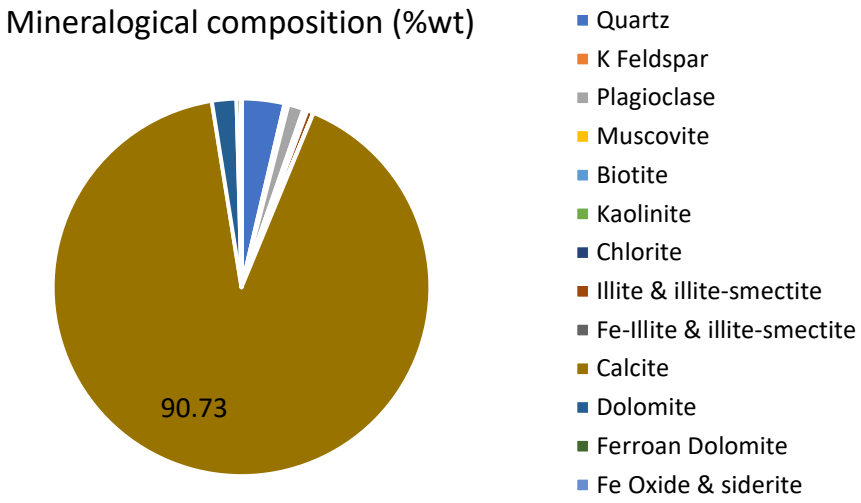

Mineralogical composition - data is in (%wt) – QEMSCAN analysis

Block Code	Pyrite	Sphalerite	Barite	Anhydrite	Halite	Rutile & Ti Silicates	Tourmaline	Chromite	Apatite	Zircon	Monazite	Total
A	0.402	0	0.0057	0.009035	0	0.0388757	0.0022815	0	0.097	0.0056	0	100

Macroporosity (%)	Grain Density (g/cm³)	Bulk Density (g/cm³)
0.403	2.713	2.707

- **MICP**

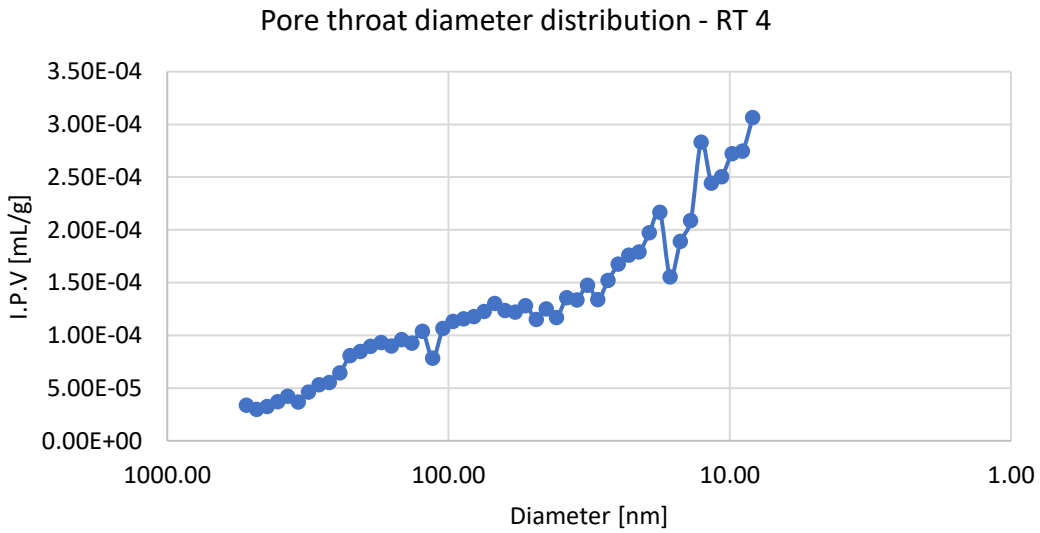

RT 4D – WA26965
Depth: 1878 (m)

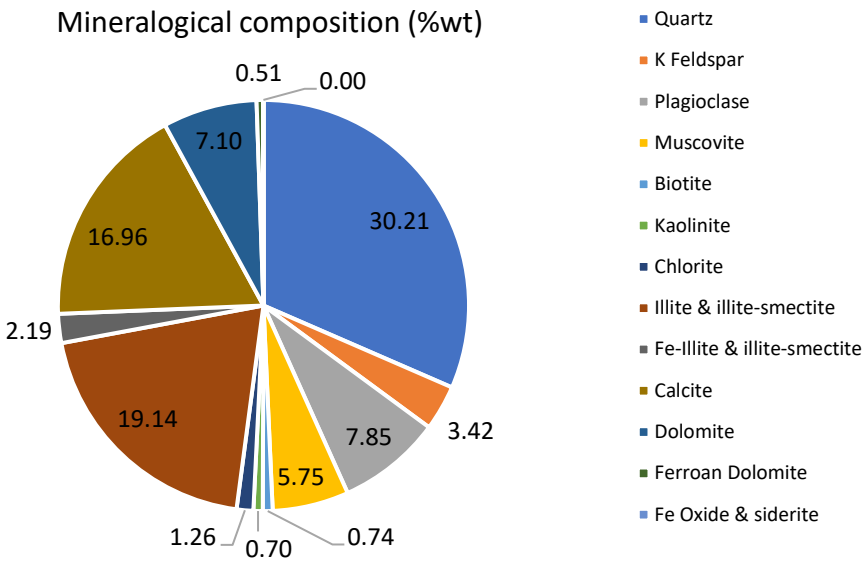

Mineralogical composition - data is in (%wt) – QEMSCAN analysis.

Block Code	Pyrite	Sphalerite	Barite	Anhydrite	Halite	Rutile & Ti Silicates	Tourmaline	Chromite	Apatite	Zircon	Monazite	Total	Macroporosity (%)	Grain Density (g/cm³)	Bulk Density (g/cm³)
A	3.353	0	0.0654	0.081922	0	0.2979808	0.0294223	0.00214	0.3004	0.0337	0.002463	100	1.954	2.723	2.690

RT 4A – WA26965
Depth: 1900.9 (m)

- MICP

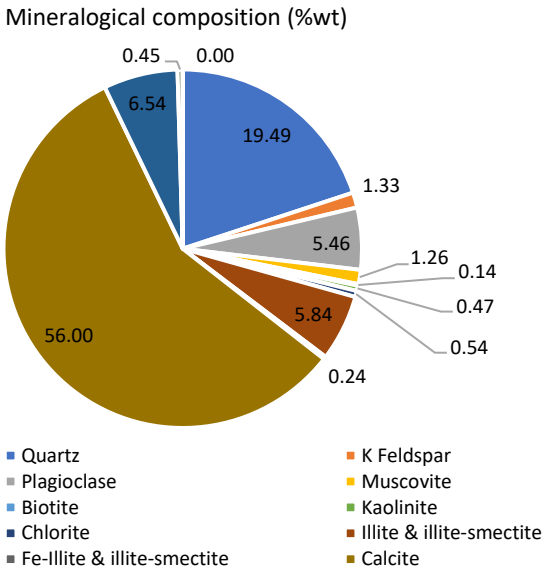

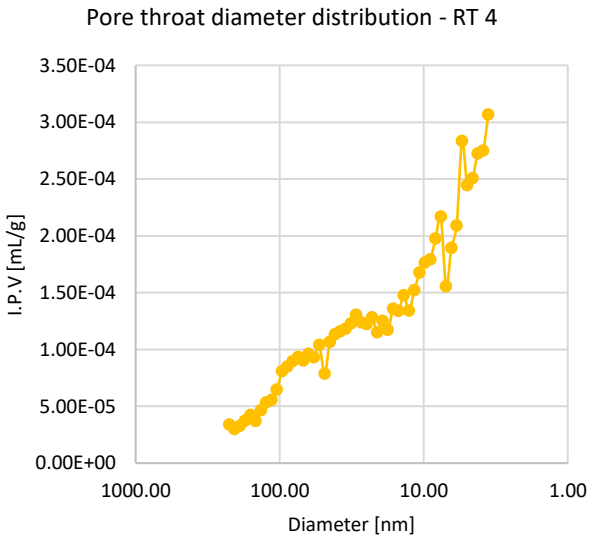

Block Code	Pyrite	Sphalerite	Barite	Anhydrite	Halite	Rutile & Ti Silicates	Tourmaline	Chromite	Apatite	Zircon	Monazite	Total	Macroporosity (%)	Grain Density (g/cm³)	Bulk Density (g/cm³)
A	1.6	0.001148	0.0137	0.103495	0	0.1894246	0.0142899	0.002266	0.2922	0.0149	0.00292	100	0.380	2.712	2.705

RT 1C – WA26965

Depth: 1885 (m)

Thin section analysis:

Faintly to very faintly laminated calcareous dolomitic, siltstone. At amplified magnification images showed interparticle porosity and in some intervals, grains are cemented by calcite. Detrital framework grains include quartz with minor K-feldspar, plagioclase, and micas.

%TOC: 0.745 (%wt)

Porosity: 2.2 (%)

Permeability: 101.218 (nd)

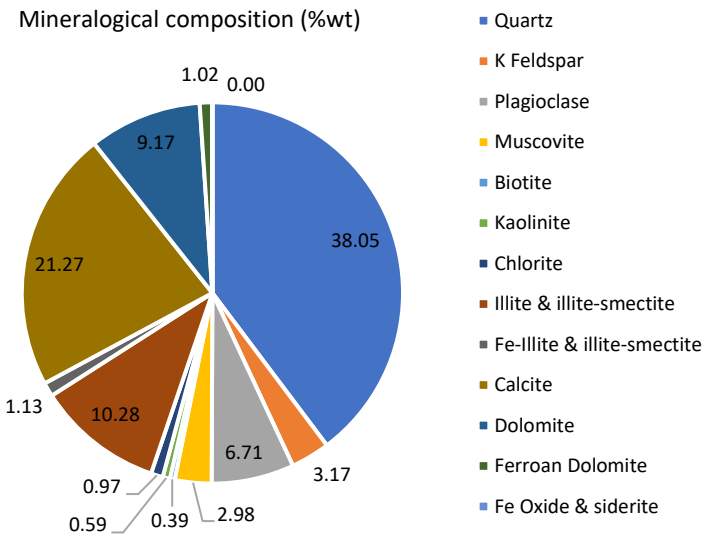

Additional images – RT 1C

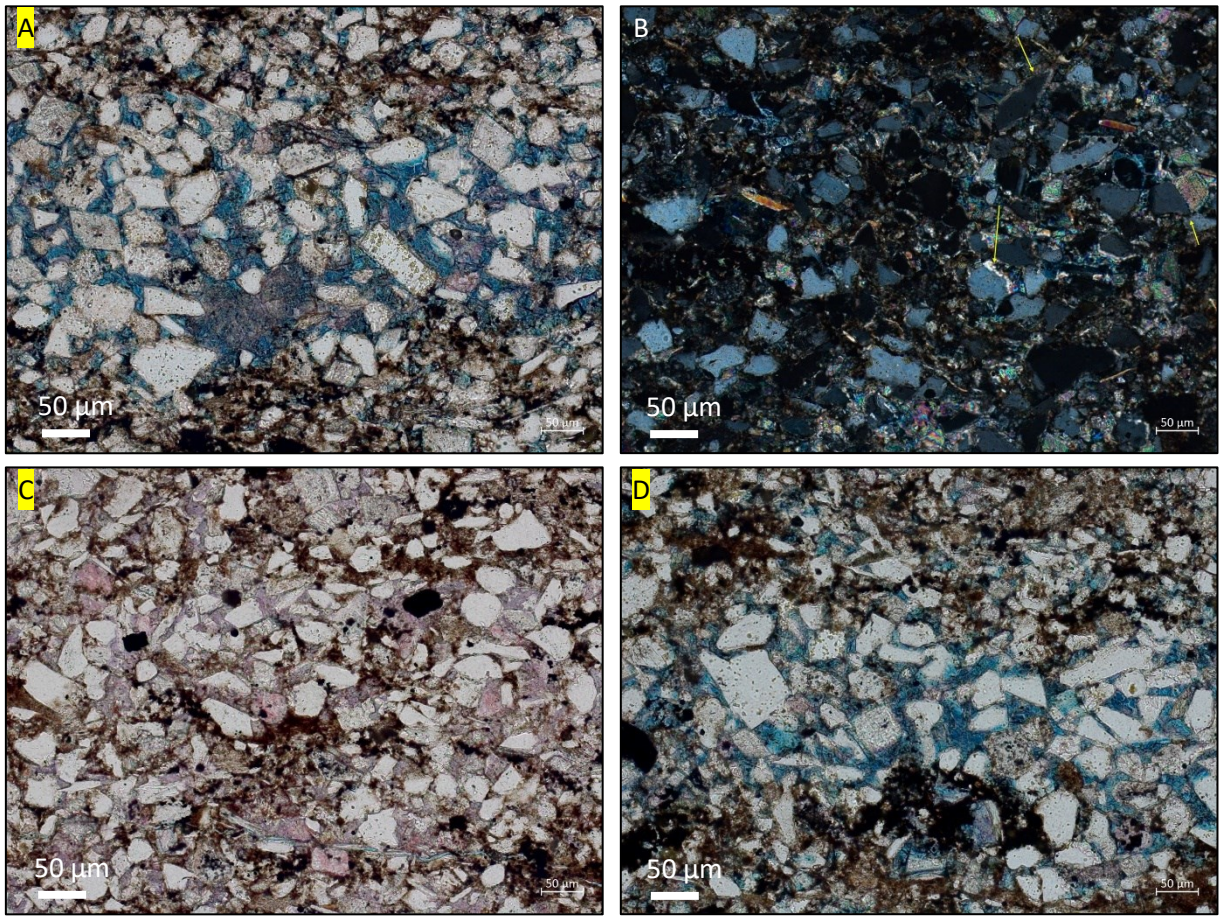

Mineralogical composition - data is in (%wt) – QEMSCAN analysis.

Block Code	Pyrite	Sphalerite	Barite	Anhydrite	Halite	Rutile & Ti Silicates	Tourmaline	Chromite	Apatite	Zircon	Monazite	Total
A	3.14	0	0.0421	0.253688	0.000137054	0.3733475	0.0325281	0.003634	0.3473	0.0544	0.00309	100

Macroporosity (%)	Grain Density (g/cm³)	Bulk Density (g/cm³)
1.013	2.723	2.705

RT 2B – WA26965
Depth: 1941.6 (m)

Thin section analysis:

Well laminated to laminated (minor bioturbation?), slightly argillaceous dolomitic, calcareous siltstone. Laminae have sharp basal contacts and are normally graded. Framework grains include quartz and plagioclase with minor K-feldspar and micas. At amplified magnification, grains are cemented by Fe-dolomite/dol. Detrital clays and organics are notice occluding the remanent pore space.

%TOC: 1.75 (%wt)

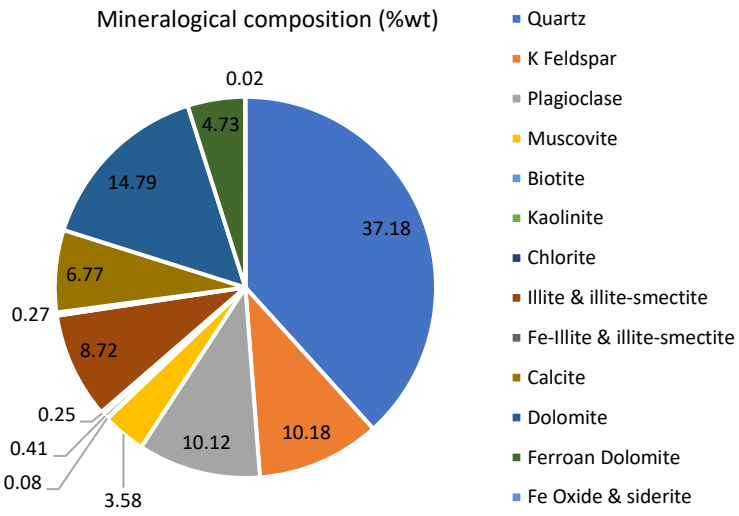

Additional data – RT 2B

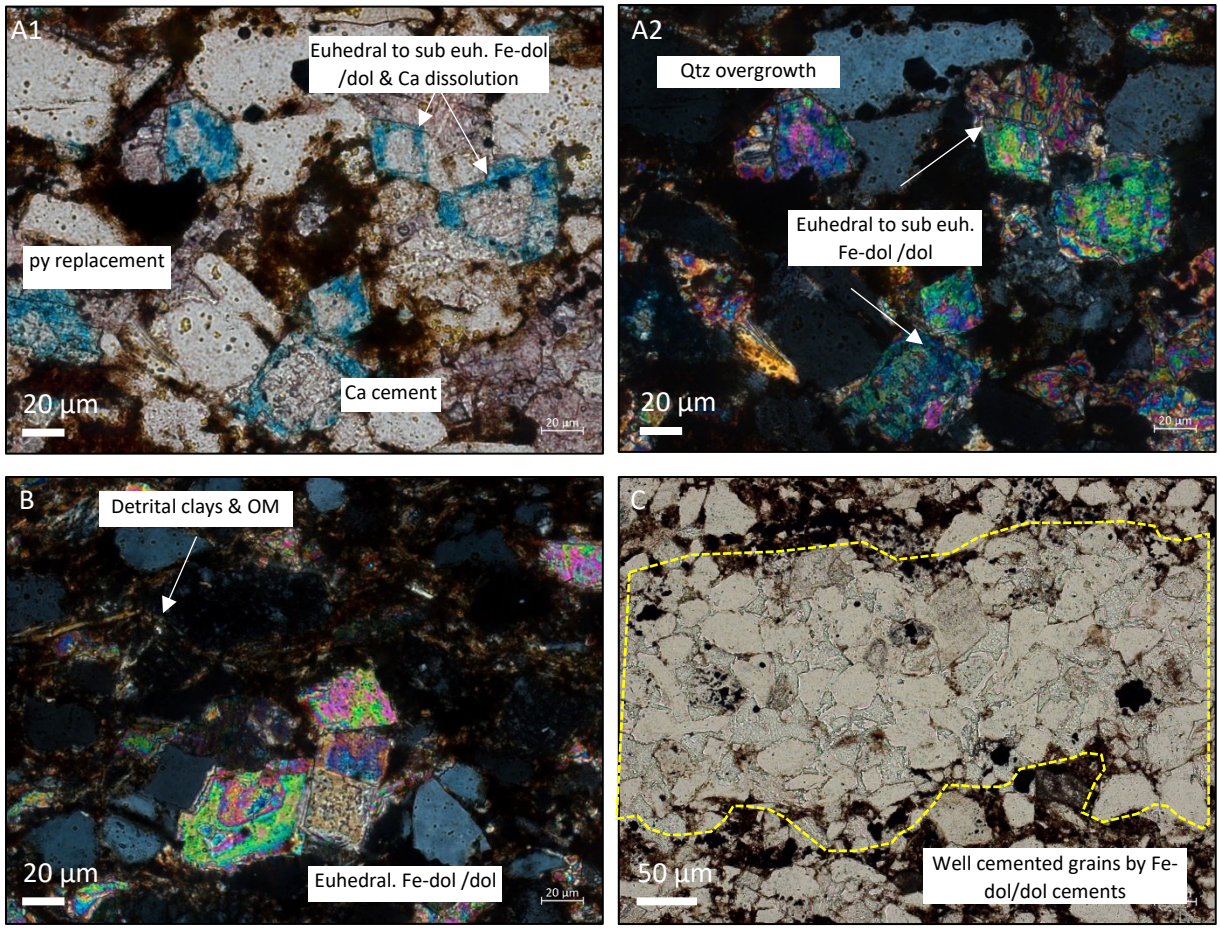

Mineralogical composition - data is in (%wt) – QEMSCAN analysis.

Block Code	Pyrite	Sphalerite	Barite	Anhydrite	Halite	Rutile & Ti Silicates	Tourmaline	Chromite	Apatite	Zircon	Monazite	Total
A	1.818	0.030544	0.0842	0.050471	0.000368587	0.4564665	0.0287855	0.001629	0.35	0.0838	0.003674	100

Macroporosity (%)	Grain Density (g/cm³)	Bulk Density (g/cm³)
7.746	2.717	2.584

- **MICP**